The University of Nottingham

MICROSTRUCTURAL CHARACTERISATION OF RUBBER MODIFIED ASPHALT MIXTURES

By

NORHIDAYAH ABDUL HASSAN

Thesis submitted to the University of Nottingham
for the degree of Doctor of Philosophy

November 2012

ABSTRACT

Research to improve the performance of asphalt mixtures through the addition of crumb rubber using the dry process has continued worldwide because of its potential as a recycling option for used tires. For decades, dry mixed rubberised asphalt mixtures have performed inconsistently in field trials and laboratory evaluations. However, current research has revealed that the performance of asphalt mixtures is highly dependent on the characteristics of its internal structure or phase constituents. A comprehensive methodology has been developed in this study to characterise the microstructural properties of dry mixed rubberised asphalt mixtures and correlate them with the mixtures' macroscopic response to compression and fatigue. The proposed methodology combines a non-destructive imaging technique; X-ray Computed Tomography (CT) and image processing and image analysis procedures to quantify the properties of air voids and cracks as well as the rubber distributions within the rubberised asphalt specimen. A gap graded mixture of Hot Rolled Asphalt (HRA60/20) containing different percentages and gradings of crumb rubber particles was compared to a conventional mixture (unmodified or control mix). The results showed that the addition of crumb rubber affects the formation and distribution of air voids in an asphalt mixture. Correlations between the internal structural damage parameters and the mechanical behaviour of the asphalt mixtures were unanimous in concurring that adding rubber improves a mixture resistance to fatigue failure. The modulus of the asphalt mixtures at peak stress under compression reduced when the rubber was introduced into the mixture although in contrast, the image analysis showed less fracture within the tested specimen in comparison to the control mix. The imaging procedures developed in this text are recommended as a guide to characterise the internal structure of rubberised asphalt mixtures.

ACKNOWLEDGEMENT

First and foremost, I would like to express my sincere appreciation to my main supervisor, Professor Gordon Airey for his continuous encouragement and guidance from the first day I applied for the PhD program. Besides his heavy work load, he still commits to ensure the success of this project. I owe him so much for all the support and for what I have learnt. I am also very thankful to Professor Andrew Collop, Dr Nick Thom (internal examiner), Professor Eyad Masad (external examiner), Dr Rawid, Dr Davide, Dr James and Dr Andrea for their valuable advice and critics.

Special thanks goes to numerous laboratory staff from Nottingham Transportation Engineering Centre, University of Nottingham who assisted in the conduct of the research especially with my laboratory works. Also, to all my friends who supported technically or emotionally and provided a pleasant environment for me in completing this project which I have an endless name list to write it here. I will always remember and pray for their success in life.

I would like to thank my husband, parents, brothers and sisters for their prayers and sacrifices to help me reach my goal. I am so lucky to have them in this world and may Allah bless them.

Last but not least I wish to acknowledge the support of University of Nottingham, United Kingdom and the Ministry of Higher Education, Malaysia who sponsored this study.

Thank you so much for all.

DECLARATION

The research described in this thesis was conducted at the Nottingham Transportation Engineering Centre, University of Nottingham between December 2008 and August 2012. I declare that the work is my own and has not been submitted for a degree of another university.

Norhidayah Abdul Hassan,

University of Nottingham,

November, 2012.

TABLE OF CONTENTS

LIST OF TABLES

LIST OF FIGURES

1.0 INTRODUCTION

1.1 Background and Motivation

For decades, waste tyre rubber has been used as an additive for constructing asphalt pavements. The use of rubber in bituminous materials started in the 1960's, at which point it became of interest to the paving industry because of its elastic properties which had the potential to improve the skid resistance and durability of asphalt mixtures (Esch 1982; Olivares 2009). The additional benefit of using rubber in the manner indicated above is that it creates an alternative or additional use of recycled waste tyres. Evidence from literature revealed that crumb rubber has been used to modify asphalt mixtures usually by employing two different processing methods. The first is the 'wet process', whereby fine rubber is blended with hot bitumen to produce a 'rubberised bitumen' binder. The second means of rubber modification is through the 'dry process' which substitutes a proportion of the mix aggregate with coarse rubber, thereby causing the rubber to function essentially as an elastic aggregate within the mixture (Heitzman 1992; Epps 1994). In this study, any mention of a rubber modified asphalt mixture or 'CRM mixtures' is made in reference to the dry process mixture.

Until recently, the design of CRM mixtures has been accomplished without any specification or official standard documentation. The asphalt mixture design modifications mentioned earlier, came into prominence as a result of several previous field trials and laboratory experiments. Studies by and Esch (1984), Schuler et al. (1986), Harvey and Curtis (1990), Heitzman (1992) and Khandal and Hanson (1993) evaluated the mechanical properties of dry mixed rubberised mixtures in terms of temperature susceptibility, moisture sensitivity,

permanent deformation and fatigue behaviour. Generally, both laboratory and field results show that CRM mixtures exhibit poor performance or show little improvement compared to wet process (rubber modified bitumen) or conventional asphalt mixtures. A detailed review is presented in Chapter 2.

Several laboratory based studies have been conducted to determine an appropriate aggregate gradation, design bitumen content or mixture preparation procedure capable of improving the consistently poor performance of a dry process originated mix (Esch 1984; Takallou et al., 1985; Chehovits et al., 1993). These studies found that mechanical properties of the mixtures formed through the dry process method are very sensitive to the changes in rubber content. Design criteria such as aggregate gradation, bitumen and air voids content were highlighted as the keys to success in designing a CRM mixture. Additionally, there are claims that a good laboratory mixture design is critical to obtain an optimum mixture with low air voids content and adequate stability. A lack of adequate space or gaps for the rubber particles to manoeuvre themselves within the mixture could result in large variations in air voids content due to the 'rubber swelling' phenomenon. This in turn has the potential to reduce the mixture mechanical performance as a result of specimen expansion following compaction. Although decades of research have been dedicated to the study of CRM mixtures, results produced have been largely inconsistent. Other studies highlighted that the performance of asphalt mixtures are influenced by their internal structure distribution (Tashman, 2003; Wang et al., 2003; Masad 2004; Qingli and Martin 2004; Hunter et al., 2004). For this reason, it is considered essential to investigate the internal structure properties, particularly the air voids and rubber distribution, which play a significant role in the overall performance of CRM mixtures. Based on this motivation, there is a need to further develop current knowledge and understanding of CRM mixtures by examining their

microstructural properties. It is also believed that the key to understanding the structure of the mixture is to investigate the structure on many scales simultaneously, particularly the microstructural characteristics and the mechanical behaviour.

Several successful attempts have been made to capture and quantify the internal structure of asphalt mixtures using imaging technology (Masad et al., 1999; Tashman et al., 2001; Masad et al., 2002; Wang et al., 2004). The imaging technology refers to X-ray Computed Tomography (CT) coupled with image analysis techniques. Previous studies have shown that the aforementioned techniques have contributed significantly to the study of damage evolution inside an asphalt mixture specimen under loading conditions (Braz et al., 1999; Tashman et al., 2004; Khan 2009). The X-ray CT has become a popular imaging tool choice primarily because of its ability to non-destructively permit the visualisation of the internal structure of the materials, in three-dimensions (3D). Moreover X-ray CT possesses a distinct advantage, in that the scanned specimen remains intact to enable further testing after the scanning process. Image analysis techniques are then used to extract relevant information from the X-ray images through the application of various mathematical procedures designed to characterise the internal structure properties of a scanned specimen. The majority of existing literature in the subject matter has revealed that for asphalt mixtures, X-ray CT has attained widespread application in the characterisation of air voids. Conversely there has been limited focus on the aggregate structure and the damage the material undergoes during deformation. To date, only a limited number of studies have been able to identify and separate the different material phases of asphalt mixture, shown in X-ray images, to the requisite standard to enable quantification. Recent studies by Zelelew and Papagiannakis (2011) and Kutay et al. (2010) propose some useful techniques for segmenting asphalt mixture compositions.

By applying the X-ray technology and an image analysis technique, it is possible to obtain more information concerning the microstructural properties of CRM mixture to account for its hitherto inconsistent performance as a pavement material. In principle this is very simple. Firstly, the X-ray CT is used to capture images of the internal structure of the laboratory compacted specimens. The images are processed to improve the image quality and then analysed to quantify the air voids distribution and rubber particles distribution as well as the damage nucleation (cracks) within the specimen. It is necessary to quantify the aforementioned properties in order to evaluate the effect or relative influences of different rubber contents, rubber sizes and mixture design procedures on the micro-properties of CRM mixtures. However, it should be noted that the purpose of this study is not mainly to produce better performing CRM mixtures but to better define the properties of the CRM mixture from the microstructural perspective.

1.2 Objectives and Methodology

The aim of this research was to investigate CRM mixtures at the micro-level using X-ray CT combined with image analysis techniques. This coupled approach was expected to develop a thorough and in-depth understanding of the internal structure of CRM mixtures to improve performance evaluation in a laboratory environment. The aim was achieved through the following objectives:

i. The development of imaging and thresholding techniques to analyse the microstructure of CRM mixtures, specifically in relation to aggregates, air voids, mastic and crumb rubber content.

ii. A study of the effect of mixture design variables, particularly the rubber addition, on the microstructure properties of CRM mixtures.

iii. Investigation and quantification of the nucleation of microstructural damage in CRM mixtures subjected to loading.

Figure 1.1 illustrates the research methodology employed in a flow diagram. Preliminary studies were conducted to clearly define the scale and scope of the problem being investigated as well as to establish the objectives of the study. A detailed literature review and preliminary investigation were comprised of two main tasks. The first task was to verify the materials and proper mixture design for the dry process method based on recommendations from the previous studies. Second task was to understand the application of X-ray CT imaging study by conducting a few trial scans on the laboratory prepared specimens. This was important to identify the materials (aggregate, crumb rubber, bitumen and filler) with properties that fulfill the needs of getting the best X-ray images and mix design criteria. A set of experimental works was undertaken to measure the properties of the selected materials and to produce the compacted specimens for the next level of investigation. The specimens were then subjected to X-ray CT scanning for image analysis study to establish complete procedures for image processing and image analysis. Following the X-ray CT scanning, the study was divided into two main investigations regarding the internal structure of CRM mixture in undamaged and damaged states.

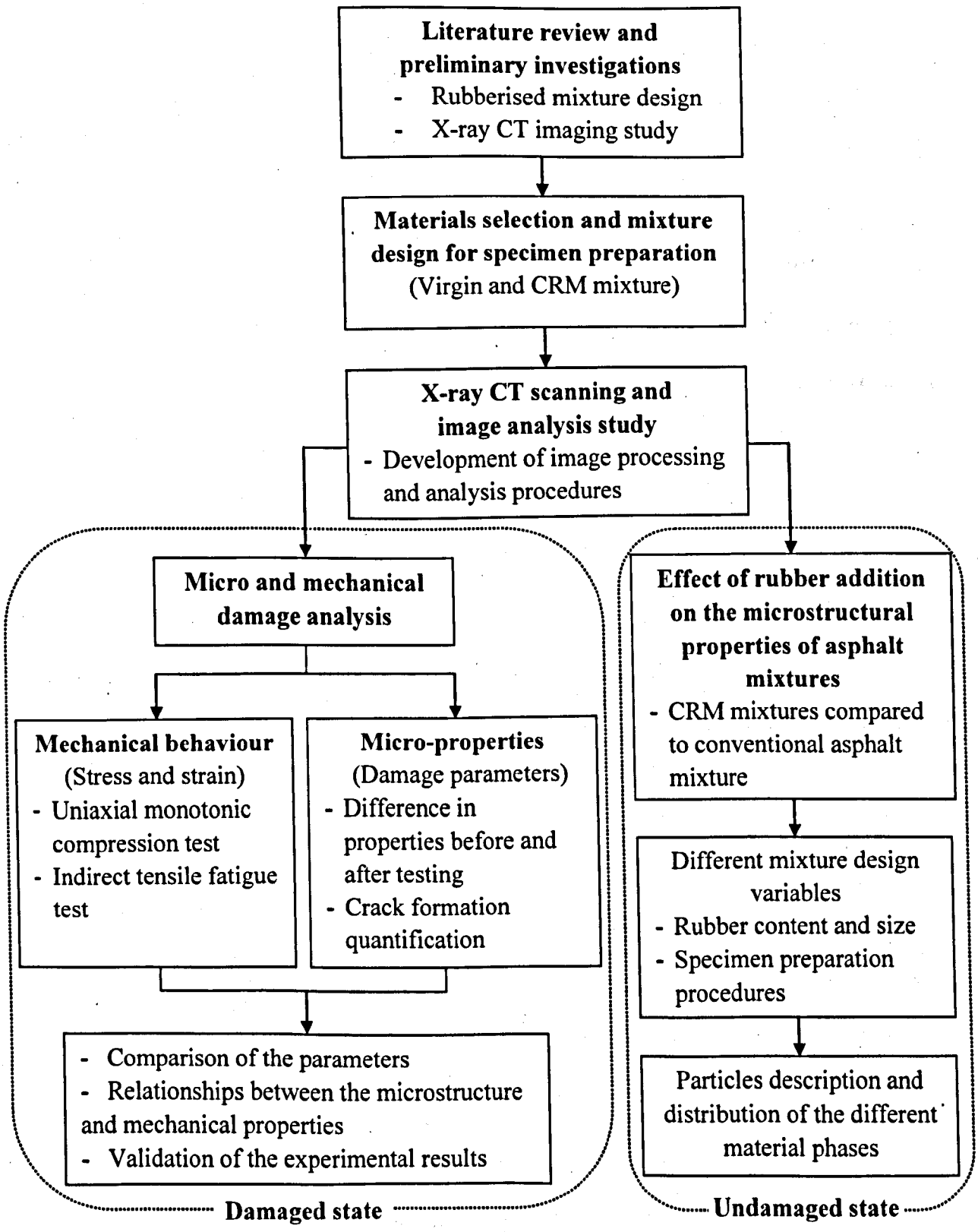

Figure 1.1 Research methodology

The first investigation was to assess the effect of rubber addition on the microstructural properties of asphalt mixtures. This was to correlate the different in mixture design variables to the changes in the internal structure properties. Second investigation focused on the micro and mechanical damage analysis. This is to find the relationship between the mechanical behaviour observed from the mechanical test and the analysed micro-properties from the X-ray images. Two laboratory tests, the Uniaxial Monotonic Compression Test and Indirect Tensile Fatigue Test, were conducted to obtain the stress and strain data (damage indicator). These tests were selected in order to simulate the two failure types of asphalt mixture i.e. under compression and tension stress for the purpose of establishing methods to characterise the damage obtained from the X-ray images. In addition, the fatigue test was undertaken to investigate the improved fatigue properties of the rubberised mixture as reported by previous studies. The specimens were X-rayed before and after testing. The damage parameters measured from the image analysis were then compared and correlated to the mechanical test results. The reliability of the experimental results was validated using specimens' replicates and statistical analysis.

1.3 Significance and Contribution to Knowledge

The majority of existing research on asphalt mixture properties typically concentrates on evaluating its macroscopic behaviour while its microscopic properties are often ignored. One of the main problems in accounting for the effect of microscopic properties of asphalt mixtures is the difficulty associated with capturing the complex microstructure of the mixture. However, advances in imaging technology have made this possible. The current technology of X-ray CT is exceptionally useful for the non-destructive capture of microstructure images, thereby facilitating the uncompromised mechanical testing of a

specimen afterwards. X-ray CT scanning is also beneficial for characterising the microstructure of asphalt mixtures which consists of three basic phases; air void, aggregate and mastic. Although these materials vary considerably in their composition, X-ray CT has proven to be a suitable tool for investigating their microstructural properties within a complex internal structure.

X-ray CT has been used in numerous studies to characterise the air voids distribution in asphalt mixtures. Many studies have used X-ray CT to characterise the coarse aggregates as it is perceived to have more potential to be used over the destructive technique (by the cutting method) for viewing the aggregate structure. This is possible due to the difference in the densities of the air voids and aggregate rendering the region of interest easily distinguishable from the background image. In this study, characterising the rubber particles within an asphalt mixture is seen as an important and relevant step in the discovery and development of a new potential application of X-ray CT imagery and image processing techniques for the characterisation of composite materials.

The introduction of a new material phase (rubber) into the basic asphalt mixture composition (of air voids, aggregates and mastic) can be said to add another dimension to the capability of imaging technology. Despite the advantages highlighted above, material phase detection can become complicated when rubber is introduced. This is because the density of the crumb rubber lies between that of the air voids and aggregate and is almost the same as bitumen. Consequently, extracting the image of rubber particles from the background image requires the utilisation of a comprehensive image processing technique. Doing this will signify a breakthrough in the otherwise limited use of image analysis techniques to extract any region of interest in a composite material directly from X-ray images. Until now, no study is known

to have investigated the microstructural properties of rubber modified asphalt mixtures. Similarly, there is little or no evidence of studies referring to the use of imaging techniques for investigating the above-mentioned mixture type. The majority of previous studies on rubberised asphalt mixtures were found to typically focus on evaluating their mechanical performance for pavement application.

This study reviews the application of imaging techniques in conventional asphalt mixtures, which currently have been widely studied and through this, fundamental ideas for characterising the CRM mixture are developed. Furthermore, a set of image analysis techniques has been established to process and analyse the CT image of the internal structural features within the CRM mixture. Therefore the study is expected to enhance insight into CRM mixtures from a microstructural perspective using X-ray CT technology. This was to introduce the internal structure of CRM mixtures and to demonstrate how they can be non-destructively characterised. Different variables in the mixture design used, such as the rubber content and rubber sizes, help to establish some information on the effect of rubber addition on the microstructural properties of asphalt mixtures. In addition, different testing conditions, such as testing temperatures and level of stress applied under compressive and fatigue tests, allow for performance evaluation of the CRM mixture over the conventional mixture. Based on the image analysis utilised, the X-ray CT images yielded a few damage parameters that were used to quantify cracks and air voids properties in the specimen after testing. The microstructure damage parameters are then quantitatively related to the mechanics that account for the structure of the CRM mixture obtained from the mechanical test (stress and strain). Overall, characterising the microstructure properties of CRM mixture provides valuable information for improving the dry process mixture design and increasing the potential of using crumb rubber in asphalt mixtures.

1.4 Thesis Outline

This thesis consists of eight chapters. Chapter 1 is an overall introduction to this study, detailing the background, objectives, and methodology of the research. It also explains the research's significance and the expected contribution to knowledge. In Chapter 2, a literature review on the properties and the use of crumb rubber in asphalt mixtures is presented. In particular, the concept of dry mixed rubberised mixtures, their mix design criteria and inconsistencies in mechanical performance. Finally, this chapter presented the recommended mixture design procedures for specimen preparation. Chapter 3 provides further details of the X-ray CT imaging method and its applications, as well as digital image processing techniques used for viewing the internal structure of materials particularly asphalt mixture. This chapter also reports on the preliminary trials that have been carried out on X-ray images of CRM mixtures for particles segmentation. Chapter 4 presents the stereological concept, image analysis for microstructure quantification with some reviews on previous studies on microstructural characterisation and damage quantification of asphalt mixtures. Chapter 5 explains in detail, the materials selection procedure and experimental programme employed, including the specimen preparation method and mechanical testing procedures. Chapter 6 reports and discusses the characterisation process of the rubberised asphalt mixture properties in its undamaged state. The focus of the discussions, centre predominantly on the effect of different mixture design variables on the microstructure properties. In Chapter 7, the results of the characterisation of the rubberised asphalt mixture properties in its damaged state are reported. Here also, the damage parameters derived from the image analysis are correlated with the stiffness results from the mechanical tests. In Chapter 8, the study is concluded, with recommendations also provided for subsequent work.

2.0 REVIEW OF CRUMB RUBBER MODIFIED ASPHALT MIXTURES

2.1 Introduction

This chapter provides an overview of the background of rubber modified asphalt mixtures with particular reference to the dry process. The dry process involves first blending rubber with hot aggregates prior to mixing with bitumen. The discussions presented henceforth (in relation to the aforementioned) include terminologies associated with the dry process as well as an explanation of the process of preparing rubber modified asphalt mixtures using the dry mix method. Furthermore, details pertaining to rubber modified asphalt mixtures design are also discussed with sufficient information from previous research. This is done to aide in proposing appropriate design guidelines useful for the preparation of rubber modified asphalt mixtures that can be evaluated mechanically in the laboratory. Finally, the review focuses on the mechanical performance of dry mixed rubberised asphalt mixtures based on laboratory and field experiences to better understand the mixture properties.

2.2 Crumb Rubber as Modifier in Asphalt Mixtures

Crumb rubber is a recycled rubber obtained by the mechanical grinding of scrap tyres into small particles. The use of crumb rubber in asphalt mixtures can be traced back to the 1840s, when natural rubber was first introduced into bitumen to enhance the binder's elastic properties (Heitzman 1992). Since the 1960s, researchers and engineers have used shredded automobile tyres in asphalt pavement. Several terminologies are associated with crumb rubber modified asphalt mixtures. Some of the commonly used terminologies include

asphalt rubber, rubber modified asphalt concrete and rubberised asphalt. The differences in the terminologies typically relate to the method by which the mixture is prepared. Currently, there are two main processes by which crumb rubber is introduced into asphalt mixtures, namely the 'wet' and 'dry' process. The wet process involves adding rubber (of at least 15% by weight of the total blend) into bitumen to produce rubberised bitumen (Figure 2.1). The modification is formulated to enhance the bitumen properties through the physical and chemical bonding of bitumen and rubber at elevated temperatures. The end product of this method is termed 'Asphalt Rubber (AR)'.

Figure 2.1 Wet process method

In the dry process, the rubber is first blended with hot aggregates before it is intimately mixed with bitumen (Figure 2.2). This process essentially modifies the dense and gap graded aggregate mixtures to which crumb rubber is added to as a substitute for a proportion of the aggregate component. The proportion of crumb rubber used varies from 1% to 3% of the total weight of the mixture or sometimes of the total weight of aggregate. The end product of the dry process produces what is often called 'Rubber Modified Asphalt Concrete' (RUMAC) or CRM mixture (Schuler et al., 1986). There are several other terminologies associated with dry-mixed rubber modified asphalt mixtures such as PlusRide, Generic and

Chunk rubber technologies. In this research, only the PlusRide and Generic methods were discussed further in the following sections.

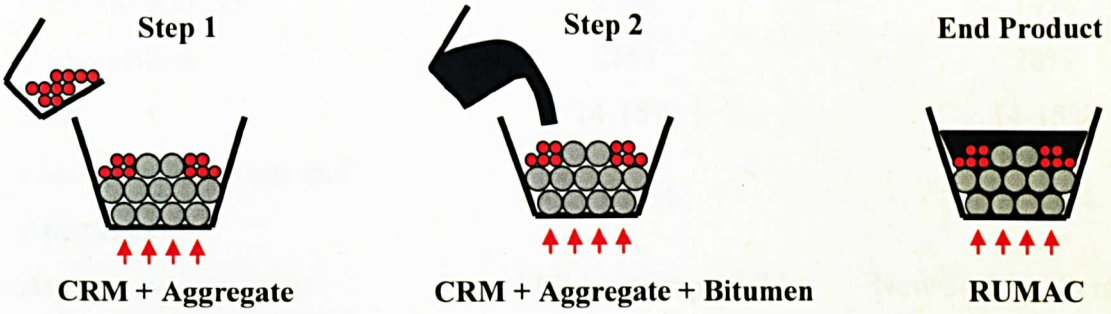

Figure 2.2 Dry process method

2.2.1 Crumb Rubber Composition

Crumb rubber is made of tyres or vulcanized rubber. Tyres are basically formed by combining natural and synthetic rubber and carbon black. The tyres are shredded into smaller particle sizes to remove wire and fabric reinforcement. The actual chemical composition of crumb rubber derived from tyres is difficult to assess because of the large variation in tyre types produced by different manufacturers. However, crumb rubber is typically referenced by its size together with basic compositions such as natural and synthetic rubber, steel, fiber and carbon black. In tyre production, the vulcanization process increases number of cross-links in a rubber's molecular structure and enhances its elasticity and strength properties. During vulcanization the rubber is treated with sulphur at temperatures between 140°C and 180°C, at which point the long chain molecules are crosslinked together with sulphur molecules (Stephen 1993). The resulting product then becomes incapable of being resoftened by further heating. Table 2.1 lists the tyre composition by percentage of the total weight of the tyre.

Table 2.1 Typical tyre composition (Rubber Manufacturers Association, USA)

Composition	Car tyre	Truck tyre
Natural Rubber	14%	27%
Synthetic Rubber	27%	14%
Carbon Black	28%	28%
Steel	14-15%	14-15%
Fillers, Extender oils and Antioxidant	16-17%	16-17%
Average weight, (kg)	New 11.3 kg, Scrap 10.2 kg	New 54.4 kg, Scrap 50 kg

Scrap tyre rubbers possess valuable components which might well contribute to the improvement of bitumen properties as well as asphalt mixture. Further details on the composition are as follows (Stephen 1993):

Natural Rubber: Natural rubber consists of linked monomers called isoprene. It provides greater elastic recovery and excellent physical strength as well as resilience and high resistance to tearing and abrasion. Natural rubber has a working temperature range of approximately -50°C to 100°C, making it ideal for anti-vibration applications and use in large tyres where excessive heat build-up could be disastrous. However, natural rubber is prone to oxidative and ozone attacks.

Synthetic Rubber: This rubber polymer is made by polymerising a mixture of two or more monomers such as butadiene and styrene. It is obtained from oil based products. The combination of the monomers produces styrene-butadiene rubber (SBR) which is widely used, with particular widespread application in car tyres. This material could improve thermal stability of the tyre compound.

Carbon Black: Carbon black is predominantly used as reinforcing agent in rubber products, especially tyres. A wide variety of carbon blacks are available and they differ in particle size and surface area. This element has been shown to add reinforcing properties to bitumen.

Fillers: The function of fillers in a rubber compound is mainly to reduce the cost of tyre production. Most filler are inorganic compounds such as calcium carbonate ($CaCO_3$). They raise the modulus (stiffen) of the rubber compound, and excessive amounts cause a loss of rubbery properties. Carbon black sometimes performs as filler in addition to being a reinforcing agent in rubber compounds.

Extender Oils: They function to plasticise the rubber polymer, making it softer and easier to process. Extender oils and carbon black have opposite effects on the rubber compound modulus. Rubber's modulus is reduced by the addition of extender oil and then brought back up to the required stiffness level by the addition of carbon black.

Antioxidants or Stabilisers: These are agents that need to be necessarily added to natural and synthetic rubbers that contain a major proportion of butadiene and isoprene. The rubber polymers are highly unsaturated and extremely susceptible to oxygen which can result in brittleness, cracking and degradation of the rubber compound. Antioxidants are components that counter the above-mentioned undesirable characteristics and increase the durability of the rubber compound.

2.2.2 Physical Properties of Rubber

Physical properties of rubber such as type, quantity, shape, gradation are said to affect the performance of rubber modified asphalt mixtures (Heitzman 1992). The size, shape and texture of the rubber particles used to modify the mixture vary with the proposed

applications to ensure expected performance is achieved. Different sizes of crumb rubber produced for recycling purposes are shown in Figure 2.3. Rubber particles with irregular shapes and relatively high surface area are more likely to react with bitumen at elevated temperature to produce a modified binder. Cubical shaped rubber particles with a relatively low surface area are typical of aggregates and desirable for use in the dry process as an elastic aggregate as they are easily integrated into the aggregate mix.

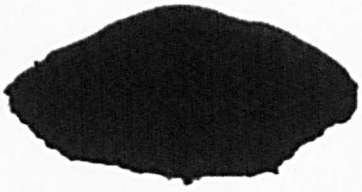

Rubber Powder (0.3-0.6 mm)

Rubber Shred (0.85-2.36 mm)

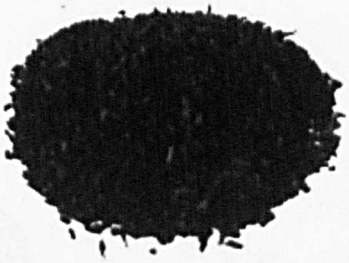

Granules (1-4 mm)

Figure 2.3 Different sizes of crumb rubber

There are two main methods for processing scrap tyres, namely ambient granulating (crackermill process) and cryogenic grinding. Figures 2.4 and 2.5 show the schematics of the ambient and cryogenic scrap tyre recycling systems. Both processes essentially reduce the size of the tyre and separate the steel belting and fiber from the rubber compound.

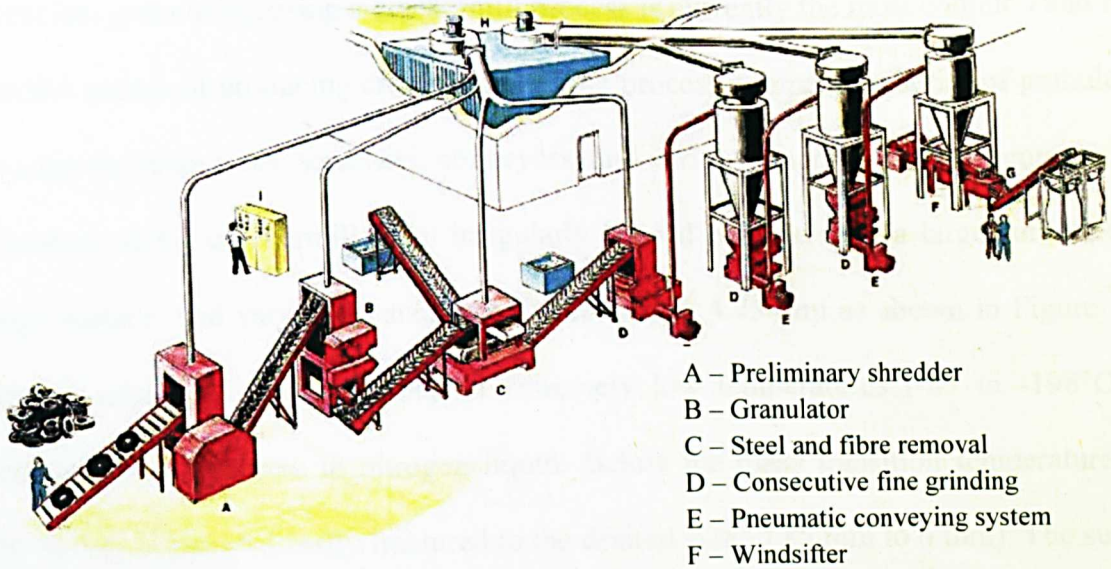

Figure 2.4 Schematic of an ambient granulating for scrap tyre recycling system (Reschner 2006)

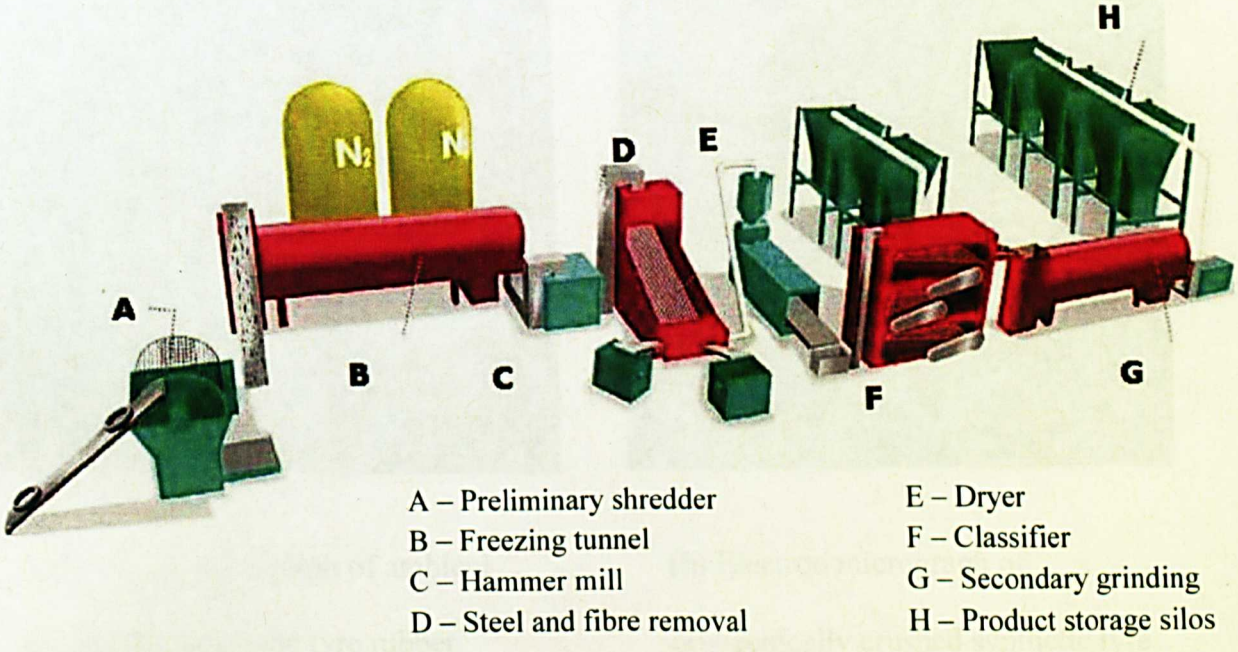

Figure 2.5 Schematic of a cryogenic grinding for scrap tyre recycling system (Reschner 2006)

The ambient granulating using a crackermill process is currently the most common and most productive means of producing crumb rubber. The process comprises a series of granulators for tearing the scrap tyres, screeners, conveyors, and various magnets for steel removal. The end product of the crackermill is an irregularly shaped particle with a large surface area, 'spongy surface' and varying in size from 0.425 mm to 4.75 mm as shown in Figure 2.6a. Cryogenic grinding is accomplished at extremely low temperatures (-87 to -198°C) by submerging the scrap tyre in nitrogen liquid. Below the glass transition temperature, the rubber is very brittle and easily fractured to the desired size (0.85 mm to 6 mm). The surface of rubber obtained from cryogenic grinding is glasslike with a lower surface area and elastic recovery compared to ambient granulated crumb rubber of similar gradation (Figure 2.6b).

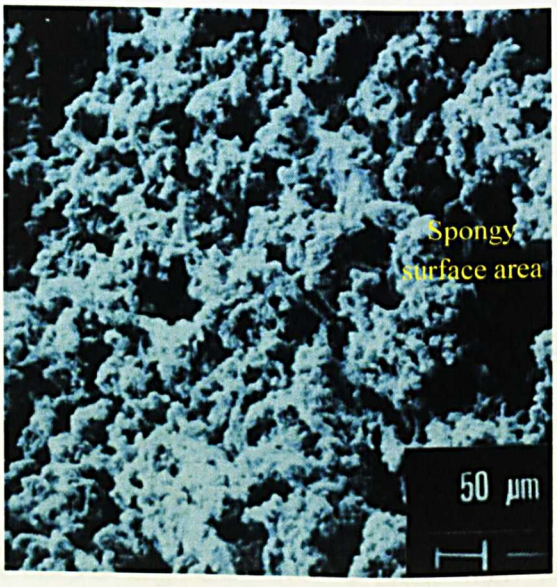

(a) Electron micrograph of ambient granulating synthetic tyre rubber

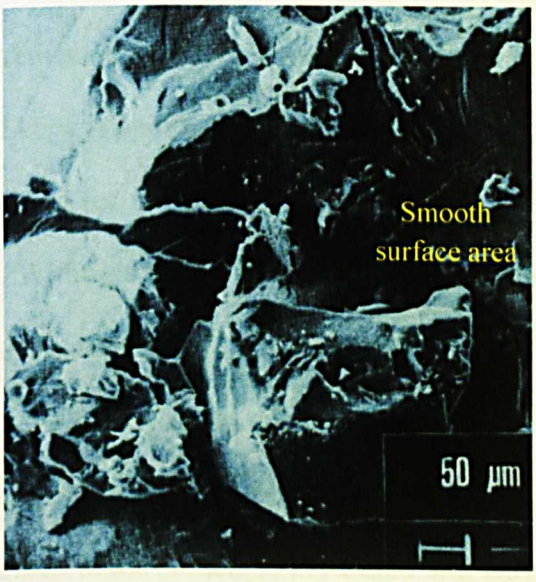

(b) Electron micrograph of cryogenically crushed synthetic tyre

Figure 2.6 Surface appearance of crumb rubber for different production methods (Oliver 1981)

Ambient granulated crumb rubber results in a higher binder viscosity than any of the modified binders produced with an equal amount of cryogenic crumb rubber (Putman and Amirkhanian 2006; Lee et al., 2007; Widyatmoko et al., 2009). This is possible due to the very high surface area and irregular shape of the ambient rubber particles which permits a faster reaction of the bitumen with the rubber than when cryogenic rubber is utilised. The above explanation demonstrates that the method used to manufacture crumb rubber has an influence on the extent to which the properties are enhanced.

2.3 Modification Concept of Dry Mixed Rubberised Asphalt Mixtures

Dry mixed rubberised asphalt mixture was developed in Sweden in the late 1960s where relatively large rubber particles were incorporated into asphalt pavements. The original purpose was to increase skid resistance and pavement durability. This mixture type was distributed under the European trade names Skega Asphalt or Rubit in Scandinavia (Northern Europe). The technology was then patented for use in the United States in 1978 under the trade name PlusRide (Heitzman 1992). With this modification, the coarse rubber particles act as elastic aggregates to increase the mixture's flexibility under loading. The finer rubber particles were reported to react partially with the bitumen, increasing its viscosity to make the binder more flexible at low temperatures, while maintaining high stiffness at high temperatures (Heitzman 1992; Green and Tolonen 1977; Bahia and Davis 1994; Zanzotto and Kennepohl 1996; Kim et al., 2001; Airey et al., 2003).

2.3.1 Rubber as an Elastic Aggregate

In the dry process method, normally around 1% to 3% coarse rubber by weight of the total mixture is added to the aggregate gradation having size between 2.0 mm and 6.3 mm (Takallou and Hicks1988). The idea of adding the rubber particles is to substitute a small portion of aggregates with rubber, for the rubber to function just like the aggregates but with additional benefit of possessing elastic properties as illustrated in Figure 2.7. By limiting the reaction time between bitumen and rubber particles and specifying a coarse granulated rubber with low surface area, the rubber particles are able to retain their physical shape and rigidity. In a gap graded mixture, the gaps provided between the fine and coarse aggregate is allocated to the rubber particles within the mixture. On the other hand, in a densely graded mixture, the aggregate gradation must be on the coarser side of the specification to permit the rubber modification. Further explanation of the rubber used as an aggregate substitute is presented in Section 2.4.

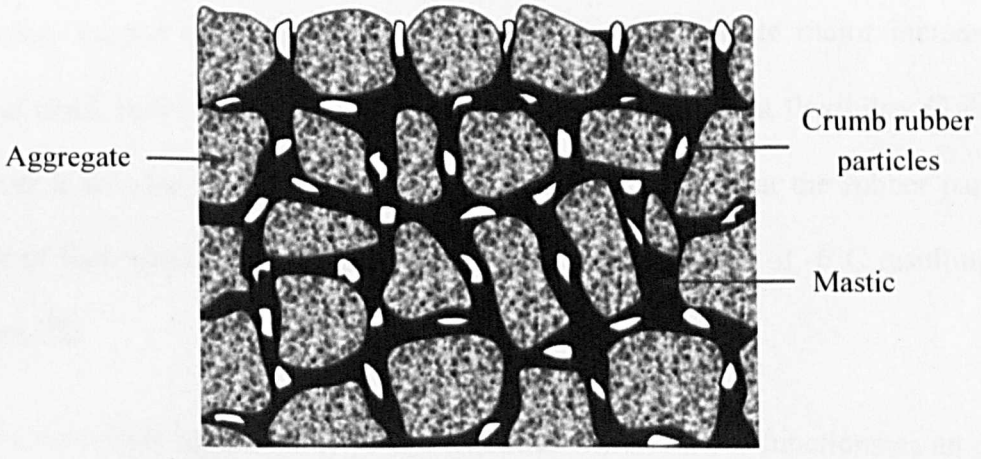

Figure 2.7 Illustration of rubber particles distribution within a gap graded rubberised mixtures (Takallou and Hicks 1988)

Initially, the dry mixing method of incorporating crumb rubber into gap graded mixture, was targeted at controlling the effects of snow and ice on pavement surfaces. The rubberised asphalt mixture was expected to have the advantage of breaking up ice and providing better skid resistance during icy conditions than conventional asphalt mixtures. Esch (1982) reported a higher skid resistance on an icy pavement constructed with the PlusRide mixture as well as a significant reduction in vehicular stopping distance. Furthermore, the Cold Regions Research Engineering Laboratory (CRREL) as reported by Federal Highway Administration, Washington, (1992) investigated the effect of dry process mixtures for debonding ice on pavements using various amounts of coarse rubber with a particle size range from 4.75 mm to 12.5 mm. They observed that incidences of ice cracking increased when the percentage of coarser rubber added to the mixture was increased. However, testing to prove the above theory was confined to the laboratory without any field trials undertaken. In a similar vein, the theory discussed above was applied in the production of a mixture with enhanced elastic recovery properties under repeated loading. This enhanced the mixture's resistance against fatigue cracking. Previous laboratory tests indicate major increases in fatigue life and crack reflection control due to an increase in pavement flexibility (Takallou 1986). However it was found later by Takallou and Hicks (1988) that the rubber particles can lose some of their elastic behaviour at temperatures in the region of -6°C resulting in a reduced fatigue life.

Several factors contribute significantly to the extent to which rubber functions as an elastic aggregate. These include the rubber gradation, rubber content and aggregate gradation. The way rubber particles perform under a stress action is illustrated in Figure 2.8. The figure shows that the rubber particles are able to recover their shape after the load is released. This is because when the load is applied the rubber particles absorb the energy of impact by

deforming but after the load is released the rubber releases the absorbed energy and in the process recover physically. By virtue of the aforementioned flexibility, rubber modification is considered to have potential to improve fatigue resistance and ice control in pavements

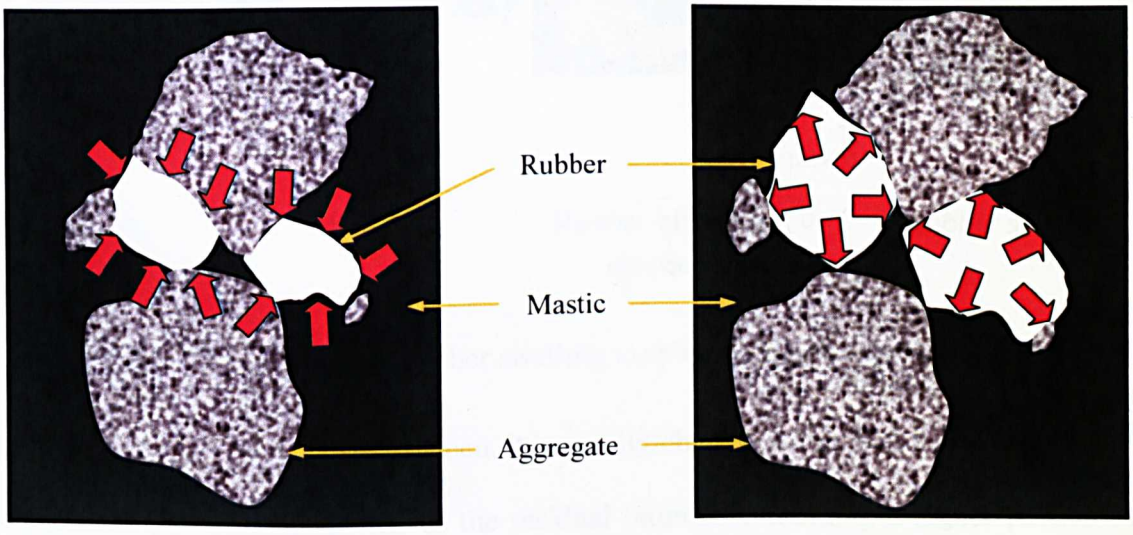

Figure 2.8 Illustration of rubber particles elastic behaviour before (with applied stress to deform-absorb energy) and after (with rebound stress-release energy) releasing the load

2.3.2 Rubber-Bitumen Interaction

While the utilisation of crumb rubber in asphalt mixtures has significantly evolved in the past few decades, there are aspects that have been continuously studied to better explain the effect of rubber on asphalt mixture properties. One such aspect relates to the interaction between the rubber and bitumen, which is considered vital to better understand the concept of rubber modification in both wet and dry process methods. The term 'interaction' used in this study refers to the diffusion of the lighter bitumen fraction (aromatic oils called maltenes) into rubber which leads to the swelling of the rubber particles. The swelling of the rubber as a result of the rubber-bitumen interaction is shown schematically in Figure 2.9.

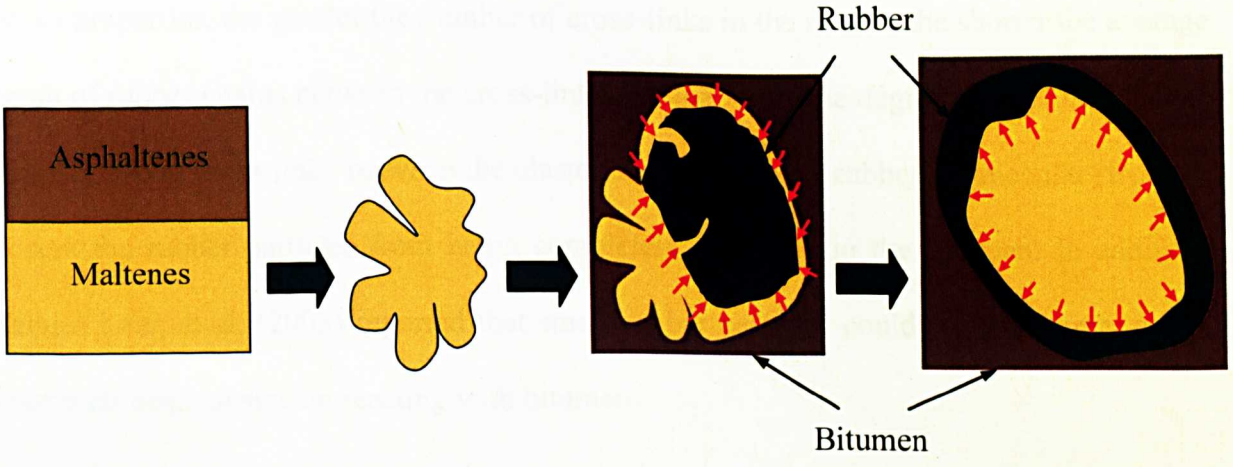

Figure 2.9 Schematic of rubber swelling in rubber-bitumen interaction

When rubber gets in contact with bitumen, it generally absorbs the maltenes fraction (which has low molecular weight) and leaves the residual bitumen containing a higher portion of asphaltenes (of high molecular weight) which increase its viscosity (Airey et. al 2003; Gawel et al., 2006; Lee et al., 2006). The maltenes fraction diffuses into the rubber particles, increasing the dimensions of the rubber network until equilibrium swelling is achieved. Factors such as the temperature and time of rubber-bitumen contact, chemical composition of bitumen, rubber type and size were all found to affect the rate of rubber swelling (Stroup-Stroup-Gardiner et al., 1993). With sufficient heat and time, higher degree of interaction between the bitumen and rubber can be increased to cause depolymerisation of the rubber particles (Xiao et al., 2006). Furthermore, the lower the molecular weight of the maltenes fraction, the more readily it will diffuses into the rubber (Epps 1994). Airey et al. (2003) conducted a binder absorption test using the Basket Draining Method to investigate the rubber-bitumen interaction by measuring the amount of bitumen absorbed and the rate of absorption. They found that using higher penetration grade bitumen (rich in aromatic oils) seemed to increase the rate of absorption and the rate of rubber swelling. In the aspect of

rubber properties, the greater the number of cross-links in the rubber, the shorter the average length of rubber chains between the cross-links and the lower the degree of swelling. This is because, strong cross-links between the elastomer chains in the rubber's molecular structure prevent the rubber particles from being completely dissolved in the bitumen. In addition, Mathias Leite et al. (2003) reported that small rubber particles could swell to three to five times their original size on reacting with bitumen.

Generally, it has been suggested that there is a greater degree of rubber-bitumen interaction with greater enhanced properties in the wet process than the dry process, thereby making the wet process the preferred method for modification. The rubber-bitumen interaction in the wet process is well established as it is considered as a major reaction that inevitably occurs within the mixture. In contrast, little has been documented regarding the rubber-bitumen interaction that occurs in the dry process. The majority of research conducted, pertaining to the dry process, generally assume that the reaction between the rubber and bitumen in the mixture is insignificant. This assumption is based on the perception that only a minor interaction can occur within a limited mixing time at elevated temperature. The aforementioned assumption was refuted by Takallou and Hicks (1988), who using PlusRide determined that it was possible for dry process mixtures to achieve a greater binder modification, by adding fine rubber particles in the mixture. Fine rubber particles have higher surface area and hence are more reactive with bitumen. Consequently, introducing fine rubber particles reduces the binder's temperature susceptibility by enhancing the elastic and resilient properties of the bitumen at low temperature.

Esch (1984) reported on a series of laboratory tests that evaluated the resistance of a dry mixed rubberised mixture to fatigue failure by adding an extra 2% of fine rubber (0.850 mm). By providing 45 minutes curing period at 204°C in loose form before undergoing compaction, the

mixtures showed an increase in fatigue life of the mixture by up to 450%. The improvement in the fatigue life was expected to be caused by the reaction between bitumen and the rubber particles. The reaction has increased the bitumen's viscosity and results in a thicker film of bitumen coating on the aggregate particles which can provide better resistance to oxidative aging and fatigue cracking. The curing period seemed necessary as to provide a sufficient time for the rubber to swell and partially dissolve in the bitumen prior to compaction. In addition, allowing optimum the rubber swelling in a loose mixture should prevent major swelling of the compacted specimen once the mixture is being compacted. Without the interaction time, Pinheiro and Soares (2003) found greater difference in the air voids content of rubberised mixture compared to conventional asphalt mixtures. As the curing period extended up to 2 hours, the mixtures showed an increase in resilient modulus and consistency in density but decrease in their fatigue life (Takallou et al., 1985; Olivares et al., 2009). This shows that better performance can be achieved by providing a long interaction time between the rubber and bitumen but not in excess of 2 hours. A possible reason could be a reduction in the bitumen fraction of the cured specimens. It must be noted that further diffusion of oils into rubber particles will adversely affect the cohesive and adhesive properties of the bitumen and reduces the binders' ability to bond with the aggregate particles. Therefore, it was recommended to use higher designed bitumen content as compared to the conventional mixture or bitumen with higher penetration grade in the mixture design of rubberised mixture (Takallou et al., 1985; Airey et al., 2004). Stroup-Gardiner et al. (1996) and Stroup-Gardiner et al. (1993) suggested a light oil, petroleum-based product as a pretreatment agent that should be compatible with the bitumen to pretreat the rubber before mixing in order to control the bitumen absorption.

2.4 Mixture Design Criteria of Dry Mixing

Currently, there is no official guideline or detailed specification for preparing the dry mixed rubberised asphalt mixtures available for UK practices. However in North America, PlusRide (gap graded) and Generic mixtures (dense graded) are two major dry process techniques that are widely practiced. This section reviews the differences in the mixture design considerations recommended by researchers and industry practitioners. The review will be a positive step in the direction of achieving an appropriate design standard with potential to be seamlessly integrated for UK practice. The design of CRM mixtures is typically accomplished using the conventional Marshall method. Based on previous research work, the gradations of aggregate and crumb rubber, bitumen content as well as low air voids content are thought to be the keys to success in designing CRM mixtures. The importance and role of these design elements used to form CRM mixtures will be considered in turn in subsequent sections for both PlusRide and Generic mixture types.

2.4.1 Aggregate Gradation

PlusRide Mixture

Aggregate gradation must be selected by first identifying whether or not the crumb rubber can be incorporated into the air void spaces provided by the existing aggregate gradation. Consideration must also be given to the fact that the rubber particles will swell when in contact with the hot bitumen during mixing and compaction. Kandhal and Hanson (1993) reported that PlusRide mixture types have high coarse aggregate content to provide spaces for the rubber particles to form a dense, durable and stable mixture upon compaction. The Alaska Department of Transportation and Public Facilities was one of the first agencies to use the PlusRide

mixtures in the United States. Three different aggregate gradations were recommended namely; PlusRide 8, PlusRide 12 and PlusRide 16 (see Table 2.2). Figure 2.10 shows a comparison of different aggregate gradation curves (log scale) for the recommended PlusRide mixtures.

Table 2.2 Three recommended specifications for patented PlusRide mixtures

Sieve size (mm)	Percent passing (%)		
	PlusRide 8	PlusRide 12	PlusRide16
19	-	100	100
9.5	100	60-80	50-62
6.3	60-80	30-44	30-44
1.70	23-38	19-32	19-32
0.600	15-27	13-25	12-23
0.075	08-12	08-12	07-11

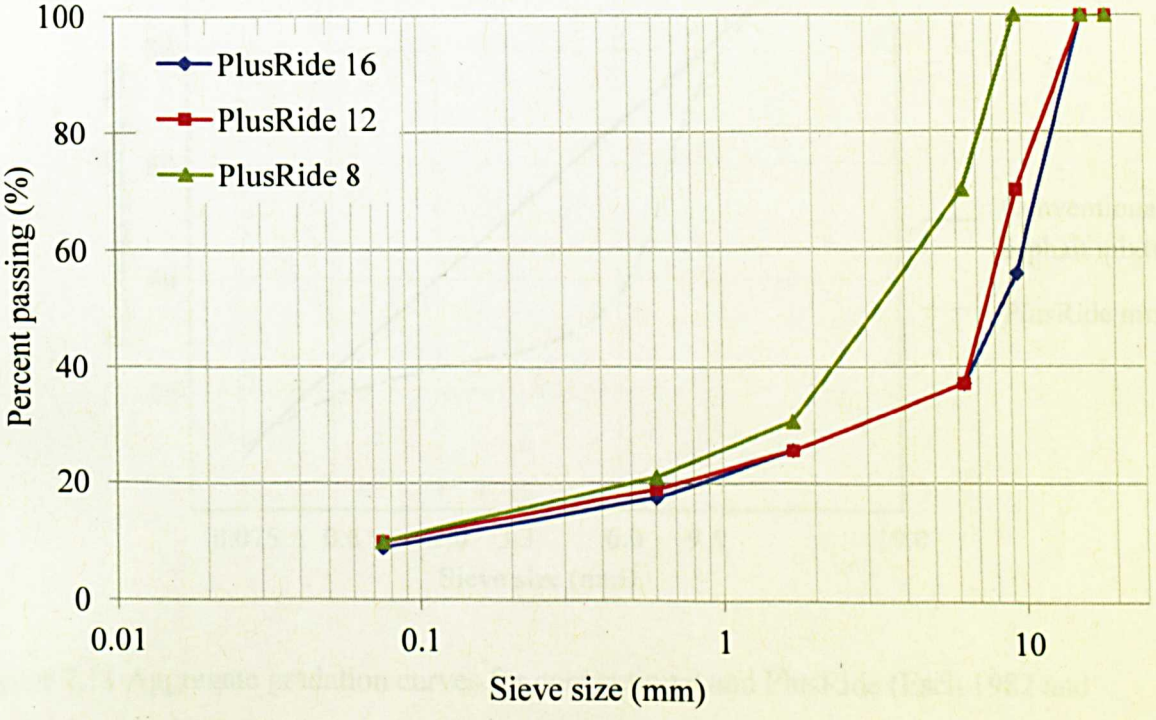

Figure 2.10 Aggregate gradation curves for PlusRide 16, 12 and 8 (Takallou 1988)

The most important difference between the rubber modified and conventional asphalt mixture is evident from the shape of the aggregate gradation curves as shown in Figure 2.11 (0.45 power gradation graph). The gap in the aggregate gradation curve for PlusRide mixture is created to provide space for rubber particles of sizes ranging between 3.175 mm and 6.35 mm. The aforementioned size range is chosen on the basis that the rubber particles that are usually used in the dry process are within this size range. Laboratory work by Chehovits et al. (1993) revealed that if the spaces are inadequate, the rubber will resist compaction and the resultant pavement will have excessively high air voids content and lack durability. Such a problem could potentially result in minor expansion of the compacted rubberised mixture. Therefore, by opening up the aggregate gradation the problem could be reduced.

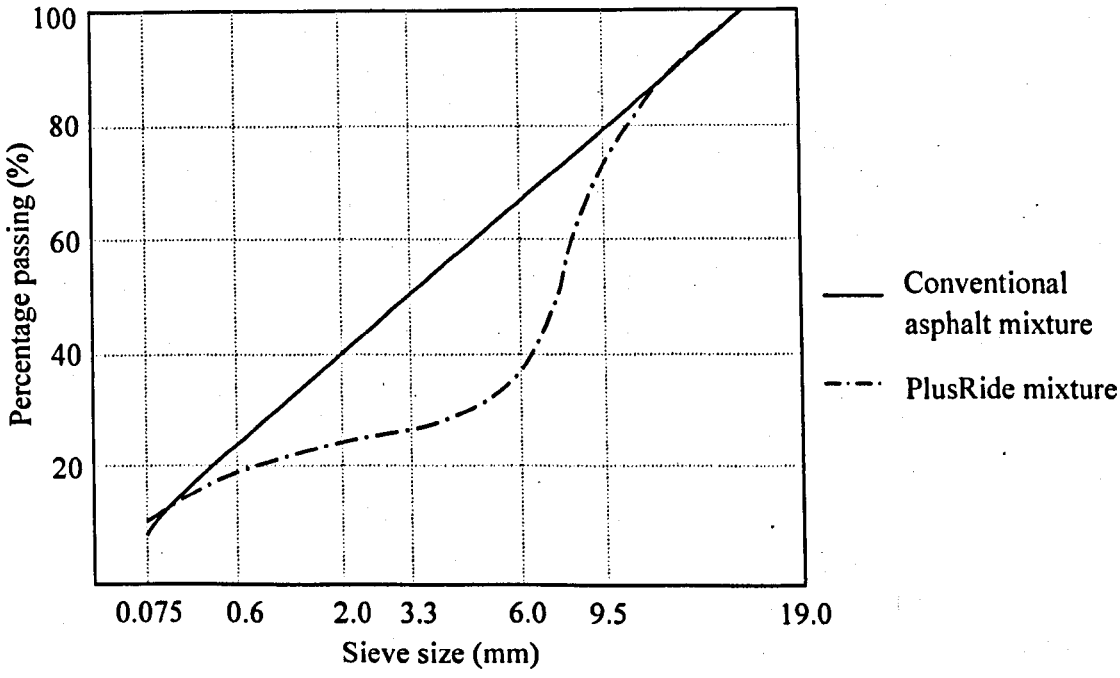

Figure 2.11 Aggregate gradation curves for conventional and PlusRide (Esch 1982 and Takallou and Hicks 1988)

Generic mixture

Generic mixture alters the conventional dense aggregate gradation. The recommended aggregate gradations for Generic mixtures, namely Generic 9.5, Generic 12.5 and Generic 19, are given in Table 2.3 (Chehovits et al., 1993). With the Generic mixture, a conventional dense aggregate gradation is used but with some adjustment made in the percentages of selected aggregate sizes to accommodate or facilitate the inclusion of the rubber particles. Figure 2.12 displays a comparison of the aggregate gradation curves (log scale) for the different Generic mixtures. The rubber particles added, substitute the percentage of aggregate that would have been taken out to produce a dense graded CRM mixture.

Table 2.3 Recommended aggregate gradations for Generic mixtures (Chehovits et al., 1993)

Sieve size (mm)	Percent passing (%)		
	Generic 9.5	Generic 12.5	Generic 19
25	-	-	100
19	-	100	90-100
12.5	100	90-100	-
9.5	90-100	-	56-80
4.75	55-85	44-74	35-65
2.36	32-67	28-58	23-49
0.3	7-23	5-21	5-19
0.075	2-10	2-10	2-8

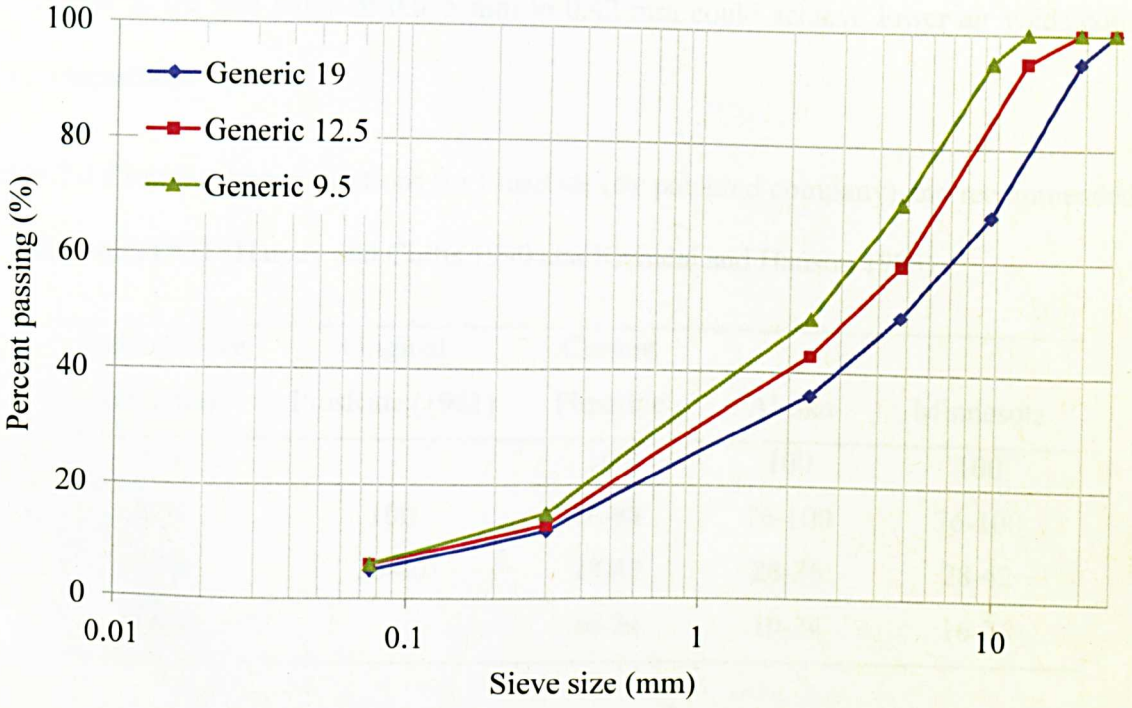

Figure 2.12 Aggregate gradation curves for Generic 19, 12.5 and 9.5

2.4.2 Crumb Rubber Gradation

In past practice, only the coarse rubber particles of granulated rubber from waste tyres (passing 6.3 mm sieve size) in a rough cubical form were added to modify mixture properties. However, further experiences with CRM mixtures have shown that better durability results can be achieved by increasing the fine rubber content. Hence, after 1981, 20% of the originally used coarse rubber grading was replaced with fine crumb rubber passing 0.85 mm sieve size (Table 2.4). Esch (1982) specified a size range of 0.425 mm to 2.0 mm of fine rubber for replacing 20% of the original coarse rubber within the CRM mixture. In addition, Gallego et al. (2000) observed that mixtures with fine rubber gradation (0.15 mm to 1.18 mm), performed better with respect to permanent deformation in comparison to conventional asphalt mixtures due to the binder modification. Pinheiro and Soares (2003) identified that rubberised mixtures with

fine rubber in the size range of 0.075 mm to 0.42 mm could achieve lower air voids content after compaction.

Table 2.4 Crumb rubber gradations for PlusRide (by patented company) and recommended by Minnesota DOT (Harvey and Curtis 1990 and Khandal and Hanson 1993)

Passing sieve size (mm)	Original PlusRide (1981)	Current PlusRide	Alaska	Minnesota
6.3	-	100	100	100
4.75	100	76-88	76-100	76-100
1.70	28-40	28-42	28-36	28-42
0.850	-	16-24	10-24	16-24

The crumb rubber used in PlusRide mixtures vary from 1% to 6% by weight of the total mixture with 3% being the most commonly used. Esch (1982) evaluated the PlusRide mixture's sensitivity to the rubber content. The study indicated that a 0.5% change in rubber content can cause a 1% change in the air voids contents for the same bitumen content added to the mixture. Therefore close attention needs to be paid to the addition of the rubber. This is essential to obtain consistent mixture properties, especially in relation to getting low air voids content, which can vary considerably with small changes in the rubber content. For Generic mixtures, the percentage of crumb rubber used is slightly lower (1% to 3%) and the rubber particle size, finer compared to the PlusRide. However Generic mixtures adopt the same concept of modification of adding coarse and fine rubber fractions to the mixture (Table 2.5). The premise behind the technique is for the coarse rubber to serve as an elastic aggregate and fine rubber could react with bitumen to produce a modified binder in the mixture.

Table 2.5 Recommended rubber gradations for Generic mixtures (Chehovits et al., 1993)

Sieve size (mm)	Percent passing (%)
4.75	100
2.36	70-100
1.18	40-65
0.6	20-35
0.3	5-15

2.4.3 Bitumen Content

Esch (1982), Esch (1984) and Takallou and Hicks (1988) specified higher bitumen content (between 1% and 2% higher) for the rubberised mixture compared to the conventional mixture for the same aggregate type and gradation. The approximate range of the bitumen content recommended for PlusRide and Generic mixtures are given in Table 2.6.

Table 2.6 Bitumen contents used for PlusRide and Generic mixtures (Takallou et al., 1986 and Heitzman 1992)

Mixture type	Optimum bitumen (% of total mix by weight)
PlusRide 8	8.0-9.5
PlusRide 12, 16	7.5-9.0
Generic	7.5

As noted earlier in the rubber and bitumen interaction section, some of the bitumen fraction in rubberised mixture may be absorbed by the rubber particles. As a result, Esch (1982) claimed that replicate specimens containing rubber could end up with high variations in air voids content, for the same mixture design. Figure 2.13 shows that as bitumen content in the

rubberised mixture decreases, air voids content will increase. Therefore, to counter the absorbed bitumen fraction into rubber particles, the optimum bitumen content is selected at low target air voids content, with 3% usually desired in the design rubberised mixture. Furthermore, higher bitumen content is significant to ensure the workability of the mixture. In addition, both PlusRide and Generic mixtures yield lower stabilities and higher flows due to their elastic properties, compared to conventional mixtures. Therefore, a proper laboratory mixture design is critical to produce a mixture with low air voids content and adequate stability. Harvey and Curtis (1990) and Chehovits et al. (1993) recommended additional design criteria for the PlusRide and Generic mixtures as shown in Table 2.7.

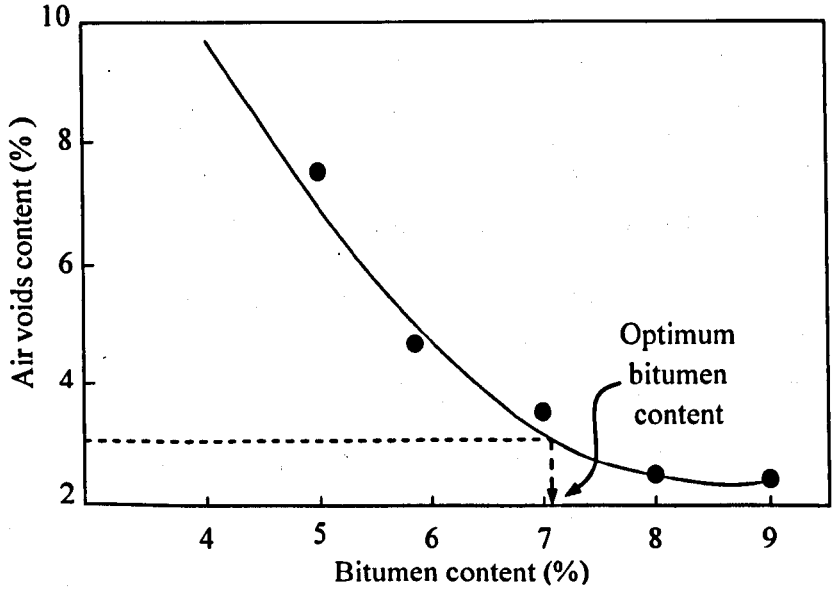

Figure 2.13 Determination of bitumen content on the basis of air voids content (Esch 1982)

Table 2.7 Design criteria for PlusRide and Generic mixtures

Criteria	PlusRide	Generic
Air voids (%)	2-4	3-5
Minimum stability (kN)	8	3.5
Flow (cm)	<5	2-5

2.5 Mechanical Performance of CRM Mixtures based on Previous Studies

This section reviews previous research undertaken to evaluate the mechanical performance of CRM mixtures. Majority of the mechanical testing was undertaken to evaluate mixtures' performance in terms of stiffness modulus, permanent deformation and fatigue resistance. In turn, the aforementioned measures of performance are reviewed to attain a better understanding of the effect of different mixture variables on CRM mixture compared to conventional asphalt mixtures. The mixture variables discussed include rubber content, rubber gradation and mixing procedures.

i. Resilient Modulus

A resilient modulus testing program is typically used to evaluate the ability of mixtures to bounce back upon releasing the applied stresses. Resilient modulus can be measured as the ratio of the repeated stress to the corresponding resilient strain (by the recoverable deformation). Gowda et al. (1996), Stroup-Gardiner et al. (1996), Kim (2001) and Pinheiro and Soares (2003) found the resilient moduli of rubber modified mixtures to generally increase with increasing rubber content demonstrating the increased elasticity of the mixtures. However, deformation was mostly recoverable indicating that the mixture's lower stiffness and greater flexibility had resulted in less stress being absorbed by the pavement surface compared to a conventional mixture. Takallou et al. (1986) and Takallou and Hicks (1988) compared three different rubber gradations, fine, medium and coarse. They found that mixtures with fine rubber had the highest modulus, which is thought to have been caused by the rubber-bitumen interaction.

ii. Tensile Strength

The indirect tensile strength test can be conducted to evaluate the tensile strength of CRM mixtures under static or repeated compressive loads. The test measures the horizontal

displacement to calculate the horizontal strain corresponding to the load applied parallel to the vertical diametral plane of the specimen. Stroup-Gardiner et al. (1996), Kim (2001) and Cao (2007) tested the tensile strength of rubber modified asphalt specimens at low temperature (-18,-10, 1°C). They found that, increasing in the rubber content led to reductions in the tensile strength of the mixtures, which indicated that the structural capacity of the rubberised mixtures had been deleteriously compromised. The corresponding horizontal strains showed a substantial increase in strain potential at low temperatures. Gowda et al. (1996) and Pinheiro and Soares (2003) also reported a reduction in the tensile strength of the rubberised mixture tested at 25°C.

iii. Fatigue Resistance

Fatigue behaviour can be characterised by relating the strain of a mixture to the number of load applications to failure. Fatigue testing can be conducted by either controlling the load (stress) or the deformation (strain). Researchers have identified several mixture variables believed to influence the fatigue life of CRM mixtures. The mixture variables found from various published literature include rubber content, rubber gradation, aggregate gradation, mixing temperature and curing time prior to compaction (for rubber-bitumen interactions). Studies undertaken have shown that CRM mixtures have a much greater fatigue life than conventional asphalt mixtures. Increasing the rubber content of an asphalt mixture having a gap graded particle size distribution with coarser rubber gradation was shown to result in better fatigue resistance compared to a rubber-modified dense graded mixture (Takallou et al., 1986; Takallou and Hicks 1988). Furthermore when a higher mixing temperature and curing time (1 hour at 150°C) was considered, the results showed an extended fatigue life (Pinheiro and Soares 2003). However, Airey et al. (2004) found that increasing curing time by up to 6 hours did not make a significant difference to the fatigue performance of the mixture. According to Takallou et al. (1986), conditioning the CRM mixture at higher temperature of 190°C or more for 2 hours

before compaction decreased the fatigue life due to binder oxidation.

iv. Permanent Deformation Resistance

The potential of permanent deformation at high temperature for CRM mixture can be determined from the permanent strain accumulated at the end of the testing under vertical compressive stresses. Researchers claim that the addition of rubber to asphalt mixtures will enhance the mixture's elasticity to recover at higher service temperature to counter the permanent deformation experienced on road surfaces. Cao (2007) and Olivares et al. (2009) evaluated the rutting resistance of the CRM mixture at 60°C using the Wheel Tracking Test to simulate the effect of traffic. They discovered that increasing the rubber content and allowing sufficient curing time improved rutting resistance. A higher number of cycles had to be applied to the CRM mixture for it to reach the same target rut depth as conventional mixture. Creep Test was conducted by Takallou and Hicks (1988) and Stroup-Gardiner et al. (1996) to characterise permanent deformation in terms of creep modulus under static axial load. Their results suggest that CRM mixtures have lower creep resistance than the conventional asphalt mixtures. The creep resistance was found to improve as fine rubber was added to the mixture. In a further study, Airey et al. (2004) used a Confined Repeated Load Axial Test to evaluate the rubberised mixture by measuring the total strain and strain rate of the test on the mixture after the application of load cycles. The inclusion of rubber as additional aggregate was found to increase the permanent strain and the strain rates over that of a conventional asphalt mixture. On the other hand, strain rates were found to decrease as the rubber content in the mixtures was increased. This demonstrates that higher rubber content could potentially improve the permanent deformation resistance of rubber-modified asphalt mixture.

2.6 Proposed Mixture Design and Mixture Preparation Guidelines based on the Review of Laboratory and Field Practices

On the basis of the reviews, several mixture design and mixture preparation guidelines have been identified based on previous research recommendations. The following general guidelines are suggested for use in the design of dry mixed rubberised asphalt mixtures.

i. Gap graded aggregates and coarse densely graded aggregates are preferred for modification.

ii. Use the same bitumen grade as used in conventional asphalt mixtures or a higher penetration grade.

iii. Add higher bitumen content (1-2%) compared to conventional asphalt mixtures.

iv. Combination of coarse and fine rubber is significant for better performance.

v. Low design air voids content on the compacted mixture is critical and desirable (approximately 3%).

vi. Use higher mixing temperatures than conventional asphalt mixtures.

vii. Mix the rubber with the aggregate prior to adding the bitumen.

viii. Provide a curing period after mixing (in a loose form) of about 2 hours (between 1 and 2 hours is recommended).

ix. Remix the mixture prior to compaction to 'warm-up' the mixture after the long curing period.

x. Apply surcharge load after compaction to counter the rubber swelling in the specimen prior to extrusion. However this step is limited to laboratory prepared specimens and may not necessarily reflect the real in-situ conditions in a road. Therefore for field practice, it was suggested by Esch (1984) that the compaction (refers to rolling action) should commence as soon as possible after placement to the highest possible density

with minimal air voids.

2.7 Summary

The literature review in this chapter has provided detailed insight and a better understanding of dry mixed rubberised asphalt mixtures. This is necessary to justify the function and behaviour of the rubber particles within the mixture prior to performance evaluation. Thus, it would be possible then to identify the factors that play a significant role in improving the CRM mixtures properties. From the review, the following general conclusions can be made:

i. The use of crumb rubber in asphalt mixtures is often considered to improve the performance of asphalt mixtures and benefit the environment. It is used to modify both gap and dense graded mixtures by means of gradation modification or substitution.

ii. Rubber particles have two main functions in the context of asphalt mixture's modification. Firstly, they perform as part of the aggregate component of the mix but exhibit greater elastic recovery characteristics. Secondly, they partially modify the binder properties through a rubber-bitumen interaction. These aforementioned functions have been found to improve the asphalt mixture's resistance to fatigue cracking and permanent deformation.

iii. The mixture design guidelines identify aggregate gradation, rubber gradation, bitumen content and air voids content as critical design criteria. They are considered important for the production of CRM mixtures.

iv. There are slight modifications in the mixing and compaction procedures adopted for preparing the CRM mixtures compared to conventional asphalt mixtures. This is for the purpose of achieving the target mixture design and enhancing the mixture's properties.

3.0 X-RAY COMPUTED TOMOGRAPHY AND DIGITAL IMAGE PROCESSING

3.1 Introduction

This chapter introduces the fundamental application of X-ray computed tomography (CT) as a non-destructive technique to visualise internal structures and obtain digital information on the microstructure properties of asphalt mixtures. The chapter then introduces the digital image concept and image processing method, particularly the thresholding technique for image segmentation that has been developed for CRM asphalt mixture. Details of the depth investigation undertaken, concentrating on finding the best way to view and differentiate the relative internal structure compositions. Finally the chapter proposes a set of image processing procedures, based on some trial results from preliminary investigation carried out on X-ray CT images, to separate the different material components present in rubberised asphalt mixtures.

3.2 Image Analysis Technique

Digital image analysis has been used to quantitatively study the structure of asphalt mixtures. This analysis involves extracting information from images by means of digital image processing techniques which utilise various mathematical procedures. Using digital image analysis, it is possible to gain information regarding the characteristics of cracks, air voids and aggregates. Image analysis techniques generally consists of three major stages namely image acquisition, image processing and image analysis (Figure 3.1). Image acquisition is a process of getting an image into the computer. This is the most important part of the entire process because a good quality image is easy to analyse compared to a poor

quality image. There are many methods to capture an image, such as using digital cameras, scanners, video recorders and X-ray CT. Sometimes it is necessary to calibrate and validate the captured image to make sure that it is an accurate representation of the real object. The second stage is image processing, which involves adjustments to improve the image quality such as altering the brightness and contrast as well as particles segmentation. This stage is essential to distinguish the region of interest from the background image in order for it to be analysed. Image analysis is the final stage which involves a process of making measurements to derive numerical data from the images for interpretation. The data may be analysed statistically or used to generate graphs. The measurements and characterisation procedures involved in this study are detailed in Chapter 4.

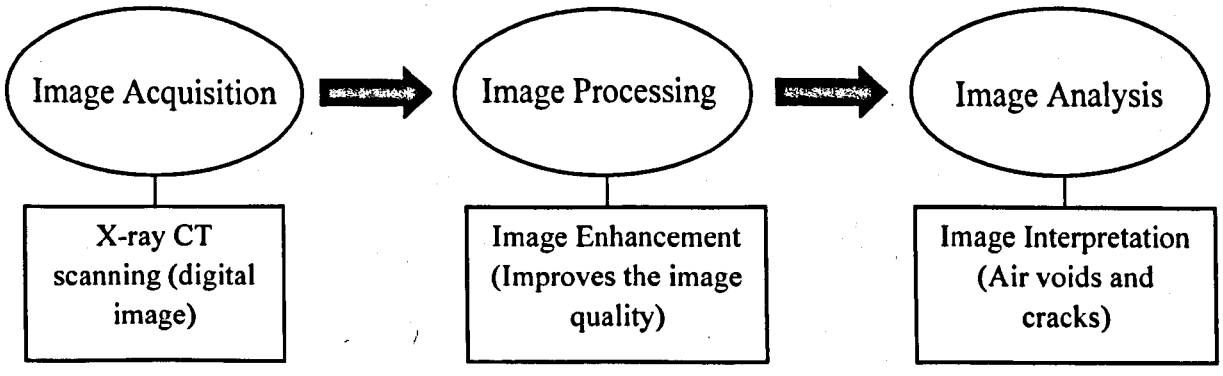

Figure 3.1 Three major stages of image analysis technique

3.3 X-ray Computed Tomography (CT)

X-ray CT is an advanced imaging technique, which generates an image of density distribution of a specimen's cross section. This technique is completely non-destructive and is used to visualise the internal features of solid objects and obtain digital information from the captured images. It was first designed for medical application and has lead to a better

way for characterising engineering materials with a capability to view the internal structure of a material for detecting volume of defects.

3.3.1 X-ray CT Concept and Instrumentation

The first commercial X-ray CT scanner was invented by Sir Godfrey Hounsfield in Hayes, United Kingdom at EMI Central Research Laboratories (Michette and Buckley 1993). The idea was to create a three dimensional image from X-ray scanning of an object by overlapping and intersecting hundreds of X-ray slices taken from different angles. Computed tomography is a concept that applies digital cutting to reveal the details of the internal structure of the solid object. The X-ray CT scanning consists of an X-ray source with collimator and detector with back filter as shown in Figure 3.2. This scanning technique uses the ability of short wavelength electromagnetic radiation (called X-rays) to penetrate objects by measuring the X-ray intensity before and after it passes through the object. As explained by Sprawls (1993), Ketcham and Carlson (2001) and Razavi (2006), the principle of the X-ray penetration is, when the initial X-ray radiation, I_0 passes through the specimen, some of the radiation are absorbed and scattered while the rest penetrate through the specimen, I. This is illustrated in Figure 3.3. The amount of absorption is a function of the linear attenuation coefficient, μ at each point within the specimen, depending on the density of the material. For example, a homogeneous material and composite material as shown in Figure 3.3a and Figure 3.3b respectively, for the same thickness, absorb the X-ray radiation differently due to the difference in density. The denser the material such as Object 2 (Figure 3.3b), the more the radiation is absorbed. In a two dimensional section, the linear attenuation coefficients of the material distribution can be expressed by the function, $\mu(x, y)$ where x and y are the Cartesian coordinates of the points location within the section. The final intensities

of the transmitted radiation along a particular path that penetrate the specimen in horizontal planes are recorded with an array of detectors. The amount of penetration depends on the X-ray's energy and the atomic number as well as the density and thickness of the object. Equations 3.1 and 3.2 describe the relationship of the X-ray penetration when the X-rays travel through a homogeneous material and composite materials respectively based on the Beer's Law. Where X is the length of the X-ray path through the material and i refers to each increment that reflects every single material over a linear extent, X_i with attenuation coefficient, μ_i. To consider over the range of effective X-ray energy spectrum (E), Equation 3.3 is required.

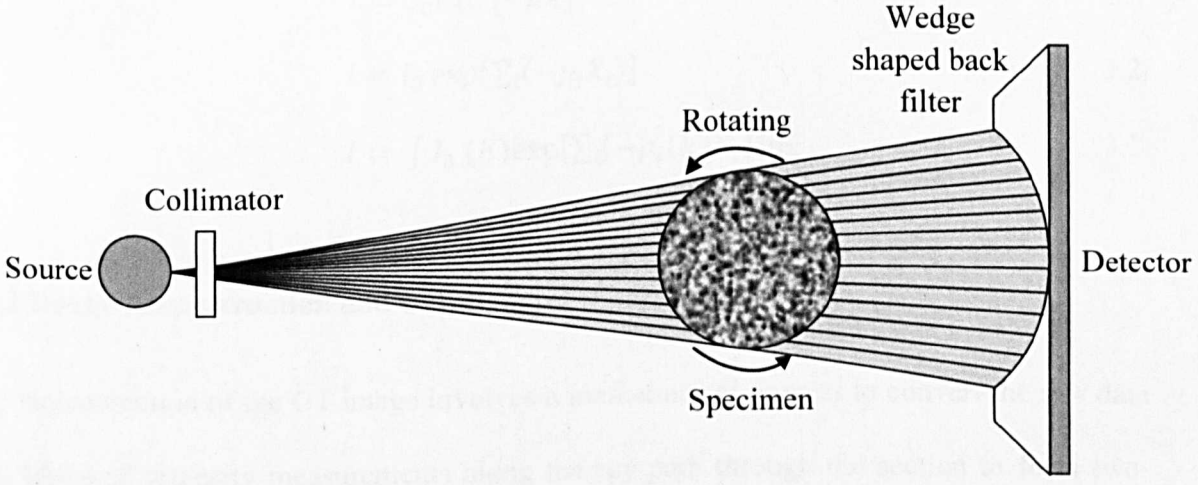

Figure 3.2 Illustration of the X-ray CT scanning (plan view)

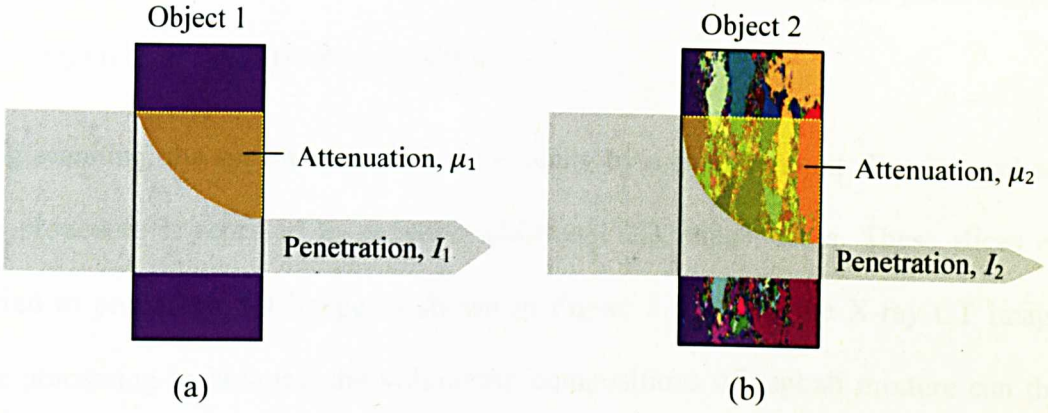

Figure 3.3 Illustration of the penetration of X-ray radiation through (a) homogeneous specimen and (b) composite material specimen

$$I = I_0 \exp[-\mu X] \quad 3.1$$

$$I = I_0 \exp[\sum_i (-\mu_i X_i)] \quad 3.2$$

$$I = \int I_0(E) \exp[\sum_i (-\mu_i(E) X_i)] dE \quad 3.3$$

3.3.2 Image Reconstruction and Defects

The reconstruction of the CT image involves a mathematical process to convert the raw data of a series of intensity measurements along the ray path through the section to form two-dimensional (2D) slice images. The resulting X-ray CT image is a map of the spatial distribution of density which indicates the presence of the internal features and their distribution. Scanning of solid objects with different density will produce an image with different ranges in the grey scale. For an 8-bit image, the pixels consists of 256 ranges of grey intensity starting from 0 (black) to 255 (white) that correspond to different densities within the specimen. The higher the difference in densities of the composite materials scanned, the better each of the materials can be identified and distinguished from each other. Figure 3.4 show a typical 2D image from an asphalt mixture specimen, the aggregate is the

brightest region (highest density), followed by mastic (bitumen and fine particles) and the darkest region is air voids (lowest density).

During scanning, the specimen is shifted vertically by a fixed amount slice interval and the entire procedure is repeated to generate additional 2D image slices. These slices can be rendered to produce a 3D image as shown in Figure 3.5. Using the X-ray CT image and image processing techniques, the volumetric compositions of asphalt mixture can then be identified easily. The volumetric images will enable other studies to be conducted on various aspects of internal structure of asphalt mixtures. However, in certain circumstances, some defects might appear in the captured images and degrade the quality of the CT image, leading to possible misinterpretation of the measured properties. This could possibly be the errors in determining the particle dimensions and the volume fraction. Therefore to optimise the image quality, it is necessary to understand the defects and identify the approaches required to prevent them. In some cases the defects can be eliminated during image processing. The three main potential defects are as follows (Ketcham and Carlson 2001, Paterson 2007 and Khan 2009):

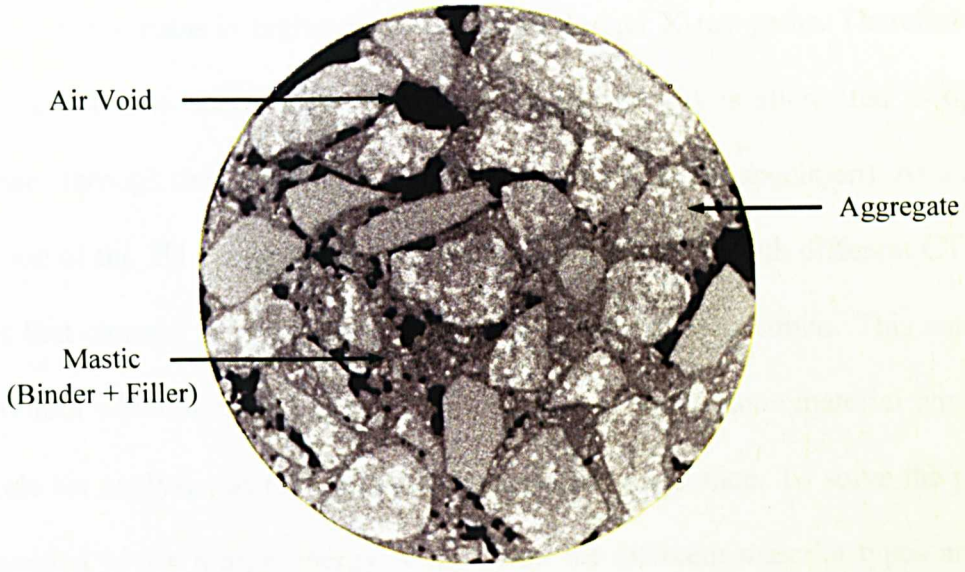

Figure 3.4 Example of X-ray CT 2D image of asphalt mixture specimen

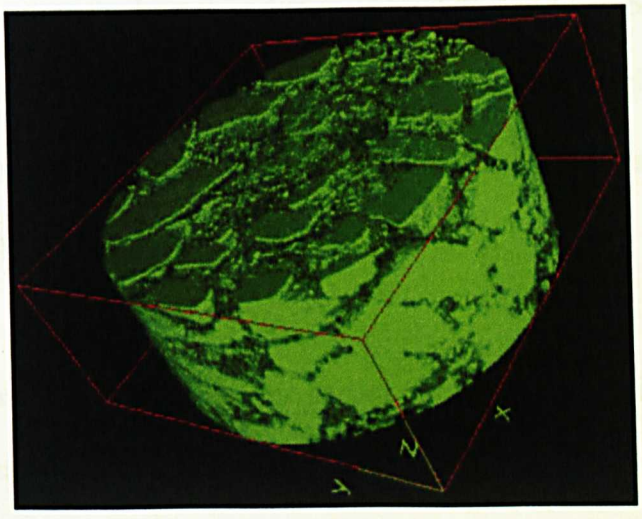

Figure 3.5 Reconstruction of 3D CT image from 2D image slices

i. Beam hardening

Beam hardening is the most common defect occurring in CT image. Figure 3.6a shows a cylindrical asphalt mixture specimen with its edges appearing brighter than the centre of the specimen. It is the result of the lowered energy of the X-ray spectrum as it passes through the scanned specimen. When the X-ray beam travels through the specimen, the mean energy

of the shorter X-ray paths is higher than that of the longer X-ray paths. Therefore within a short distance (close to specimen's edge) more X-rays energy is attenuated as opposed to when it passes through the longer distance (close to middle of the specimen). As a result, the reconstruction of the 2D image for the same material is assigned with different CT values or grey levels that cause a bright region around the edge of the specimen. This can however cause a problem when thresholding particles that belong to the same material type based on the greyscale for analysis, as they vary throughout the image slice. To solve the problem, it is recommended to use a high energy X-ray beam for different material types and sizes as the beam will become insensitive to attenuation contrasts in materials. Another approach is to use an attenuation filter to pre-harden the X-ray beam using flat pieces of metal (copper or aluminium placed in front of the beam) and to post-harden the X-ray beam using the wedge shaped back filter (placed in front of the detector). This is to remove the low energy X-rays travelling from the source while the back filter is used to ensure the beams travel through the same length and absorb equal amounts of energy.

ii. Ring artifacts

Ring artifacts appear as one or many full or partial circles within an image at the centre of the specimen on its rotational axis as shown in Figure 3.6b. These are usually caused by a detector fault whereby the detector gives a consistently anomalous reading on every image resulting in a circular artifact. A few factors relating to the scanning conditions can cause the detectors to respond differently against the rays such as the changes in temperature and the strength of the energy of the beam. By doing frequent recalibrations and controlling the experimental conditions, the defects can be minimised or eliminated.

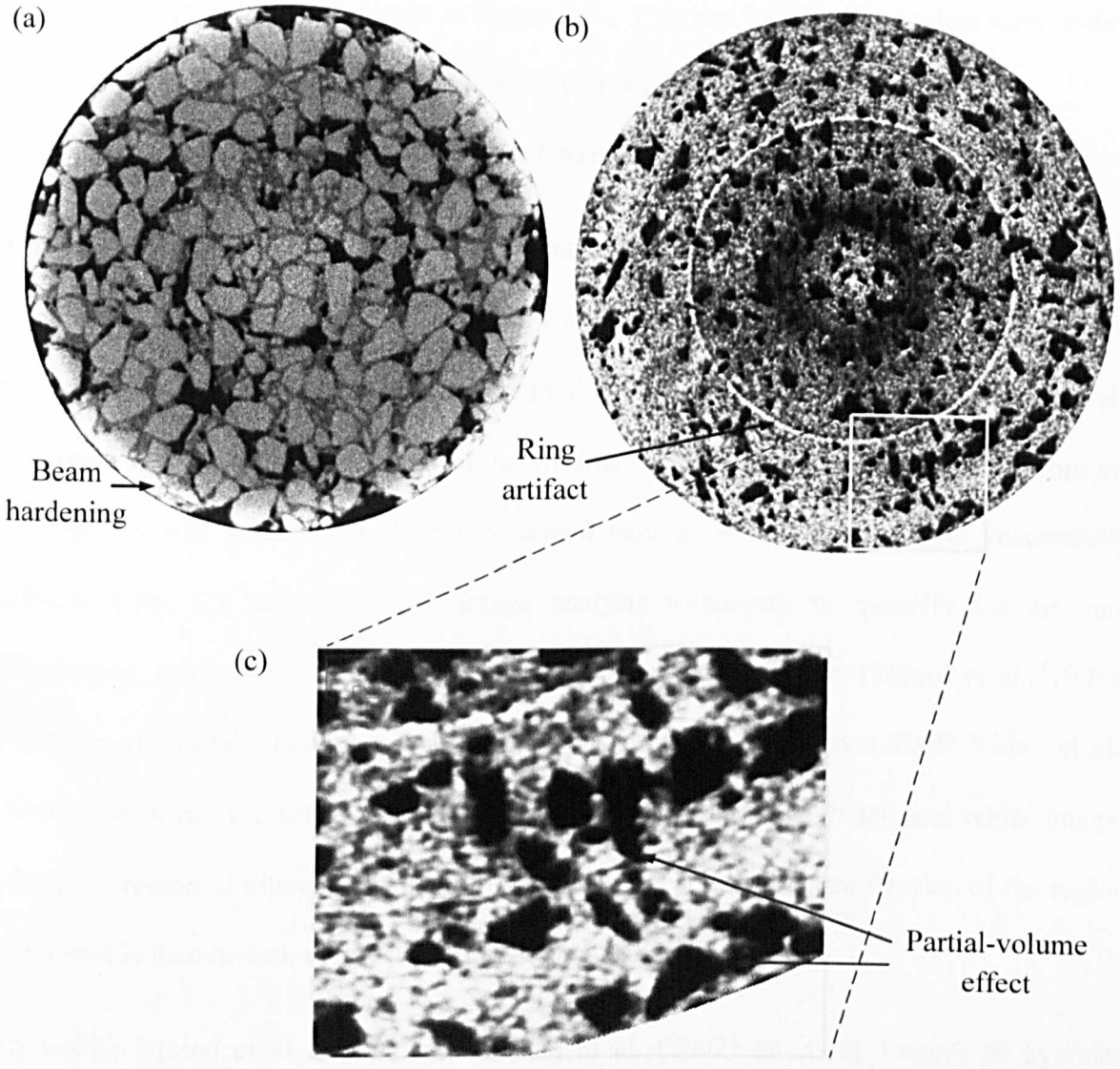

Figure 3.6 Different images of (a) asphalt mixture and (b & c) mastic with rubber particles

iii. Partial-volume effects

Partial-volume effect is a phenomenon that usually occurs in a scanned specimen that comprises different materials, whereby it yields CT values that represents the average attenuation of the different materials properties. This can happen particularly on the object boundaries where the pixels can appear blurred with a slightly different grey scale compared

to the surrounding pixels as shown in Figure 3.6c. This can be a problem when thresholding the object of interest as the pixels' grey scale varies within the selected area.

3.3.3 Applications for Asphalt Mixture Characterisation

X-ray CT combined with testing instruments and image processing techniques provide researchers with a capability to characterise the microstructure and monitor materials' performance. The advantage of this method is that the objects are non-destructively examined with no prior preparation of the specimen surface being necessary. Therefore the specimen is still intact for further mechanical testing. A few studies have successfully utilised X-ray CT combined with image analysis techniques to quantify the air void distribution, aggregates orientation and damage in asphalt mixtures (Masad et al., 1999a; Masad et al., 1999b; Tashman et al., 2001; Masad et al., 2002; Khan 2009; Kutay et al., 2010). The X-ray CT image is transformed into a binary image (black and white image) where the region of interest is isolated from the background. The area fraction of the region of interest is then measured directly from the images.

Studies by Masad et al. (1999a) and Masad et al. (2002) on X-ray images of gyratory compacted specimens, found that the air voids distribution followed a 'bathtub shape' where higher air voids were concentrated at the top and bottom of the specimen. This shape was found to be more pronounced at higher compaction efforts (Figure 3.7). This finding was a breakthrough leading to a better understanding of the air voids distribution within a specimen using a non-destructive imaging technique. The air voids distribution has been further investigated for the effect of different compaction methods, specimen size (height and diameter ratio) and aggregate size distribution (Tashman et al., 2001; Masad 2004).

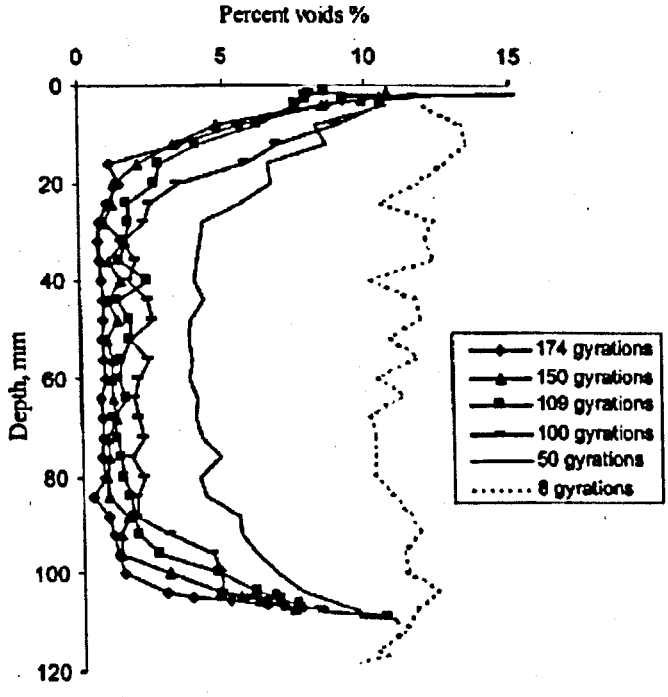

Figure 3.7 Distribution of air voids in gyratory specimen (Masad et al., 1999)

Several studies have also been conducted to quantify the damage within asphalt mixtures using X-ray CT by characterising the voids after applying damage. Wang et al. (2001) and Wang et al. (2003) used damage parameters namely damaged surface area and mean solid path (average spacing among cracks) to quantify the damage. Tashman et al. (2004) monitored the damage evolution by measuring the increment in the voids content (cracks and air voids) from X-ray images in a specimen before and after being deformed to prescribed strain levels in a triaxial compression set up. They observed a considerable crack growth at the top and middle regions compared to the bottom region of the specimen as shown in Figure 3.8. The same concept of monitoring the damage was adopted by Khan (2009), where the specimens were X-rayed at different stages of load cycles of fatigue testing. The damage was quantified in terms of the voids growth within the specimen after completing each stage for a number of load cycles. The results showed that the voids area increased with the increase in the number of load cycles.

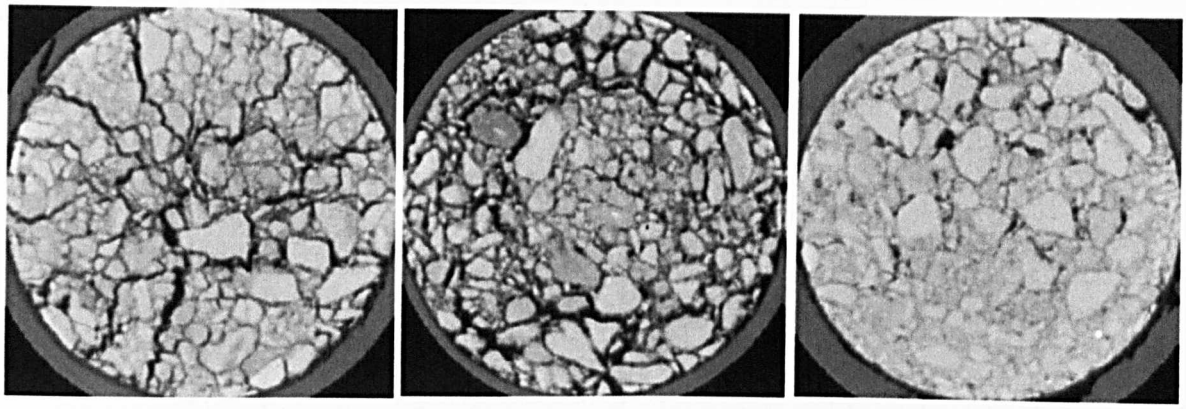

(a) (b) (c)

Figure 3.8 X-ray images at 8% strain levels (a) top (b) middle and (c) bottom regions (Tashman et al., 2004)

For aggregate characterisation, Kutay et al. (2010) studied the aggregate packing in an asphalt mixture in terms of the contact points and orientation using 3D images reconstructed from 2D X-ray images. They developed an image processing technique which is very useful to obtain quantitative information of the aggregate characteristics.

3.4 Digital Image Processing

Digital image processing consists of algorithms which are used to improve the image quality and extract the region of interest from the background image. These algorithms include contrast enhancement, noise reduction, object recognition and segmentation (Wojnar 1999 and Sonka et al., 1998). One can develop their own image processing algorithm depending on the type of operation needed for a specific job (Masad et al., 1999b; Tashman et al., 2001; Razavi 2006 and Kutay et al., 2010). In this study, digital image processing is used to process X-ray CT images of compacted specimens of unmodified and rubber modified asphalt mixtures, to characterise their microstructural properties and internal damage. This will need the development of an image processing technique specifically for this particular

composite which embraces of different materials with different sizes and densities. The main operations for the image processing technique are presented in Figure 3.9. Detailed explanations of the operations are discussed further in the following sections.

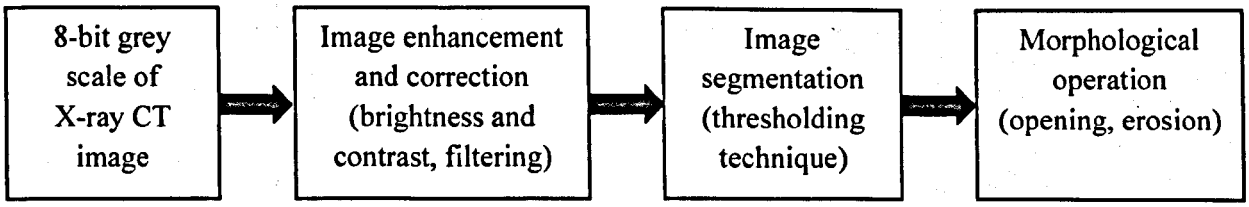

Figure 3.9 Main operations of image processing technique

3.4.1 Digital Image

3.4.1.1 Image Definition

Gonzalez and Woods (2008) define a digital image as a numerical representation of an object which allows for image processing and analysis by performing numerical calculations on its discrete units. Bitmap graphic formats treat each graphic as a collection of image elements called pixels in a 2D image or voxels in a 3D image and specific colours are assigned to each of the elements. Pixels are small square shaped elements arranged in rows and columns that form the main domain of the image. While voxels are small box shaped elements, formed with the extension of a planar element to a volume element to form a 3D image (refer Figure 3.10).

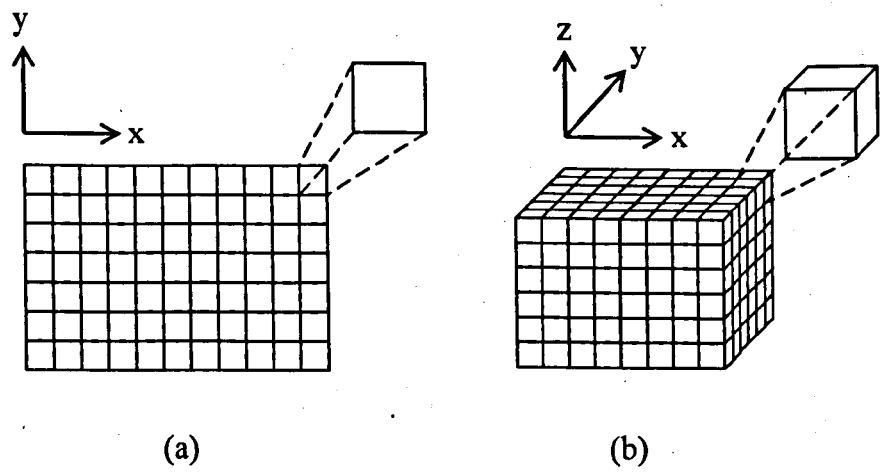

Figure 3.10 (a) Pixel and (b) voxel elements in digital image (Razavi 2006)

Through this chapter, the word pixel will be used to describe the elements referring to 2D images. When viewed as a whole, an array of pixels forms an image as shown in Figure 3.11. When the image is zoomed into for the selected area, the different grey scale assigned for each pixel can be seen. The more pixels present, the more information is available. Pixels can contain different amounts of information known as bit-depth. A digital image can be binary (1-bit), have multiple grey levels (8-bit) or colour (24-bit). 1-bit image is either black (pixel=0) or white (pixel=1). For 8-bit grey image, each pixel is assigned with eight integer, where 0 to indicate black (00000000) and 255 (11111111) to indicate white. A colour image with 24 bit per pixel is basically a combination of three 8-bit integer arrays which are red, blue and green. The array consists of three brightness values corresponding to each of the three primary colours. Figure 3.12 shows the asphalt mixtures cross section images at different bit-depth.

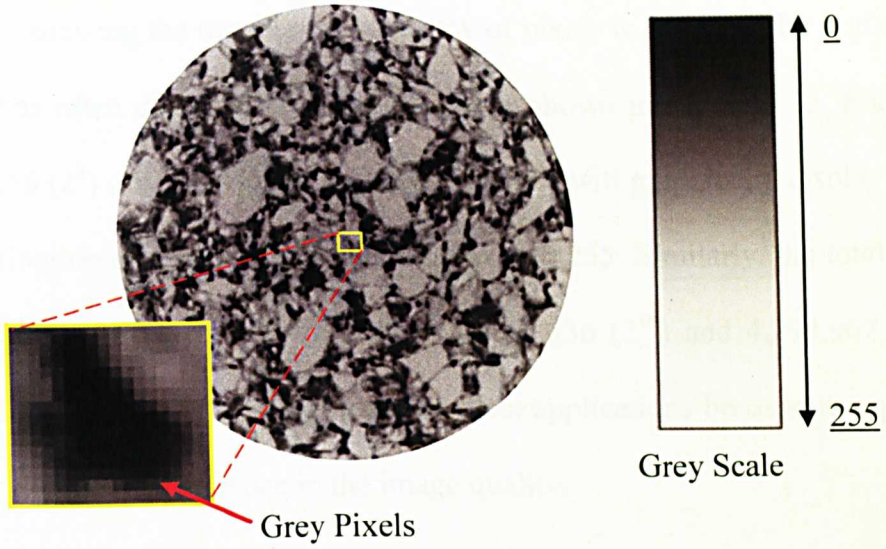

Figure 3.11 Image digitisation

a) 1-bit black and white b) 8-bit grey scale c) 24-bit colour image

Figure 3.12 Example of digital images at different bit-depths

3.4.1.2 Image Brightness Histogram

The image brightness histogram is a vital tool for manipulating the pixel values in an image. It is very helpful in determining a threshold value for image segmentation based on histogram shape analysis (described in Section 3.4.3). Therefore, it is necessary to understand the use of the image histogram for examining the image content. An Image

histogram is a plot showing the number or frequency of pixels in an image for a given range of grey level that is often displayed as a bar graph, as shown in Figure 3.13. For an 8-bit image there are 256 (2^8) different possible grey values that will graphically display 256 bars showing the distribution of pixels within the range of 0 to 255. Similarly, the total numbers of possible shades for 16-bit and 32-bit images are 65,536 (2^{16}) and 4,294,967,296 (2^{32}) respectively. The 8-bit image is typically used for most applications because it requires less memory with no significant difference in the image quality.

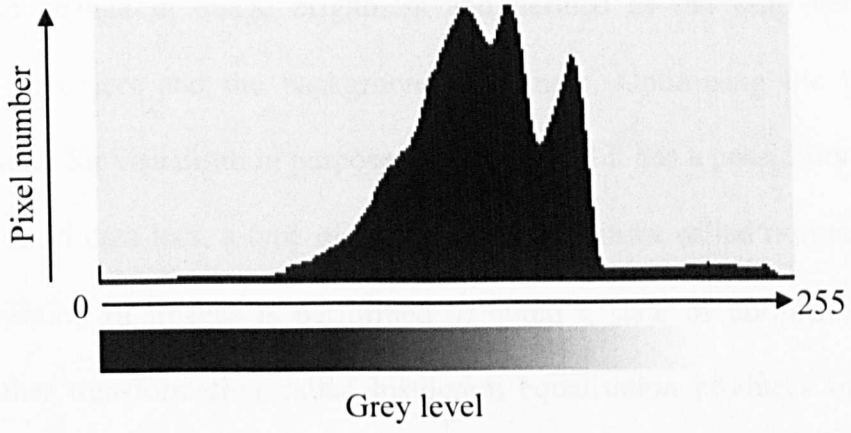

Figure 3.13 Image brightness histogram

3.4.2 Image Enhancement and Correction

To achieve better segmentation results, images with perfect contrast, accurate colour representation and uniform illumination are required. This section introduces the basic concept of how adjustment to pixel values can be performed to improve image quality. Understanding the principles of grey image enhancement gives sufficient background for image treatment using several mathematical functions.

i. Geometric transformations

Geometric transformations involve changing the image size, image rotation and scaling. A digital image can be very large, therefore it is sometimes necessary to reduce its size to enable full image viewing. Sometimes enlarging an image is also important to view the small details of the image's features. A combination of image rotation and scaling is required to align one image with another and to define the spatial scale for analysis purposes.

ii. Brightness and contrast

Contrast is the change in image brightness and defined as the ratio between average brightness of an object and the background brightness. Optimising the brightness and contrast are useful for visualisation purposes but in general it has a possibility to cause some data loss. To avoid data loss, a type of brightness and contrast called normalisation can be used. Normalisation of images is performed to attain a state of uniform brightness and contrast. Another transformation called histogram equalisation produces images with the highest possible contrast and preserves approximately all the details of the initial image. These functions are useful prior to image thresholding.

iii. Filtering

Image filtering includes smoothing and sharpening operations. Digital images are often polluted with noise due to insufficient illumination. Noise should be removed prior to quantitative analysis. Smoothing is the simplest filtering method and can be achieved by taking the mean of the pixel values. Furthermore it works well with images that have minor noise problems. Better results can be obtained by using median filter to treat images with heavy noise problems. This considers the pixel value situated exactly in the middle of the series of pixel values in an ascending order. The sharpening operation is used to enhance the

details of the image by responding to the abrupt changes in the pixel intensity, which is very useful for edge detection.

3.4.3 Image Thresholding

Image thresholding is an operation that helps to define disjoint regions and extract desired features from an image's background. This is done by converting a grey scale image into a binary image. It is widely used for image segmentation, since proper thresholding leads to better segmentation (Sonka et al., 1998). Thresholding is carried out to isolate a region of interest within an image from the background based on pixel intensity. For example, the grey values of pixels in 8-bit images represent a level of greyness or brightness, ranging from completely black (0) to completely white (255). Thresholding is performed on the image by choosing a range of grey intensity values which allow the recognition of the region of interest in the image. It is recognised by a single or multiple threshold values whereby each pixel in the image is compared with the threshold value. Pixels with grey levels below the threshold value are converted to black and pixels with grey levels greater than the threshold value are converted to white. A suitable threshold value may be selected by visual examination of the separated regions based on a reasonable estimation made on the images. However, this is subjective and may not give the best and accurate threshold value. Sometimes using human judgment for image recognition creates problems which can lead to errors and inconsistency. In addition, there are likely to be grey level variations in the object and background due to input device parameters. For instance, images captured with X-ray CT machine depend on the physical properties of the material and beam energy settings. Note that for the same material, different energy settings will produce different image

quality and different grey scale values. Therefore, the threshold value is only a preliminary estimate that requires further validation.

For X-ray images, the brightest area indicates the highest density (aggregates) and darkest area represents the lowest density object (air voids). Therefore the threshold value for air voids is estimated to be close to zero (black). Yet it is adjusted such that the air voids content measured from images matches the laboratory measured air voids content. For aggregates, the measured size distribution from the images is compared with the designed aggregate gradation. Figure 3.14 shows the example of images after adjusting the threshold values, T for a CT slice of asphalt mixture specimen. The single threshold value is adjusted for selecting the region of interest. From the original X-ray image (Figure 3.14a), the image is thresholded by getting the selected regions at T=10 and T=100 (Figures 3.14b & c) in a form of binary image.

a) Original Image b) T = 10 c) T = 100

Figure 3.14 A CT slice of asphalt mixture and adjusted images at different threshold value "T"

3.4.4 Morphological Operations for Binary Image

Thresholding transforms the grey image of selected features into a binary image to prepare the resulting images for measurement. However, in certain circumstances the region of interest can be over or under segmented after thresholding due to the variation in the pixels' grey values. Morphological operations enable detection of the features exact area and shape as well as the boundary between two adjacent objects in the binary image. Morphological transformations for binary images are available for the following operations. Combination of these operations can improve the segmented features for getting better property measurements.

i. Erosion, dilation and holes-filling

Erosion and dilation operations are used to reshape the initial object. Holes-filling is used to fill any internal object within the region of interest by replacing the missing pixels. These operations are suitable for ridding the region of interest of any unwanted objects resulted from thresholding. The outcomes of these operations can be observed by comparing the circled area as shown in Figure 3.15. The holes-filling operation has successfully removed all the unwanted objects from the aggregate region caused by non-uniform grey levels during thresholding. The dilation operation expands the aggregate region (region of interest) and minimises the unwanted objects while erosion operation erodes or reduces the aggregate region resulting an expansion in the region of unwanted objects.

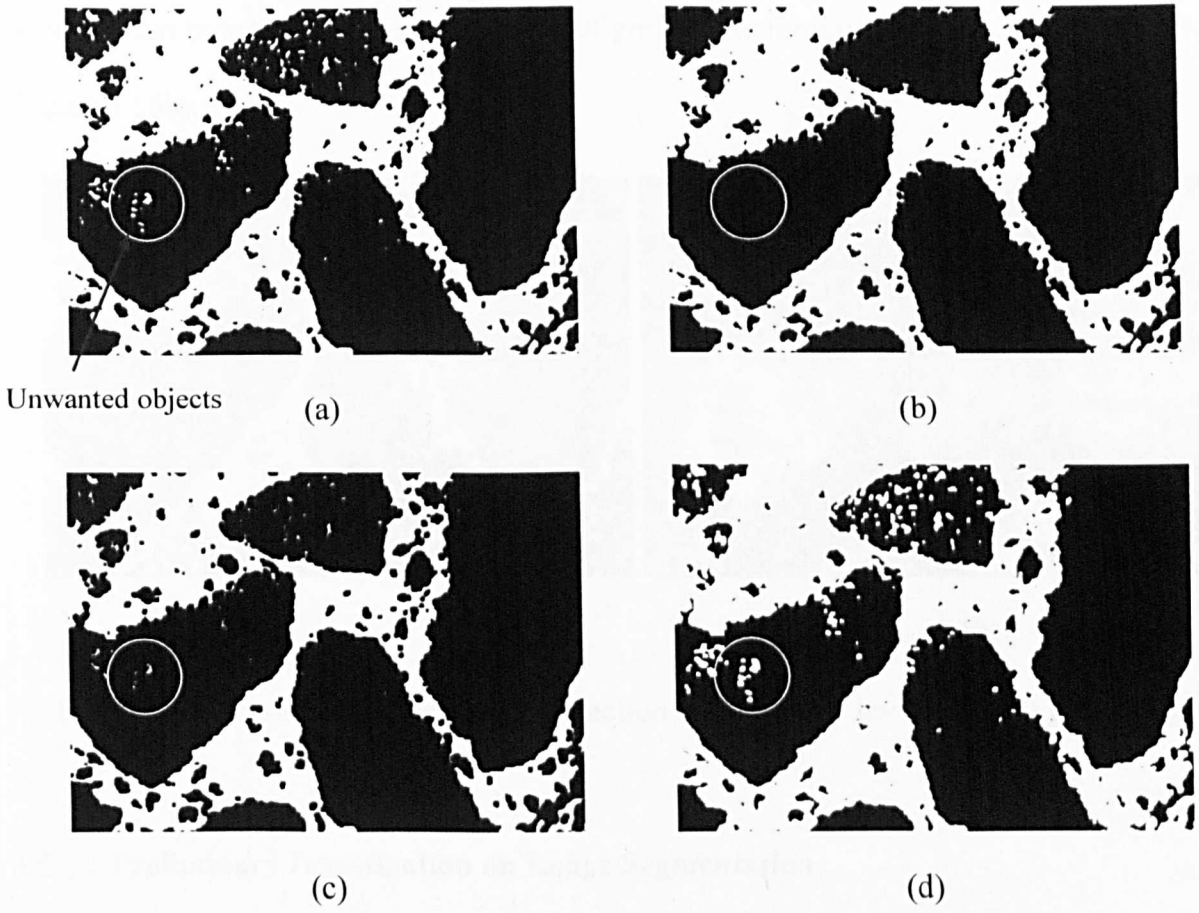

Figure 3.15 Example transformations for aggregate region (a) image after thresholding, (b) holes-filling (c) dilation and (d) erosion

ii. Watershed detection

This operation is widely used for edge detection on a binary or grey image. It can be interpreted as a map of continuous lines used to better define the boundary of the region of interest. It detects any concave surface between two adjacent objects that merge together as a result of thresholding and separates them into two convex objects (refer to red arrows in Figure 3.16a as an example using aggregate particles). However this creates a problem when the operation detects any concave surface at the edge of an object, leading to over segmentation as pointed out (see yellow arrows) in Figure 3.16a. For grey images, the

detection can be set within the target range of grey levels for any particular region of interest (Figure 3.16b).

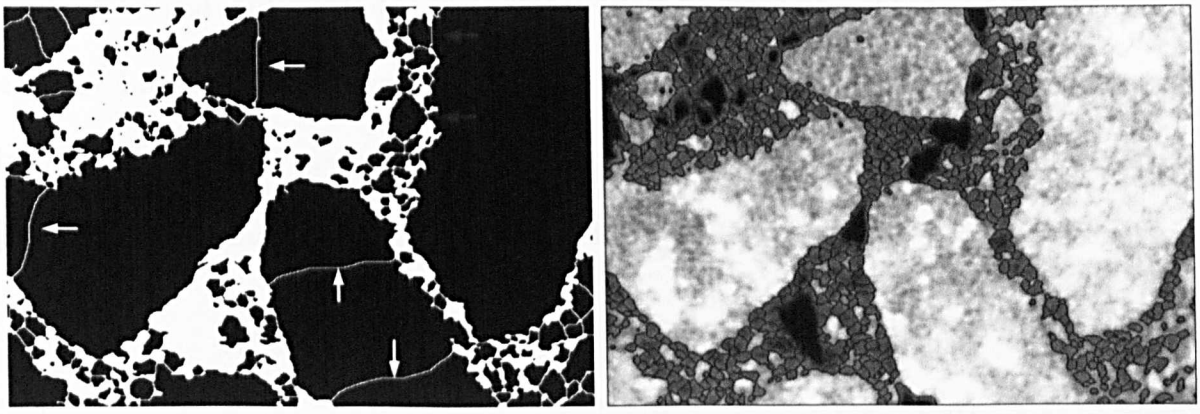

(a) (b)

Figure 3.16 Illustration of watershed detection on (a) binary image and (b) grey image

3.5 Preliminary Investigation on Image Segmentation

For the purpose of finding the method of image segmentation, specimens with different material combinations were prepared in the laboratory for X-ray CT scanning. The captured images were then processed and examined to determine the image quality and propose with a potential thresholding method for segmenting the region of interest. These were performed using imaging software packages, ImageJ and Image-Pro Plus. The goal was to separate the different material phases in the rubberised asphalt mixture particularly the air voids, mastic, aggregates and rubber particles. The main concern was that the addition of rubber in the asphalt mixture with its density almost similar to bitumen's density might create difficulty with regards to differentiating between the rubber and the mastic which comprises bitumen and filler. Therefore, this preliminary investigation was necessary in order to select the most appropriate thresholding algorithms to be used in this study. Details of the laboratory prepared specimens with different material combinations are summarised in Table 3.1 and

Figure 3.17. Gyratory compacted specimens (No. 1 and 2) of Dense Bituminous Macadam (DBM 20) and Hot Rolled Asphalt (HRA 60/20-gap graded) were prepared according to (BS 4987-1:2001) and (BS EN 13108-4:2006) respectively (refer Figure 3.17(a&b). For specimens 3 to 5, different quantities of materials were selected on the basis of getting well-mixed portions of the different material combinations. They were uniformly blended together in a transparent container as shown in Figure 3.17(c-e) prior to X-ray CT scanning.

Table 3.1 Percentage of different material combinations

No.	Specimens	Percentage of material (%)				
		Aggregate	Rubber	Filler	Bitumen	Total
1.	DBM 20 (dry mixed)	85	5	5	5	100
2.	HRA 60/20 (dry mixed)	87	2	5	6	100
3.	Rubber + Filler + Bitumen	-	10	55	35	100
4.	Rubber + Aggregate	80	20	-	-	100
5.	Rubber + Bitumen	-	5	-	95	100

(a) DBM 20

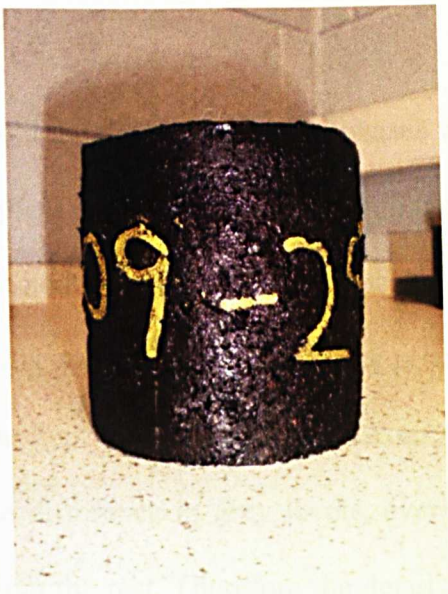

(b) HRA 60/20

(c) Rubber + Filler + Bitumen

(d) Rubber + Aggregate

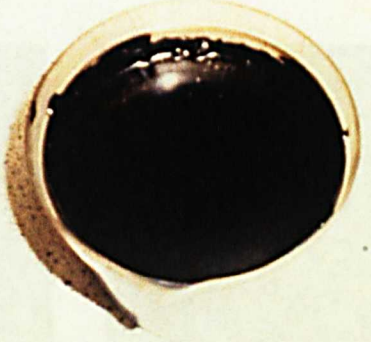

(e) Rubber + Bitumen

Figure 3.17 Mixtures of different material combinations for X-ray CT scanning

3.5.1 Image Histogram and Image Profile

The priority at this stage of the trial was to threshold the different material phases within the mixtures. Instead of the compacted rubberised asphalt mixtures, three other mixtures with a lesser number of material combinations were selected to reduce the variation in grey level (intensity) of the X-ray images. The idea behind this was that the thresholding process could be simplified if the variation in the grey levels was kept to the minimum necessary, to better identify the region of interest. By comparing the difference in grey levels, every material component would then be traced and extracted from the rest. Therefore the details of the X-ray images for the selected mixtures needed to be examined prior to thresholding, particularly the image histogram and image profiles. This was done to determine whether the images would require a simple or detailed thresholding method.

An *image histogram* enables us to better identify the best threshold value for image segmentation. Most thresholding algorithms perform well with an image that has a bimodal (two distinct peaks) or a multi-modal intensity histogram depicting areas of sufficiently equal sizes with substantially non-overlapping distributions (Figure 3.18). When this criteria is not met, major difficulties can be encountered when thresholding the images.

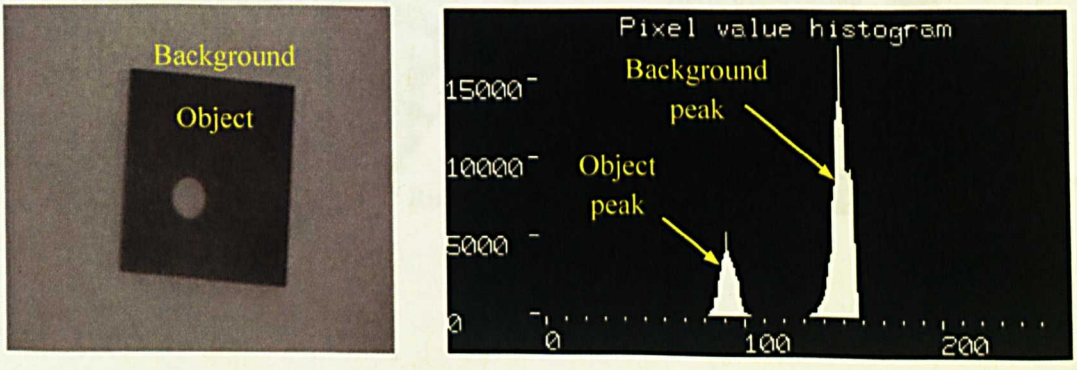

(a) (b)

Figure 3.18 (a) An image with its (b) bimodal histogram (Gonzales and Woods 1992)

Figures 3.19 to 3.23 show the X-ray images of each of the scanned specimens and their associated image histograms from the preliminary scanning work. Generally, it can be seen that the peaks tend to merge into each other, which explains why the grey level of the material phases are hardly distinguished. When this occurs, thresholding operation becomes increasingly difficult. From a visual assessment, it is much easier to recognise the internal features of a gap graded mixture (Figure 3.20) compared to a dense graded mixture (Figure 3.19) due to the gaps within the aggregate gradation. A similar problem is observed in Figure 3.21 because the grey level of crumb rubber and bitumen are almost similar due to their close density values. The pixel intensity values of both rubber and bitumen overlap significantly, making the image gradient histograms more likely to be unimodal. A unimodal histogram is defined as a histogram with one distinct peak where the distributions of the grey levels for different materials are concentrated in one particular range.

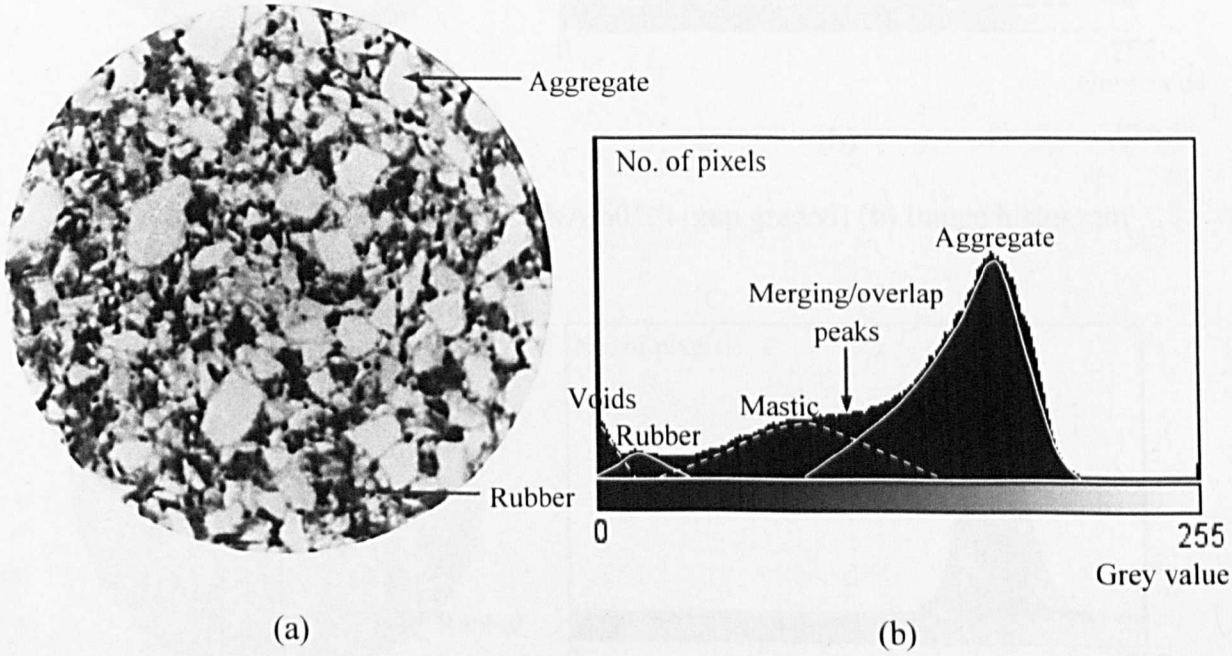

Figure 3.19 (a) X-ray image of DBM 20 (dense graded) (b) Image histogram

However, for the mixtures illustrated in Figures 3.22 and 3.23, even though the peaks have partially merged together, the rubber and the remaining material phases are clearly visible. This is because the number of materials' component within the image was set to minimum with great difference in their densities. It can be concluded that the previous criteria for simple thresholding were not met for all images. Therefore, it was almost impossible to successfully segment those images using a simple thresholding method without further enhancement. The histogram-based thresholding method is discussed further in the next section.

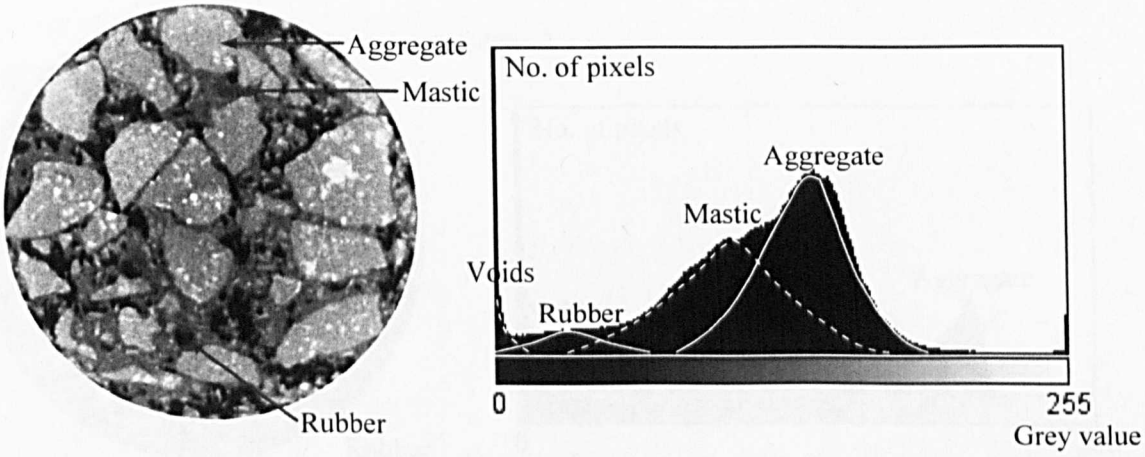

Figure 3.20 (a) X-ray image of HRA 60/20 (gap graded) (b) Image histogram

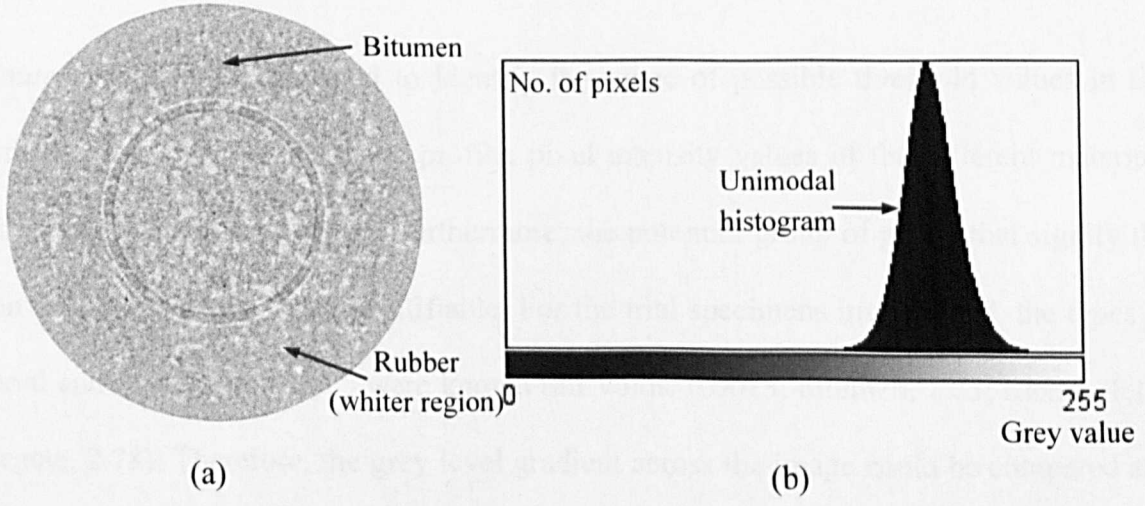

Figure 3.21 (a) X-ray image of a mixture of bitumen and rubber (b) Image histogram

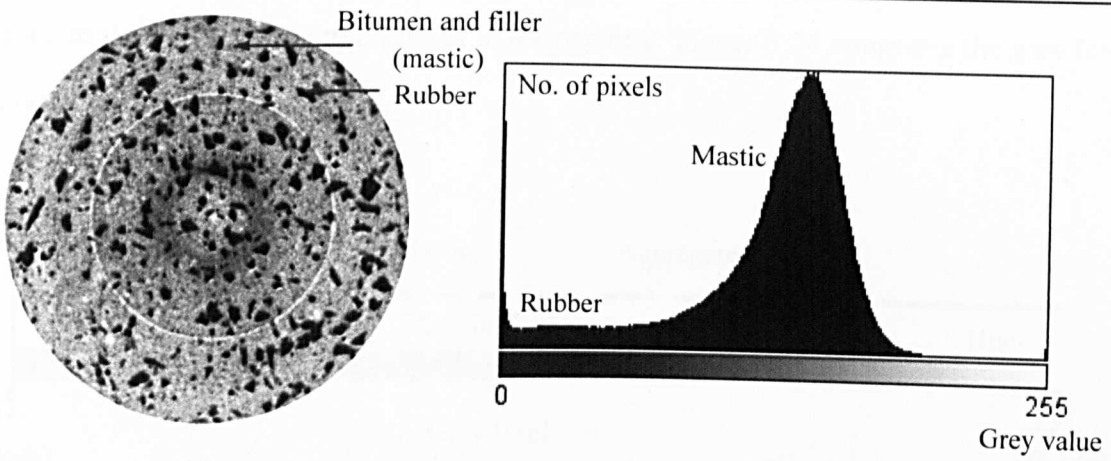

Figure 3.22 (a) X-ray image of a mixture of bitumen, filler and rubber (b) Image histogram

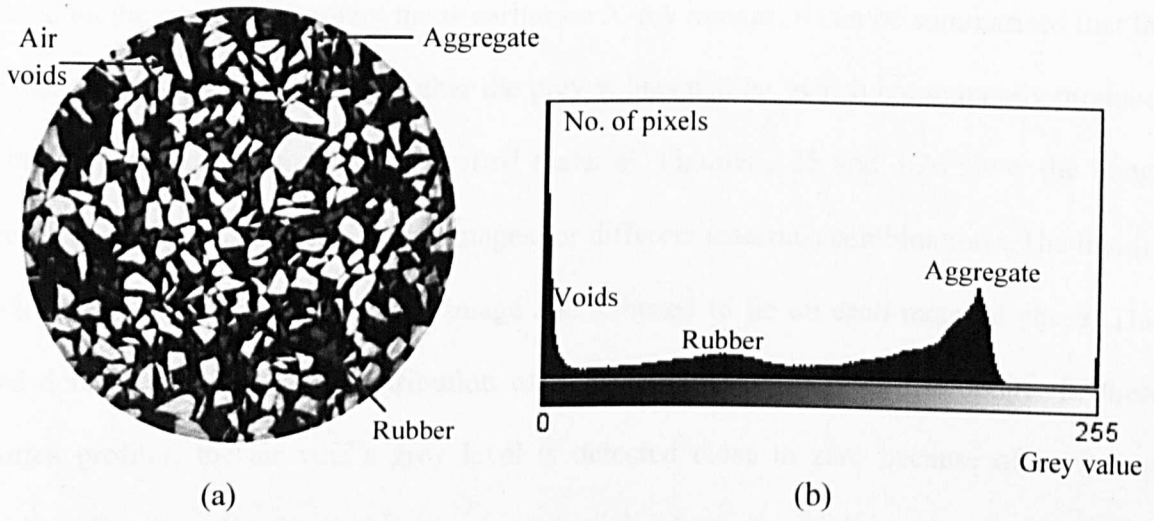

Figure 3.23 (a) X-ray image of a mixture of aggregate and rubber (b) Image histogram

An *Image profile* was generated to identify the range of possible threshold values in the region of interest. Using an image profile, pixel intensity values of the different materials within an image can be detected. Furthermore, the potential group of pixels that signify the region of interest may also be identifiable. For the trial specimens investigated, the types of material and density (in g/cm^3) were known (air voids, 0.0013; bitumen, 1.03; rubber, 1.15; aggregate, 2.78). Therefore, the grey level gradient across the image could be compared and

assigned to the different material phases in the mixture. Figure 3.24 compares the grey level with the material density.

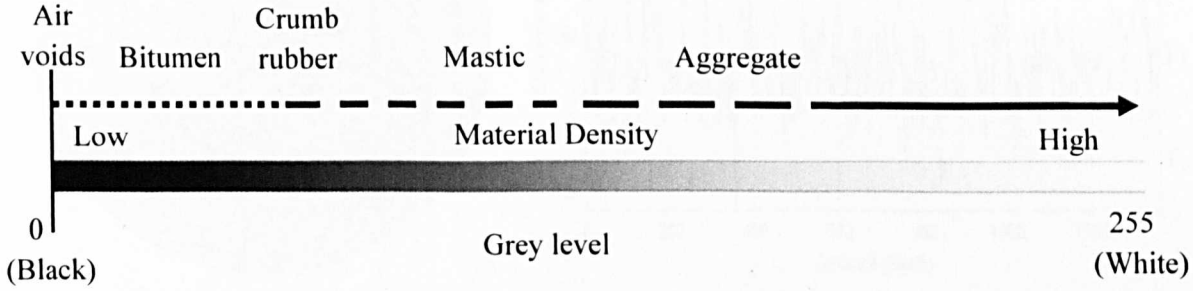

Figure 3.24 Comparison between material density and grey level for the captured images

Based on the visual assessment made earlier on X-ray images, it can be summarised that the higher the material density, the higher the grey values will be, which consequently produces a brighter image region for the specified material. Figures 3.25 and 3.26 show the image profiles of the pixels detected in the images for different materials combinations. The line (in yellow) has been drawn across the image and adjusted to lie on each material phase. This was done to determine the distribution of the grey level throughout the image. In these plotted profiles, the air void's grey level is detected close to zero because of its lowest density. On the other hand the aggregate particles have the highest grey level and the remaining grey levels represent mastic and rubber particles. Therefore, image of air voids appears as the darkest region (in black), followed by crumb rubber, the mastic as a grey region and finally aggregates, having the brightest region. The air voids are highlighted in red (initially black) to distinguish the air voids region from the rest. The ranges of the grey values for the specified regions of different material phases are then classified as shown in the profiles.

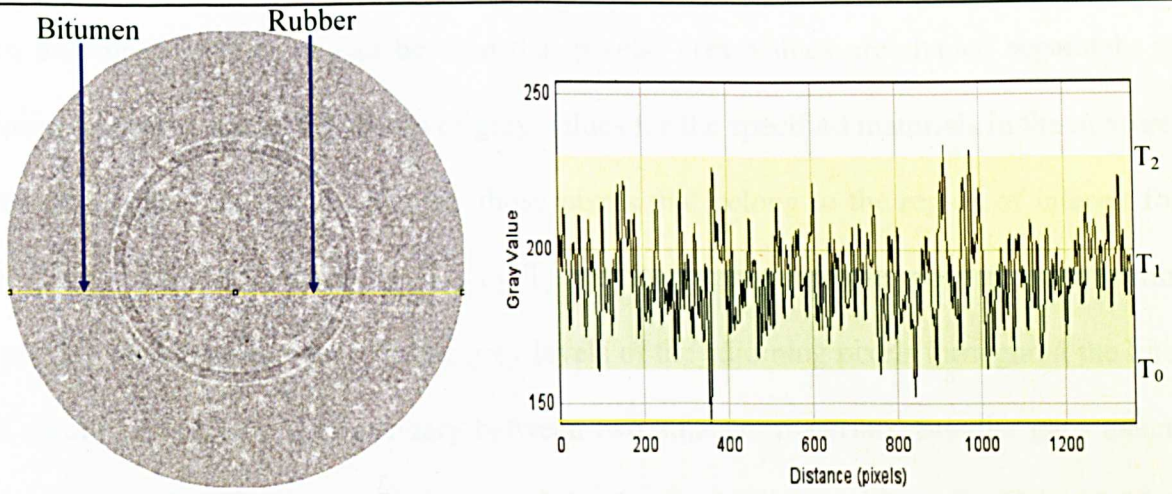

(a) A mixture of bitumen and crumb rubber

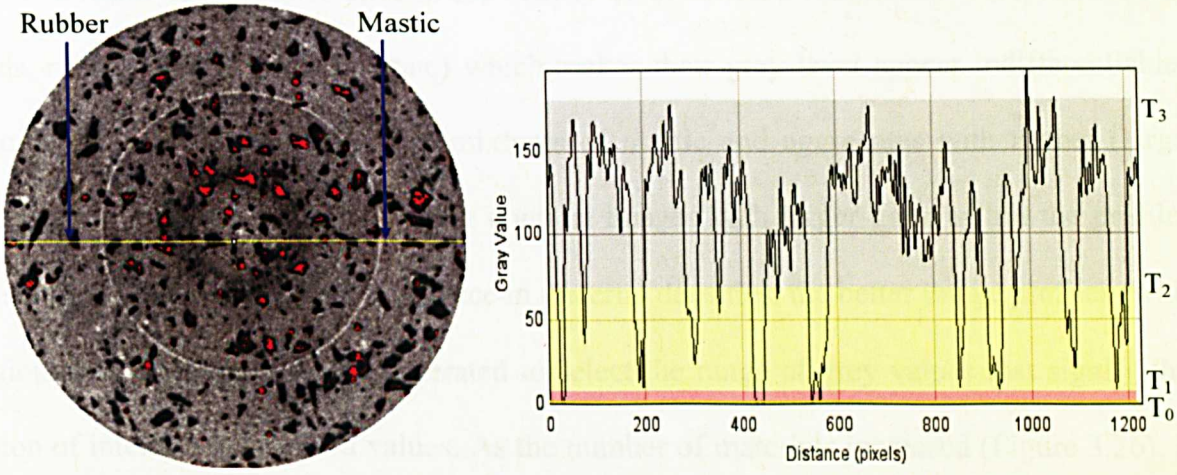

(b) A mixture of crumb rubber and mastic (bitumen and filler)

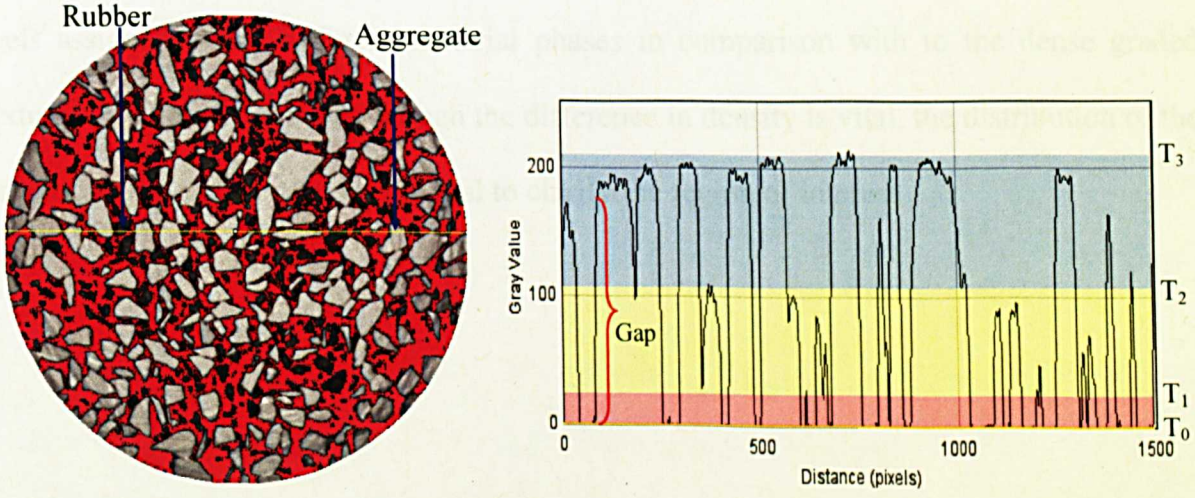

(c) A mixture of aggregate and crumb rubber

Figure 3.25 Image profile for different material combinations. Shade indicator: Aggregate (blue); mastic (grey); bitumen (green); rubber (yellow); voids (red)

From the image profiles, it can be seen that pixels' grey values are shaded separately in different colours to group the ranges of grey values for the specified materials in the mixture. These grey values are used to identify those pixels that belong to the region of interest for detecting the threshold values (T_0, T_1, T_2, T_3 and T_4) as shown in the profiles. Gaps within the profiles describe differences in the grey levels of the adjoining pixels throughout the line. This would best refer to the boundary between two adjacent materials. Smaller gaps means there is not much difference in the grey level for the specified materials (refer Figure 3.25a). This is a result of least difference in the density of the different materials' composition (air voids, rubber, mastic and aggregate) which makes their grey level appear indifferentiable. Figures 3.25b and 3.25c show that mixtures of mastic and aggregates with rubber (large difference in density) produced higher contrast images with larger gaps within the profile. This concludes that the higher difference in material densities, the better image profiles (with obvious transition gap) can be generated to select the range of grey values that signify the region of interest as threshold values. As the number of materials increased (Figure 3.26), it seems that the gap graded mixture produced an image profile with clearer visible pixel grey levels assigned to the different material phases in comparison with to the dense graded mixture. This shows that even though the difference in density is vital, the distribution of the particles within the mixture is essential to clarify the region of interest.

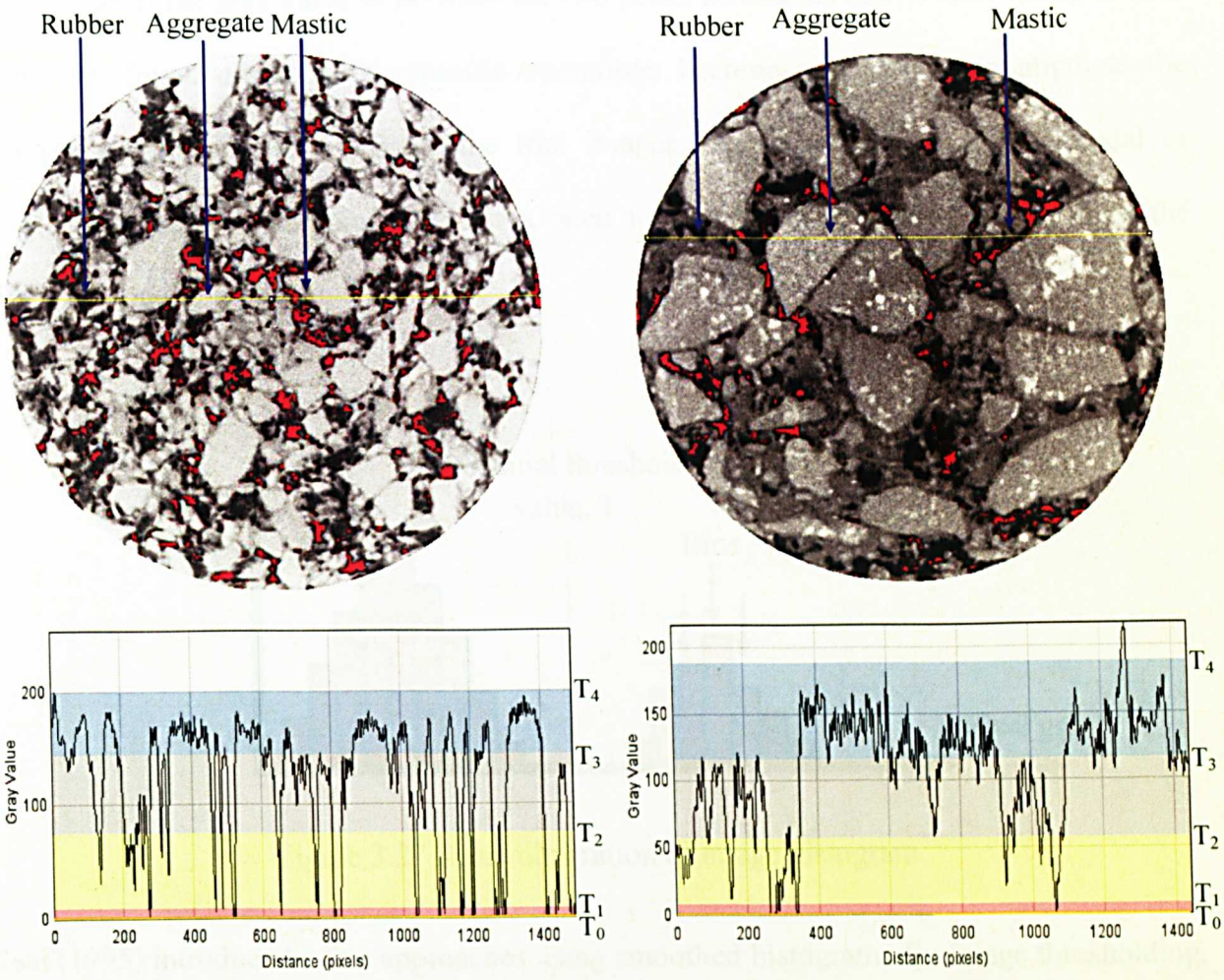

Figure 3.26 Image profile for (a) DBM 20 (b) HRA 60/20. Shade indicator: Aggregate (blue); mastic (grey); rubber (yellow); voids (red)

3.5.2 Histogram-Based Thresholding

This thresholding method is based on the shape properties of the histogram. Basically, an image histogram is constructed from the grey values with 256 bins (from 0 to 255). Figure 3.27 shows two distinct peaks in the histogram corresponding to the object of interest and the background image. It can be clearly observable that the pixel grey values within the objects are distinctly different from the background pixels. The threshold value can be easily

determined as the grey value in between the two peaks (Gonzales and Woods 1992). If such peaks are found not to exist, specific operations become necessary to manipulate the histogram shape properties. Since the trial images, shown earlier possess unimodal or overlapping peaks histograms, there is a need to find the best method to threshold the different material phases.

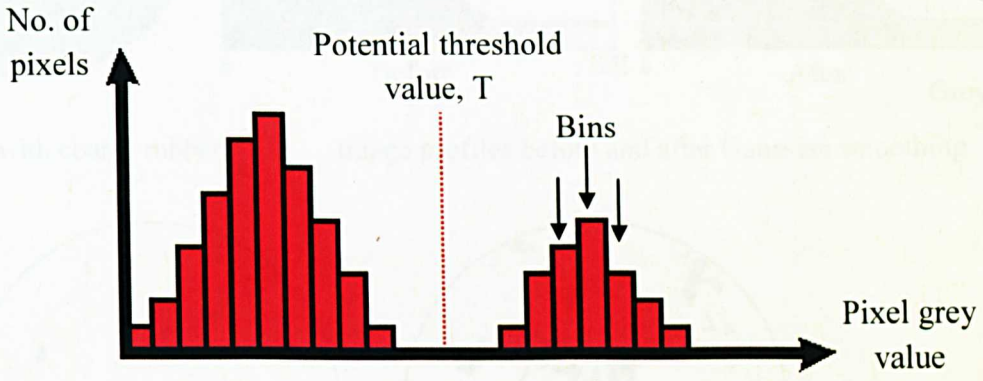

Figure 3.27 Basic illustration of image histogram

Tsai (1995) introduced a few approaches using smoothed histograms for image thresholding. The first approach produces a smoothed histogram via a Gaussian filter which was found to work well for images with an overlapping peaks histogram. The Gaussian smoothing is an operation to replace each pixel value with the average intensity of its neighbouring pixel to reduce the amount of intensity variation. This has the effect of eliminating pixel values which are unrepresentative of their surroundings. The resulting histogram is subsequently inspected for the presence of sharp curvature points or peaks. The smoothing level is then adjusted until the histogram shows clear distinct peaks for the different material phases. The trough or valley (minimum) point between the peaks is selected as the threshold value. Two threshold values (band thresholding) are used to segment the pixels belonging to the region

of interest from the background pixels. Figure 3.28 shows the result of Gaussian smoothing on the image histogram and the segmented images after thresholding.

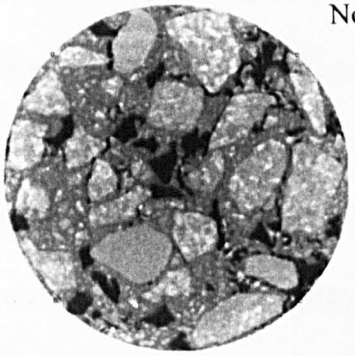

HRA 60/20 with coarse rubber

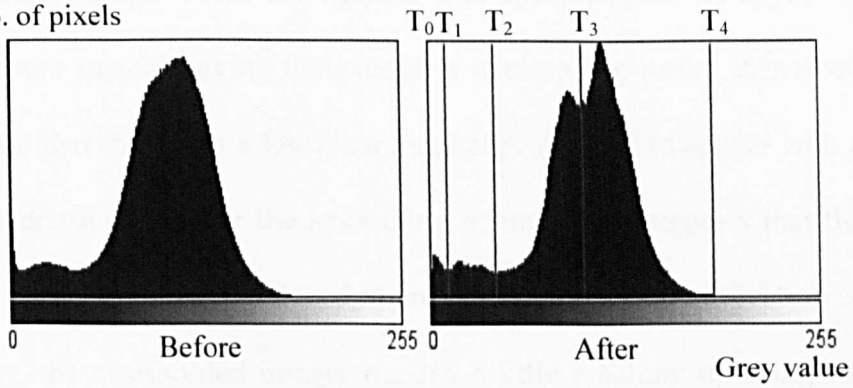

Image profiles before and after Gaussian smoothing

Air voids (T_0-T_1)

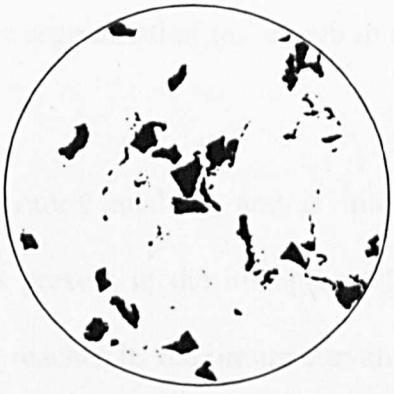

Coarse rubber (T_1-T_2)

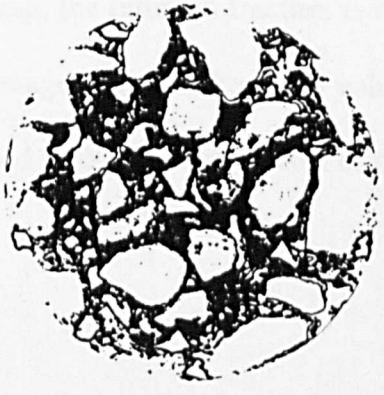

Mastic (T_2-T_3)

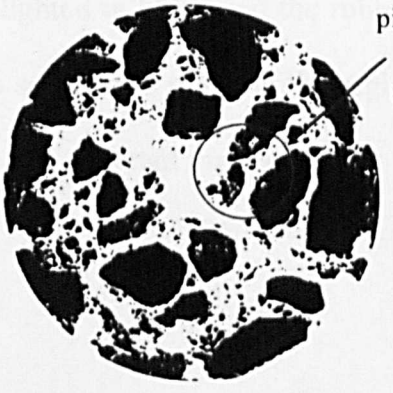

Aggregate (T_3-T_4)

Figure 3.28 Image histograms for gap graded with coarse rubber before and after Gaussian smoothing and images after thresholding for the detected threshold values, T

Band threshold values were selected as the upper and lower limits for each of the material phases namely air voids, rubber, mastic and aggregates. After thresholding, the object of interest was converted to binary image. From the figures, it is apparent that the approach works well with asphalt mixture images having the excessive overlapping peaks, described earlier. The image histograms also show that a few clear distinct peaks tend to appear with a small variance in the pixels distribution after the smoothing operation. It suggests that the variation in the pixels grey level had become reduced, thereby enabling the identification of the threshold values. Finally, the thresholded images needed a little touching up using the morphological operation to refine the non-uniformity in pixel distribution within the area of the object of interest, due to over or under segmentation (as shown in the thresholded image of aggregate, Figure 3.28).

Tsai's second approach focuses on curvature analysis and is intended for a unimodal histogram where only one main peak is present in the histogram. The threshold value is selected at the point where the histogram reaches its maximum curvature. Figure 3.29 shows the image of a mixture of bitumen and rubber with a unimodal histogram. After thresholding, the bitumen fraction is highlighted in black and the rubber particles, in white. For this image, a single threshold value is selected to segment the region of interest and the background as the mixture consist of only two different materials.

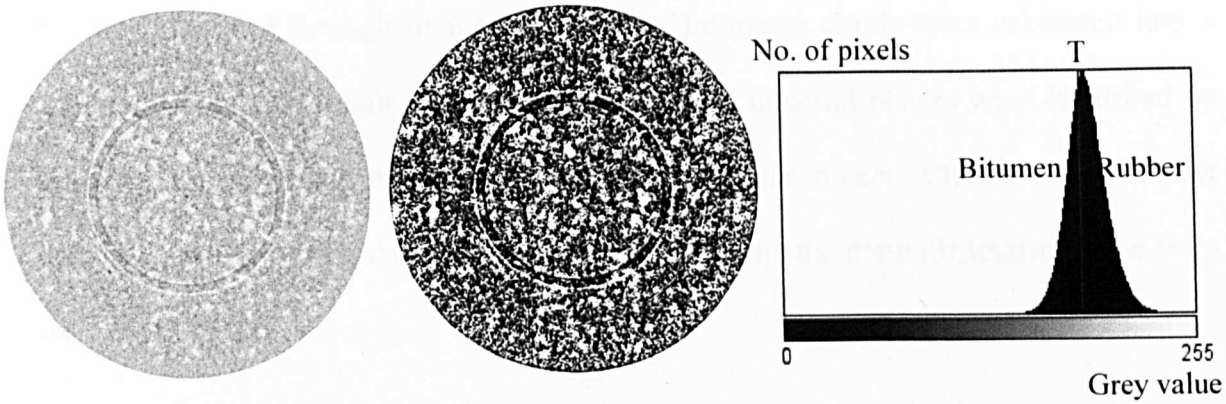

Figure 3.29 Images of a mixture of bitumen and rubber before and after thresholding for the detected threshold values, T (at maximum curvature point)

From this investigation, it is deducible that this thresholding method can be useful for dealing with asphalt mixture image segmentation. This approach becomes effective when the histogram has lost its bimodality due to the excessive merging peaks of the class histograms as observed in the asphalt mixture images. However further enhancement is needed to improve the selection of the region of interest after thresholding. In addition, it would be more helpful if a good quality of original X-ray CT image could be produced before using any thresholding method as this would lead to more reliable results.

3.6 Image Processing and Thresholding Technique Developed for Asphalt Mixture

Detailed image processing and thresholding technique have been developed to characterise the internal structure of X-ray CT images of rubberised HRA 60/20. These techniques apply various mathematical procedures to enhance and extract significant information from the images. The detailed procedures are summarised as follows:

1. *Clarification*: The internal structure of rubberised asphalt mixture consists of four material phases i.e. aggregates, crumb rubber, air voids and mastic. These materials must

be clearly defined through image processing. The image pixels were calibrated into a physical measurement unit (e.g. mm). The different material phases were identified by choosing the right threshold value for that particular object. Choosing the correct threshold value is a longstanding problem. In this study, the main difficulties come from the following facts:

i. Difficulty in distinguishing between crumb rubber and bitumen. This comes from the fact that they have almost similar densities (crumb rubber, 1.15 g/cm^3 and bitumen, 1.03 g/cm^3 approximately) and their grey scales are not very different, making these materials look alike in the image. This occurs, although the bitumen is considered to have been well mixed with fines and filler to form mastic during mixing and the compaction was performed without any major separation. Even if there is an individual separation, the area is too small compared to the whole slice area.

ii. Images of aggregates having different grey scales which depend on their mineral compositions. The variations in dark and light grey appear within the aggregate cross section. This makes it difficult to choose a specific threshold value to isolate aggregates from other materials.

iii. Two or more fine aggregates that touch each other can be recognised as one large aggregate by the imaging software.

iv. The mastic surrounding the aggregates consists of bitumen and fine particles. This blend produces different grey levels for the mastic. Small portions of bitumen or fines which are not uniformly blended will increase the variation in grey scale.

To identify the problem area, a pseudo colour was applied to the original image to view the material phases, by assigning each of them with a different colour spectrum. The pseudo

colour technique applies an artificial colouring which can reveal an image's hidden texture and qualities that may not have been apparent in its original grey scale image (refer Figure 3.30). Figure 3.31 shows an X-ray image of gap graded asphalt mixture before and after pseudo colour transformation. The pixel intensity for aggregates is not much different from the mastic which makes the particles' boundary hardly distinguishable.

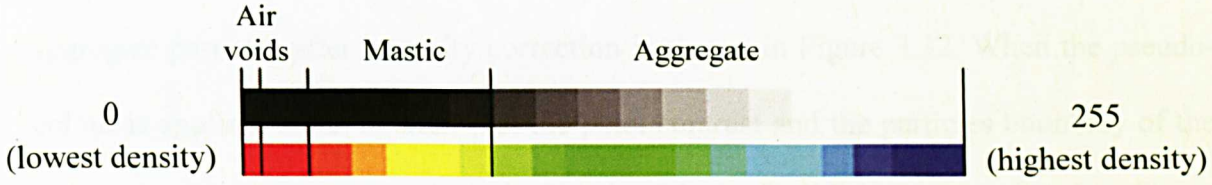

Figure 3.30 Comparison of the pseudo colour spectrum and grey level for different materials

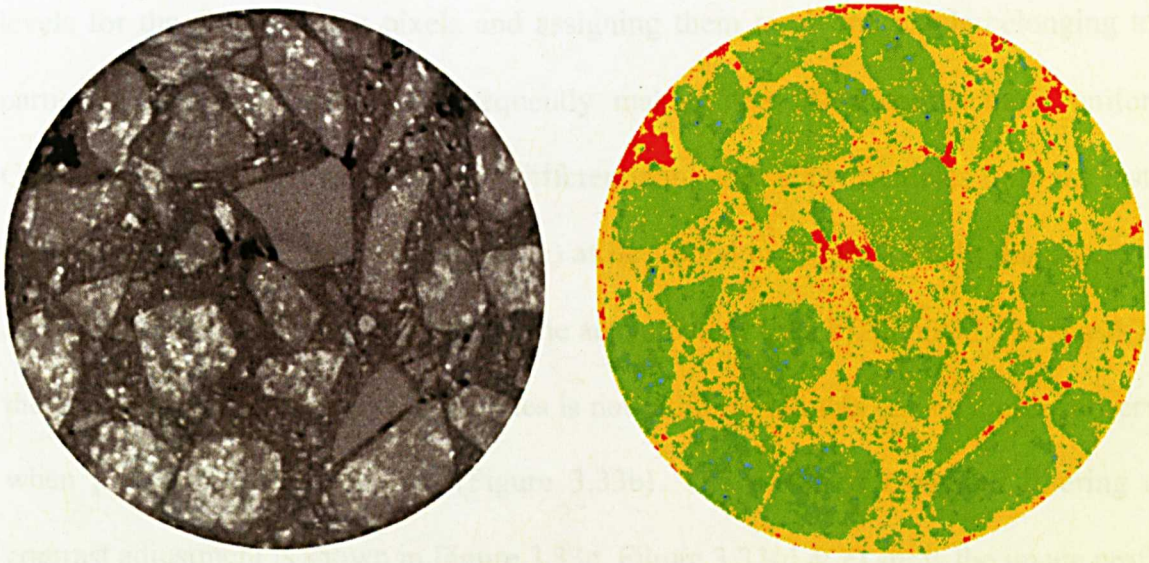

(a) (b)

Figure 3.31 (a) Original X-ray CT image and (b) after pseudo colour transformation

2. *Enhancement*: To overcome the aforementioned difficulties, different procedures for image processing were investigated and numerous repeat scans were undertaken. Preliminary treatments were necessary prior to segmentation because the possible

variability in the quality of the original image. It must be noted that sometimes different combinations of image enhancement procedures are needed for the different materials under consideration. To enhance the clarity of the different material phases, the brightness and contrast of the images were adjusted using 'pixel intensity equalisation'. The colour and contrast were enhanced to produce an image with the highest possible contrast, whilst preserving almost all the detail of the original image. A sample image of aggregate particles after intensity correction is shown in Figure 3.32. When the pseudo-colour is applied, it can be seen that the pixel contrast and the particles boundary of the aggregates are clearly recognisable following pixel equalisation as compared to Figure 3.31b. Gaussian filtering was used to reduce the noise problem as well as the variation in the grey levels of the surrounding pixels. This was done by taking the means of the grey levels for the neighbouring pixels and assigning them to all the pixels belonging to a particular region of interest, consequently making the filled colour more uniform. Gaussian filtering was really useful in differentiating the rubber particles from the rest of material composition (background image) as described in Figure 3.33. In this figure, the air voids are highlighted in red and not the actual colour (black). Figure 3.33a shows that the grey level within the rubber particles is not uniform and this can be clearly observed when pseudo colour is applied (Figure 3.33b). The result of Gaussian filtering and contrast adjustment is shown in Figure 3.33c. Figure 3.33(d & e) show the image profiles of the AB line (in yellow) drawn in Figure 3.33(a & c). By comparing both profiles, less fluctuation in the grey values can be observed in the profile after enhancement (refer Figure 3.33e) implying a reduction to the minimum of variations in the grey values. In addition, the grey values are much higher compared to the original image due to the brightness and contrast adjustment. Finally, the pixel grey values of the different

materials can be detected and classified according to the group of pixels that signify the object of interest for segmentation.

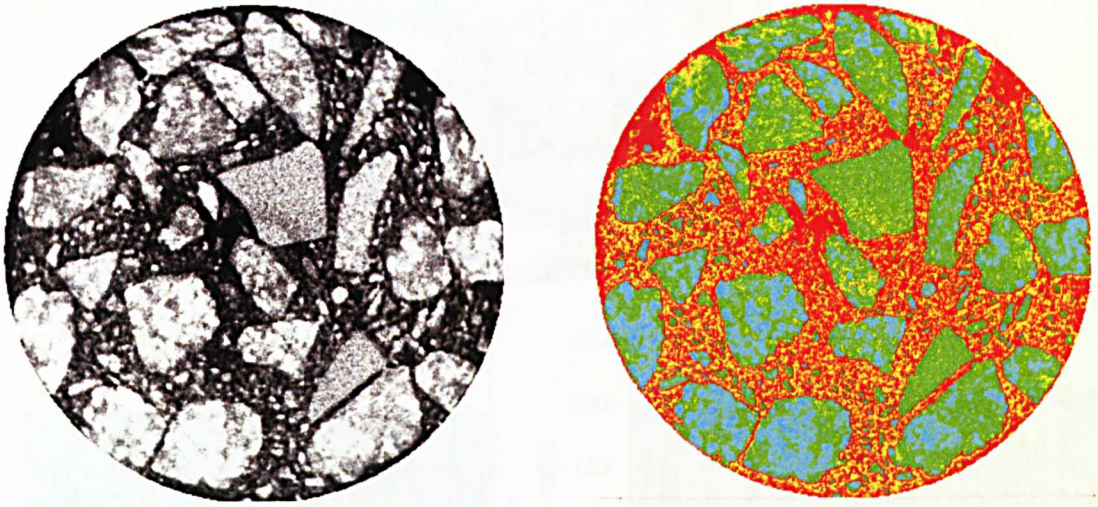

(a) (b)

Figure 3.32 X-ray image after (a) pixel equalisation and (b) pseudo colour transformation

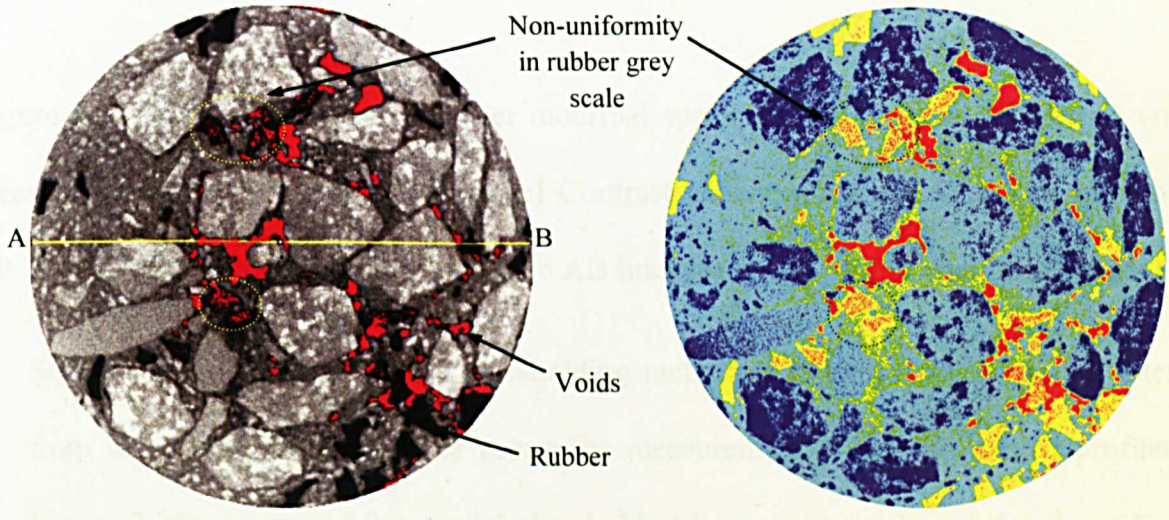

(a) (b)

Figure 3.33 continues below

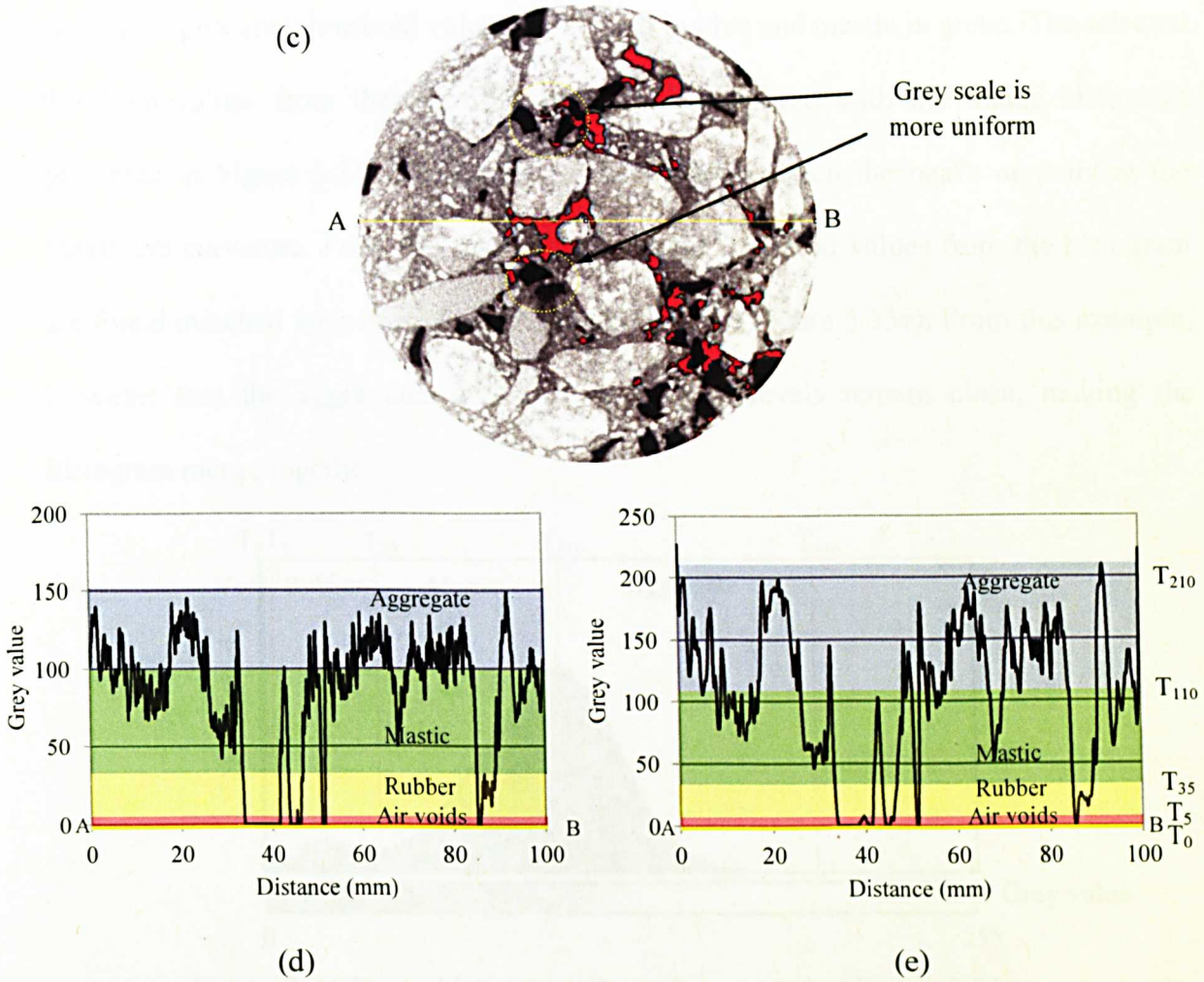

Figure 3.33 Image processing of rubber modified specimens (a) Original image (air voids thresholded in red) (b) Pseudo colour (c) Contrast enhancement and Gaussian smoothing (d) Image profile of original image (refer to AB line) (e) Image profile after enhancement

3. *Segmentation*: This step uses a thresholding technique to extract the object of interest from the background image for properties measurement. From the plotted profiles in Figure 3.33e, a range of potential threshold values can be selected for the different materials phases (aggregates, mastic, rubber and air voids) with reference to their designed content. It must be noted that, a number of image profiles were analysed throughout the process of segmentation. From the image profile, the range of threshold values for rubber particles and air voids have been shaded in yellow and red respectively.

Aggregate potential threshold values are shaded in blue and mastic in green. The selected threshold values from their profiles were then compared with the image histogram presented in Figure 3.34 which targeted the valley between the peaks or point at the maximum curvature. From the figure, the potential threshold values from the histogram are found matched with those from the image profile (Figure 3.33e). From this example, it seems that the aggregates and the mastic grey levels remain close, making the histogram merge together.

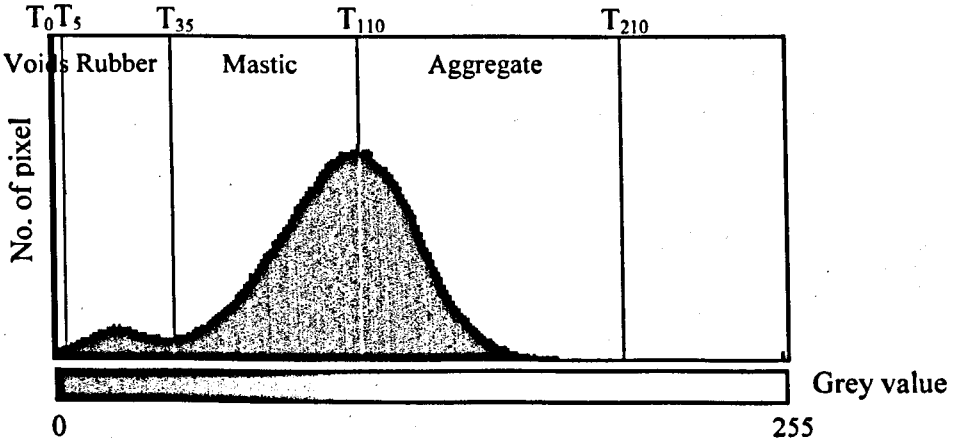

Figure 3.34 Image histogram after enhancement of Figure 3.33c

4. *Morphological operation*: After thresholding, a few potential problems can occur within the thresholded region of interest. This is particularly evident with aggregate particles. The boundary between two particles in contact is unclear due to the small difference in grey levels. Therefore the thresholding operation is unable to satisfactorily detect the boundary's pixels. As a result, two aggregates in contact are detected as one large aggregate. In addition, the difference in mineral composition creates a non-uniformity of grey level within the selected region. Using morphological operations such as edge detection, holes removal or region filling, merging and splitting tools, the image is then further enhanced. These image editing tools are used to detect the boundaries and remove the non-uniformity of the grey level (holes) within the selected area. For

example with the splitting tool, the image of two aggregates in contact is outlined and divided into regions as shown in Figure 3.35(a-b). The holes removal tool fills the holes within the selected aggregate area (refer Figure 3.35(c-d)).

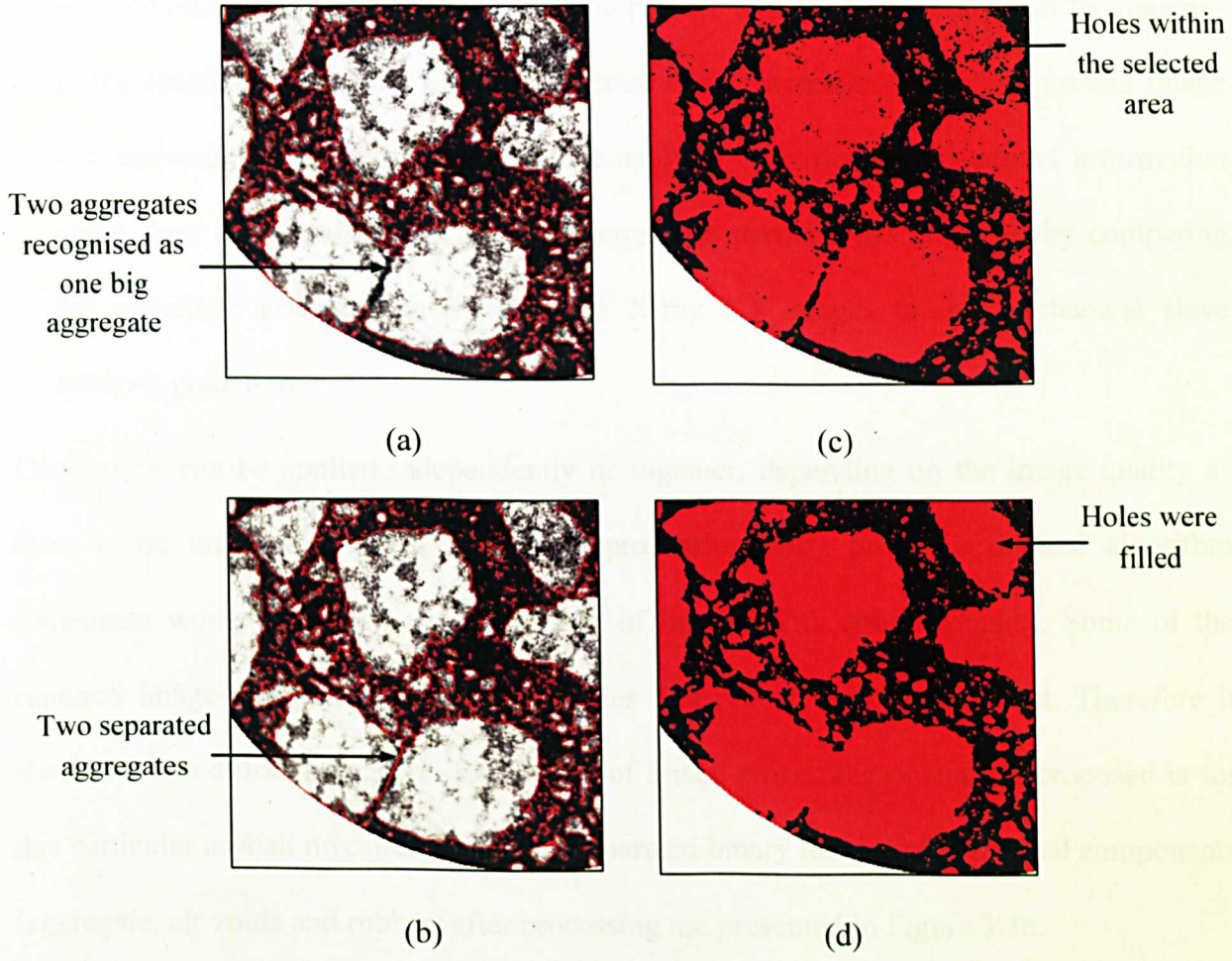

Figure 3.35 Aggregates image with (a) Outlined before splitting (b) Outlined after splitting (c) Filled area with holes (d) Filled area after holes-filling

In the final image, only aggregates with sizes approximately ≥ 2 mm are counted while the rest are considered as part of the mastic to avoid any unnecessary over-selected pixels that might belong to the background. Previous research found that studying the distribution of large aggregates will adequately describe the changes in the main structure of aggregate (Yue and Morin 1996 and Masad et al., 1999a). It is important to

note that these processes have to be performed with great care to avoid unnecessary over segmentation or the loss of any information.

5. *Verification*: The threshold values are adjusted based on the fact that a proportion of the selected total area in all image slices is comparable to the total percentage of the material in the specimen. Once the region of interest is segmented from the background image and converted to a binary image, image analysis is carried out to extract information about their characteristics. In addition, aggregate particles are validated by comparing the aggregate gradation measured from X-ray CT images to the mechanical sieve analysis gradation.

These steps can be applied independently or together, depending on the image quality as there is no universal method for image processing. Any precisely defined algorithm sometimes works only for a limited group of images with similar quality. Some of the captured images may have specific properties that require special treatment. Therefore it should be noted that the general framework of image processing operations proposed is for this particular asphalt mixture. Finally the separated binary images of individual components (aggregate, air voids and rubber) after processing are presented in Figure 3.36.

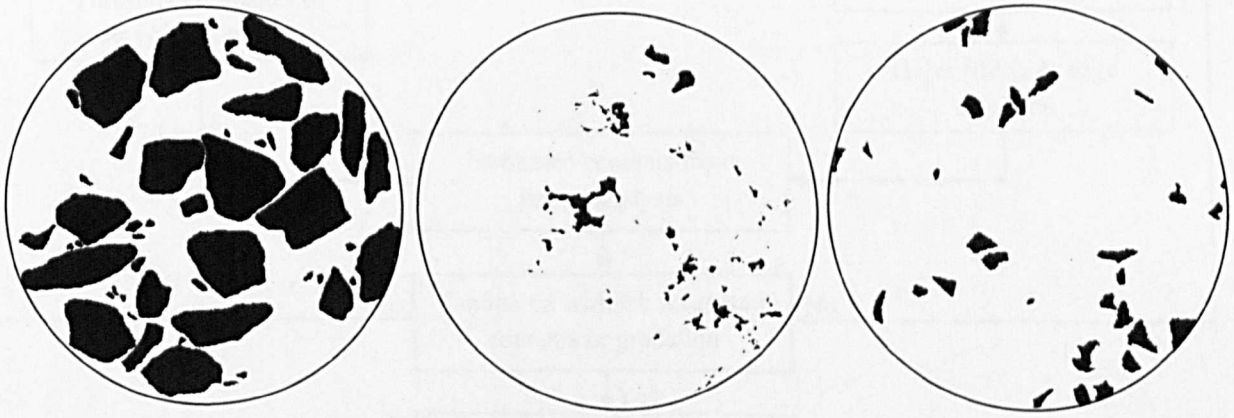

(a) (b) (c)

Figure 3.36 Images of (a) aggregates, (b) voids and (c) coarse rubber after segmentation

Their properties such as area, dimension, centroid, etc. are then determined for image analysis. The brief steps of the proposed image processing are summarised in Figure 3.37.

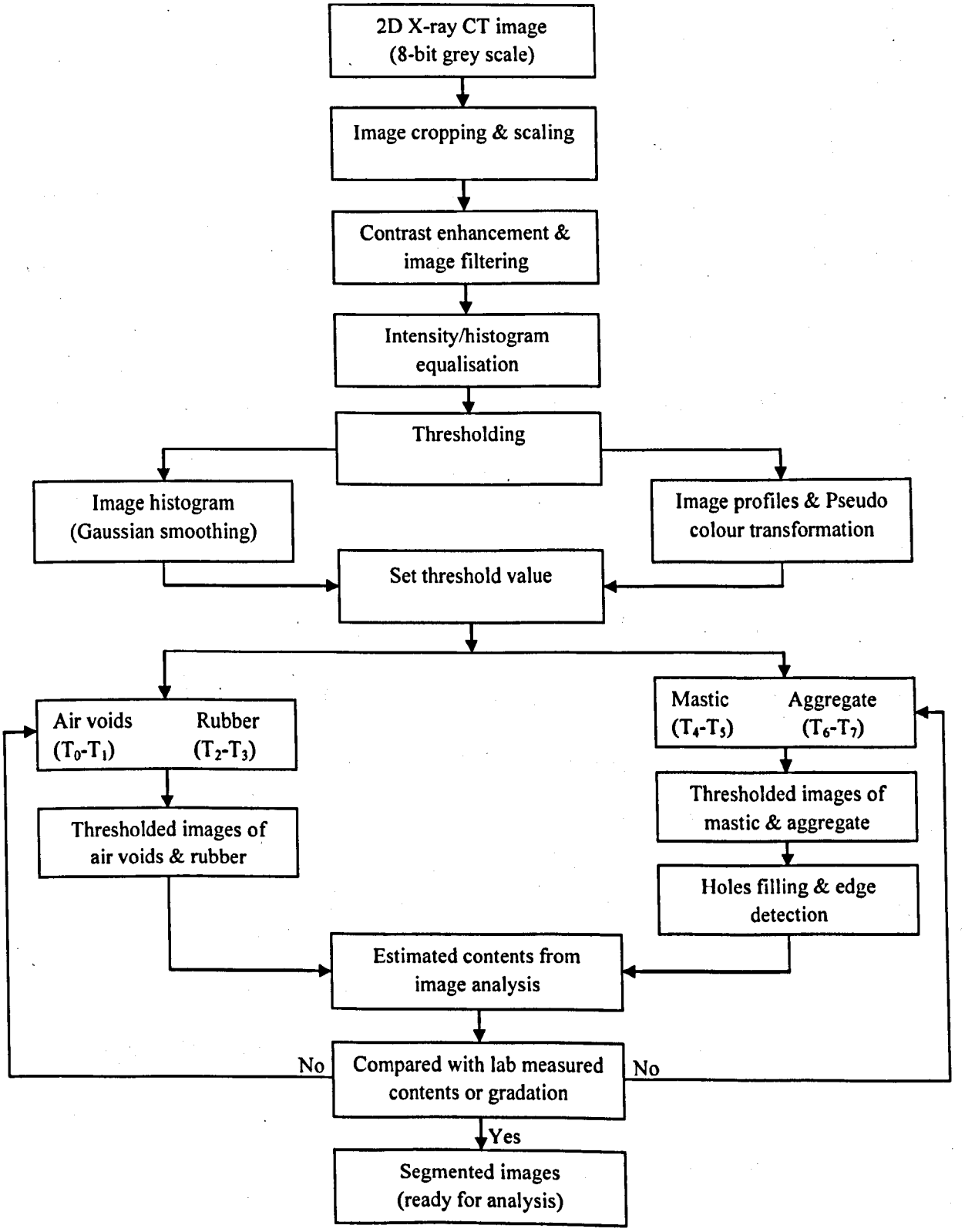

Figure 3.37 Flowchart of the detailed steps involved in image processing

3.7 Summary

From the literature review, it can be summarised that X-ray CT has been successfully used to characterise air voids, aggregates and damage in asphalt mixtures. For this study, the need for X-ray CT to non-destructively characterise the microstructural properties of rubberised mixtures is important because this particular mixture contains rubber particles which tend to fall out if any cutting or trimming work is carried out on the specimen. The material dislodging will have an influence on the volumetric composition and consequently affect the microstructural properties.

In addition, digital image processing is a vital stage in determining the success of image analysis. Extensive comparisons using trial specimens have shown that different types of images lend themselves to one or another processing and thresholding method. This confirms that no single method always produces a good result in segmenting the region of interest in any images but a proper method for specific images should appear among the existing ones. It comprises a variety of methods to enhance image quality, particularly to improve the visibility of the desired features and for particles segmentation. The following guidelines summarise the main procedures for processing images:

i. A stack of grey scale images were obtained from X-ray CT. The more images captured during the scanning (with smaller scan interval) the more information can be collected during image analysis.

ii. Geometric transformations: conversion of image size, image rotation, cropping and scaling.

iii. Image enhancement: involved with brightness and contrast adjustment and filtering

iv. Image segmentation: The object of interest was thresholded and converted to binary image by selecting the threshold values. For 8 bits images the values vary from 0 to 255. Image histogram and image profile can be referred for threshold values.

v. Morphological operations: useful in touching up the selected object of interest within images (to detect the particle's boundary and remove any defect within the selected area).

vi. Verification: The segmented images were validated by comparing the total percentage of the area analysed from images to the actual percentage of the material under consideration determined from the laboratory.

Overall, this study is a good start for the utilisation of X-ray CT combined with an image analysis technique to quantify the microstructure properties of rubberised asphalt mixtures.

4.0 MICROSTRUCTURAL ANALYSIS FOR ASPHALT MIXTURES CHARACTERISATION

4.1 Introduction

This chapter aims to establish information on the characterisation procedures which are intended to obtain parameters to quantify the microstructure properties of asphalt mixtures. For microstructure quantification, the explanation includes the stereological concept and the parameters used to characterise air voids structure, aggregates and internal structure damage. This is to obtain a fuller understanding of the basic concepts underlying measurements made on X-ray images of asphalt mixtures and to establish parameters to be used in this study to measure the microstructure properties of compacted specimen in undamaged and damaged states. In undamaged condition, the internal structure parameters include the distribution of rubber particles and air voids properties within the specimen. Whereas in damaged state, the parameters measure the changes in the air voids and crack properties. This is achieved using reviews made on previous studies and results from preliminary microstructural analysis undertaken. The following sections describe a simple technique in viewing the damaged area from X-ray images and validation of the damage comparison between images.

4.2 Stereological Concept

Stereological concept of analysis is a method that is widely used for quantifying microstructural properties from images. It is used to describe the mathematical relationships between measurements made in the 2D plane such as areas, lengths and numbers and 3D features such as volumes, surfaces and lengths.

The following are some of the basic parameters that describe the geometrical properties of microstructural elements:

- V_V: volume fraction (total volume of features analysed per unit volume of a material)
- S_V: specific surface area (total surface area of features analysed per unit volume of a material)
- L_V: specific length (total length of lineal features analysed per unit volume of a material)
- N_V: numerical density (mean number of features analysed per unit volume of a material)
- A_A: area fraction (total surface area of intercepted features per unit test area of a specimen)
- L_A: specific length (total length of linear features analysed per unit test area of a specimen)
- N_A: surface density (mean number of interceptions of features per unit test area of a specimen)
- L_L: linear fraction (total length of linear intercepts analysed per unit length of a test line)
- N_L: linear density (number of interceptions of particles per unit length of a test line)
- P_P: point fraction (mean number of point elements or test points in area features per test point)

The parameters described above were developed for microstructure description of 3D materials from 2D images of the materials' cross sections. According to stereological analysis, the image of 2D section planes can be analysed to obtain the volume fraction, V_V using the estimation of area, A_A, linear, L_L and point, P_P analyses (Equation 4.1).

$$P_P = L_L = A_A = V_V \qquad 4.1$$

In this study, area analysis is used for image analysis of the X-ray CT images of the asphalt mixture specimens. The imaging software can easily measure the particle surface area by calculating the pixels forming the particle in the image. Using areal analysis, the volume fraction is measured from the area fraction, which is calculated as the ratio of the total particles area to the total area of the image. A French geologist, Delesse in 1848 was amongst the first to study the equivalence of A_A and V_V and conclude that the area fraction was an unbiased estimate of the volume fraction. To that effect, simple derivations (Equations 4.2 to 4.8) were undertaken by Weibel and McLean as in Underwood (1970). Figure 4.1a shows a test cube of volume $V_T = l^3$ which contains irregularly shaped particles (e.g. of α-phase), and a thin slice of thickness δ_x and area $A_T = l^2$ parallel to ZY-plane. The volume of α-phase in the thin slice is given by:

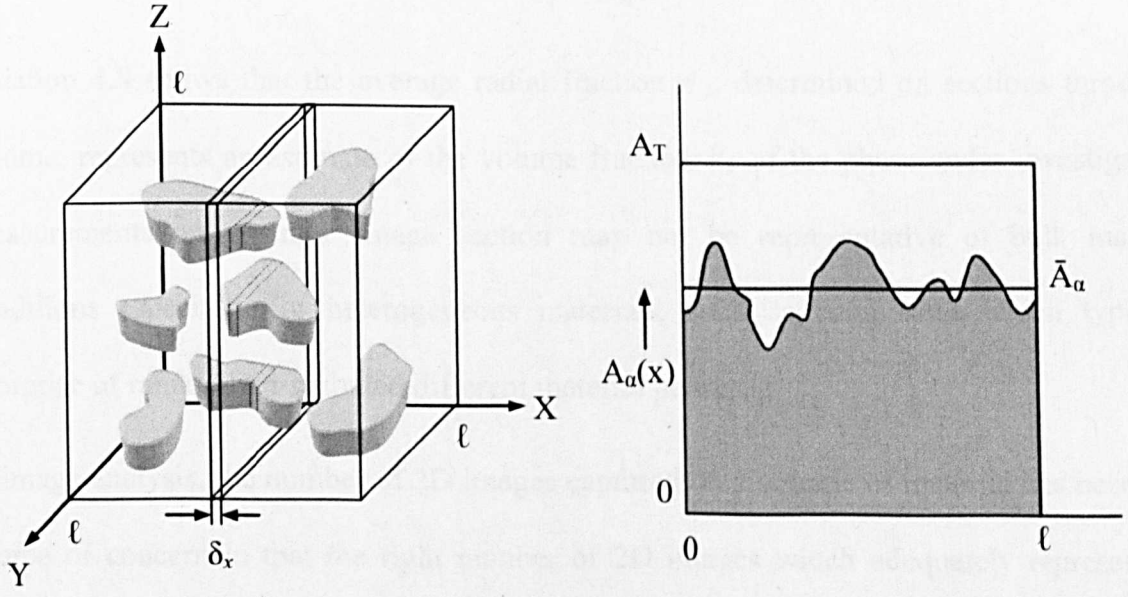

Figure 4.1 The relationship of $V_V = A_A$, (a) cube containing particles of α-phase cut by a thin slice (b) variation of area of α-phase in thin slice, $A_\alpha(x)$, as a function of slice position , x

$$\delta V_\alpha = l^2 \delta_x (V_V)_\alpha \text{ mm}^3 \quad 4.2$$

And when δ_x is sufficiently small:

$$\delta V_\alpha = A_\alpha(x) \delta_x \text{ mm}^3 \quad 4.3$$

Where $A_\alpha(x)$ is the area of α-phase on the slice surface as a function of slice position x. $A_\alpha(x)$ varies with x, as indicated in Figure 4.1b, and the average value between 0 and l:

$$\bar{A}_\alpha = (1/l) \int_0^l A_\alpha(x)\, dx \text{ mm}^2 \quad 4.4$$

In the limit, the total volume of α-phase in the cube is given by:

$$V_\alpha = \int_0^l dV_\alpha = \int_0^l A_\alpha(x)\, dx \quad 4.5$$

By comparing Equations 4.4 and 4.5:

$$V_\alpha = l\bar{A}_\alpha \quad 4.6$$

By dividing Equation 4.6 with V_T and A_T, final relation is given by Equation 4.8:

$$V_\alpha / V_T = \bar{A}_\alpha / A_T \quad 4.7$$

$$V_V = A_A \quad 4.8$$

Equation 4.8 shows that the average radial fraction A_A, determined on sections through a volume, represents an estimate of the volume fraction V_V of the phase under investigation. Measurements on a single image section may not be representative of bulk material conditions especially for heterogeneous materials, such as composites which typically comprise of randomly distributed different material phases.

In image analysis, the number of 2D images captured on a volume of material has become a source of concern in that the right number of 2D images which adequately represent the whole volume to achieve unbiased measurements with sufficient accuracy is largely subjective. In general, to get an unbiased characterisation, the images of the object under observation should be taken randomly. From the stereological perspective, this is sufficient

for the image sampling of 1D and 2D objects but not for 3D element which require at least a pair of images (or more), depending on its size. Systematic sampling using the vertical sectioning method is preferred, where the 3D element can be reconstructed from a set of parallel 2D image sections. The more images of the parallel sections, the more information conveyed for that particular measured volume. Validation of the 2D analysis is described in the following section.

4.2.1 Preliminary Investigation on Validating the 2D Analysis

To better interpret the measurements made on the X-ray images from the 2D analysis, it was necessary to ascertain the image slice interval required to obtain an unbiased characterisation of the specimens' microstructure properties. A specimen of approximately 60 mm height was X-rayed and analysed for air voids distribution at different slice interval (of between 0.1 mm and 8 mm) as shown in Figure 4.2. It can be seen that the curves of the air voids distribution analysed at 0.1 mm to 2 mm are very close with minimal different in the air voids content along the height of the specimen. They also seem to convey more details of the air voids distribution compared to the curves analysed at 4 mm and 8 mm slice interval. Chosen interval was considered practical with respect to obtaining optimal results and the time necessary to scan, as more images will need more time to complete the CT scanning.

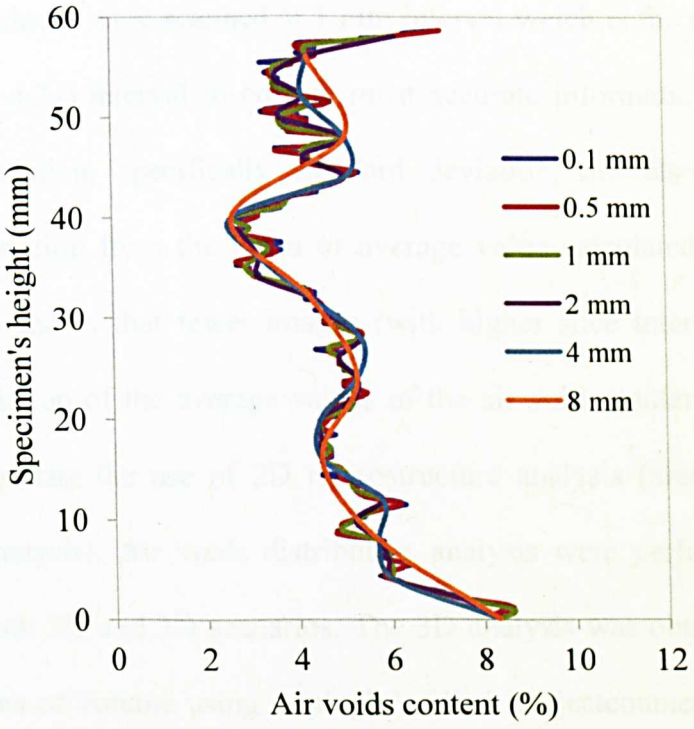

Figure 4.2 Comparison of air voids distribution analysed with different slice interval

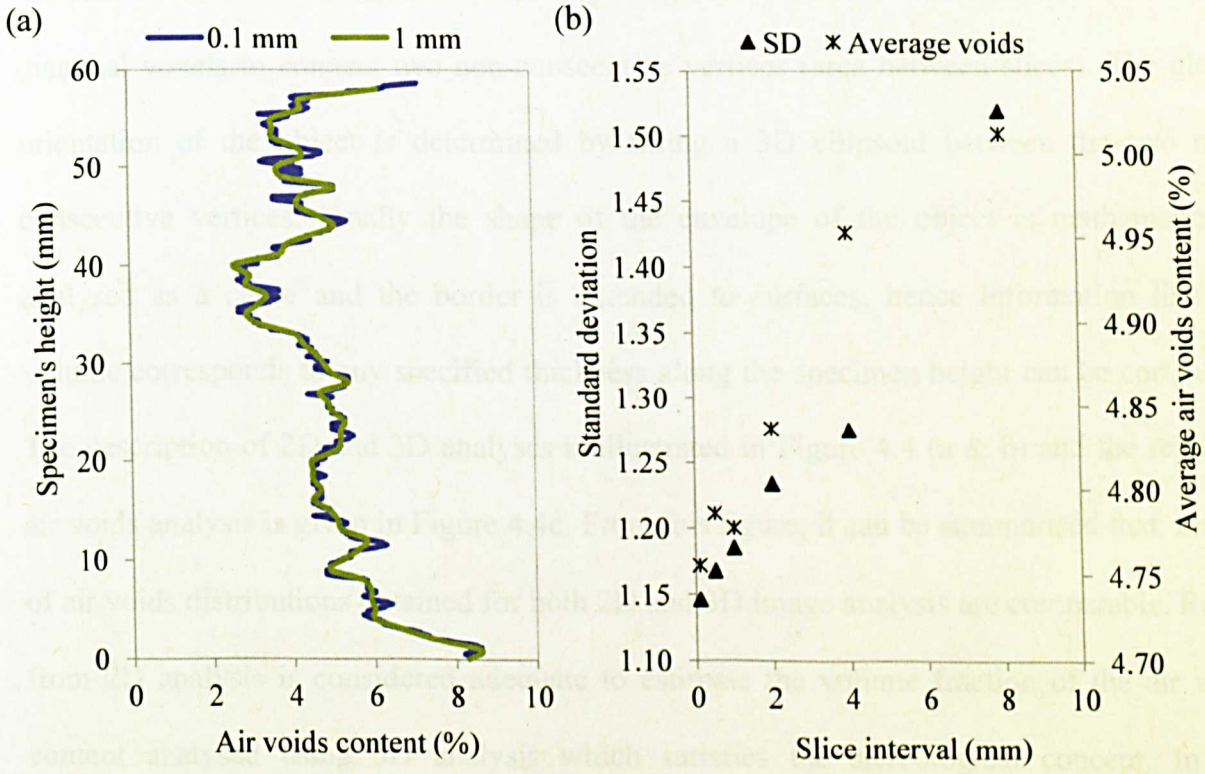

Figure 4.3 (a) Analysis of air voids distribution at 0.1 mm and 1 mm slice interval (b) standard deviation and average voids content for different slice interval

In this study all specimens were scanned at 1 mm interval which is the closest match to the 0.1 mm (see Figure 4.3a) interval to convey most accurate information from the images. This Statistical validation, specifically standard deviation, *SD* also provided a good indication of the variation from the mean or average value calculated from a number of images. Figure 4.3b shows that fewer images (with higher slice intervals) will lead to a higher standard deviation of the average values of the air voids content. The analysis was then extended to validate the use of 2D microstructure analysis (area analysis) over 3D analysis (volume analysis). Air voids distribution analysis were performed using ImageJ analysis tools for both 2D and 3D scenarios. The 3D analysis was obtained by performing the 3D measurements of volume using a 'plugin' called 'Objectcounter3D'. The volume is referred to the number of voxels belonging to the object of interest and can be computed as the sum of 2D areas multiplied by the *z* spacing (slice interval). This is done by allowing diagonal voxels to connect two non-consecutive vertices (area between slices). The global orientation of the object is determined by fitting a 3D ellipsoid between the two non-consecutive vertices. Finally the shape of the envelope of the object is mathematically analysed as a curve and the border is extended to surfaces, hence information like the volume corresponds to any specified thickness along the specimen height can be computed. The description of 2D and 3D analyses is illustrated in Figure 4.4 (a & b) and the result of air voids analysis is given in Figure 4.4c. From this figure, it can be summarised that, results of air voids distributions obtained for both 2D and 3D image analysis are comparable. Result from 2D analysis is considered adequate to estimate the volume fraction of the air voids content analysed using 3D analysis which satisfies the stereological concept. In this investigation, the air voids content determined from the laboratory was 4.8%.

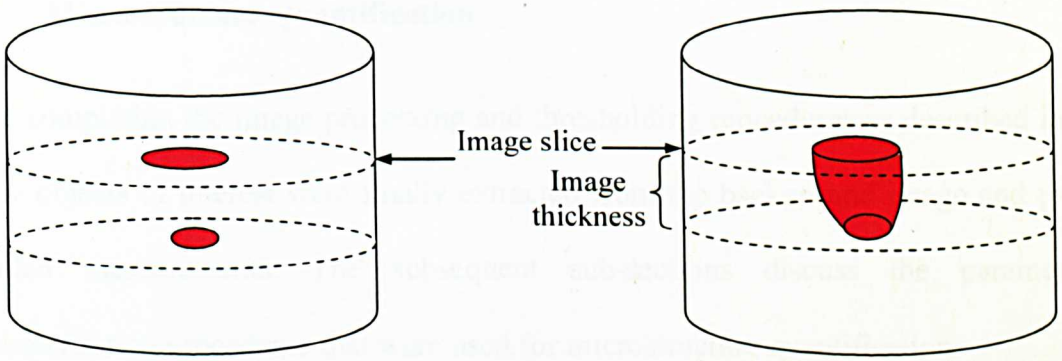

$$Area\ fraction = \frac{Total\ area\ of\ object\ of\ interest}{Total\ area\ of\ the\ image\ slice}$$

$$Volume\ fraction = \frac{Total\ volume\ of\ object\ of\ interest}{Total\ volume\ of\ the\ thickness}$$

(a) Area analysis (area in each slice)

(b) Volume analysis (volume in each thickness)

(c)

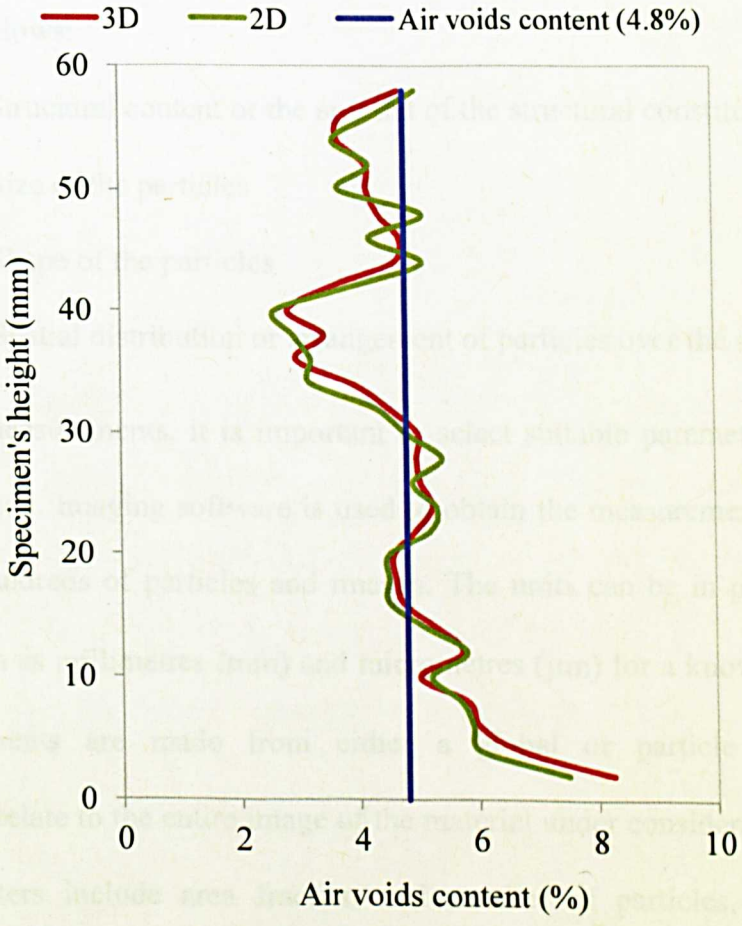

Figure 4.4 Comparison of 2D and 3D analysis of air voids distribution

4.3 Microstructure Quantification

After completing the image processing and thresholding procedures as described in Chapter 3, the objects of interest were finally extracted from the background image and primed for detailed measurements. The subsequent sub-sections discuss the parameters and characterisation procedures that were used for microstructure quantification.

4.3.1 Materials Distribution and Shape Description

The image analysis procedures explained in this section presents parameters which are used to quantify the internal structure of materials. The parameters can be divided into broad categories as follows:

i. Structural content or the amount of the structural constituents
ii. Size of the particles
iii. Shape of the particles
iv. Spatial distribution or arrangement of particles over the material volume

When taking measurements, it is important to select suitable parameters to enable correct data interpretation. Imaging software is used to obtain the measurements and the process is repeated for hundreds of particles and images. The units can be in pixels or calibrated to other units such as millimetres (mm) and micrometres (μm) for a known distance or length. The measurements are made from either a global or particle perspective. Global measurements relate to the entire image of the material under consideration. Some measured global parameters include area fraction and number of particles. On the other hand, individual particles measurements focus on detailed analysis of the size, shape and location of each single particle. In this study, the aforementioned parameters were used to quantify

the internal structure properties of rubberised asphalt mixture e.g. the air voids structure, aggregate structure, crumb rubber distribution and internal damage. Further detail is provided in the subsequent sections of this document.

4.3.1.1 Air Voids Structure

Air voids properties

Different aspects of air voids properties can be analysed including air voids content, average air void size, number of air voids and air voids shape factor. The distribution of the air voids properties at the different heights of a specimen can be plotted to indicate the variation in air voids properties throughout the specimen. This method is well established in previous research work (Masad et al., 1999b; Wang et al., 2001; Masad et al., 2002; Tashman 2004; Khan 2009). The *air voids content* and the *average void size* can be calculated using Equations 4.9 and 4.10. The air voids fraction is taken as the ratio of the total air voids area to the total area of an image's cross-section. To validate the total air voids fraction calculated (with Equation 4.9) from a number of 2D image slices, the value is compared with the air voids content measured in the laboratory. The average size of air voids is the ratio of the total voids area to the number of voids. A smaller ratio indicates smaller sized voids, discretely distributed within the specimen while a higher ratio is indicative of larger sized voids that are also more connected voids as shown in Figure 4.5.

$$Air\ voids\ fraction = \frac{Air\ voids\ area}{Total\ image\ area} \quad 4.9$$

$$Average\ air\ voids\ size = \frac{Total\ voids\ area}{Number\ of\ voids} \quad 4.10$$

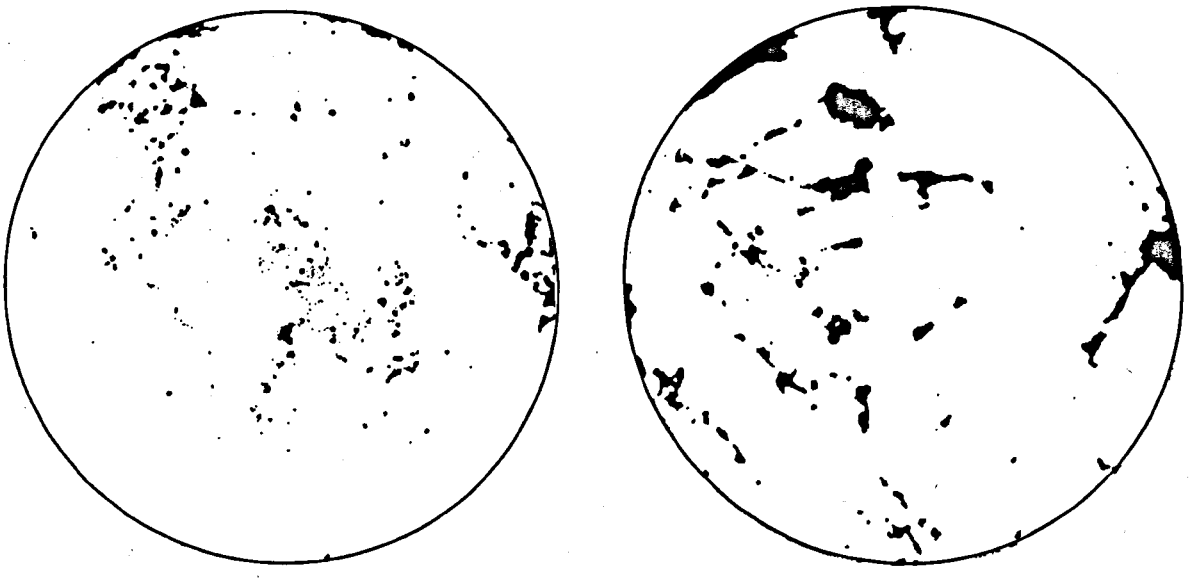

(a) (b)

Figure 4.5 Comparison between (a) small distributed voids and (b) large connected voids

Number of air voids and average air voids size have been found to be significant for the characterisation of air voids properties. This is based on an observation which showed that two replicate specimens, produced with the same target air voids content, can possibly have different distributions of air void number and average air voids size throughout both specimens. Specimens having the same total air voids content could be a result of contributions from a lesser number of large air voids or higher number of smaller-sized air voids. As a consequence, two replicate specimens may fail differently under the same loading condition even though they would have been designed to achieve the same target air voids content. In comparison to smaller void sizes, samples with large voids are more susceptible to relatively earlier failure because of the increased likelihood of larger strains being induced once the specimen is subjected to loading conditions. The scenario described may cause instability, where the existing voids may potentially propagate throughout the specimen and interlink (or connect with other voids) to cause severe damage. Wang et al. (2004) related the air voids content to the concept of effective stress as illustrated in Figure

4.6. The concept agrees that the presence of more air voids will decrease the mixture's resistance against pavement damage. This is because air voids cannot transmit loading and therefore weaken the material due to the reduced effective area available to resists the applied forces (higher concentrated forces per area). The effective stress, σ_e is calculated using Equation 4.11.

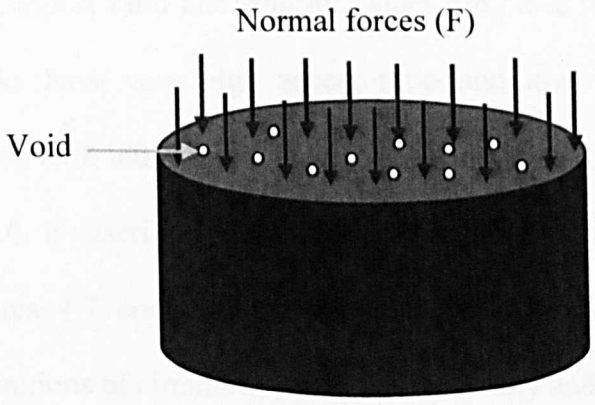

Figure 4.6 Illustration of the concept of effective stress on asphalt mixture specimen

$$\sigma_e = \frac{F}{A - A_v} \qquad 4.11$$

Where,

F = total normal force applied

A = cross section area

A_v = cross section area of voids

Shape factor is another important air voids property that can be used to characterise air voids. Shape analysis is very useful for differentiating between original air voids and cracks in a specimen after deformation (Tashman et al., 2004). Many earlier studies used shape analysis to evaluate aggregates' characteristics in terms of the surface irregularities or angularity (Masad et al., 2003, Saadeh et al., 2003 and Garboczi 2002). The most common shape factors used in image analysis are circularity, roundness, solidity and aspect ratio. These

parameters measure the extent to which a particle shape differs or deviates from a perfect circle or sphere, which are ideal reference shapes. Shape factor can be said as a measure of the compactness of a shape, where a circle is regarded as the most compact shape, such that more compact a shape, the more closely it resembles a circle. Circularity, roundness, aspect ratio and solidity can be calculated using Equations 4.12 to 4.15 respectively. If the circularity, roundness, aspect ratio and solidity values are close to 1.0, it indicates circular air voids while cracks have very high aspect ratio and low values of roundness and circularity (approaching 0.0), indicating an increasingly elongated shape. When the value of solidity approaches 0.0, it describes the particle shape as more angular or irregular or in a concave shape. Figures 4.7 and 4.8 illustrate the difference in the particles shape in accordance to the definitions of circularity, roundness, solidity and aspect ratio.

$$Circularity = \frac{4\pi \times Area}{Perimeter^2} \quad 4.12$$

$$Roundness = \frac{4 \times Area}{\pi \times Major\ axis^2} \quad 4.13$$

$$Aspect\ ratio = \frac{Length\ of\ major\ axis}{Length\ of\ minor\ axis} \quad 4.14$$

$$Solidity = \frac{Actual\ particle\ area}{Convex\ area\ of\ particle} \quad 4.15$$

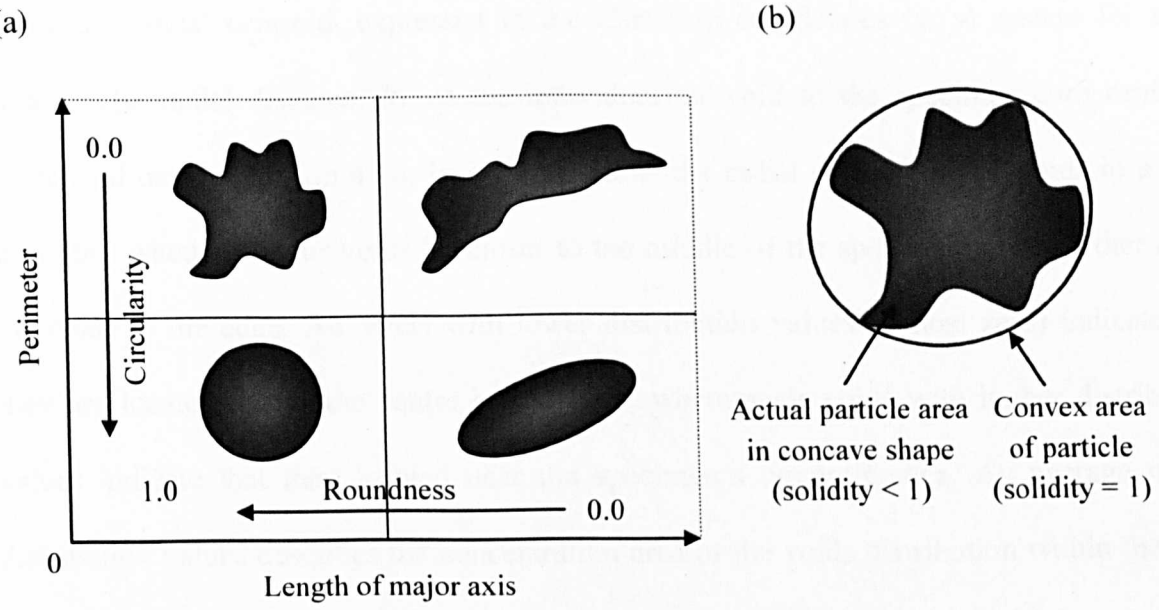

Figure 4.7 Illustration of (a) circularity and roundness (b) solidity

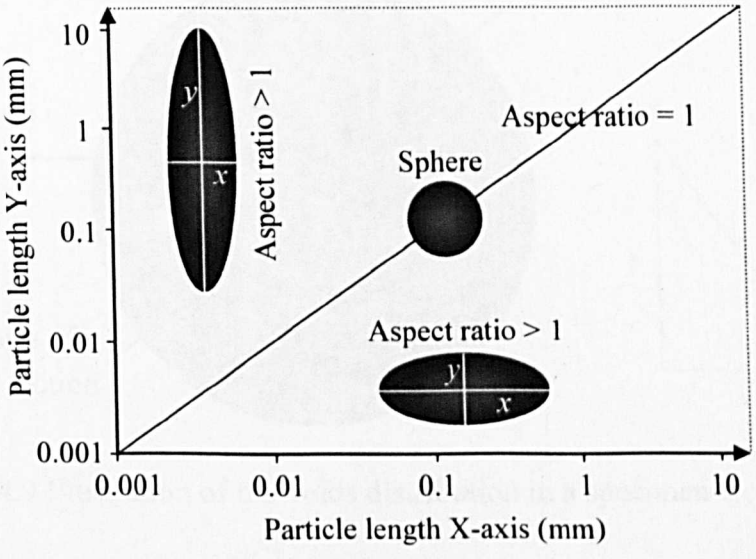

Figure 4.8 Illustration of particles aspect ratio

Air voids distribution

The air voids distribution in a 2D image of a compacted cylindrical asphalt specimen can be calculated by locating the position of air voids from a reference point such as the centre of the compacted asphalt specimen as shown in Figure 4.9. The locations of voids are identified

using the voids' centroid, expressed in the Cartesian coordinates (x, y) system for a 2D image. The radial distance, R_D of the individual air void to the specimen core centre is calculated using Equation 4.16. In a planar view, the radial distance of air voids in a slice describes whether the air voids lie closer to the middle of the specimen or lie further away i.e. close to the edge. Air voids with lower distribution values (almost zero) indicate that they are located nearer the centre of the slice, whereas air voids with higher distribution values indicate that they located near the specimen's circumference. An average of the distribution values describes the concentration area of the voids distribution within the slice or within the volume of the specimen.

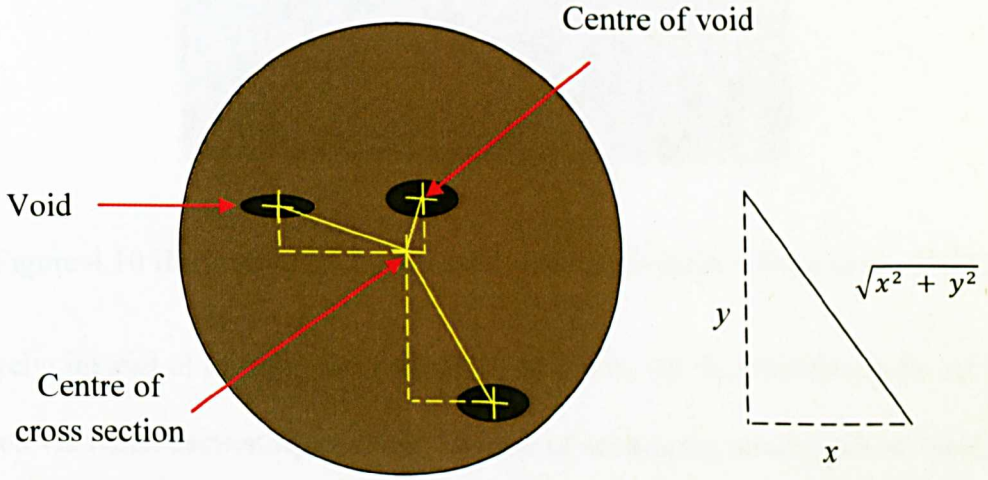

Figure 4.9 Illustration of the voids distribution in a specimen's cross section

$$\textit{Air voids radial distance, } R_D = \sqrt{x^2 + y^2} \qquad 4.16$$

Where,

x = horizontal distance of a void's centroid from the centre of the slice

y = vertical distance of a void's centroid from the centre of the slice

Using the coordinates of the centroid, the distance between individual air voids can also be calculated to measure the interaction between the voids. When two air voids are far apart,

their interaction is negligible but when they are close, they can interact with each other and weaken the asphalt mixture especially when loaded. Figure 4.10 shows that, based on the distances between the voids, the interaction between voids A and B would be potentially larger than the interaction that would occur between voids C and D.

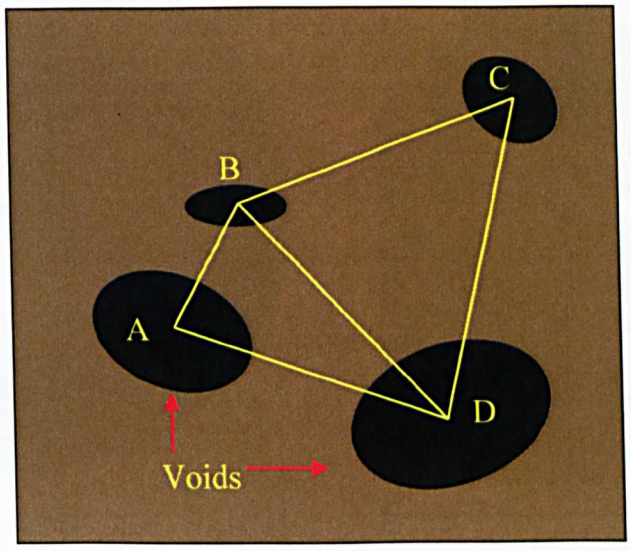

Figure 4.10 Illustration of the distance among air voids (Wang et al., 2004)

Alternatively, instead of locating the individual air voids, the distribution of the air voids can be analysed via radial sectioning method. The use of sectioning method for air voids analysis is very useful for characterising the homogeneity in the air voids distribution throughout a compacted specimen. Furthermore, Muraya (2007) asserted that, investigating the homogeneity of a specimen in terms of air voids distribution is significant because homogenous specimens allow for an appropriate evaluation of test results and minimise inconsistency between specimen replicates. In radial sectioning, ring and core analysis can be conducted by virtually cutting the stack of X-ray images of the cylindrical compacted asphalt specimen into core and ring sections as shown in Figure 4.11. In this study the

analysis was conducted at intervals of 25 mm (25, 50, 75 and 100 mm). The air voids content was then compared between the cut sections throughout the specimen's height.

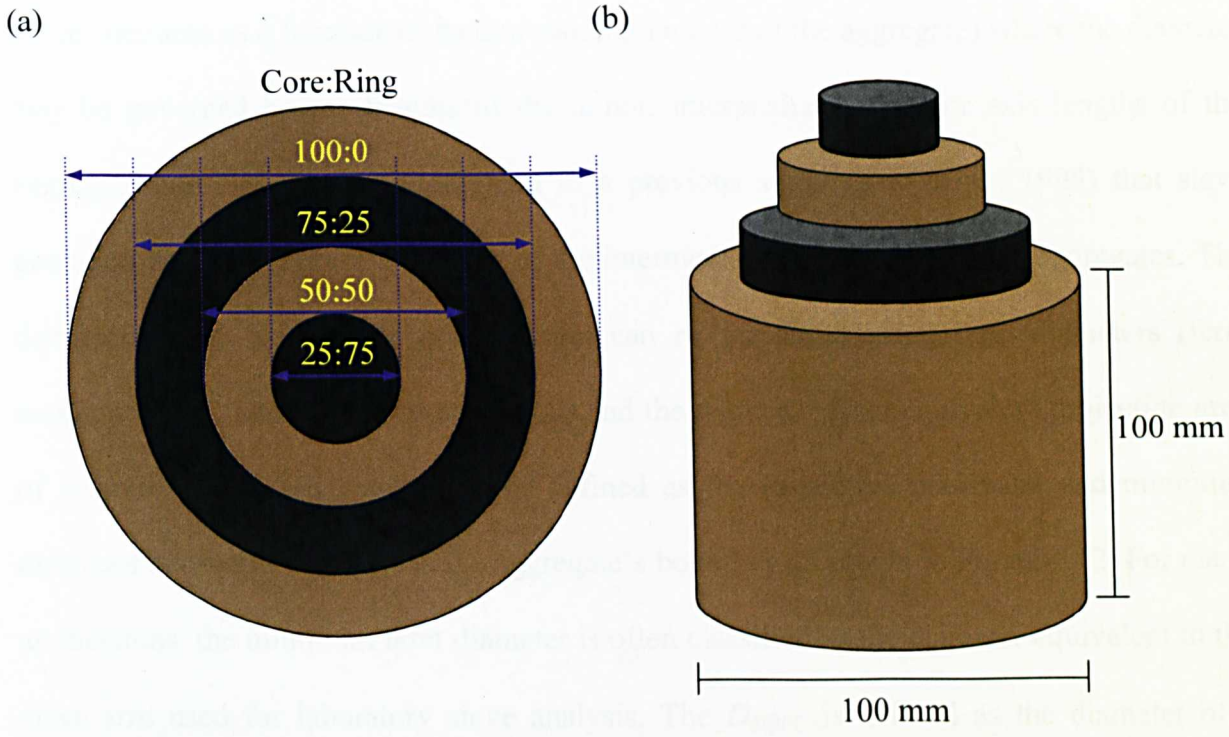

Figure 4.11 (a) Plan view and (b) side view of the radial sections of compacted asphalt mixture specimen for core and ring analysis

In this study, different mixtures of compacted rubberised asphalt specimen were analysed in terms of their air voids and rubber distribution within the specimens. This is to ascertain any relationship between the resulted air voids properties and the rubber distribution within the rubberised asphalt mixtures. This is important as it was revealed in the literature review (Chapter 2), that air voids content is very sensitive to the addition of rubber. Therefore, the distributions of both components of air voids and rubber were analysed regarding the proximity of the air voids location to the location of rubber particles. The rubber distribution was measured for the different cut sections described in Figure 4.11 and compared to the measured air voids.

4.3.1.2 Aggregate gradation

In a 2D image, aggregate gradation can be estimated by calculating the percentage of aggregates area as a function of its dimension (diameter of the aggregate) where the diameter may be governed by the lengths of the minor, intermediate or major axis lengths of the aggregate particles. It was highlighted in a previous study (Yue et al., 1995) that sieve gradation is governed by the lengths of the intermediate and minor axes of aggregates. The diameters of an aggregate's cross-section can be measured using feret diameters (feret maximum, F_{max} and feret minimum, F_{min}) and the diameter of an equivalent projection area of a circle, D_{EQPC}. F_{max} and F_{min} are defined as the respective maximum and minimum distances between two pixels at the aggregate's boundary as shown in Figure 4.12. For many applications, the minimum feret diameter is often classified as the diameter equivalent to the sieve size used for laboratory sieve analysis. The D_{EQPC} is defined as the diameter of a perfect circle that has the same area as the measured aggregate particle (refer to Equation 4.17). It is widely used for evaluating particles sizes from the projection area of a non-spherical particle.

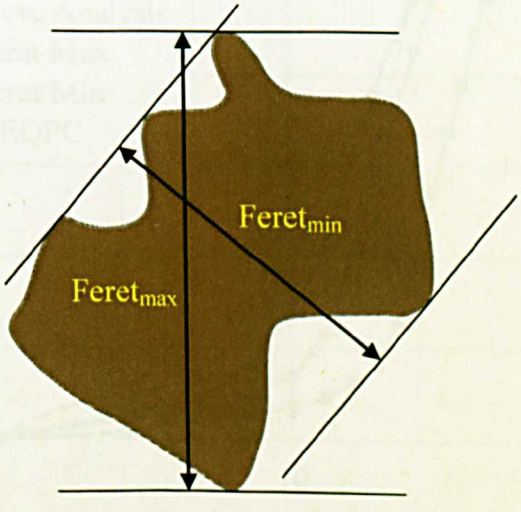

Figure 4.12 Maximum and minimum feret diameter of an aggregate

$$D_{EQPC} = \sqrt{\frac{4 \times Area}{\pi}} \quad 4.17$$

In this study, the aggregate gradation analysis, with aggregate dimension, d using feret diameters and D_{EQPC} were respectively characterised for coarse aggregate particles as being greater than or equal to 2 mm ($d \geq 2$ mm). In asphalt mixture compacted specimen, the boundaries of the coarse aggregate sizes were easily identified and differentiated from the other material phases but the fine aggregates were assumed to be part of the mastic due to the difficulty in identifying small individual aggregates within the X-ray images. It was expected that this would minimise the error caused by the aggregate clustering whereby two or more fine aggregates in contacts could be misrecognised as a single large aggregate. Moreover, previous studies conclude that studying the distribution of coarse aggregates (with $d \geq 2$ mm) will adequately describe the aggregates structure in compacted asphalt mixture specimens (Yue and Morin 1996; Kutay et al., 2010). For validation, a preliminary investigation was conducted to compare the image gradations to the sieve derived laboratory particle size distribution as shown in Figure 4.13.

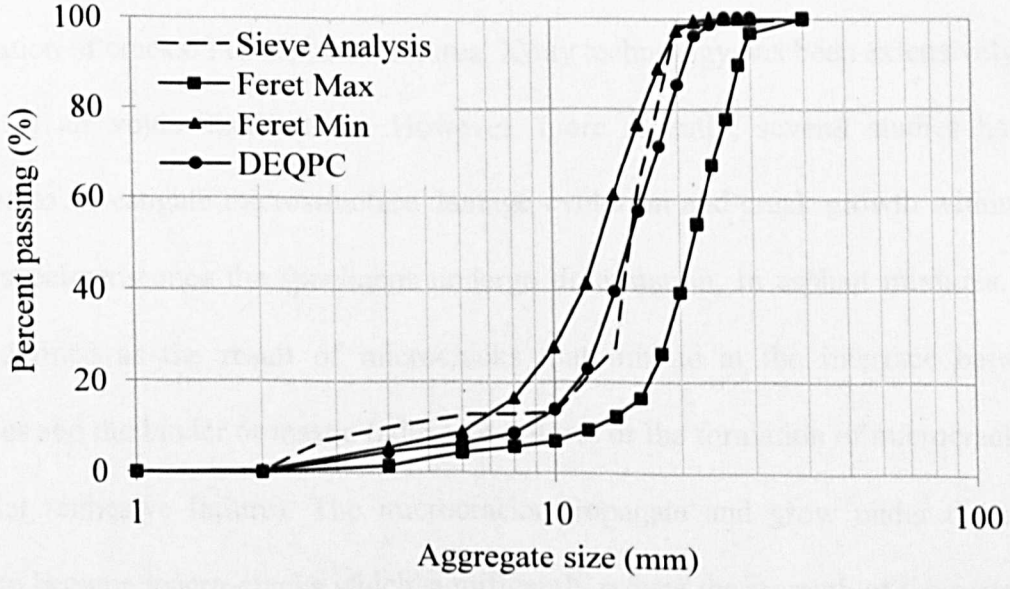

Figure 4.13 Comparisons of image gradations for gyratory specimen gap graded mixture

It can be observed that the area gradations calculated from the image analysis match reasonably well to the laboratory measured gradation indicating their comparability. Furthermore, the area gradation for D_{EQPC}, is the closest to the laboratory sieve gradation. It should be noted that a slight difference in the 2D analysis compared to the actual gradation is inevitable. This may be partly due to fact that this analysis was conducted with the assumption that the aggregate particles are randomly oriented during mixing whereas the major planes of aggregate particles are more likely to lie parallell to the specimen cross section. However, it is also true that 2D slices thrrough aggregate particles will, on average be of smaller area than the particle dimension as found from sieve analysis.

4.3.2 Damage Characterisation

A few researchers have been able to utilise X-ray CT to monitor the evolution of internal failure in some engineering materials such as soils (Shi et al., 1999), mortar (Landis and Keane 1999) and metal (Maire et al., 2001) and relate it to measured strain. Internal failure is measured in terms of internal displacement associated with the permanent deformation and the formation of cracks. For asphalt mixtures, X-ray technology has been extensively used to characterise air voids distributions. However, more recently, several studies have been conducted to investigate microstructure damage evolution and crack growth within asphalt mixture specimens once the specimens undergo deformation. In asphalt mixtures, damage can be defined as the result of microcracks that initiate at the interface between the aggregates and the binder or mastic (adhesive failure) or the formation of microcracks within the binder (cohesive failure). The microcracks propagate and grow under the action of loading to become macro-cracks which significantly reduce the strength of the material until complete failure ultimately occurs (Tashman et al., 2007).

The following sections explain potential damage parameters for the damage characterisation of asphalt mixtures, based on a review of previous research and a preliminary study conducted by the author. The term 'voids', is used throughout the forthcoming text in this section to describe both cracks and air voids in the specimens. Two main categories of damage parameters are specified, namely microstructural changes in voids properties and the quantification of crack formation. Details on the procedures proposed for extracting the damaged area (i.e. identifying increase in voids area after deformation) and for verifying the image slices (by X-ray) before and after deformation for damage comparison are provided herein.

4.3.2.1 Microstructural Changes in Air Voids Properties

In Section 4.3.1.1, some parameters used to characterise air voids properties such as the voids content, voids number, average voids size, voids shape and voids distribution were discussed. In the study of microstructural damage, air voids size and spatial distribution provide valuable information, leading to a better understanding of the damage mechanisms in asphalt mixtures. Changes in these parameters (by comparing the parameters before and after deformation), provide information on the severity of the damage at different depths within the compacted asphalt mixture specimen. In other words, the changes in the voids properties are able to reflect the accumulation of damage under different loading conditions. The larger the increase in the voids area and average voids size, the more severe the damage. Tashman et al. (2004) measured the changes in the voids properties throughout compacted asphalt specimens to characterise the damage evolution before and after the deformation caused by triaxial compression. They were able to relate changes in the voids properties to the materials behaviour at different strain levels and confining pressures. Song, (2004)

quantified microstructure damage in terms of the amount of voids and characteristics of voids such as voids area, average voids perimeter as well as the average radius of the voids and cracks and relates them to changes in stiffness. The voids area is quantified using the same formula as in Equation 4.9 and the average radius is calculated using Equation 4.18.

$$Average\ radius = \sqrt{\frac{\sum_{i=1}^{n} A_i}{n \times \pi}} \qquad 4.18$$

Where,

A = area of each void and crack

n = number of voids and cracks

Wang et al. (2001, 2003 and 2004) proposed damage parameters, namely specific damaged surface area (area per unit volume), average spacing between the damaged surfaces and the average size of defect (average segment length in different orientation). These parameters can be used to describe the damage and the strength of the interaction between two damaged surfaces. Figure 4.14 illustrates the damaged surfaces and the spacing between the surfaces.

Khan (2009) used voids parameters including voids fraction (area), number of voids and average voids size to characterise the damage in asphalt mixtures by conducting Monotonic Compression and Tension Compression Fatigue Tests which corresponded to the increase in strain to failure. His study correlated the area of the defects (voids fraction) measured from the X-ray images to the strain and stiffness values obtained from the mechanical testing.

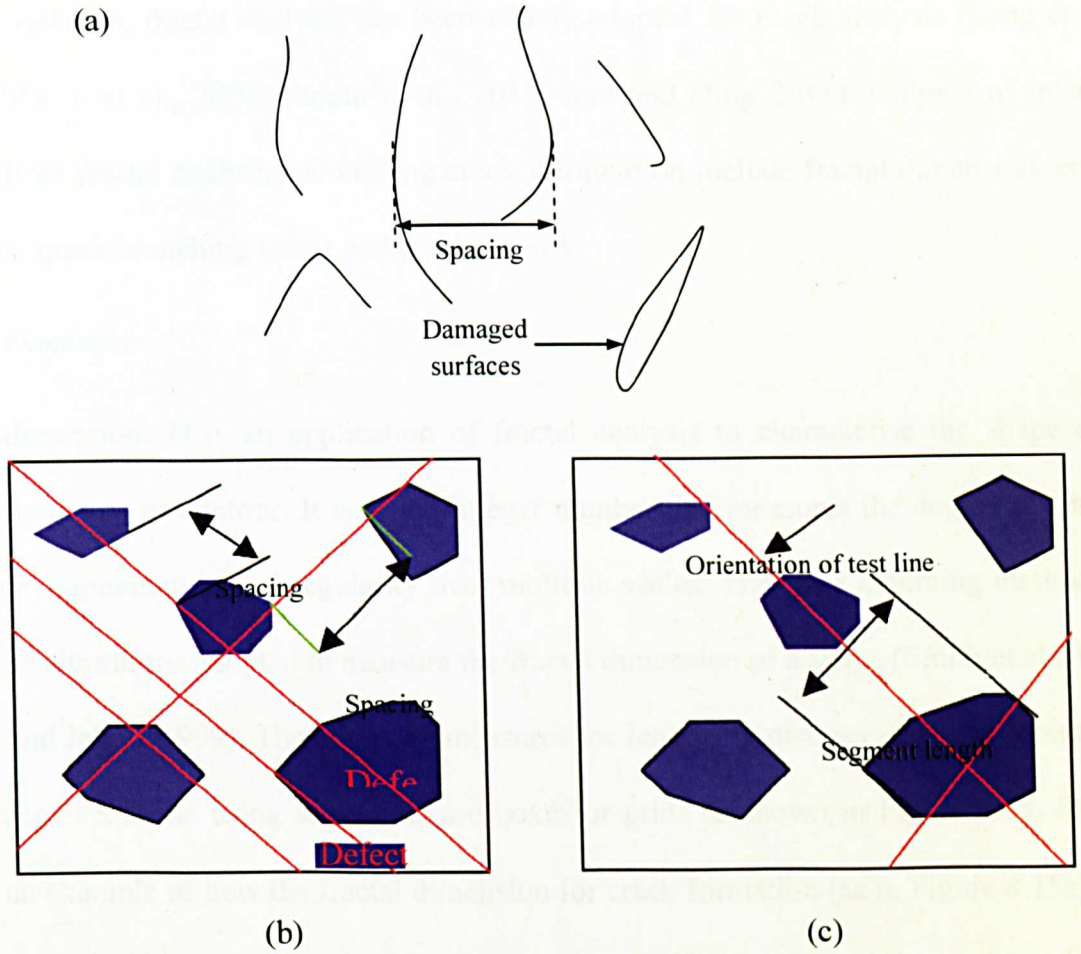

Figure 4.14 Illustration of the (a) damaged surfaces, the (b) spacing among the surfaces and (c) average segment length (size of defect) (Wang et al., 2003)

4.3.2.2 Quantification of the Crack Formation and Crack Propagation

In this study, it is necessary to quantify the cracks in the rubberised asphalt mixtures after damage. It is intended to apply the concept of fractal analysis to study the formation and propagation of cracks in the mixtures. For decades this concept has been used in many disciplines including medicine, geology and material sciences. For asphalt mixtures, it has been used to measure the geometry of irregular shapes and the surface roughness of aggregate particles, which are both important factors with potential to affect the mechanical properties of asphalt mixtures (Arasan et al., 2010; Geng et al., 2011). In cement and

concrete research, fractal analysis has been widely adopted for crack analysis (Song et al., 2005; Mihashi et al., 2006; Erdem et al., 2011; Sun and Ding 2011). Outputs of interest derived from fractal analysis, containing crack information include fractal dimension, crack tortuosity, crack branching factor and crack density.

Fractal Dimension

Fractal dimension, D is an application of fractal analysis to characterise the shape of a crack's boundary or contour. It is a non-integer number that measures the degree of fractal boundary fragmentation or irregularity over multiple scales. The 'Box Counting method' is one of the algorithms adopted to measure the fractal dimension of a shape (Smith et al., 1996; Berube and Jebrak 1999). The approach measures the lengths or distances between points on the border of a shape using sets of square boxes or grids as shown in Figure 4.15. Figure 4.15 is an example of how the fractal dimension for crack formation (as in Figure 4.15a) can be determined. The image is assigned to boxes of a specific size (r) and the total number of boxes (N) containing the cracks area is counted as (N(r)) or (N(1)) as in Figure 4.15b). Here, the number of boxes necessary to cover the cracks is expressed as a function of the box size. The process is repeated with different box sizes as shown in Figure 4.15(c&d). The logarithm of the number of boxes (log N(r)) is then plotted against the logarithm of the size of the boxes (log r) (Figure 4.15e). The fractal dimension is then calculated by finding the slope, S of the linear plot as shown, where the fractal dimension is the negative value of the slope (D = -S) (refer Equation 4.19). Higher fractal dimensions denote a wider crack or larger crack area. If the measured crack areas are the same, different crack distributions (or propagation patterns) will produce different fractal dimensions. The value of fractal dimension can be generated using imaging software, ImageJ.

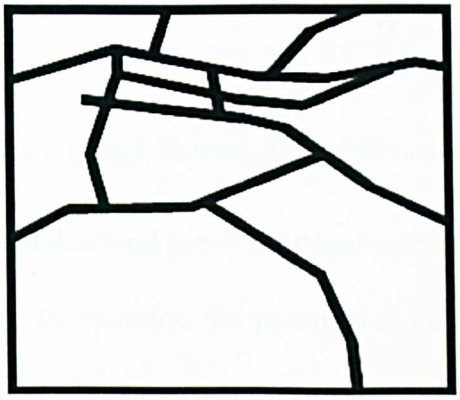

(a) Crack formation

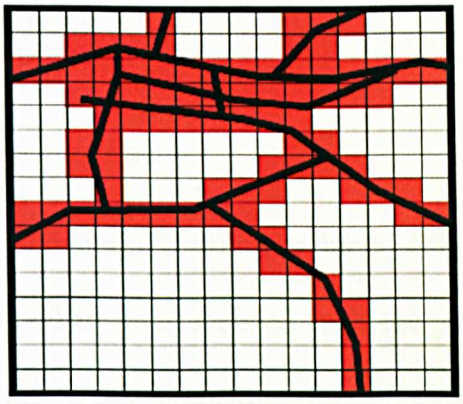

(b) N(1) = 86

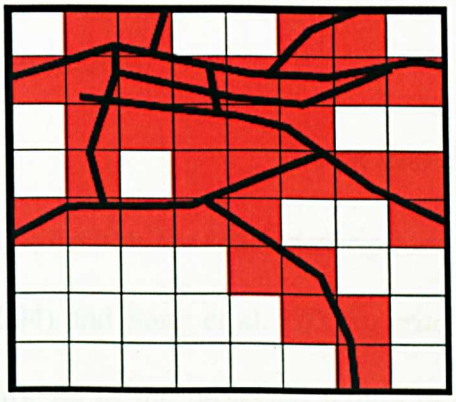

(c) N(2) = 34

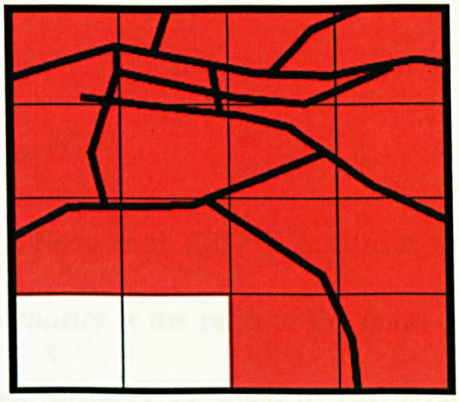

(d) N(4) = 14

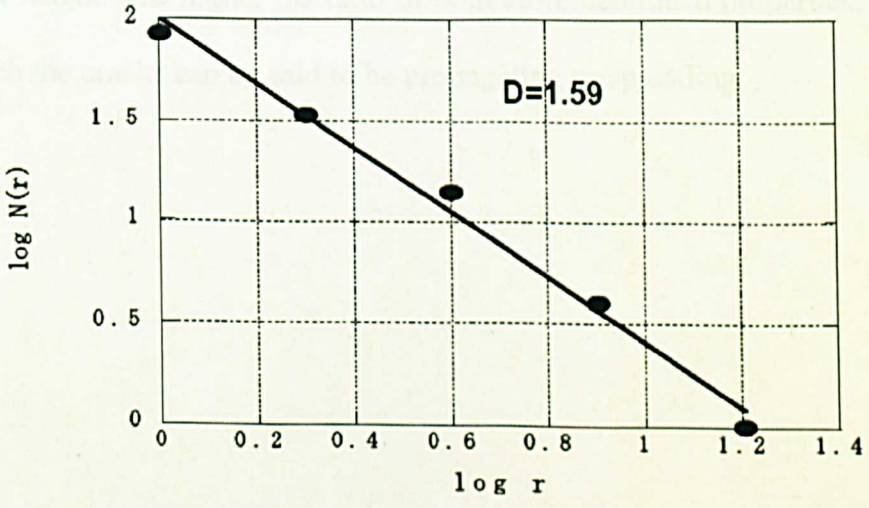

(e) A plot of log of box count against the log of box size

Figure 4.15 Fractal dimension by Box Counting method (Mihashi et al., 2006)

$$D = -\frac{Log\,(N(r))}{Log\,(r)} \qquad 4.19$$

Crack Density, Crack Tortuosity and Crack Branching Factor

In order to understand crack propagation within a material's structure due to deformation, it is necessary to examine the parameters considered to be associated with the phenomenon namely crack density, crack tortuosity and the crack branching factor. *Crack density* (expressed in mm/mm^2) can be calculated as the ratio of the total crack length, ℓ to the total image area, A under consideration (refer to Equation 4.20) (Akcaoglu et al., 2005; Glinicki and Litorowicz 2006).

$$Crack\ density = \frac{\sum_{i=1}^{N} \ell_i}{A} \qquad 4.20$$

Figure 4.16 illustrates the crack descriptions as in Song et al. (2005). According to Tong and George (2004) and Song et al. (2005), *crack tortuosity* is the ratio of the main crack length (true length), L_m to the projected length or linear distance between its end points, L_p. The *crack branching factor* is the ratio of the total length of all the branches of the crack, L_b to the main crack length. The higher the ratio of both aforementioned properties, the larger the area over which the cracks can be said to be propagating or spreading.

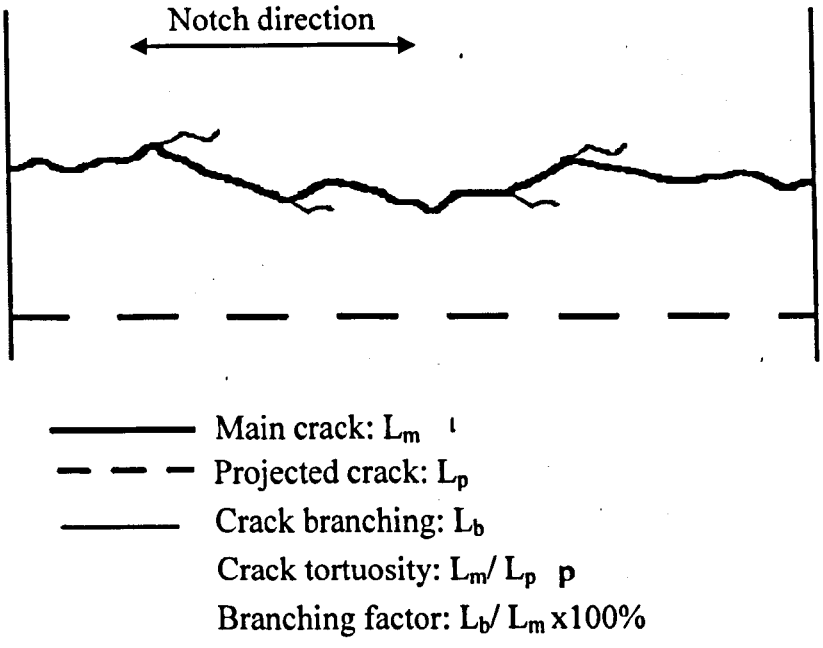

Figure 4.16 Illustration of the crack descriptions (Song et al., 2005)

Akhavan et al. (2011) quantified crack tortuosity (illustrated in Figure 4.17) using Equation 4.21. In Figure 4.17a, the actual image of a crack is converted into a crack profile with *x-z* coordinates (Figure 4.17b). From the crack profile, the nominal crack length, X_{max} and the effective length, L_e can be determined. L_e is the total sum of the length of the $\bar{Z}$ lines (lines connecting the intersect points of the segment lines and the crack profile), which depend on the segment length, λ. The shorter the segment length used, the longer the measured effective length.

$$\tau = \left(\frac{X_{max}}{L_e}\right)^2 \qquad 4.21$$

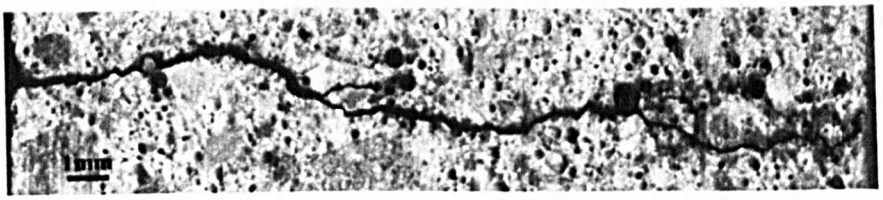

(a)

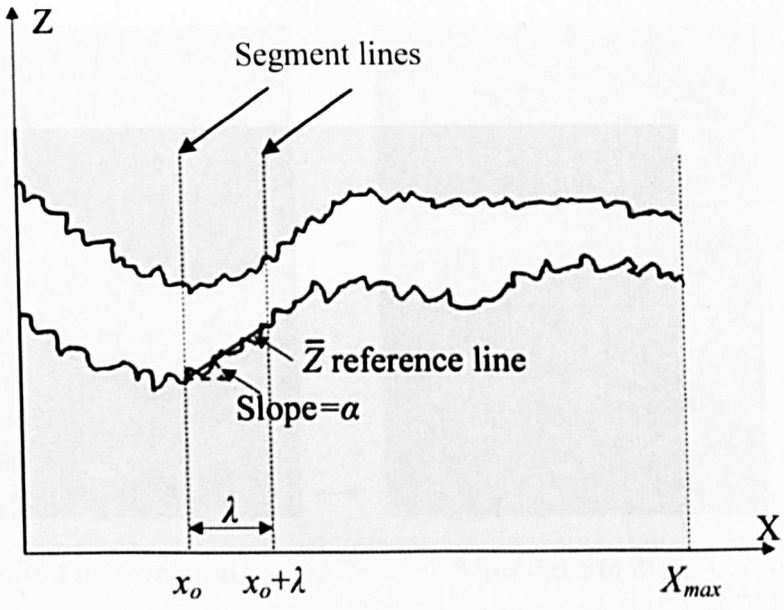

(b)

Figure 4.17 (a) An image of the actual crack; (b) schematic of a crack profile (Akhavan et al., 2011)

4.3.2.3 Extracting the Damaged Area

In order to characterise the connectivity between voids or the preferred travel path of cracks, it is imperative to quantify the increase in voids area (or damaged area), A_i, caused as a result of deformation. This study proposes a procedure for differentiating and extracting the image of the original air voids area, A_o (specimen in an undamaged state) from the total final air voids content, A_t of an X-ray image slice of a compacted asphalt mixture specimen in its damaged state using digital image processing. This is explained using Equation 4.22 and

Figure 4.18. By differentiating and extracting the increase in voids area from the original void area, the characteristics and concentration of the damaged areas within the material's composition can be analysed.

$$At = Ao + Ai \quad 4.22$$

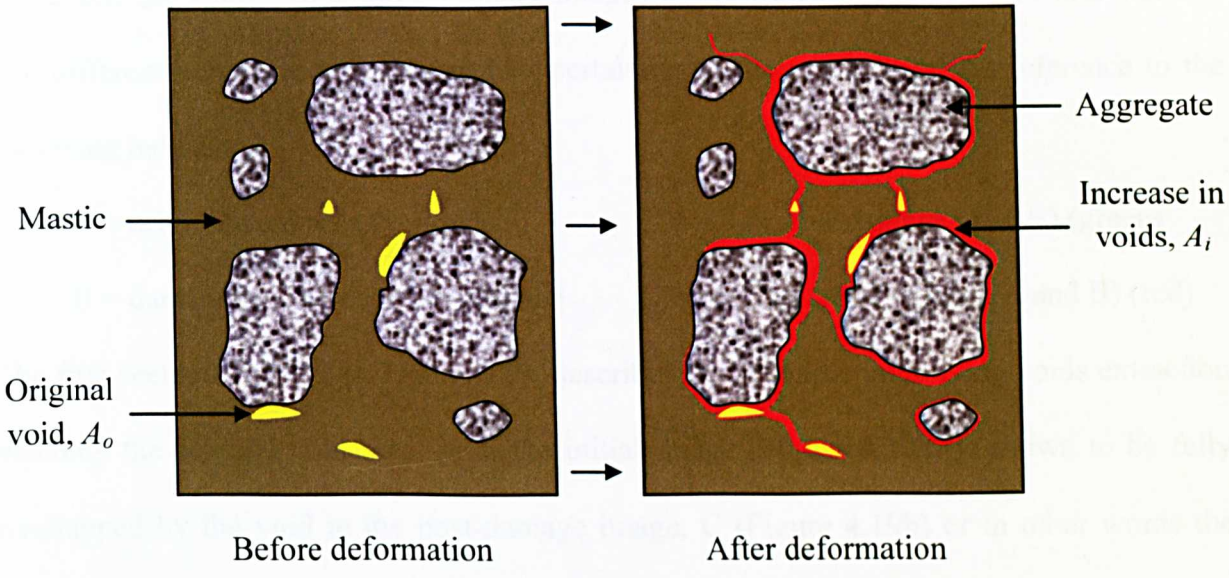

Figure 4.18 Illustration of the increase in voids area after deformation

The extraction procedure utilises a superimposition technique or so called 'operations between images' which involve a set of mathematical operations namely, image logical operations. For getting good results from these operations, the basic restriction is that the initial images have to be of the same dimensions and data type. These operations are very useful for feature extraction when dealing with binary images. In common practice, there are three basic functions of logic operators i.e. AND (logical intersection), OR (logical sum) and NOT (negative of image). Other logic operators can be implemented by combining these three basic functions including XOR (exclusive or) and AND(NOT) (logical difference). For example, the 'logical difference' can be used to detect differences between two images. Details of these logical functions will not be discussed further in this document with

complete details contained in Gonzalez and Woods (2008), but the transformations resulted from these logical operations will be demonstrated using a simple example as follows. In this study, the above mentioned operations are performed on two stacks of X-ray images (before and after deformation) using the ImageJ software. An example of utilising these operations for voids extraction on binary images is illustrated in Figures 4.19 and 4.20 for two different scenarios. Subsequent text pertaining to the example makes reference to the following indicators:

A = original void area (yellow) C = voids after damage (A + B) (green)

B = damaged area (increase in voids) D = overlap area (between A and B) (red)

The first scenario, shown in Figure 4.19, describes the principle underlying voids extraction whereby the original void area, A in the initial image (Figure 4.19a) is shown to be fully overlapped by the void in the post-damage image, C (Figure 4.19b) or in other words the area of A is equal to area of D (A = D) (refer to Figure 4.19c). Therefore the increase in voids caused by the damage, B can be directly extracted as shown in Figures 4.19f. The scenario described above might occur at an early stage of the loading when strains are generally minor. However, in other instances, the tested specimen undergoes major deformation with some changes in the geometry or shape disintegration, making the first scenario inapplicable. The second scenario ($A \neq D$) as described in Figure 4.20 then becomes relevant. For the two overlapping images (between Figures 4.20a and 4.20b), it can be seen in Figure 4.20c, that the position of the voids created by the damage deviates from the location of the initial voids. As a result of the added discrepancy in voids configuration, the extracted damaged area in Figure 4.20f is slightly higher than the actual damaged area because the difference is occupied by the original void area.

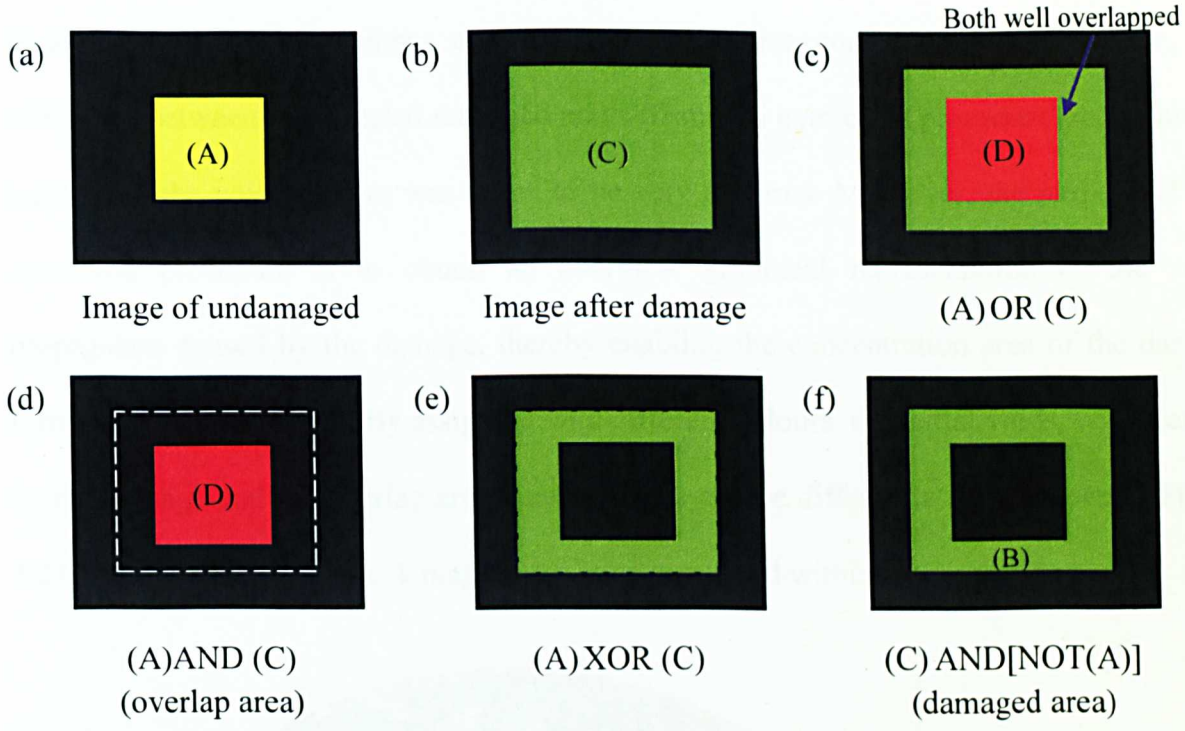

Figure 4.19 Illustration of the different logical operations on image A (initial void) and image C (voids after damage) for (A = D)

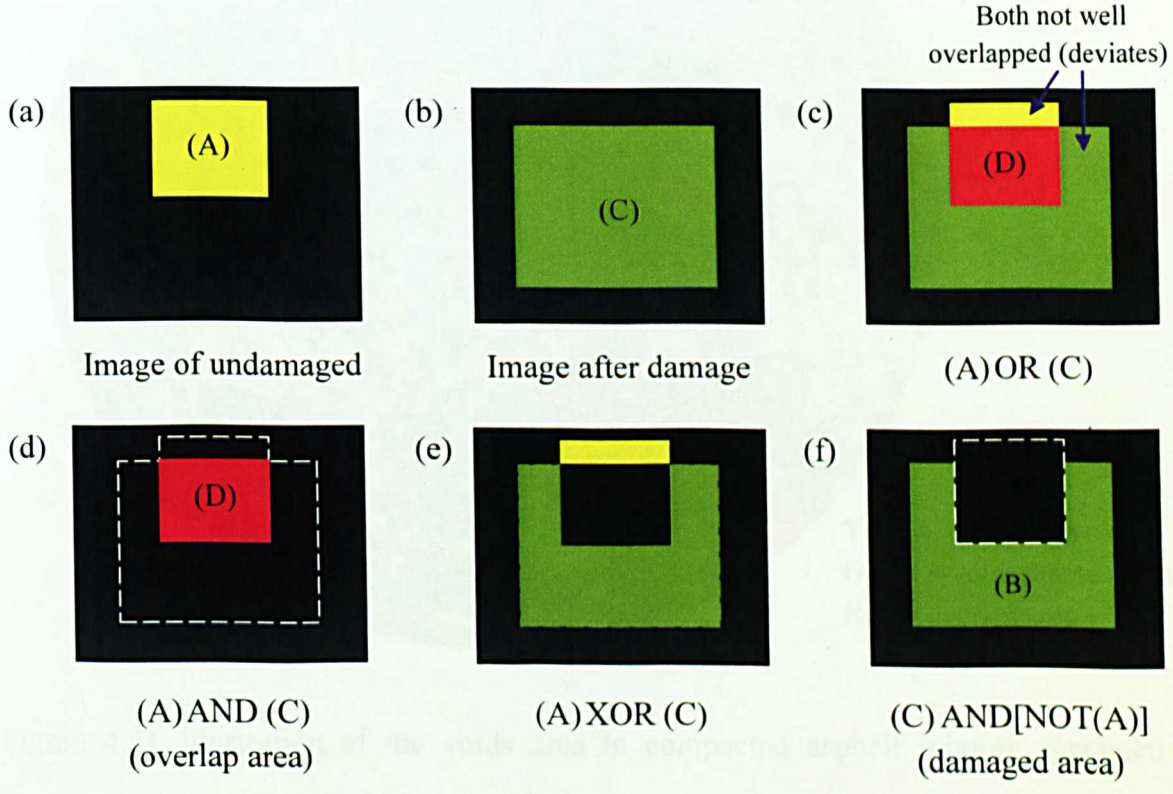

Figure 4.20 Illustration of the different logical operations on image A (initial void) and image C (voids after damage) for (A ≠ D)

However, based on a number of extraction procedures conducted by the author, the difference between the selected damaged areas (from the extraction procedure) to the actual increase in the voids content was found to be very minimal. Moreover, the purpose of this extraction procedure is to obtain an overview graphical representation of the voids propagation caused by the damage, thereby enabling the concentration area of the damage formation to be identified. By assigning with different colours, the initial voids, voids caused by the damage and the overlap area between them can be differentiated as shown in Figure 4.21. It can be seen that, the damaged area is concentrated within the circled area.

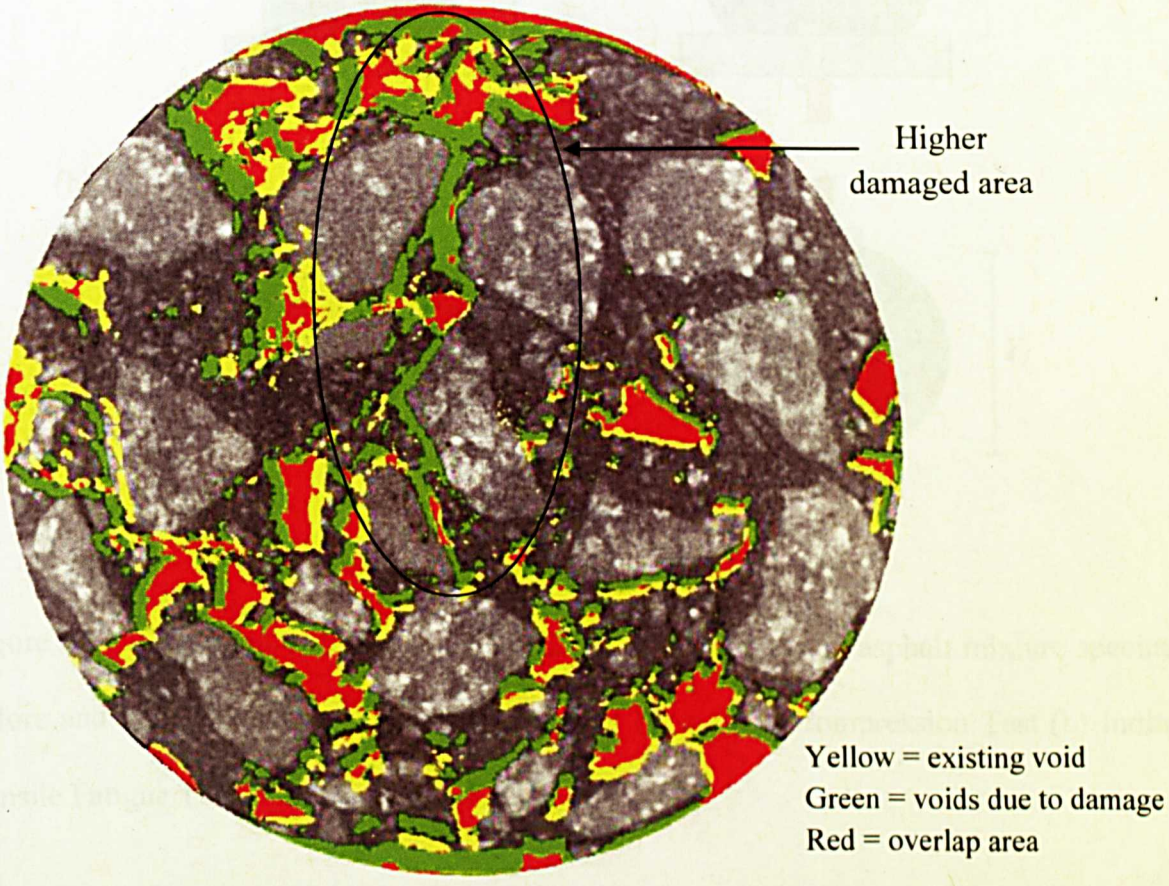

Figure 4.21 Illustration of the voids area in compacted asphalt mixture specimen after deformation (Indirect Tensile Fatigue Test)

4.3.2.4 Image Slices Verification for Damage Comparison

For damage characterisation, the compacted asphalt mixture specimens were scanned before and after conducting the destructive test to assess any changes to their microstructure. After completing the destructive tests, the deformed specimens were noted to have reduced in height ($X_0 > X_1$) or having a different diametral geometry ($Y_0 > Y_1$), as shown in Figure 4.22.

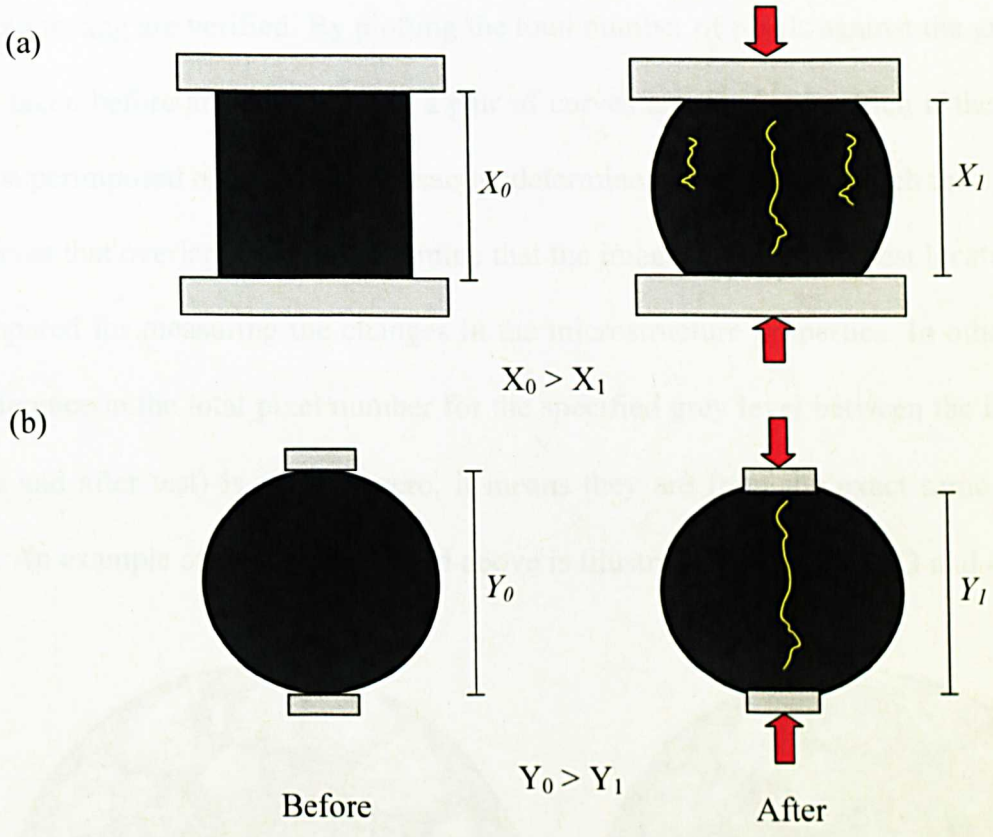

Figure 4.22 Illustration of the changes in shape of the compacted asphalt mixture specimen before and after the destructive test (a) Uniaxial Monotonic Compression Test (b) Indirect Tensile Fatigue Test

The deformed specimen was then X-rayed at the same slice interval as used for scanning before the test, which produced fewer image slices and some aggregate displacements. This process can cause misinterpretation or measurement errors as the captured image slices (of

the same specimen) would technically be at a slightly different location after undergoing deformation.

Therefore, to ensure that the analysed X-ray image slices of the specimen are comparable before and after testing, (which means the image slices are compared exactly or at the closest possible to the initial location before testing) the grey levels of the image slices prior to and following testing are verified. By plotting the total number of pixels against the grey level of images taken before and after testing, a pair of curves are obtained, which if they match or can be superimposed on one another exactly, determines the extent to which the slices differ. The curves that overlap the most determine that the images from the closest location that can be compared for measuring the changes in the microstructure properties. In other words, if the difference in the total pixel number for the specified grey level between the image slices (before and after test) is close to zero, it means they are from the exact same location or height. An example of the plot described above is illustrated in Figures 4.23 and 4.24.

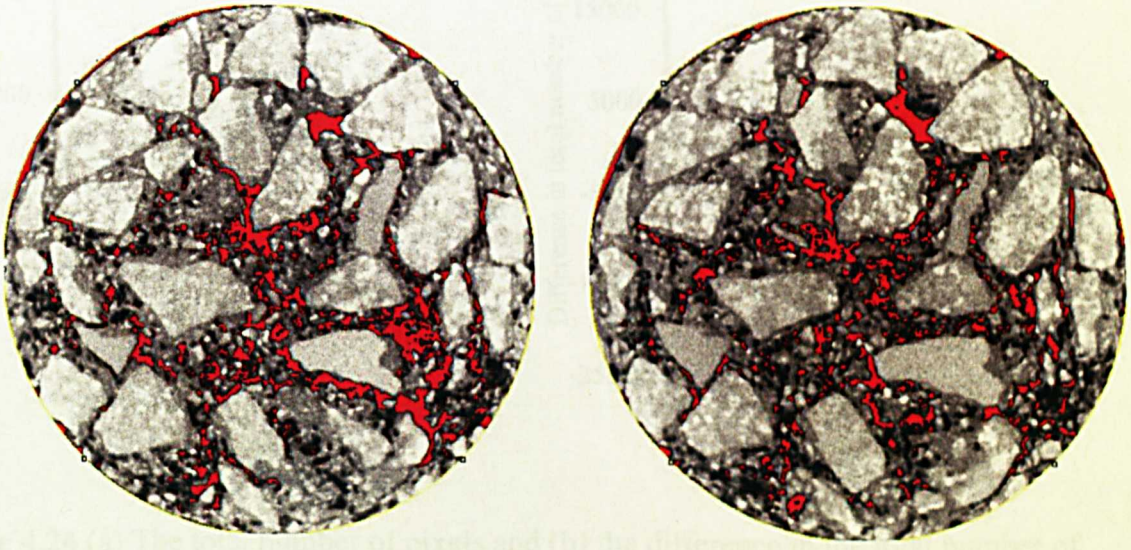

(a) 5B (b) 6B

Figure 4.23 continues below

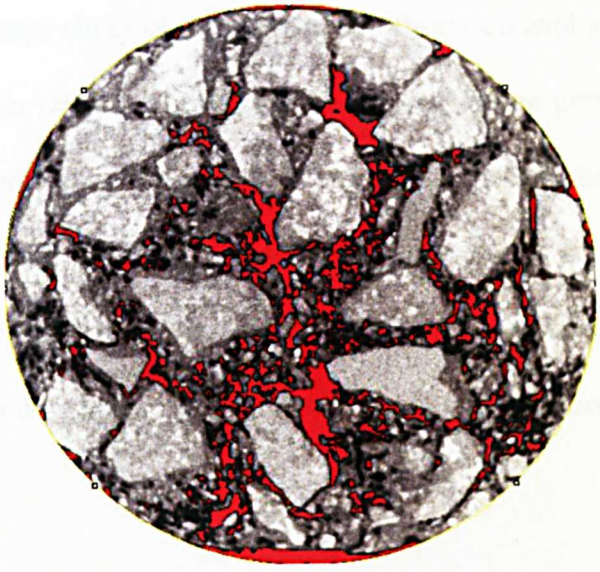

(c) 5A

Figure 4.23 X-ray images of rubberised asphalt mixture before the test (a) slice 5 (5B), (b) slice 6 (6B) and after the test (c) slice 5 (5A) (air voids highlighted in red)

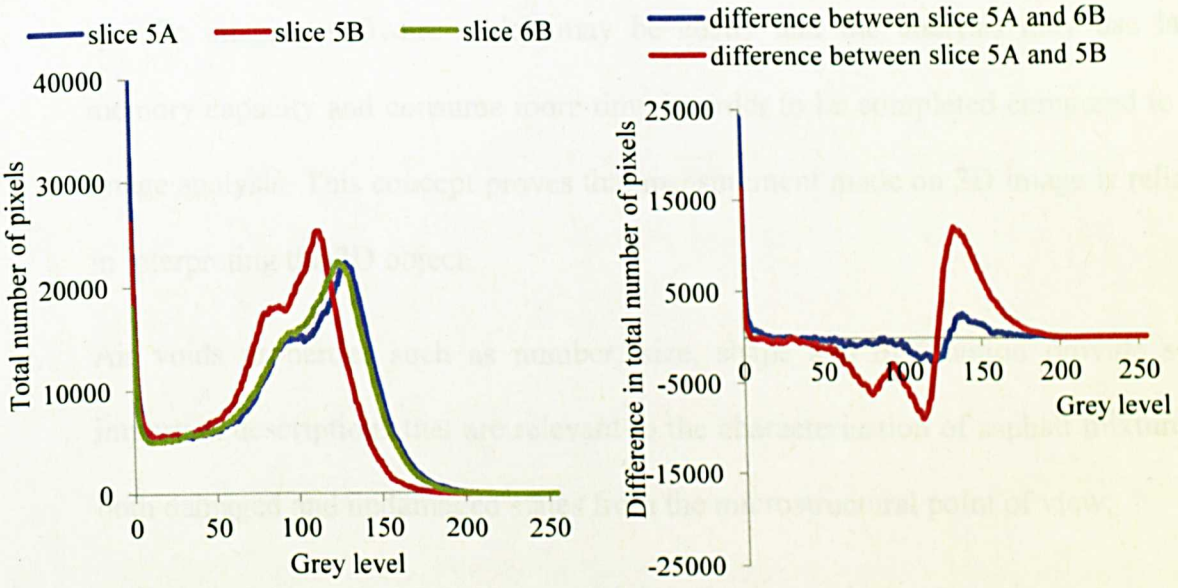

(a) (b)

Figure 4.24 (a) The total number of pixels and (b) the difference in the total number of pixels for different grey level within the X-ray images

Figure 4.23 shows the image slices of a specimen of rubberised asphalt mixture before (slice 5B and slice 6B) and after (slice 5A) the test. By comparing the grey level distribution and the difference in total number of pixels in both images i.e. before the test and after the test, as shown in Figure 4.24, it is clear that slices 6B and 5A are more comparable than slices 5B and 5A. Therefore, for damage characterisation, the changes in the microstructure properties of slices 6B and 5A would be more suitable candidates for comparison.

4.4 Summary

To conclude this chapter, the following remarks are noteworthy:

i. The stereology concept is very significant in image analysis, because sometimes 3D analysis can be complicated and challenging. This is because it usually requires specific imaging software which may be costly and the analysis may use large memory capacity and consume more time in order to be completed compared to 2D image analysis. This concept proves that measurement made on 2D image is reliable in interpreting the 3D object.

ii. Air voids properties such as number, size, shape and distribution provide some important descriptions that are relevant to the characterisation of asphalt mixtures in both damaged and undamaged states from the microstructural point of view.

iii. A few damage parameters in quantifying the internal structure damage are very significant such as measurements made on the changes of microstructure properties of air voids and cracks. A technique developed for viewing the damaged area is very useful for identifying the localisation in the damage distribution within the rubberised asphalt mixture components as a result of the loading action.

5.0 MATERIAL SELECTION AND EXPERIMENTAL PROGRAMME

5.1 Introduction

This chapter describes the materials properties and mixture design for specimen preparation. Furthermore details of the experimental programme, particularly the X-ray CT scanning and the mechanical testing for damage characterisation are also provided. The experimental programme consists of two mechanical tests, the Uniaxial Monotonic Compression Test and Indirect Tensile Fatigue Test. A flowchart of the experimental works carried out in the chapter is summarised in Figure 5.1.

5.2 Materials

Materials used in this laboratory study consisted of aggregate, bitumen and crumb rubber. Detailed explanations on the material properties are presented in subsequent sections.

5.2.1 Aggregates

The aggregates (granite) were supplied by Midland Quarry Products, Leicester. In this study, all the aggregates were sieved to obtain their size fractions and blended to achieve the mixture design of a gap graded, hot rolled asphalt (HRA 60/20) that conforms to BS 954-1:2005. Detailed gradations are presented in Section 5.3. Two batches of aggregates were blended together: the coarse aggregates with the maximum size of 20 mm and the dust (filler

to 4 mm). The physical properties and gradations for different aggregate batches are presented in Tables 5.1 and 5.2.

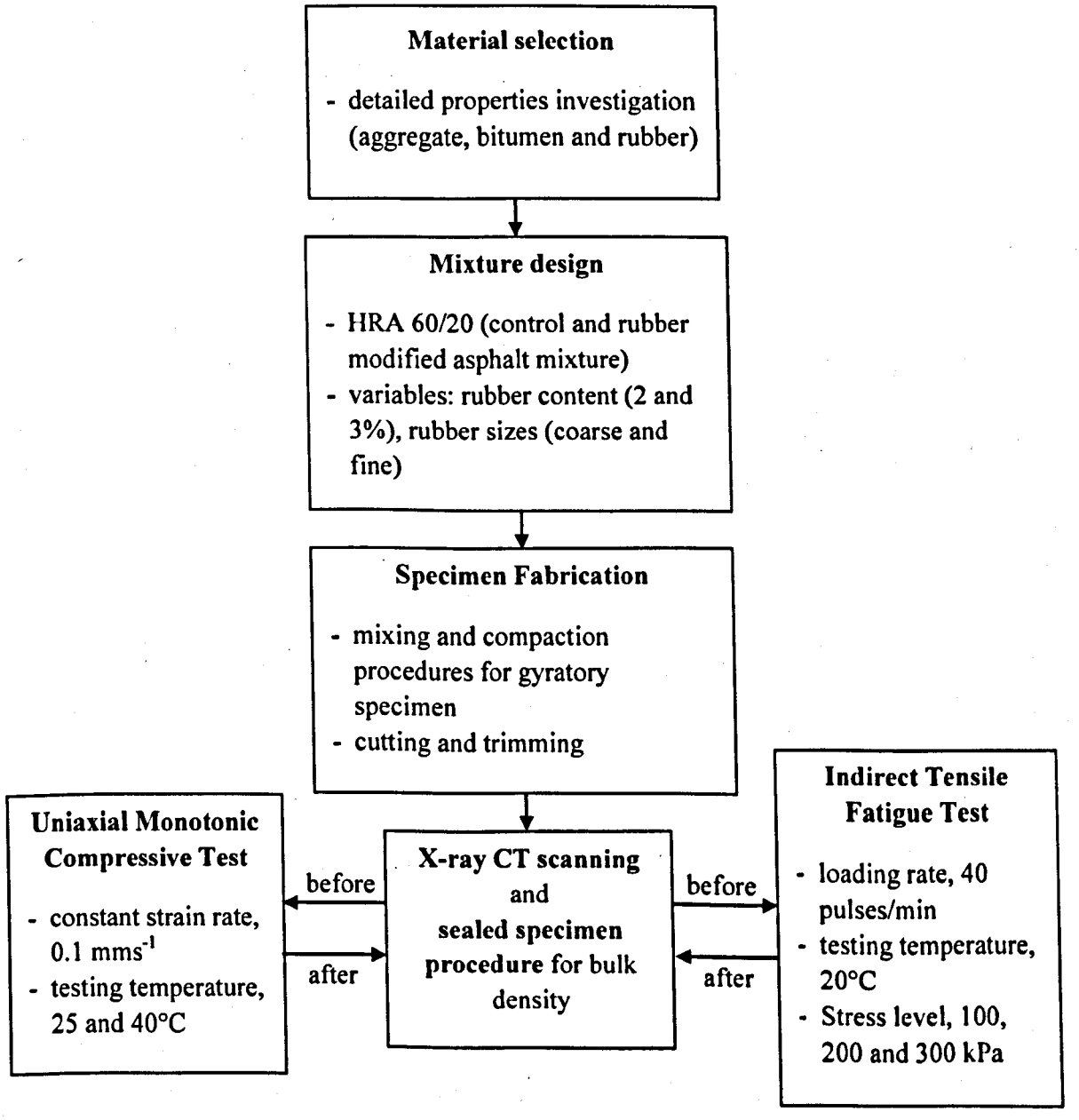

Figure 5.1 Experimental programme

Table 5.1 Physical properties of the aggregates (BS EN 1097-6:2000)

Aggregates	Properties	
	Bulk specific gravity	Absorption (%)
Coarse Aggregate	2.7838	0.4
Fine Aggregate (dust)	2.7730	0.7

Table 5.2 Particles gradations for different aggregate batches or sizes (BS EN 933-1:1997)

Sieve size	Percentage passing (%)	
(mm)	20 mm	Dust
31.5	100	-
20.0	98.30	-
14.0	17.18	-
10	0.95	100
4.0	0.32	95.87
2.0	-	82.44
0.5	-	44.28
0.25	-	30.45
0.063	-	13.53

Granite aggregates were selected because they are commonly used in asphalt pavements and for the X-ray scanning purposes. Furthermore, based on the preliminary investigation presented in Chapter 3, after X-ray scanning, it was found that granite with higher mineral density produces image of particles with a better contrast compared to limestone. This proved very helpful for differentiating and segmenting the aggregate particles from the rest of material composition within the image.

5.2.2 Bitumen

Bitumen 100/150 penetration grade was used and its physical properties are given in Table 5.3. The bitumen was supplied by Shell Bitumen, UK. From the review made earlier on the rubber-bitumen interaction in Chapter 2, it is expected that the rubber particles will absorb some of the bitumen's lighter fraction (aromatic oil) which could lead to an increase in the bitumen stiffness. This could also possibly reduce the adhesive bond between the bitumen and aggregate particles. Therefore, bitumen with higher penetration grade was selected to compensate for the rubber-bitumen interaction.

Table 5.3 Physical properties of the bitumen

Test	100/150	Test specification
Density (g/cm^3)	1.03	BS EN 15326:2007
Viscosities:		
120 °C, (cP)	553.1	BS EN 13302:2003
150 °C, (cP)	134.4	
180 °C, (cP)	51	
Penetration at 25 °C (0.1 mm)	120	BS EN 1426:2007
Softening point (°C)	44.6	BS EN 1427:2007

5.2.3 Crumb rubber

The crumb rubber was supplied by SRC limited, Manchester, having been recycled from truck tyres at ambient temperature using grinding method. The average sizes of the rubber particles used were 1-3 mm for fine and 5-6 mm for coarse rubber (refer Figure 5.2). The rubber gradations are given in Table 5.4.

Fine rubber Coarse rubber

Figure 5.2 Fine and coarse crumb rubber

Table 5.4 Fine and coarse crumb rubber gradation

Sieve size (mm)	Percentage passing (%)	
	Fine rubber	Coarse rubber
6.3	100	100
4.0	100	0
2.0	76.5	0
1.0	11.9	0
0.5	0.7	0

Initially the rubber density was determined to be 1.10 g/cm^3 using 'Gas jar method' as prescribed in BS EN 1097-6:2000. However during preparation, it was observed that a lot of air bubbles became trapped around the rubber particles as shown in Figure 5.3a. Therefore a Helium pycnometer (Micromeritics AccuPyc-1330) was used to verify the density, as the helium gas was expected to perfectly fill all the gaps among the rubber particles and penetrate the finest pores, thereby ensuring maximum accuracy (Figure 5.3b). The measured density values were 1.12 g/cm^3 and 1.15 g/cm^3 for fine and coarse rubber respectively.

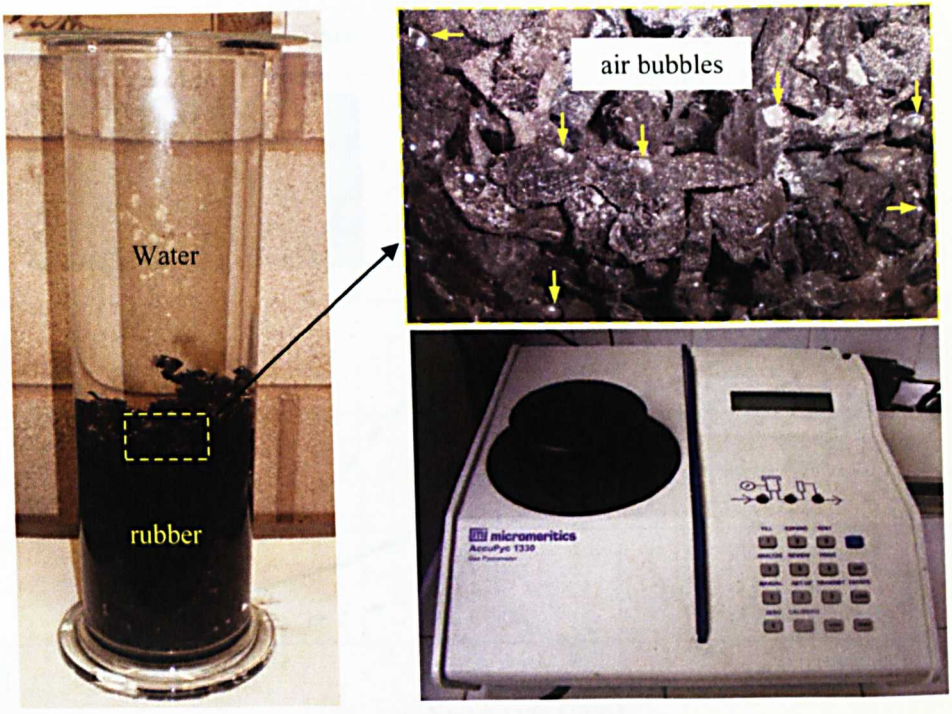

(a) (b)

Figure 5.3 Density determination using (a) gas jar method and (b) helium pycnometer

5.3 Specimen Fabrication

In this study, a gap graded mixture of Hot Rolled Asphalt (HRA 60/20) was selected in accordance to BS 954-1:2005. The HRA 60/20 contains 60 percent coarse aggregate with a maximum aggregate size of 20 mm and it was compacted using gyratory compactor. This mixture type was chosen for ease of scanning as the gaps between the (coarse and fine) aggregates were expected to make it easier to identify the different material phases within the specimen. Figure 5.4 shows the lower and upper limit gradation curves of the HRA 60/20 and that of the virgin or control mixture gradation (combined from the two batches of fine and coarse aggregates).

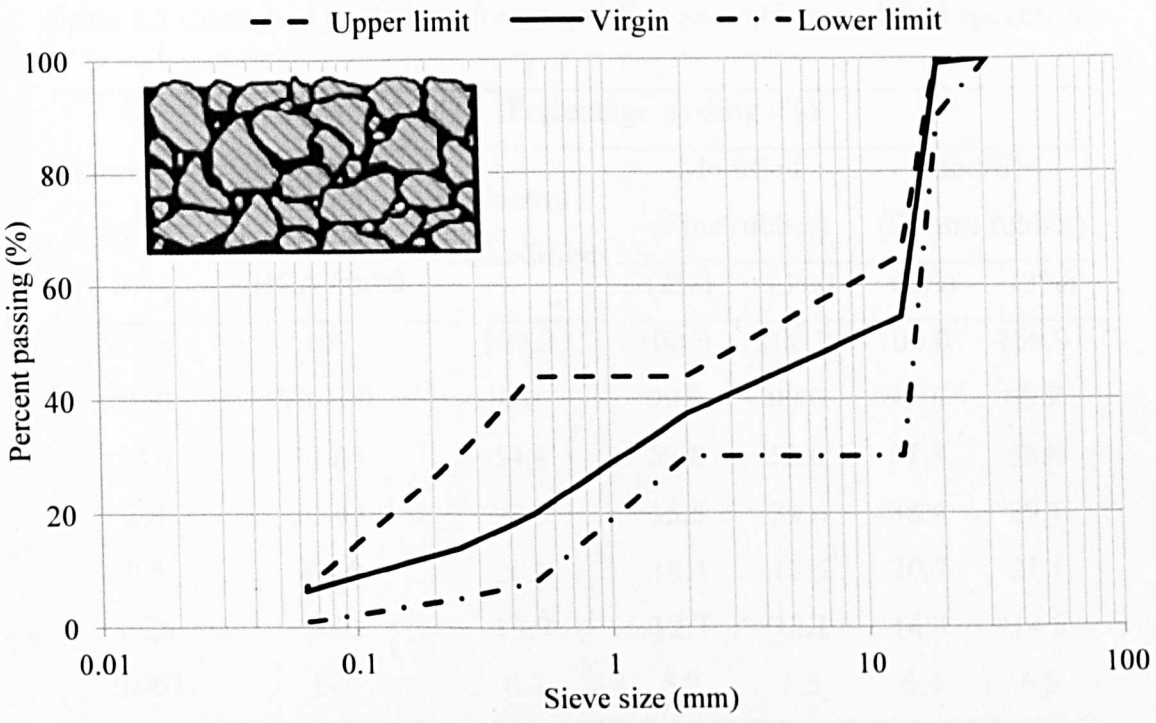

Figure 5.4 HRA 60/20 aggregate gradation curves

5.3.1 Mixture Design

Five types of mixtures were designed for comparison including the control mixture and four rubberised mixtures with different rubber content and size. Table 5.5 shows the control and combined gradations of aggregate and crumb rubber for rubberised mixtures used in making the gyratory specimens. The amount of crumb rubber added was expressed as percentages (2% and 3%) of the total weight of aggregate. The premise behind this modification was to substitute a portion (volume) of the aggregate from the original aggregate particle size distribution with an equivalent volume of crumb rubber.

Table 5.5 Combined gradations for unmodified and rubber modified specimens

Sieve size (mm)	Percentage passing (%)					
	BS 594-1:2005 HRA 60/20	Control (unmodified)	Modified (Fine rubber)		Modified (Coarse rubber)	
			(2%)	(3%)	(2%)	(3%)
31.5	100	100.0	100.0	100.0	100.0	100.0
20.0	90-100	99.1	99.0	99.0	99.1	99.2
14.0	30-65	54.4	52.8	52.0	57.3	58.8
2.0	30-44	37.3	35.5	34.6	38.4	39.1
0.5	8-44	20.1	18.4	17.5	20.7	21.1
0.25	5-30	13.9	12.7	12.1	14.3	14.5
0.063	1-7	6.3	5.7	5.5	6.4	6.5

The mixtures were designed to achieve 5% air voids content. An optimum bitumen content of 5.7% was selected for the control mixture as recommended in BS 594-1:2005. As highlighted in Chapter 2, the rubber modified mixture was recommended to be added with 1% to 2% higher bitumen content than the control mixture (which means the bitumen content is in the range between 6.7% and 7.7% for this mixture type) to compensate for the rubber-bitumen interaction (Takallou et al. 1985). Therefore trial specimens with varying bitumen contents (at approximately 6.8, 7.5 and 8%) and different target densities were prepared for the rubberised mixtures (at 2% and 3% rubber content) whilst the volume of aggregate + rubber within the rubberised mixtures remained unchanged as compared to volume of aggregate in the control mixture. Two replicates of specimen were prepared for each bitumen content for averaging purposes. The idea here was to estimate the design bitumen content and target compacted density, in order to attain a compacted rubberised specimen with a target air voids content of 5%. The air voids content was determined using a

laboratory sealed specimen method. The results are plotted in Figure 5.5. The graphs exhibit linear relationships for both mixtures with the R-squared (R^2) values close to 1. From the graphs, the target compacted density and the bitumen content at 5% air voids content were estimated and have been summarised in Table 5.6. It can be seen that, the more rubber added to the mixture, the higher the estimated bitumen content. In exact figures, 1% addition of rubber in the mixture requires approximately 0.6% more bitumen compared to the original bitumen content in order to reach the same air voids level. Using the estimated values, the design percentage of each material composition (i.e. aggregate, rubber, bitumen and air voids) by mass and volume of the total mixture were then calculated, as detailed in Figure 5.6. As mentioned earlier the total aggregate and crumb rubber in the modified mixtures are volumetrically the same as the total aggregate in the control mixture.

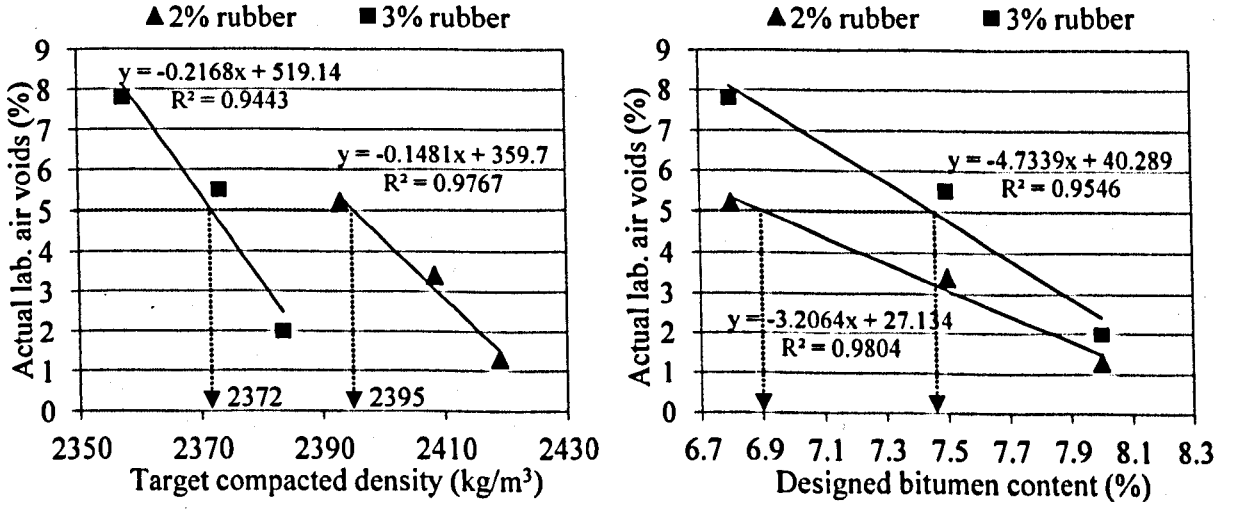

(a) (b)

Figure 5.5 Relationships of the actual laboratory air voids to the (a) target compacted density and (b) designed bitumen content

Table 5.6 Designed properties for the different mixture types

Designed properties	Mixture type		
	Control	2% rubber	3% rubber
Target compacted density, kg/m^3	2438	2395	2372
Bitumen content, % (to the nearest 0.1%)	5.7	6.9	7.5
Designed air voids content for the target compacted density, %	5.0	2.5	1.0
Actual laboratory determined air voids content, %	5.0	5.0	5.0

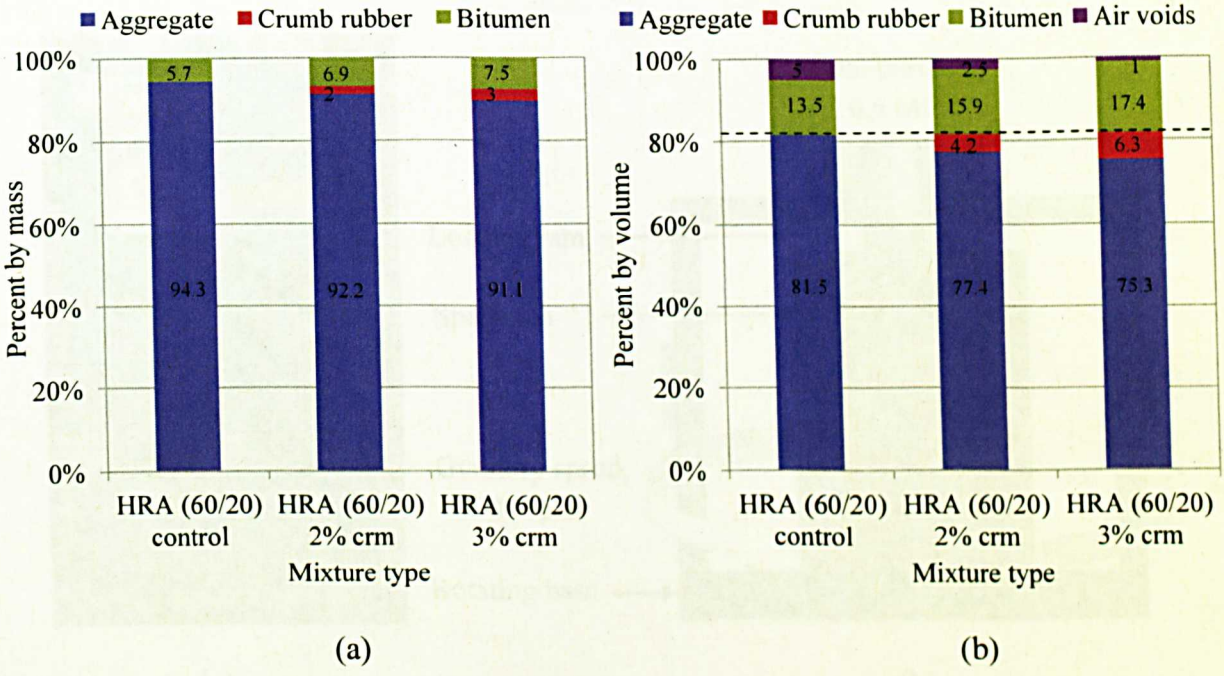

Figure 5.6 Designed percentage of each material by (a) mass and (b) volume of the total mixture

5.3.2 Mixing and Compaction Procedures

The specimens were mixed and compacted using a Cooper gyratory compactor, in accordance to BS EN12697-35:2004 and BS EN 12697-31:2007 respectively (Figure 5.7a). This compactor, by design is capable of producing laboratory asphalt mixture specimens that can be simulated to a reasonable degree, similar to the compaction produced in the field. The compaction effort applied to the mixture was controlled by a vertical pressure (0.6 MPa), angle of gyration (1.25°) and gyration speed (30 revolutions per minute) as described in Figure 5.7b.

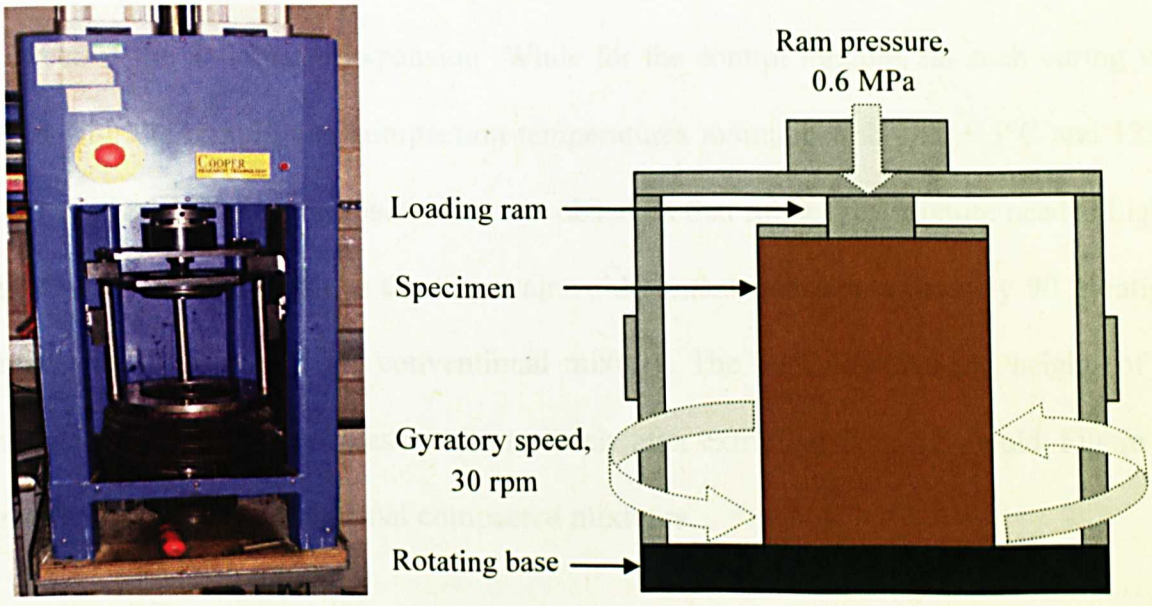

Figure 5.7 (a) Cooper gyratory compactor and (b) schematic diagram of the control parameters

In this study, the specimens were compacted to achieve the target density with a specimen of diameter, 100 mm and height, 100 mm. The design procedures adopted for rubber modified mixtures were slightly different and followed previous studies (Esch 1984; Schuler et al.,

1986; Takallou et al., 1986; Harvey and Curtis 1990; Heitzman 1992; Khandal and Hanson 1993; Chehovits et al., 1993; Amirkhanian 2001). The bitumen and the aggregate were pre-heated overnight in the oven at 145°C. Materials forming the rubberised mixture were mixed and cured for 2 hours in the oven at 160°C in a loose form before compaction. The higher mixing and curing temperatures were adopted with a view to maximise the 'rubber swelling' prior to compaction, in order to reduce the tendency of the specimen to expand after the compaction. This is said to improve the resilient modulus and the fatigue life (Takallou et al., 1985). The mixture was then remixed at 160°C and finally compacted at 135 ± 5°C. After compaction, the top end plate with a weight of 630 g was left on top of the specimen and maintained for 24 hours at room temperature before extrusion. This was expected to control the effect of the anticipated expansion. While for the control mixture, no such curing was applied with the mixing and compaction temperatures maintained at 145 ± 5°C and 135 ± 5°C respectively. During compaction, it was observed that rubberised mixture needed higher number of gyration to achieve the target air void content with approximately 90 gyrations compared to 30 gyrations for conventional mixture. The bulk densities and heights of the compacted specimens were measured immediately after extruding from the mould. Figure 5.8 shows the cut sections of the final compacted mixtures.

(a) (b) (c)

Figure 5.8 Cut sections of HRA60/20 mixtures for (a) control, added with (b) fine rubber and (c) coarse rubber (rubber particles pointed to with arrows)

5.4 Bulk Density Determination Using Sealed Specimen Procedure

Bulk density and the air voids content of the specimens were determined using the sealed specimen procedure as described in BS EN 12697-6:2003. This method was selected with the concern that some material within the trimmed specimen, particularly fines or rubber particles, might fall out or loosen when the specimens were submerged in the water when measuring the mass in water. Additionally, it was observed that some of the rubber particles tended to trap air bubbles when they were directly immersed in the water and could have affected the density results which require no air bubbles to adhere to the surface of the specimen. In this study, an aluminium foil of known density, (1603 kg/cm^3), ρ_{sm} was used as the sealing material. The specimens were sealed such that the internal voids in the specimen were taken to be part of the volumetric material composition and no extra voids existed between the seal or seal folds and the specimen. The mass of the dry specimen and dry sealed specimen were determined as m_1 and m_2 respectively. The sealed specimen was then immersed in a water bath (water density, ρ_w) and the mass underwater, m_3 was taken

when it became certain that no air bubbles had adhered to the sealing. Finally the bulk density, ρ_b was calculated using Equation 5.1. Figure 5.9 shows the specimen preparation and the water immersion apparatus.

$$\rho_b = \frac{m_1}{(m_2 - {}^{m_3}/_{\rho_w}) - (m_2 - {}^{m_1}/_{\rho_{sm}})} \quad 5.1$$

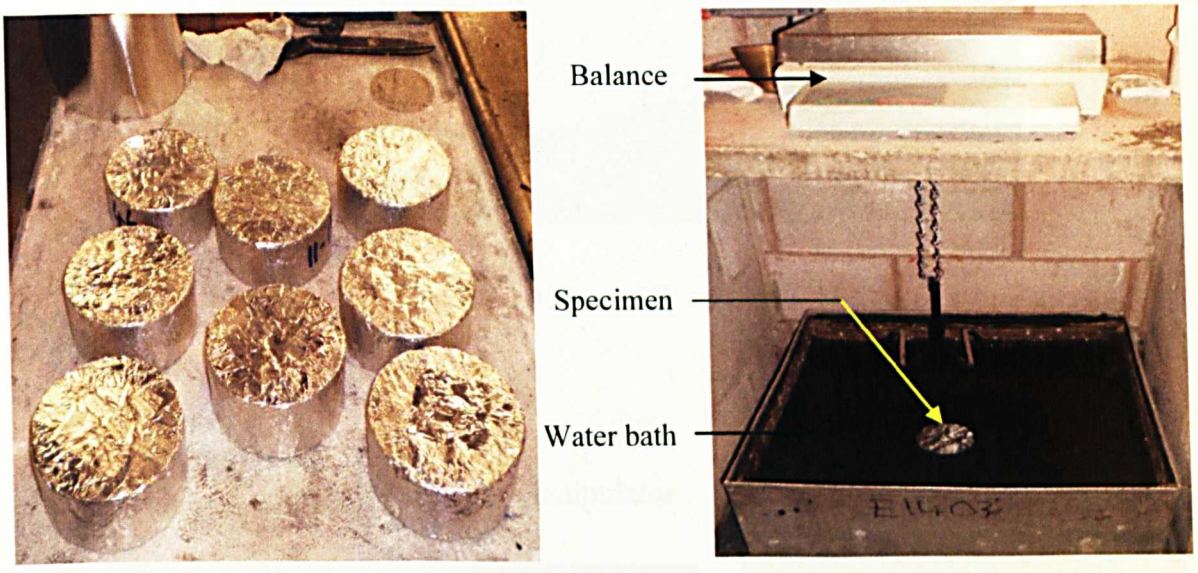

Specimens sealed with foil Water immersion apparatus

Figure 5.9 Sealed specimen and apparatus for determining bulk density

5.5 X-ray Computed Tomography Scanning

To investigate the microstructural properties of the rubberised mixtures, a sequence of X-ray 2D images were captured along the height of the compacted specimens at an interval of 1 mm. Figures 5.10 and 5.11 show the laboratory X-ray CT machine (X-Tek Industrial Ltd) available in Nottingham Transportation Engineering Centre.

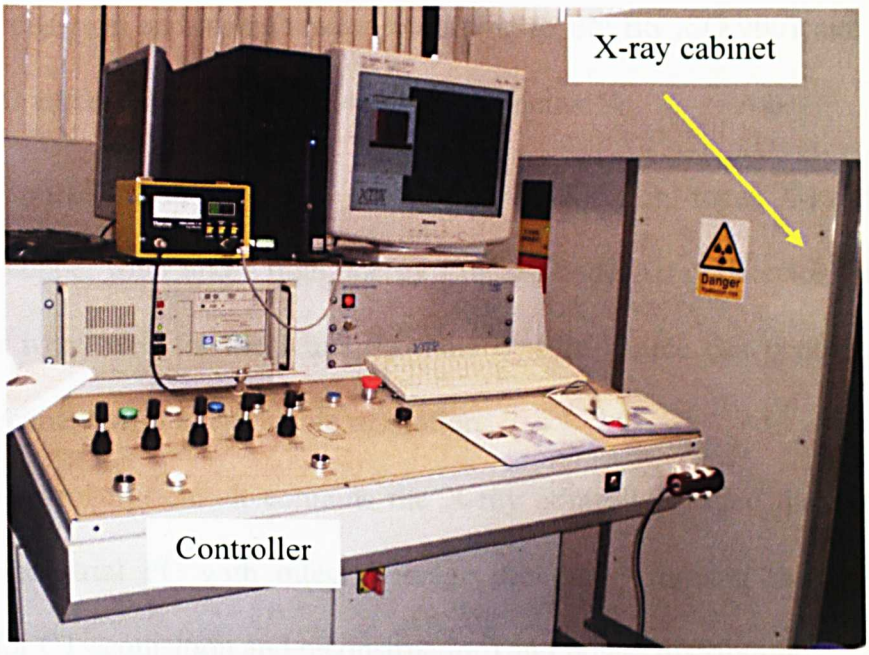

Figure 5.10 X-ray CT machine

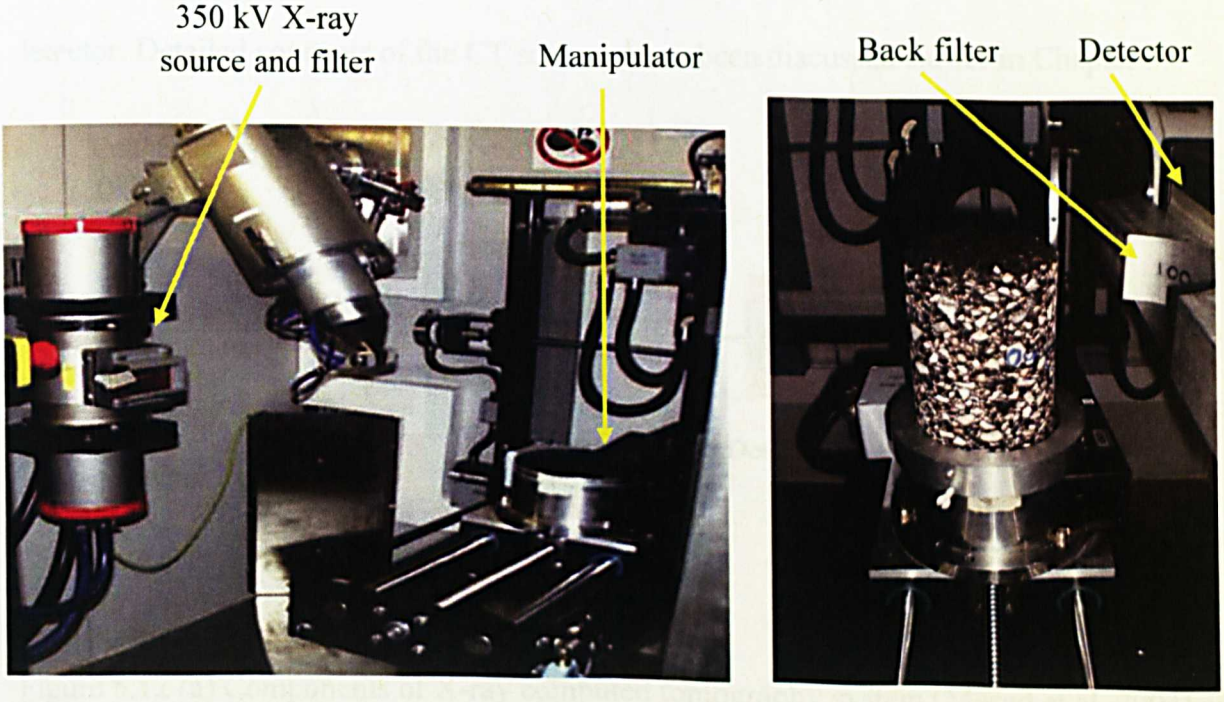

Figure 5.11 X-ray CT machine (inside view of the X-ray room)

The system is designed and manufactured according to EN BS ISO 9001 and the European CE Regulations and consists of the following components:

i. An X-ray source, manipulator and detector: A 350kV mini-focus X-ray source with 2 mm thick copper filter and a high energy Linear Diode Array detector with aluminium back filter were used for the scanning. This type of source can penetrate thicker and denser specimens with a reasonable resolution.

ii. Operator control System: It contains the X-ray controller, video display, manipulator controls, industrial PC with integral image processor (running the X-Tek IMPS III software for CT acquisition and reconstruction) and power distribution.

Figure 5.12 illustrates the X-ray CT components that consist of the X-ray source, specimen and detector with the specimen placed on the manipulator in between the source and detector. Detailed concepts of the CT scanner have been discussed earlier in Chapter 3.

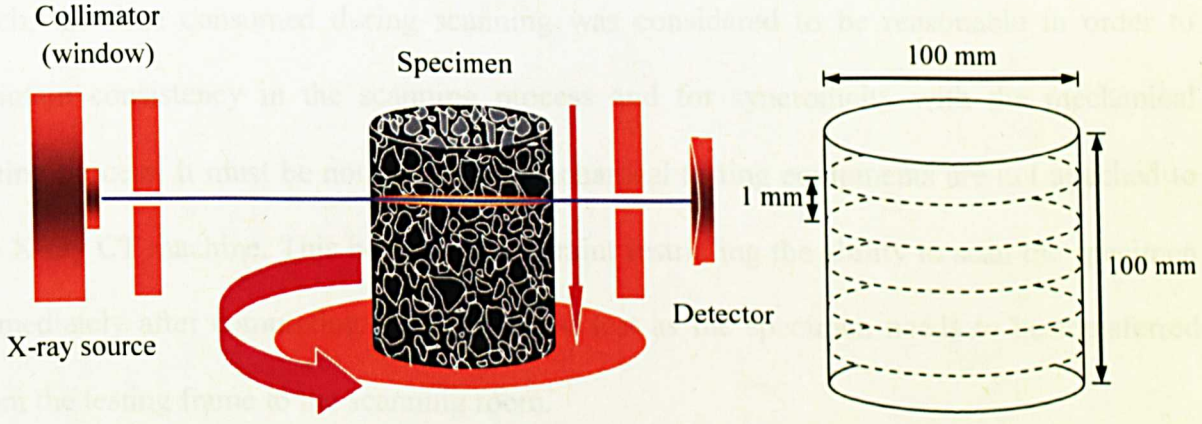

Figure 5.12 (a) Components of X-ray computed tomography system (Masad et al. 2004) and the (b) slice interval

During the scanning, the specimen was rotated through 180° to capture its density at every point in the horizontal plane from different angles. The X-rays were collimated and measured using a linear detector array that acquires data one slice image at a time. The specimen was then vertically moved downward at the specified interval between the image slices to complete the scanning from the bottom to the top of the specimen. Scanning of the slices was completed after collecting the intensity measurements for a rotation of the specimen at approximately 7 minutes per slice. For image analysis, the more images taken, the more information can be gathered and the better the results will represent the actual materials' properties. However, this has raised a concern that allowing longer times for scanning might introduce some changes in the specimen properties such as the geometry or shape particularly for damage characterisation due to specimen recovery. Consequently in this study, a total of 100 image slices for the specimen with 100 mm height were captured at the interval of 1 mm. taking almost 12 hours for a single specimen. For the entire specimen batch, the time consumed during scanning was considered to be reasonable in order to maintain consistency in the scanning process and for syncronicity with the mechanical testing process. It must be noted that the mechanical testing equipments are not attached to the X-ray CT machine. This became a constraint restricting the ability to scan the specimen immediately after completing the mechanical test as the specimen needs to be transferred from the testing frame to the scanning room.

5.6 Uniaxial Monotonic Compression Test

The stiffness modulus of asphalt mixtures can be considered a key performance parameter. The uniaxial monotonic compression test is the simplest method to measure the stiffness as well as the compressive strength under monotonic uniaxial loading. This test was selected based on the need to understand an asphalt mixture's material properties with reference to its load-deformation or stress-strain characteristics.

5.6.1 Theoretical Methodology

Compression testing provides information on the strength and deformation of specimens under uniaxial compressive stress. The stress and strain are expressed by Equations 5.2 and 5.3 where P is the load in Newton and A is the cross-sectional area in mm^2 with the strain corresponding to the displacement, δ from the original specimen length, L. The mixture stiffness, S is then calculated using Equation 5.4.

$$\sigma = \frac{P}{A} \quad 5.2$$

$$\varepsilon = \frac{\delta}{L} \quad 5.3$$

$$S = \frac{\sigma}{\varepsilon} \quad 5.4$$

A typical graph plot (stress-strain curve) from the test is shown in Figure 5.13. Two critical points across the three main stages of the specimen behavior can be observed from the plot. At the early portion of the curve, the stress is proportional to the strain up to the elastic limit (EL) with the constant of proportionality being the modulus of elasticity. This stage (Stage 1) is considered to be undergoing elastic deformation where the material is able to return to its original shape upon unloading. As the deformation continues and exceeds the elastic limit, the material reaches the second stage, known as strain hardening region as a

consequence of plastic deformation until it reaches the ultimate strength (US). The plastic deformation causes a permanent change in shape and continues to Stage 3 where the failure is shown to occur beyond the maximum stress.

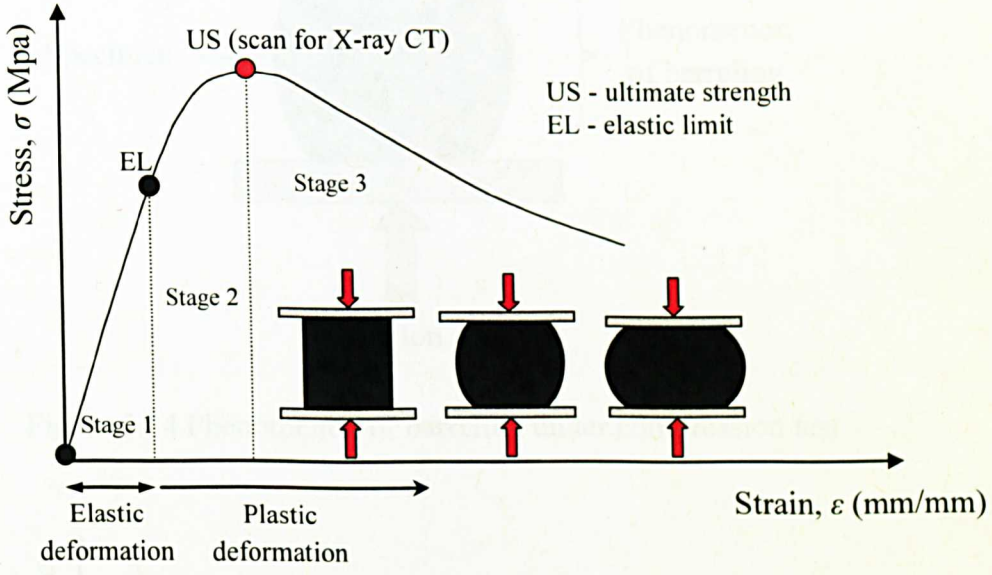

Figure 5.13 Stress and strain response for asphalt mixture under monotonic compression test

When testing to failure, the middle part of the specimen tends to expand in the lateral direction thereby increasing the specimen's cross-sectional area. This phenomenon is known as 'barrelling' where the specimen attains a barrel shape under loading conditions (Figure 5.14). When the load is released, the relationship between stress and strain is shown by Figure 5.15.

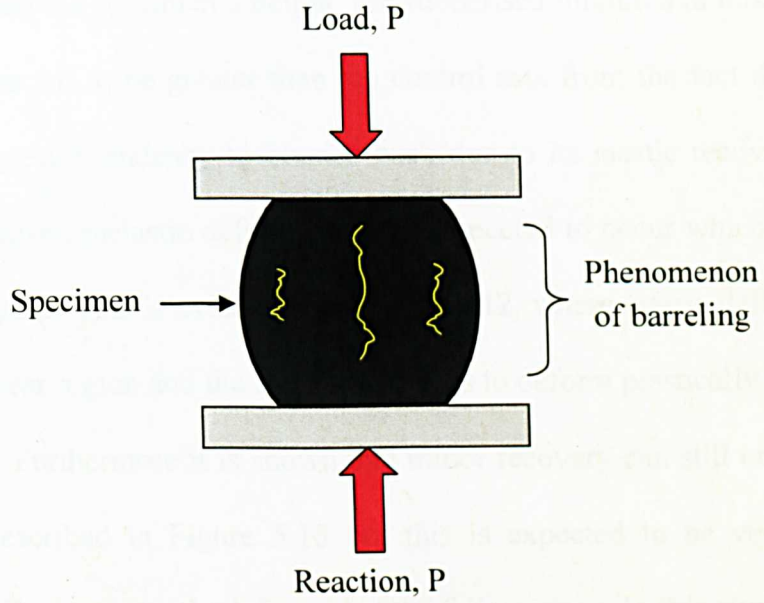

Figure 5.14 Phenomenon of barreling under compression test

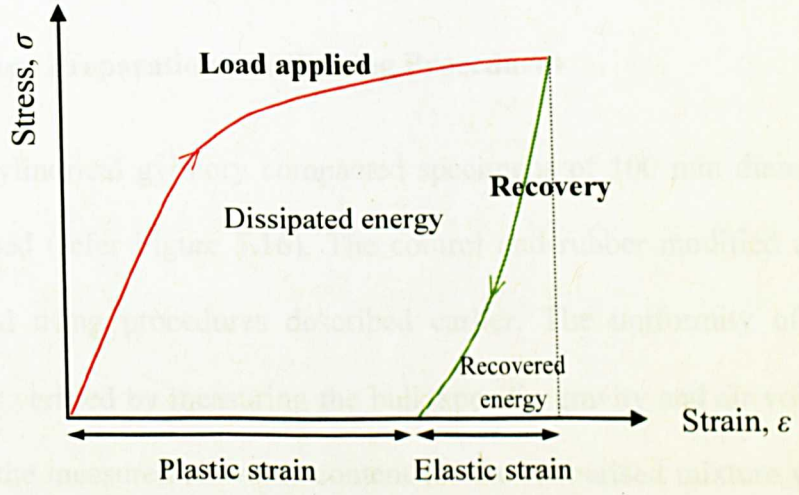

Figure 5.15 Typical of load and unload behaviour in a stress-strain curve

The elastic strain is recoverable but the plastic strain is non-recoverable. The energy dissipated and energy recovered during a full cycle of loading and unloading is represented by the area contained within the diagram below (Zhiming 2009). Khan (2009) conducted a compression test on control dense graded asphalt mixture to evaluate the damage at pre-selected strain levels. He observed some recovery while scanning the specimen up to 12

hours, by measuring the specimen's height. For rubberised mixtures in this investigation, the recovery was expected to be greater than the control mix from the fact that the rubberised specimen has a greater tendency to bounce back due to its elastic recovery behaviour. At maximum stress level, inelastic deformation was expected to occur which was desirable for the scanning purpose. This is evident from Figure 5.12, where elastic deformation is shown to occur at the linear region and the specimen begins to deform plastically until it reaches the maximum stress. Furthermore it is shown that minor recovery can still occur when the load is released as described in Figure 5.15 but this is expected to be very minimal as the specimen is usually permanently deformed at the failure stage. In this study, the damage was characterised at the peak stress as it was considered the critical stage prior to failure.

5.6.2 Specimen Preparation and Testing Procedures

For this test, cylindrical gyratory compacted specimens of 100 mm diameter and 100 mm height were used (refer Figure 5.16). The control and rubber modified asphalt specimens were fabricated using procedures described earlier. The uniformity of all the prepared specimens was verified by measuring the bulk specific gravity and air voids content. It was observed that the measured air voids content for the rubberised mixture was slightly varied compared to the target design air voids content, (5%). This was particularly so for specimens with higher rubber content. This might be contributed by the minor expansion of the specimen after being extruded from the mould due to the rubber swelling effect. Therefore acceptable replicates that had air voids closest to the target air voids content were chosen for each test condition and mixture type.

Figure 5.16 Specimen ready for compression testing

In this study, a servo-hydraulic testing machine comprising a temperature controlled cabinet with loading rams attached was employed. Figure 5.17 shows the experimental set up for the uniaxial compression test. The loading system was controlled by a digital server called 'Rubicorn' and had a loading capacity of ±100 kN with a ±50 mm axial stroke. The stress applied on the specimen was measured as a function of strain under unconfined conditions at a fixed temperature. The axial deformations were measured by the stroke displacement.

Two test temperatures, 25 and 40°C were selected to simulate the damage at ambient and high temperatures respectively. The specimens and the machine's cabinet were conditioned at the target test temperature and the test was performed at a constant strain rate of 0.1 mm/s. One strain rate was selected in order to have a uniform basis for comparison between the different mixtures and in such a way that the load was sustained for 100-200s. This test length was chosen to ensure that the tested specimens reached the failure stage within a reasonable testing time, thereby reducing the effect of aging on the other queued specimens

(under conditioning) waiting to be tested. Table 5.7 shows the detailed conditions for the compression test.

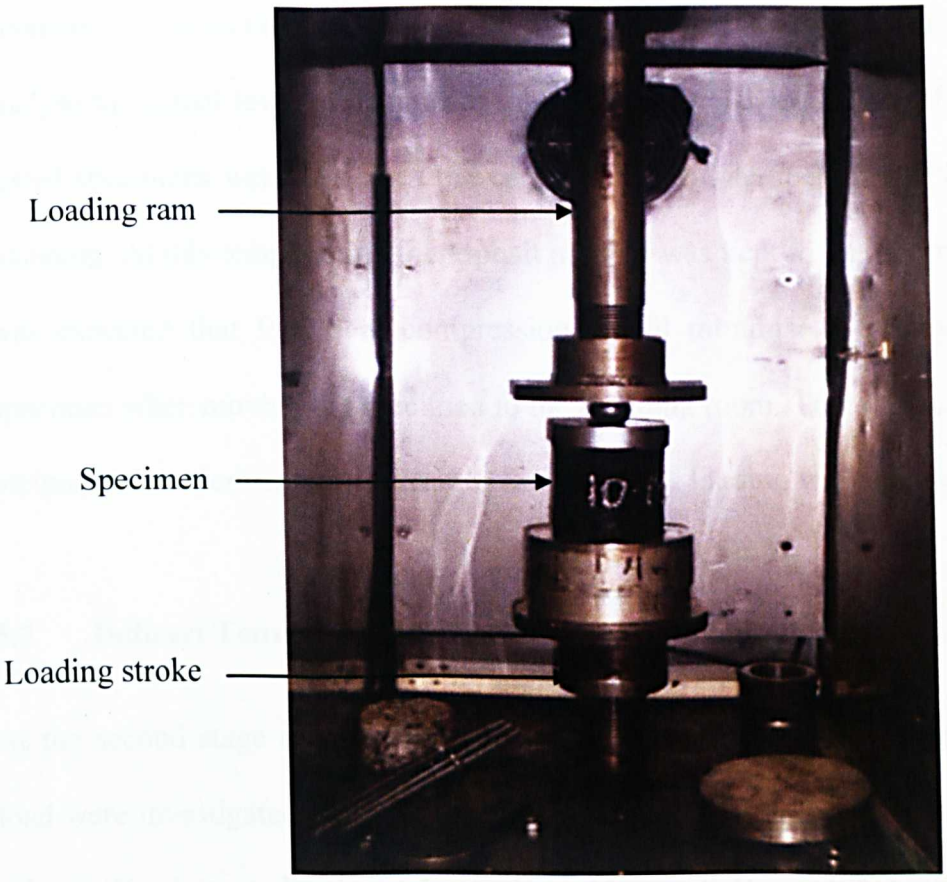

Figure 5.17 Setting up of the uniaxial monotonic compression testing machine

Table 5.7 Detailed conditions for compression test

Condition	Value
Specimen size	Ø, 100 mm and *t*, 100 mm
Test temperature	25°C and 40°C
Constant strain rate	0.1 mms^{-1}
Failure criterion	Exceed peak stress

The specimens were X-rayed before and after testing. The load was applied until it reached the peak stress required to induce micro and macro-damage and then released for scanning.

The readings of load and stroke displacement were recorded by plotting the stress-strain curve. Prior to scanning, it is important for the specimens not to have major changes in their geometry which could potentially be caused by recovery action. This is important in order to analyse the actual level of damage at the peak stress. To reduce the effect of recovery, the tested specimens were placed in the cool store at low temperature, 5°C while queuing for scanning. At this temperature, the asphalt activity was kept to the minimum. Furthermore, it was expected that failure in compression would minimise any minor distortion on the specimen when moving the specimen to the scanning room. This was to ensure that the exact picture of the microstructural changes caused by the loading was captured for analysis.

5.7 Indirect Tensile Fatigue Test

At the second stage of mechanical testing, the performance characteristics under repeated load were investigated with respect to increased content and size of rubber (fine and coarse rubber). Previous studies have shown that rubber particles contribute to the control of fatigue cracking in asphalt pavement due to their elastic behaviour (Esch 1982; Takallou et al., 1986; Takallou and Hicks 1988; Cao 2007).

5.7.1 Theoretical Methodology

In the Indirect Tensile Fatigue Test, a specific stress level is applied in a dynamic form (repeated controlled stress pulse) to estimate the fatigue potential of an asphalt mixture. The loading configuration of the test is illustrated in Figure 5.18. The repeated load acts along the vertical diameter of a cylindrical specimen. The vertical loading produces various magnitudes of vertical compressive stress and horizontal tensile stress along the diameter of

the specimen with the maximum at the centre of the specimen as shown in Figure 5.19 (Read 1996; Read and Whiteoak 2003).

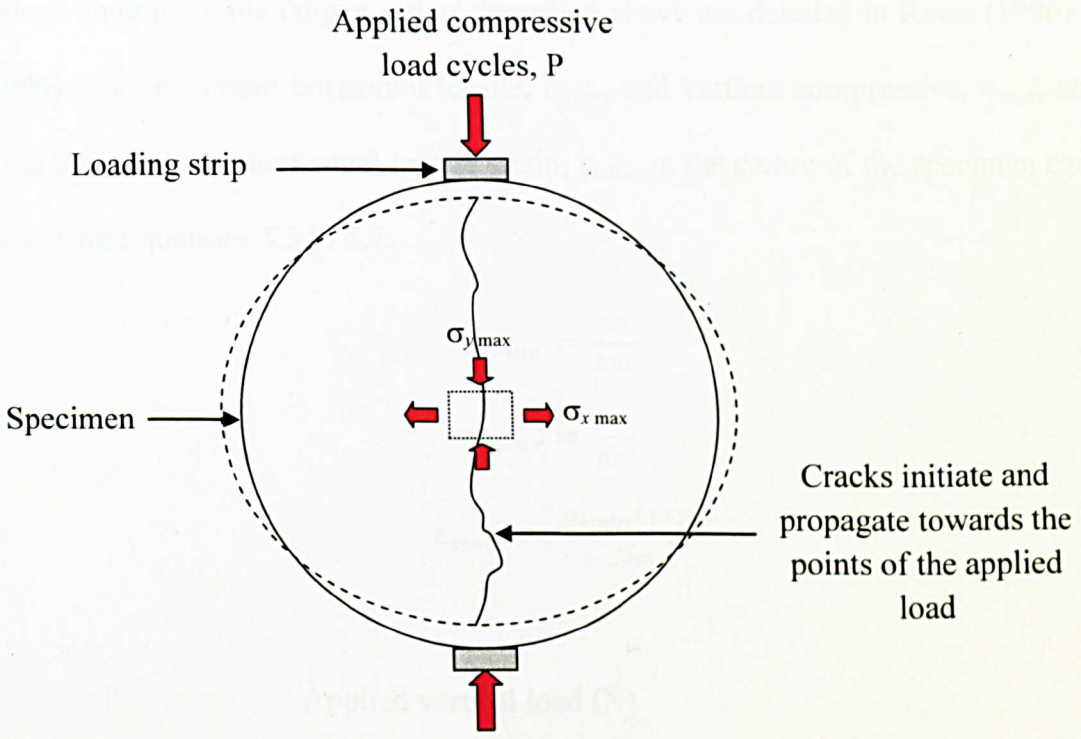

Figure 5.18 Illustration of the fatigue test method

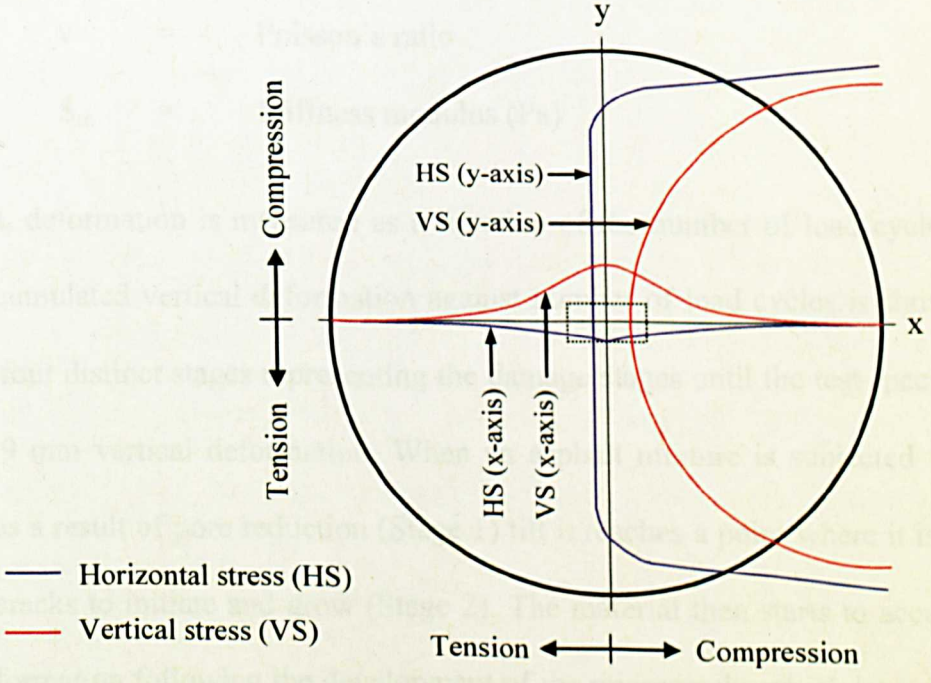

Figure 5.19 Stress distributions within the specimen under indirect tensile test

Basically the analysis of the indirect tensile test of an asphalt mixture concerns calculating the stress and strain for an element of the material located at the centre of a specimen. Assumptions underlying the fatigue test as described above are detailed in Rowe (1996) and Read (1996). The maximum horizontal tensile, σ_{xmax} and vertical compressive, σ_{ymax} stress (N/m^2) and the maximum horizontal tensile strain, ε_{xmax} at the centre of the specimen can be calculated using Equations 5.5 to 5.7.

$$\sigma_{xmax} = \frac{2P}{\pi dt} \quad 5.5$$

$$\sigma_{ymax} = \frac{6P}{\pi dt} \quad 5.6$$

$$\varepsilon_{xmax} = \frac{\sigma_{xmax}(1+3v)}{S_m} \quad 5.7$$

Where:

P	=	Applied vertical load (N)
d	=	Diameter of the specimen (m)
t	=	Thickness of the specimen (m)
v	=	Poisson's ratio
S_m	=	Stiffness modulus (Pa)

In this test, deformation is measured as a function of the number of load cycles. A typical plot of accumulated vertical deformation against number of load cycles is shown in Figure 5.20 with four distinct stages representing the damage stages until the test specimen reaches failure at 9 mm vertical deformation. When an asphalt mixture is subjected to loading, it densifies as a result of pore reduction (Stage 1) till it reaches a point where it is stiff enough for microcracks to initiate and grow (Stage 2). The material then starts to accumulate more plastic deformation following the development of the microcracks which later propagate and

coalesce under the tensile condition to form macro-cracks (Stage 3). The cracks growth proceeds to cause disintegration, consequently resulting in specimen breakdown or splitting as it reaches the failure stage (Stage 4).

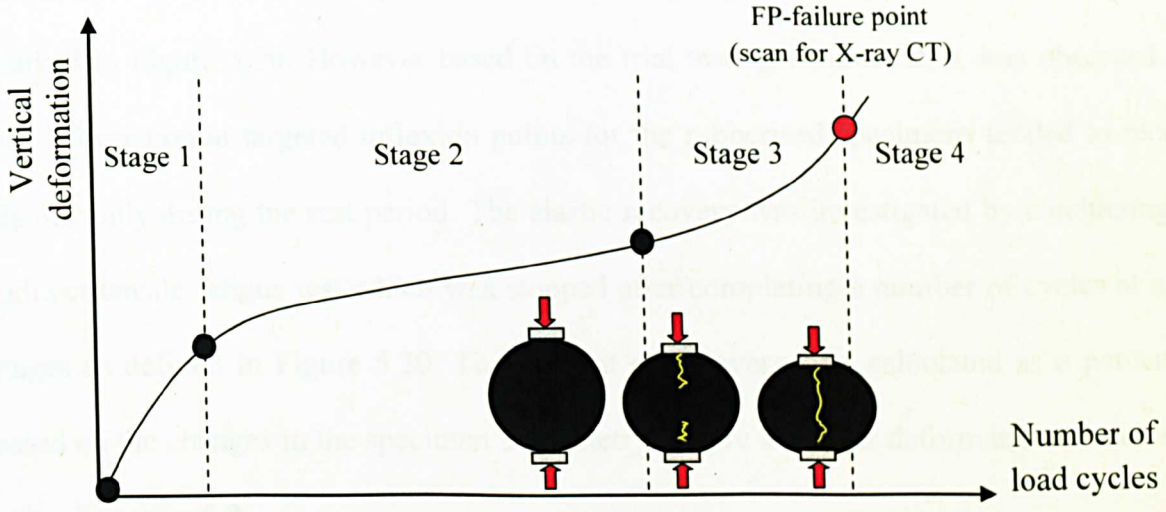

Figure 5.20 Typical graph plot from indirect tensile fatigue test

For the purpose of determining the appropriate stress levels and stages for damage characterisation (to avoid specimen breakage for the purpose of X-ray CT scanning), a preliminary study was carried out to address the following concerns:

1. Specimen Breakage

To determine the target stress level for this test a few specimens were tested at several stress levels between 100 kPa and 600 kPa. This is to ensure that the specimen did not break apart after reaching the failure stage which was required for X-ray CT scanning. As a result, low target stress levels (100, 200 and 300 kPa) were then selected for characterising the damage with the increased stress level.

2. Specimen Recovery Post Loading

Initially it was planned to analyse the microstructure properties at different magnitudes of load cycles until a vertical deformation of 9 mm was reached. The purpose of this was to assess the degree of the damage at a few critical stages, particularly at the inflexion points as marked in Figure 5.20. However based on the trial testing conducted, it was observed that the deformation at targeted inflexion points for the rubberised specimens tended to recover significantly during the rest period. The elastic recovery was investigated by conducting the indirect tensile fatigue test which was stopped after completing a number of cycles at a few stages as defined in Figure 5.20. The amount of recovery was calculated as a percentage based on the changes in the specimen's geometry, before and after deformation at each stage using Equation 5.8.

$$\%\ Recovery = \frac{\emptyset_{after} - \emptyset_{before}}{\emptyset_{before}} \times 100 \qquad 5.8$$

Recovery was assumed to have an effect on the actual size and shape of the cracks that were evident immediately after the loading was completed. In this investigation, the recovery was thought to have occurred whilst the specimens were queuing to be scanned and also during the scanning as it was conducted at the room temperature, requiring about 5 hours to complete the entire process of image capture (specimen with 40 mm thickness). As a result, the likelihood that the image analysis misinterpreted the actual degree of damage at the specified stages is thought to be potentially significant. Figure 5.21 compares the initial deformation and percent recovery for the different mixtures measured at a few load stages. From the figure, it can be concluded that, the specimen recovery for control mixture (with no rubber) decreases with increasing load cycles. Furthermore, higher percent recovery can be observed for rubberised mixtures (added with 2 and 3% rubber), of which the most

significant is recovery shown to have occurred as the specimen deformation reached the inflection point (marked as A and C) leading to the final stage, and decreasing to a minimum on approach to the failure point (marked as B and D) where major disintegration takes place. Therefore, the final failure stage with 9 mm vertical deformation, and being least affected by recovery was selected for damage characterisation.

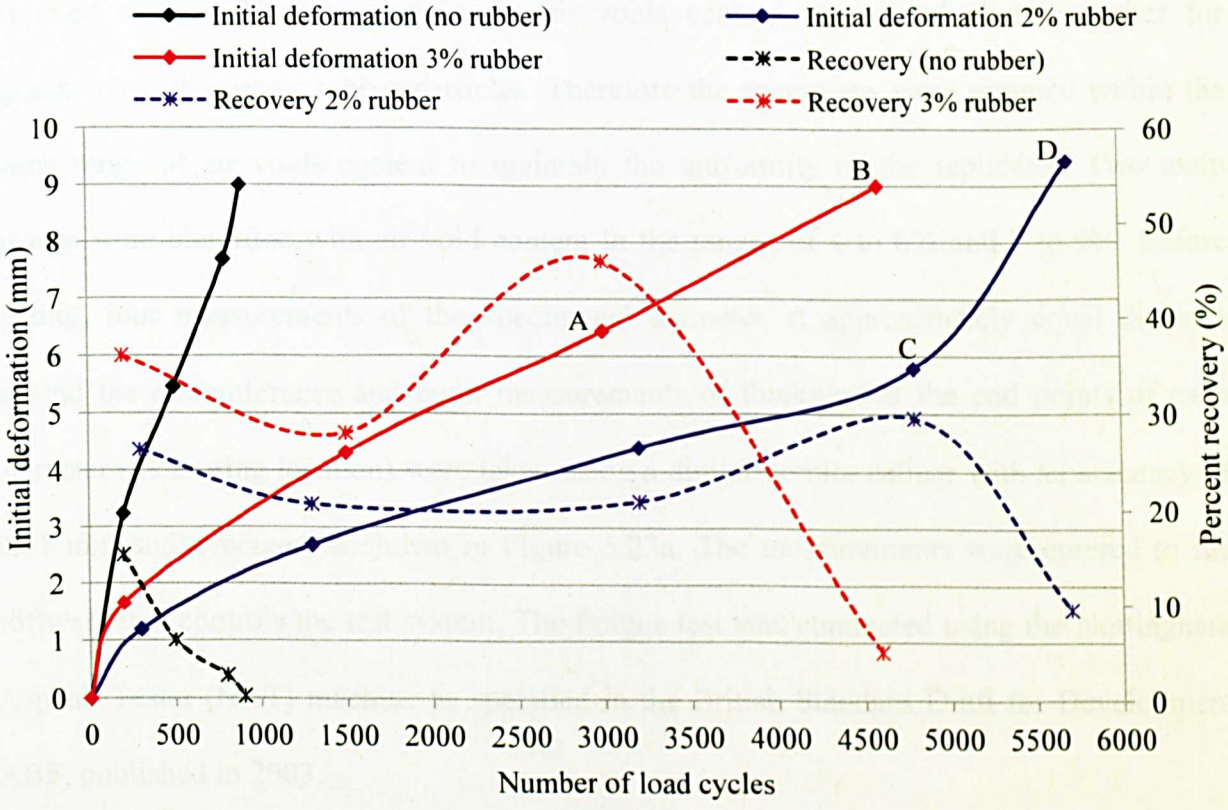

Figure 5.21 Relationship between the deformation and the recovery as a function of load cycles

5.7.2 Specimen Preparation and Testing Procedures

In this test, cylindrical specimens with 100±3 mm diameters and 40±5 mm thicknesses were used. The specimen were cut and trimmed from their actual size (of 100 mm diameter and

100 mm height). Figure 5.22 illustrates the sections cut from the compacted specimen. The final trimmed specimens ready to be tested are shown in Figure 5.23a. However it was noted that specimens to which rubber had been added proved difficult to cut, with some particles dislodging and/or breaking off the trimmed surface (Figure 5.23b). This is thought to have somehow affected the total air voids content of the final cut sections. The air voids content was determined using the sealed specimen method to avoid any fine particles falling off the trimmed surface. The variation in the air voids content was found slightly higher for specimens with coarser rubber particles. Therefore the specimens were grouped within the same range of air voids content to maintain the uniformity of the replicates. Two main groups were identified with air void content in the ranges of 4 to 6% and 7 to 9%. Before testing, four measurements of the specimens' diameter at approximately equal distance around the circumference and eight measurements of thickness at the end points of each diameter (measuring location) were taken using a digital vernier caliper with an accuracy of 0.01 mm and averaged as shown in Figure 5.23a. The measurements were entered to the software that controls the test system. The fatigue test was conducted using the Nottingham Asphalt Tester (NAT) machine as specified in the British Standard Draft for Development ABF, published in 2003.

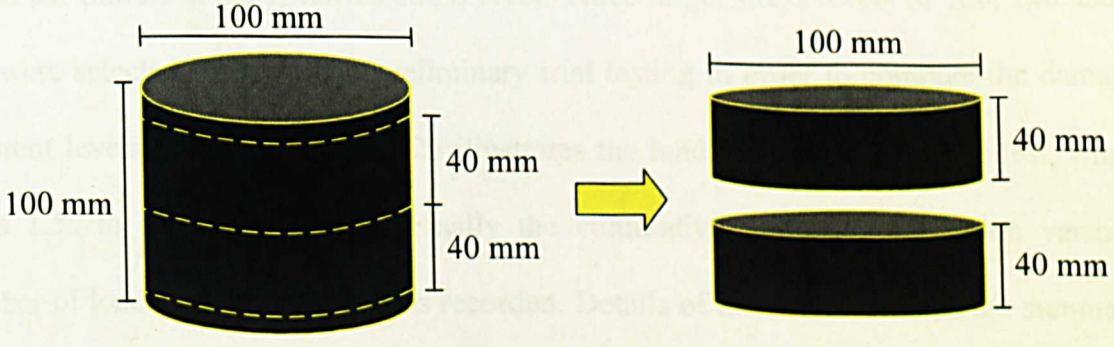

Figure 5.22 Illustration of the cut and trimmed sections on the compacted specimen

(a) (b)

Figure 5.23 Specimens for fatigue testing after cutting and trimming

The NAT testing system has software and the hardware elements to facilitate its function. The hardware comprises a load cell, testing frame, linear variable differential transformers (LVDT's) and data logging equipment (Figure 5.24). For the microstructure analysis, the specimens were X-rayed before and after the testing. Firstly, the specimens and the machine's cabinet were conditioned at the test temperature, 20±1°C. The specimens were then positioned perpendicularly between the top and bottom loading strips. The LVDT's were mounted on the testing frame and adjusted to allow for linear measurement over a range of at least 9 mm. A repeated controlled stress pulse was then applied at a rate of 40 pulses per minute at the specified stress level. Three target stress levels of 100, 200 and 300 kPa were selected based on the preliminary trial testing in order to compare the damage at different levels of stress. Figure 5.25 illustrates the load pulse applied in the test, where it takes 1.5s to complete 1 pulse. Finally the cumulative vertical deformation versus the number of load cycles to failure was recorded. Details of the test conditions are summarised in Table 5.8.

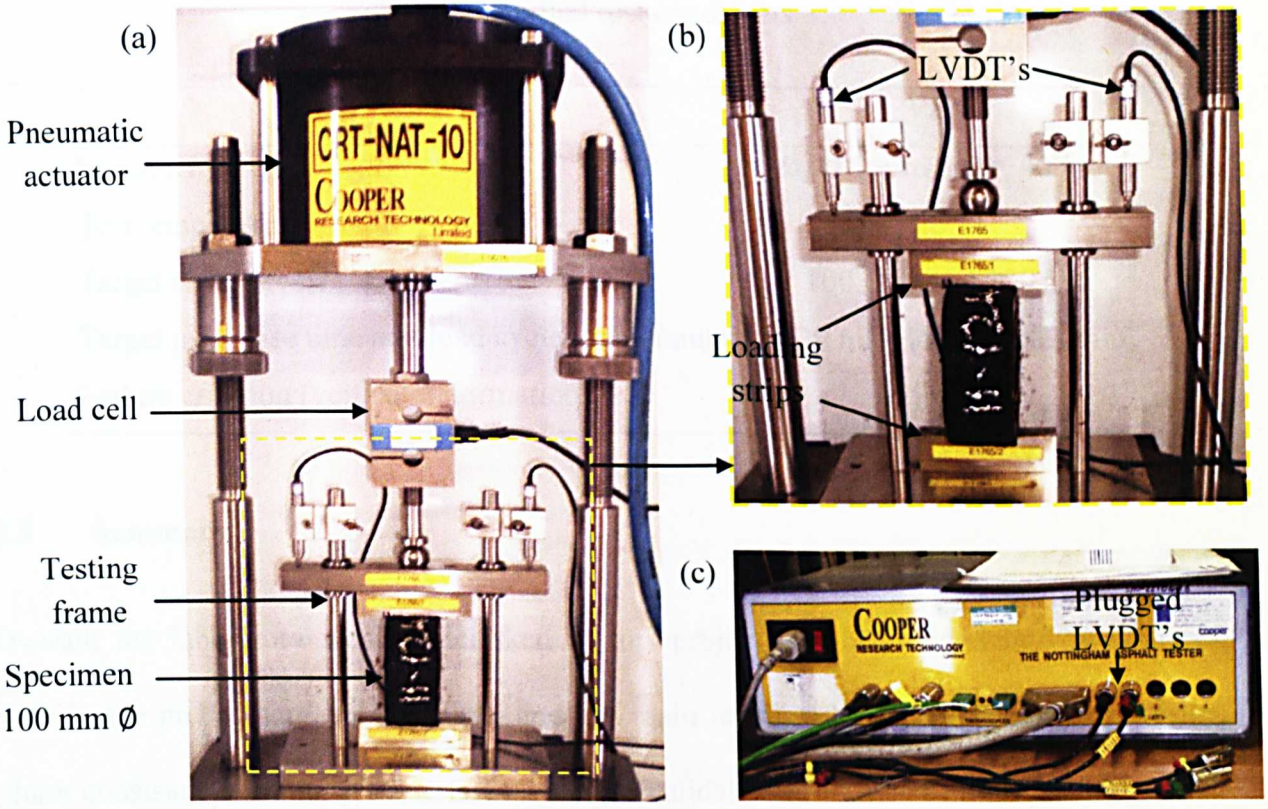

Figure 5.24 (a) Nottingham asphalt tester, (b) testing frame and (c) data logging equipment

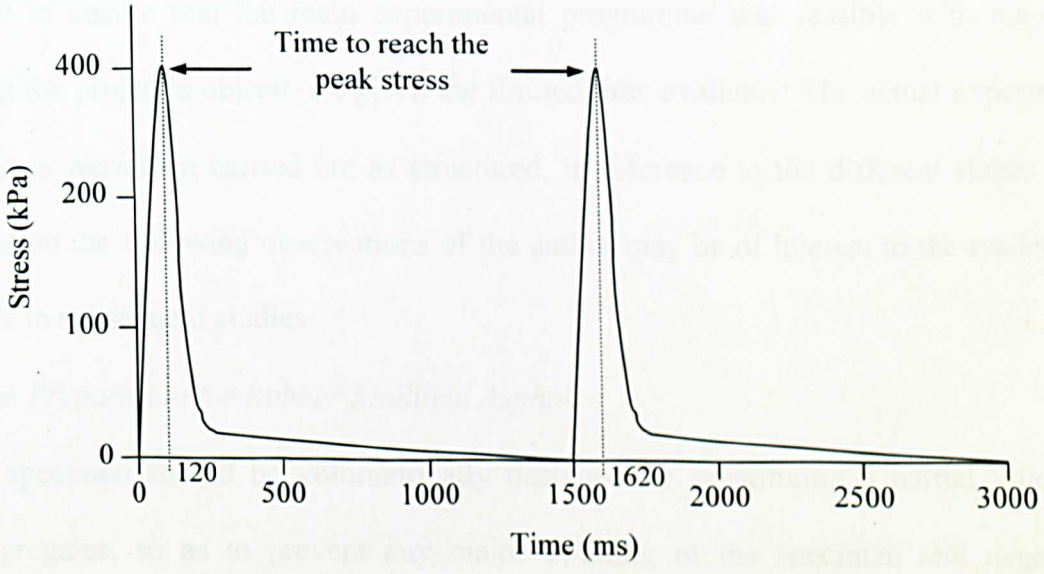

Figure 5.25 Graphical illustration of the load pulse (Read, 1996)

Table 5.8 Detailed test conditions

Condition	Value
Specimen size	Ø, 100 mm and *t*, 40 mm
Test temperature	20°C
Target stress levels	100, 200 and 300 kPa
Target pulse rise time and load cycles per minute	120 ms and 40 cycles/min
Failure criterion (vertical deformation)	9 mm

5.8 Summary

Overall, the laboratory work undertaken in this project can be divided into two phases, namely the preliminary testing phase and the main testing phase. The preliminary testing phase consisted of initial pilot tests designed to validate and to assist in the planning of the main experimental programme. The pilot tests were particularly important with respect to material selection and determining subsequent testing parameters. Furthermore they were important to ensure that the main experimental programme was feasible with respect to achieving the project's objectives, given the limited time available. The actual experimental programmes were then carried out as structured. In reference to the different stages of the investigation the following observations of the author may be of interest to the reader or of relevance to subsequent studies:

Specimen Preparation for Rubber Modified Asphalt

1. A specimen should be volumetrically designed by substituting a partial volume of aggregates, so as to prevent any major swelling of the specimen and negate any resistance to compaction.
2. It was found that, between identically designed or prepared replicates of rubberised mixture specimens there were inconsistent air voids content compared to those of the

control mixture. The rubberised mixture specimens also had difficulty in achieving low air voids content. Therefore to achieve the target air voids content, higher bitumen content was added with the increased rubber content.

X-ray CT Scanning and Mechanical Testing

1. It was found that, the addition of rubber increased the specimen's ability to recover elastically in comparison to the control mixture. The specimen showed partial elastic recovery of strain during the rest period after the deformation. The recovery was found to be more significant as the content of the rubber particles increased.
2. With regards to the removal of the specimens from their original position to facilitate scanning at a different location, there were concerns pertaining to the physical integrity of the specimens. There may be an issue about the possibility of minor distortion during movement of the specimen. It would have been much better, had the testing equipment been attached to the CT scanner to facilitate direct monitoring of the specimen's behaviour at every critical stage during testing. It is also believed that this would reduce inaccuracy in measurements arising from specimen recovery after the specimen has been unloaded. Measurements following the aforementioned recommendation may then be taken to represent the 'true' damage of the tested specimens between initial and the final failure stage. However there is a concern raised from the fact that minor recovery would still occur at a time when the test is stopped temporarily while completing the scanning for several hours. In addition, the ability to fit the different testing facilities together with the X-ray CT machine is also a factor that should be taken into consideration as further adjustment to the operating system might be needed.

6.0 ASSESSING THE EFFECT OF RUBBER ADDITION ON THE AIR VOIDS PROPERTIES OF ASPHALT MIXTURES

6.1 Introduction

In this chapter the results of microstructure properties, as analysed from X-ray CT images, of compacted rubberised specimens produced using different design variables are compared to an unmodified (control) mixture. The internal structure of the specimens are herein characterised in terms of their rubber distributions and air voids properties, ascertained vertically and radially over each specimen's height. The rubber and air voids properties were determined using techniques as detailed earlier in Chapter 4, where an evaluation of the effect of rubber addition on the air voids properties (including the voids content, voids size, voids number, voids distribution and voids shape) was conducted. In this chapter, however, the specimen's air voids and rubber distributions are analysed for possible correlations between them by mapping their locations relative to each other within the asphalt mixture. This was done to ascertain if there was any association between the rubber particles and the formation of air voids in their vicinity. Furthermore the outcome was expected to clarify the significance (if any) of air voids and rubber distributions within rubberised mixtures, which could be beneficial for characterising damaged rubberised specimens (Chapter 7).

6.2 Determination of Rubber Distribution

Rubber distributions were determined for specimens containing different amounts and sizes of rubber particles. Figure 6.1 shows the rubber distributions representing four types of rubberised mixtures containing 2% fine rubber (2%F), 3% fine rubber (3%F), 2% coarse rubber (2%C) and 3% coarse rubber (3%C). Each curve on the plot represents rubber content values averaged from 4 to 5 specimens, each of 100 mm height and 100 mm diameter. The rubber distributions were determined along the height of the specimens from the bottom to the top of the specimen (starting from 1 mm to 100 mm). In general, all the rubberised mixtures had similar distributions, in that the rubber particles were evenly distributed with small variations along the specimens' heights. The rubber distributions within the specimens were considered uniform as the rubber content analysed at each level was close to the rubber content added to the mixture (2% and 3%). This is evidenced by the standard deviation (σ) values, shown in Table 6.1, and calculated to measure the variability of the rubber distribution along the height of the specimens. Table 6.1 shows that all the mixtures had low standard deviation values, implying that the rubber distributions were vertically uniform throughout the specimens.

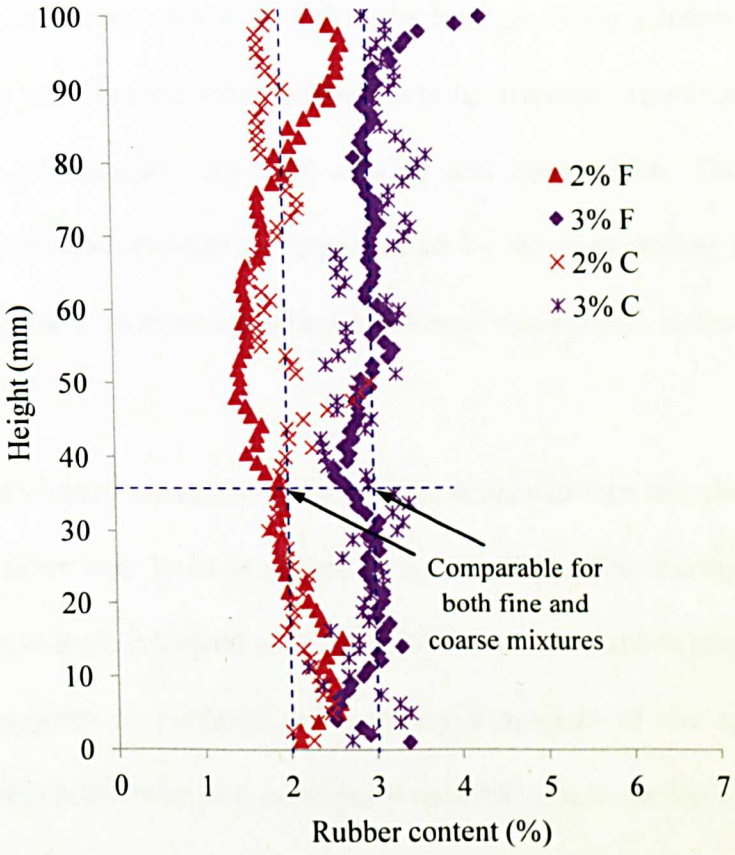

Figure 6.1 Rubber distributions for specimens with different rubber amounts and sizes

Table 6.1 Mean and standard deviation for the rubber distribution

Rubberised Mixture	2% F	3% F	2% C	3% C
Rubber content (%)	2	3	2	3
Standard deviation, σ	0.40	0.27	0.28	0.34

Figure 6.2 shows a group of X-ray images representing the different specimens' cross sections, each captured at a height of approximately 35 mm. This height was considered adequate to facilitate the necessary comparisons between the different rubberised specimens. In the images, the rubber particles can be identified by the dark grey coloured regions and the air voids are highlighted in red. From the images, the fine rubber particles appear to be well distributed within the mastic and around the aggregates, while the coarse rubber

particles of the same content are clustered within the mixture. This is believed to be due to the comparatively easy mobility the small rubber particles have in comparison to the coarse rubber particles during laboratory specimen mixing and compaction. The coarse rubber particles within the mastic are thought to be prevented by the surrounding aggregates from freely separating from their clusters in spite of external mechanical interventions such as mixing and compaction.

Observations of the laboratory compacted specimens, indicated that the clusters formed by the coarse rubber particles may have produced a 'cushioning' effect during the specimens' compaction. This would have occurred as a result of the coarse rubber particles effectively acting as elastic aggregates to enhance the recovery properties of the specimens during compaction. Due to this behaviour, the mixtures would have been easily compressed under loading thereby causing the specimens containing coarse rubber to require a lower compaction effort (less number of gyrations) to achieve their target densities in comparison to the fine rubber mixtures which required a higher number of gyrations. If the mixtures had been designed without provision for gaps in the aggregate gradation, the compressed rubber clusters would have 'pushed' the surrounding mastic and aggregates as they recovered their original shape. This would have resulted in specimen density inconsistencies when the specimens were extruded from their moulds as the specimens were no longer confined by the mould wall. Moreover the absence of gradation gaps would have resulted in the rubber particles resisting the compaction as in the case of a dense bituminous rubberised mixture. Rahman (2004) applied extra compaction effort to minimise the rebounding effect of rubber within a dense graded mixture.

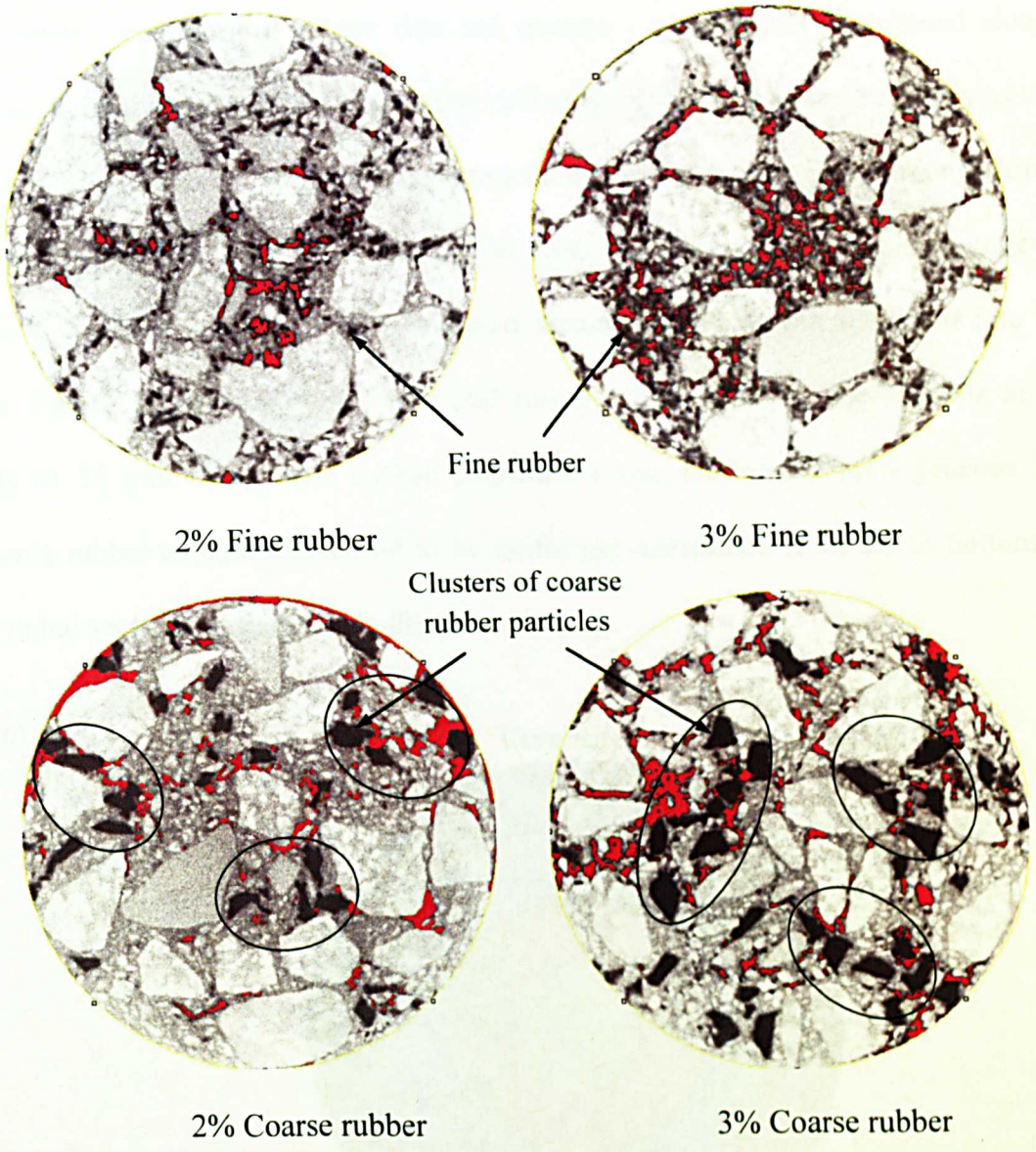

Figure 6.2 X-ray images of CRM mixtures specimens' cross section with fine and coarse rubber at a height of approximately 35 mm

Fortunately, in this study, both the fine and coarse rubber filled the gaps provided in the aggregate gradation very well and the presence of these gaps minimised the potential for specimen density inconsistencies between replicates. Furthermore, the specimens rebounded less following compression because they were designed using the principle of volumetric substitution wherein the volume of aggregates removed was equal to the volume of rubber introduced, for any given mixture. From Figures 6.1 and 6.2 it is evident that, even though

rubber content (regardless of rubber size and quantity) is uniformly distributed along the specimens' height, the majority of the coarse rubber particles are clustered radially as shown in Figure 6.2. In order to validate the homogeneity of the rubber distributions along the specimens' height, assessments of the rubber distributions were additionally undertaken using core and ring analysis, which involved virtual cutting of the specimen into radial sections. Figure 6.3 illustrates the core and ring sections used for the analysis at radial intervals of 25 mm. A specific rubber distribution was considered homogeneous if that specimen's rubber content was found to be uniformly distributed from top to bottom when the cut radial sections were individually examined.

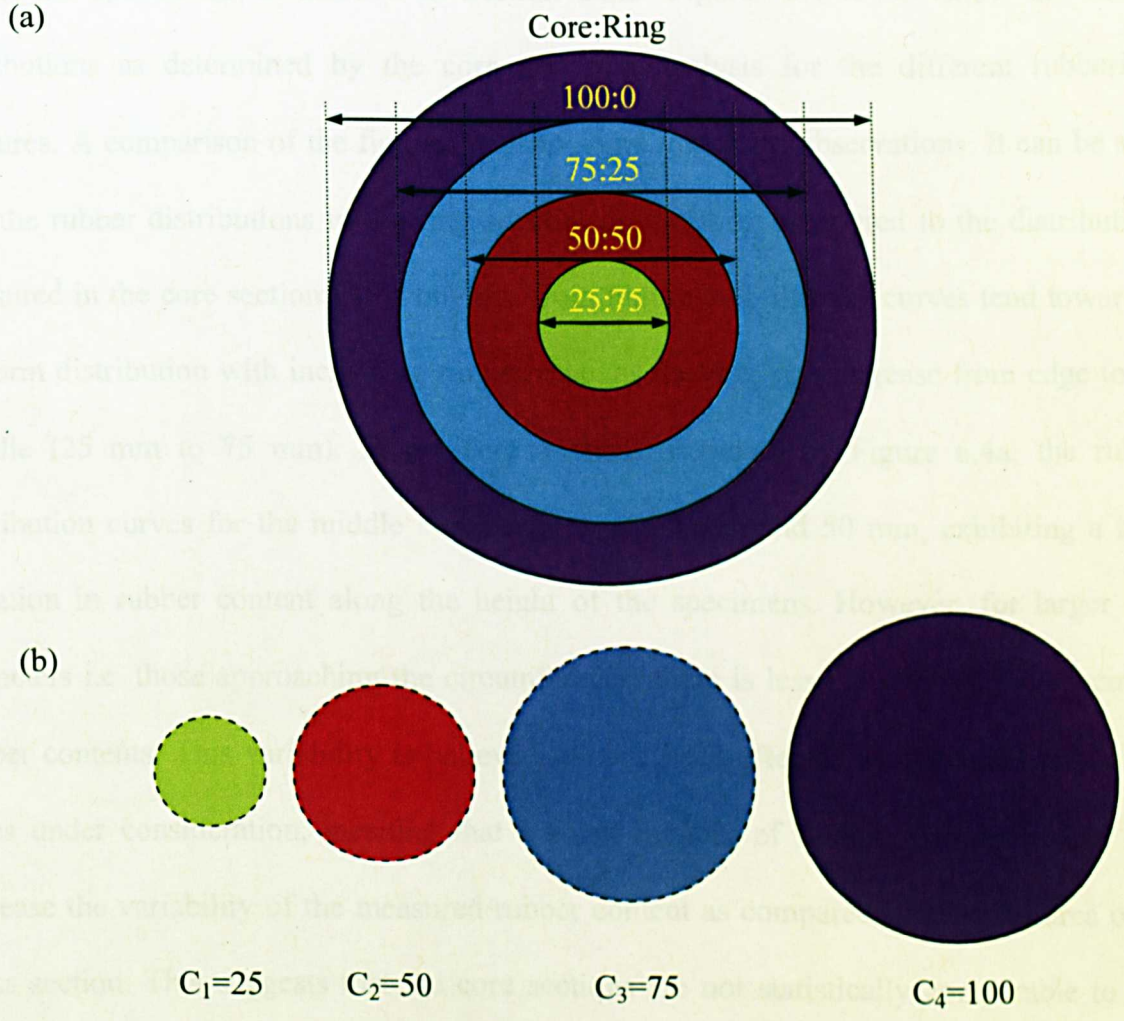

Figure 6.3 continues below

(c)

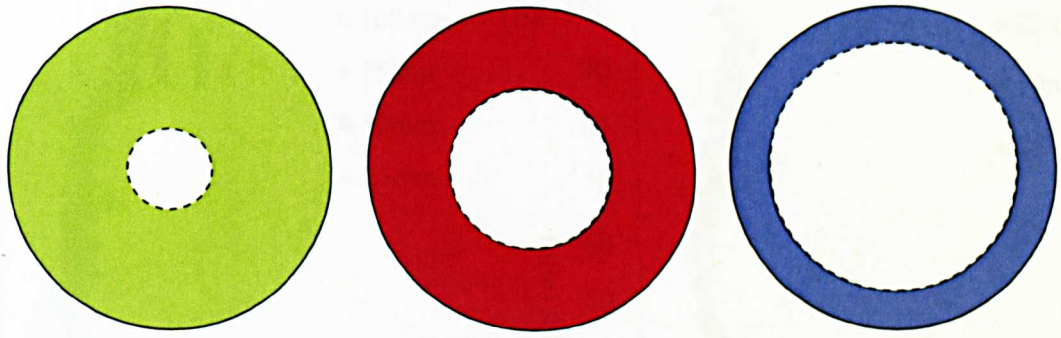

R_1= 75 R_2= 50 R_3= 25

Figure 6.3 Radial sections for core and ring analysis (a) plan view, (b) core and (c) ring sections

The same radial sections were used to analyse the homogeneity of the air voids distributions for all the specimens, as detailed in Section 6.3.2. Figures 6.4 to 6.7 show the rubber distributions as determined by the core and ring analysis for the different rubberised mixtures. A comparison of the figures leads to some important observations. It can be seen that the rubber distributions in the ring sections are uniform compared to the distributions measured in the core sections. It is obvious from Figure 6.4b that the curves tend towards a uniform distribution with increasing ring size i.e. as the ring size increase from edge to the middle (25 mm to 75 mm). In the core analysis, depicted by Figure 6.4a, the rubber distribution curves for the middle core sections of 25 mm and 50 mm, exhibiting a large variation in rubber content along the height of the specimens. However, for larger core diameters i.e. those approaching the circumference, there is less variation in the specimens rubber contents. This variability is believed to have been affected by the small area of the cores under consideration, meaning that a small number of rubber particles would have increase the variability of the measured rubber content as compared to the total area of the cross section. This suggests that the core sections are not statistically comparable to each other.

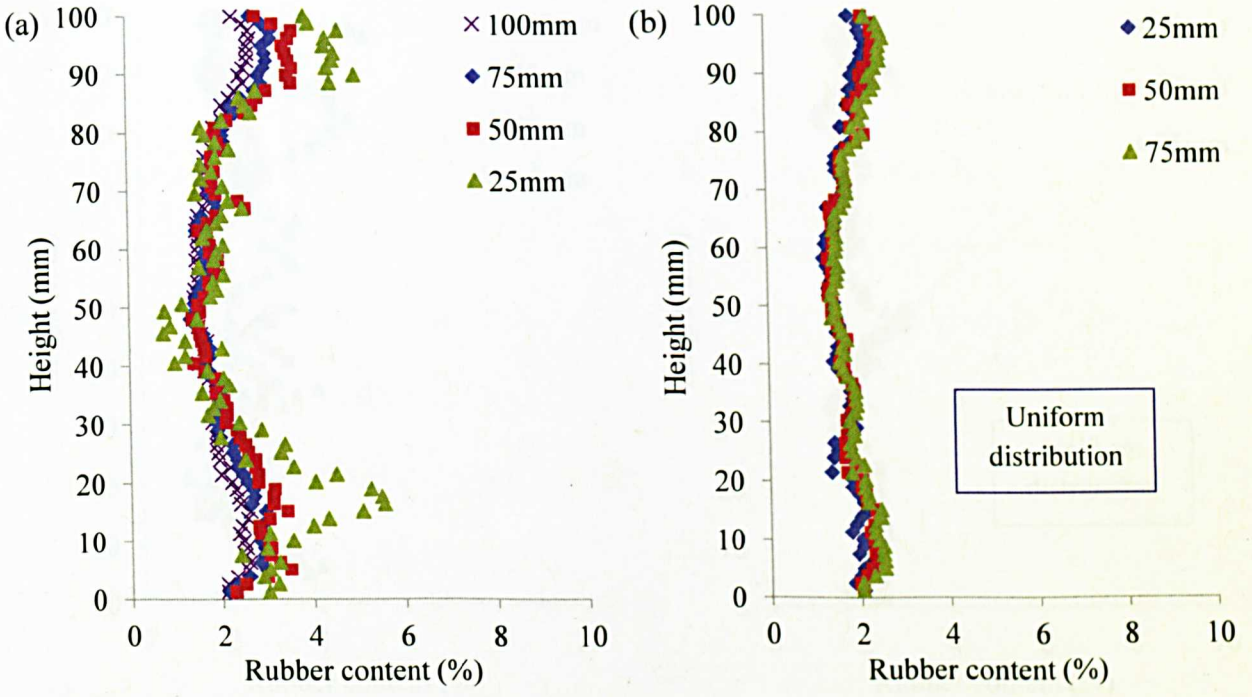

Figure 6.4 Rubber distributions in radial direction for (a) core, C (b) ring, R for specimen with 2% fine rubber (2% F)

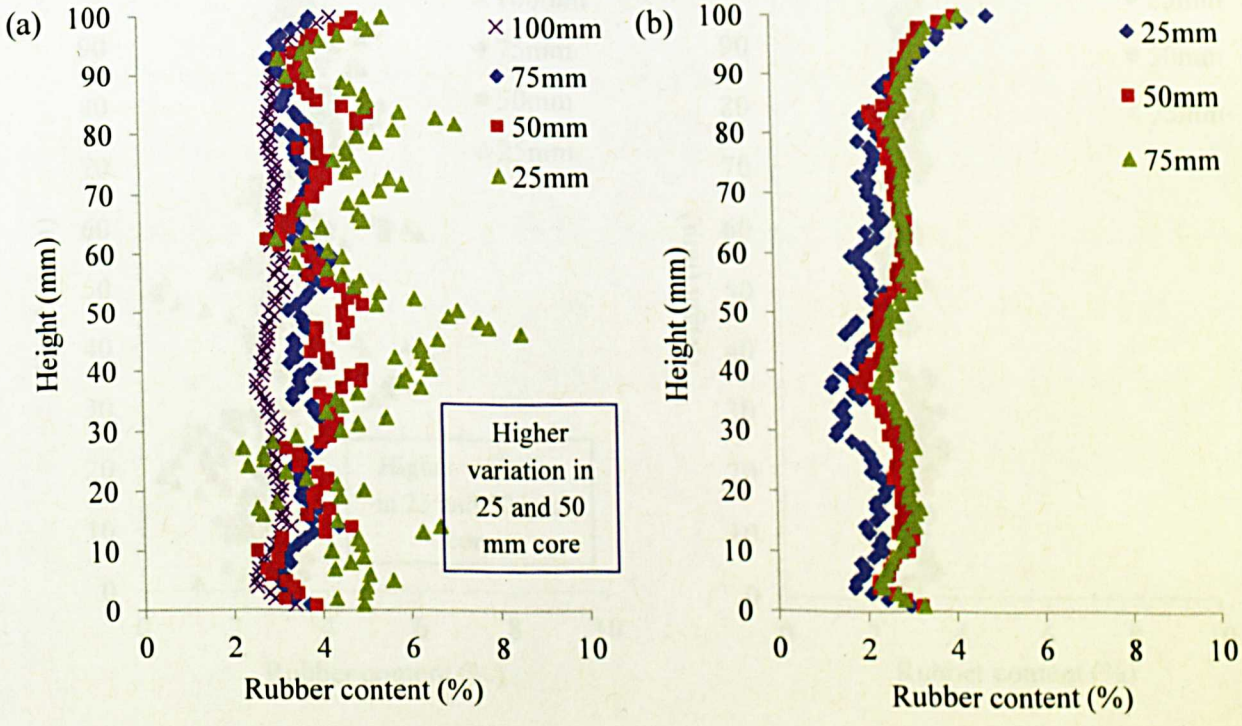

Figure 6.5 Rubber distributions in radial direction for (a) core, C (b) ring, R for specimen with 3% fine rubber (3% F)

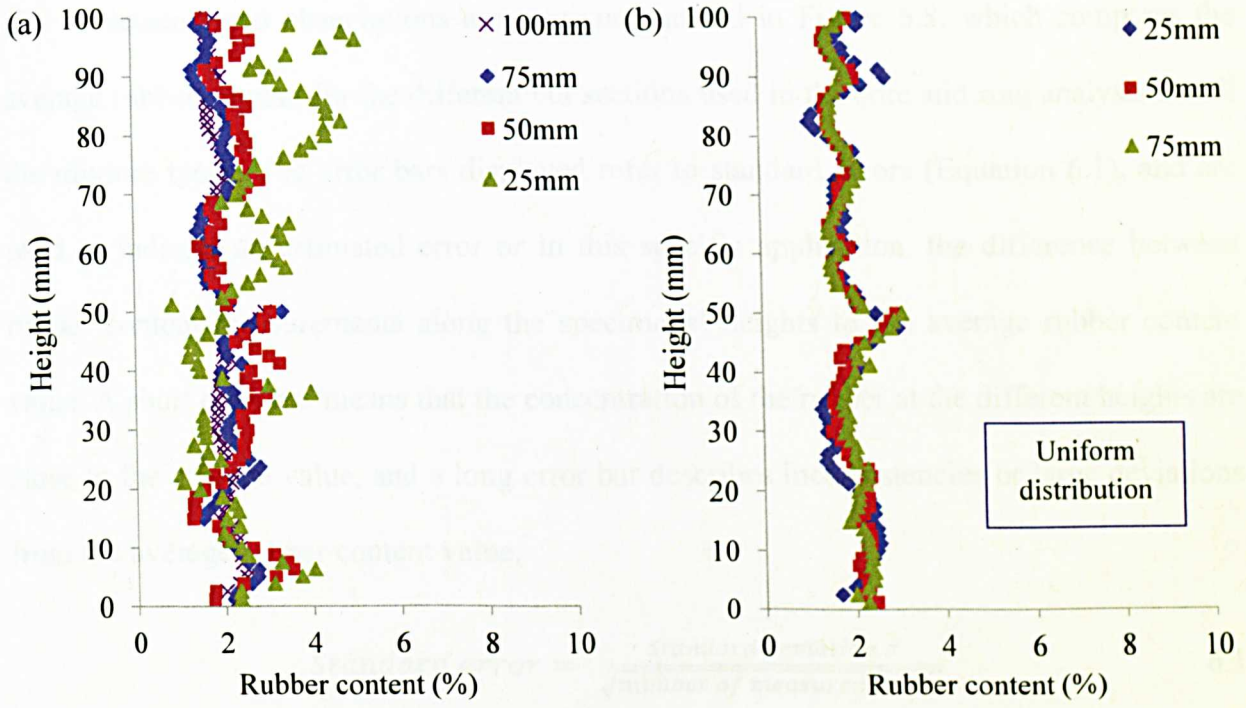

Figure 6.6 Rubber distributions in radial direction for (a) core, C (b) ring, R for specimen with 2% coarse rubber (2% C)

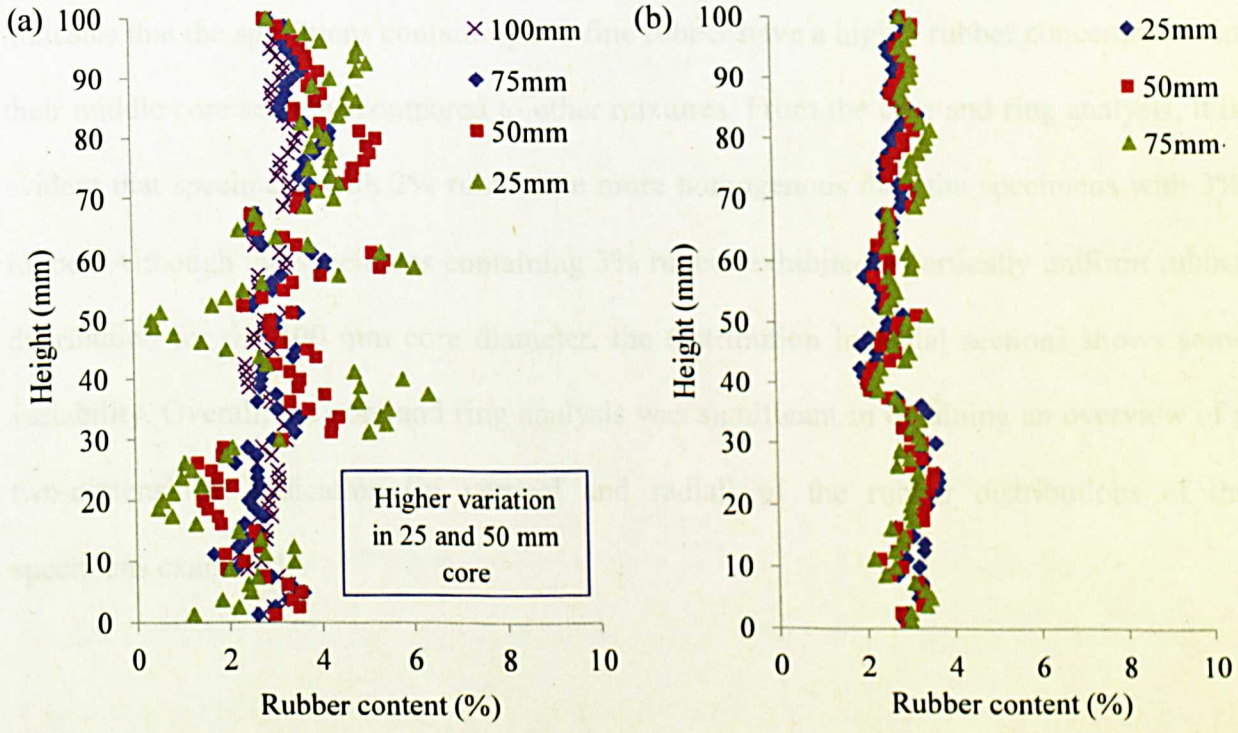

Figure 6.7 Rubber distributions in radial direction for (a) core, C (b) ring, R for specimen with 3% coarse rubber (3% C)

The aforementioned observations are also summarised in Figure 6.8, which compares the average rubber content for the different cut sections used in the core and ring analysis for all the mixture types. The error bars displayed refer to standard errors (Equation 6.1), and are used to indicate an estimated error or in this specific application, the difference between rubber content measurements along the specimens' heights to the average rubber content value. A short error bar means that the concentration of the rubber at the different heights are close to the average value, and a long error bar describes inconsistencies or large deviations from the average rubber content value.

$$Standard\ error = \frac{Standard\ deviation, \sigma}{\sqrt{number\ of\ measurements, n}} \qquad 6.1$$

Figure 6.8a shows that the middle cores exhibit high variation in the rubber content along the specimens' height, particularly for the specimens containing 3% rubber. The analysis also indicates that the specimens containing 3% fine rubber have a higher rubber concentration in their middle core sections compared to other mixtures. From the core and ring analysis, it is evident that specimens with 2% rubber are more homogenous than the specimens with 3% rubber. Although the specimens containing 3% rubber exhibited a vertically uniform rubber distribution for the 100 mm core diameter, the distribution in radial sections shows some variability. Overall, the core and ring analysis was significant in obtaining an overview of a two-dimensional indication (in vertical and radial) of the rubber distributions of the specimens examined.

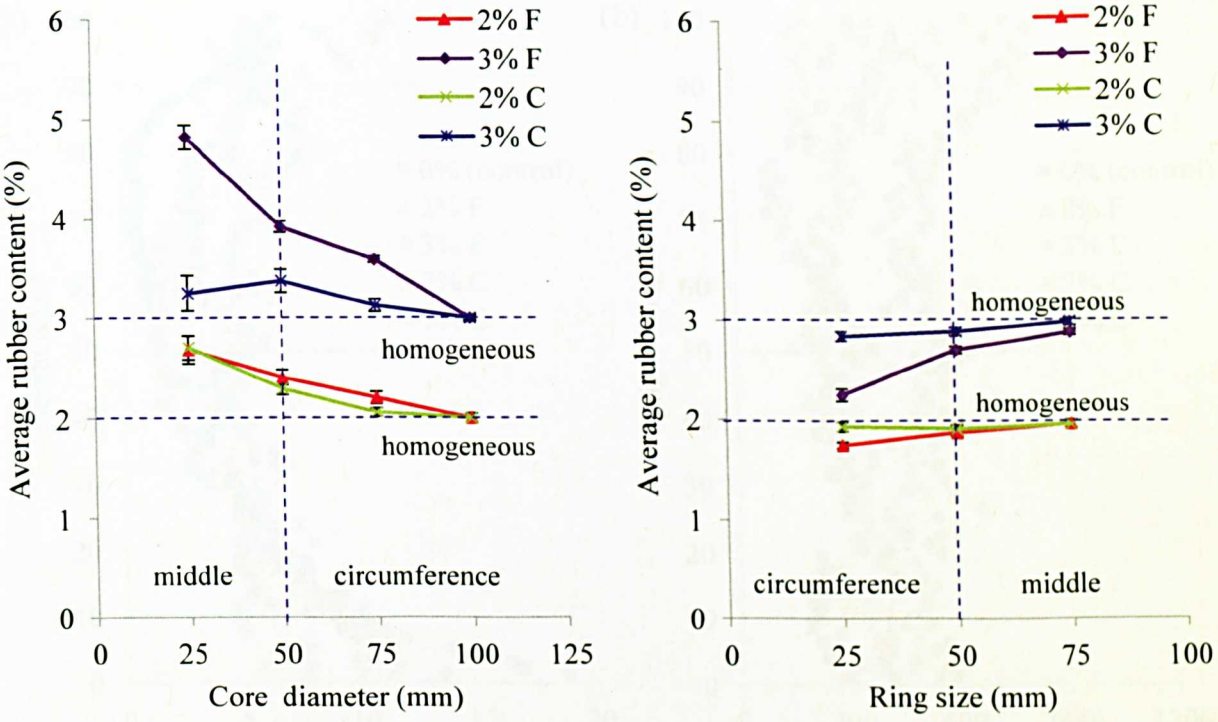

Figure 6.8 Average rubber content (distributions in radial direction) for (a) core, C (b) ring, R for different rubberised specimens

6.3 Characterisation of Air Voids Properties

6.3.1 Air Voids Content, Number of Voids and Average Voids Size

Air voids characterisation of rubberised asphalt mixtures was undertaken and compared to the air voids properties of a control specimen of the same mixture type (HRA 60/20). In Figure 6.9, the distributions of the air voids properties, namely air voids content, number of voids and average voids size are presented for the different mixtures considered in this study using laboratory compacted specimens of 100 mm in diameter and height for the different mixtures. Table 6.2 presents the average values of the air voids properties and the standard deviations of the air voids content as an indication of the variability in the distribution. The plotted results represent measurements taken from 4 to 5 specimen replicates having a total air voids content (determined in the laboratory) of 4% to 6%.

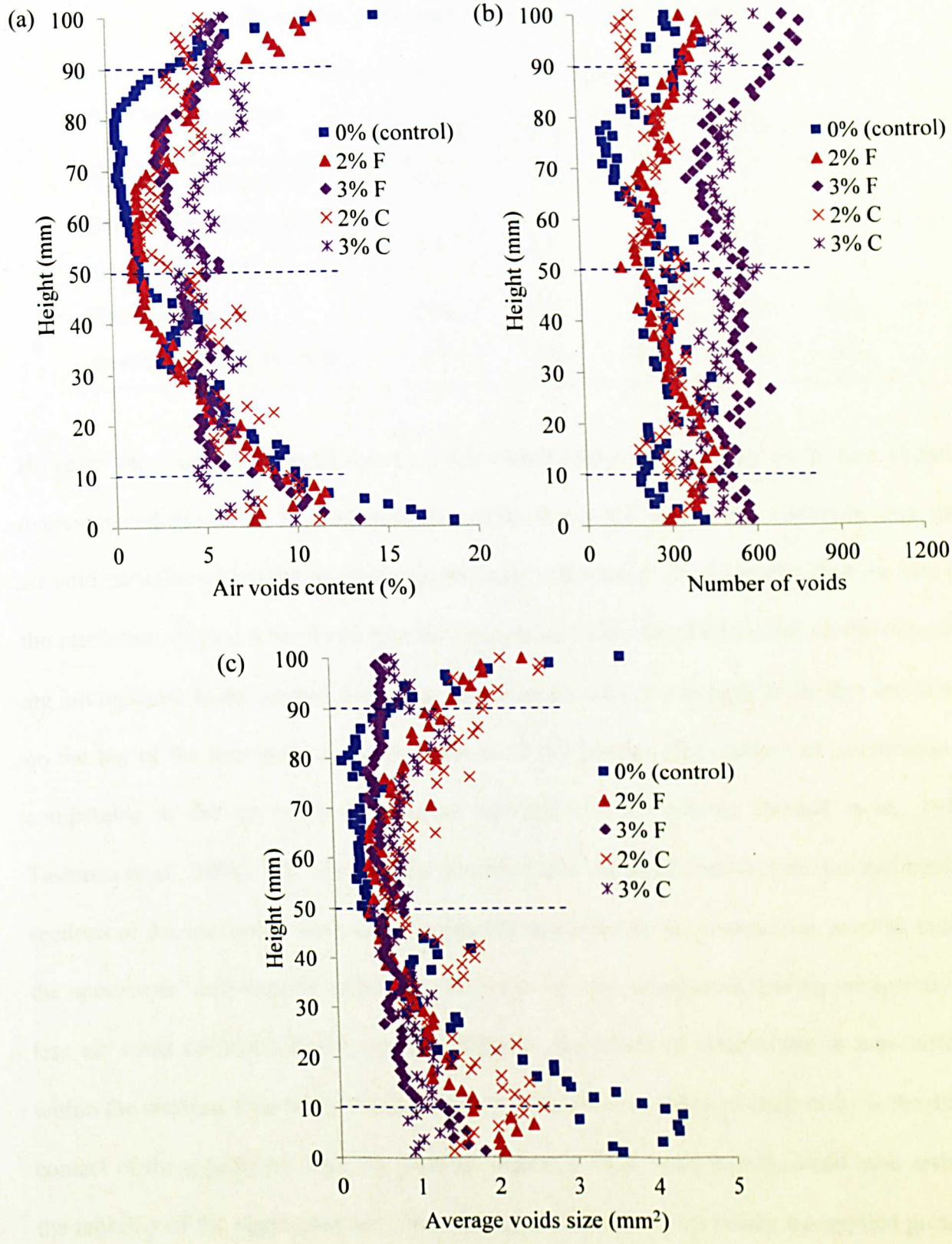

Figure 6.9 Distribution of (a) air voids content, (b) number of voids and (c) average voids size in the control and rubber modified specimens

Table 6.2 Air voids properties for different mixtures

Air voids properties	Mixtures				
	Control	2% F	3% F	2% C	3% C
Air voids content (%)	4.5	4.8	5.2	5	5.6
Standard deviation of the air voids content, σ	2.8	3.1	2.1	2.2	1.2
Number of voids	270	314	550	282	486
Average voids size (mm^2)	1.3	1.1	0.7	1.4	0.9

However the total of the extracted air voids content from images may have been slightly overestimated due to the limited resolution of the X-ray CT machine in capturing very fine air void particles within the specimen particularly when their size is smaller than the size of the resolution. Figure 6.9a shows that the vertical air voids distributions for all the mixtures are not uniform. In the control specimen, the air voids content was high in the first few slices on the top of the specimen and even more so at the bottom. This pattern of distribution is comparable to the air voids distribution reported in other studies (Masad et al., 1999; Tashman et al., 2001). The observation described also suggests that both the top and bottom sections of the specimens were not significantly impacted by the compaction process, unlike the specimens' mid-regions which are shown to be over-compacted, having comparatively less air voids contents. Based on this evidence, the effect of compaction is non-uniform within the mixture. One of the reasons that can contribute to this non-uniformity is the direct contact of the aggregates with the gyratory plates (at both ends) which would have resisted the mobility of the aggregates and fines during compaction. As a result, the applied pressure is not transmitted uniformly through the compacted specimen resulting in the bottom section and a few X-ray slices at the top being less compacted than the other regions. Furthermore,

Muraya (2007), Thyagarajan et al. (2009) and Vincent et al. (2010) concluded that, a specimen's dimensions also determines the amount of compaction energy transmitted through it. According to them, different specimen dimensions can lead to variations in the compaction energy transmitted through a specimen, resulting in different air voids distribution patterns. It is evident from Figure 6.9a, that the specimen containing 2% rubber exhibits a similar pattern of air voids distribution to the unmodified specimen, in that its middle section is more compacted than the other sections. When the rubber content was increased to 3%, the air voids distribution became more uniform i.e. there was less variation in the air voids content along the specimen height as indicated by the smaller standard deviation value (refer Table 6.2). Figure 6.10 illustrates the energy distribution during compaction (inspired by Thyagarajan et al., 2009), for the control and rubberised mixtures. As a gap graded mixture, the specimen's gradation utilised in this study contained a small percentage of mid-size range which is believed to have made the specimen prone to minor segregation between the coarse and fine aggregates during placement. It is thought that the coarse aggregates settled downwards and interlocked to form a stone skeleton at the bottom of the mixture, leaving the majority of the fines in the middle and top region. This is supported by Hassan et al. (2012), in whose study a larger percentage of coarse aggregate was found at the bottom than at the top section of the specimen for the same mixture type (HRA 60/20). This is simply explained for the control specimen (refer Figure 6.10a), where the aggregates' 'stone to stone' contacts develop rigid contacts amongst the aggregates. This phenomenon is believed to limit the movement of the aggregates and fines, thereby increasing compaction resistance or transmission of compaction energy to certain areas within the specimen. This is thought to occur at the bottom section of the specimen where

more coarse aggregates are prevalent. The lack of mobility of the aggregates in the bottom section prevents the fines from occupying the spaces between the coarse aggregate particles.

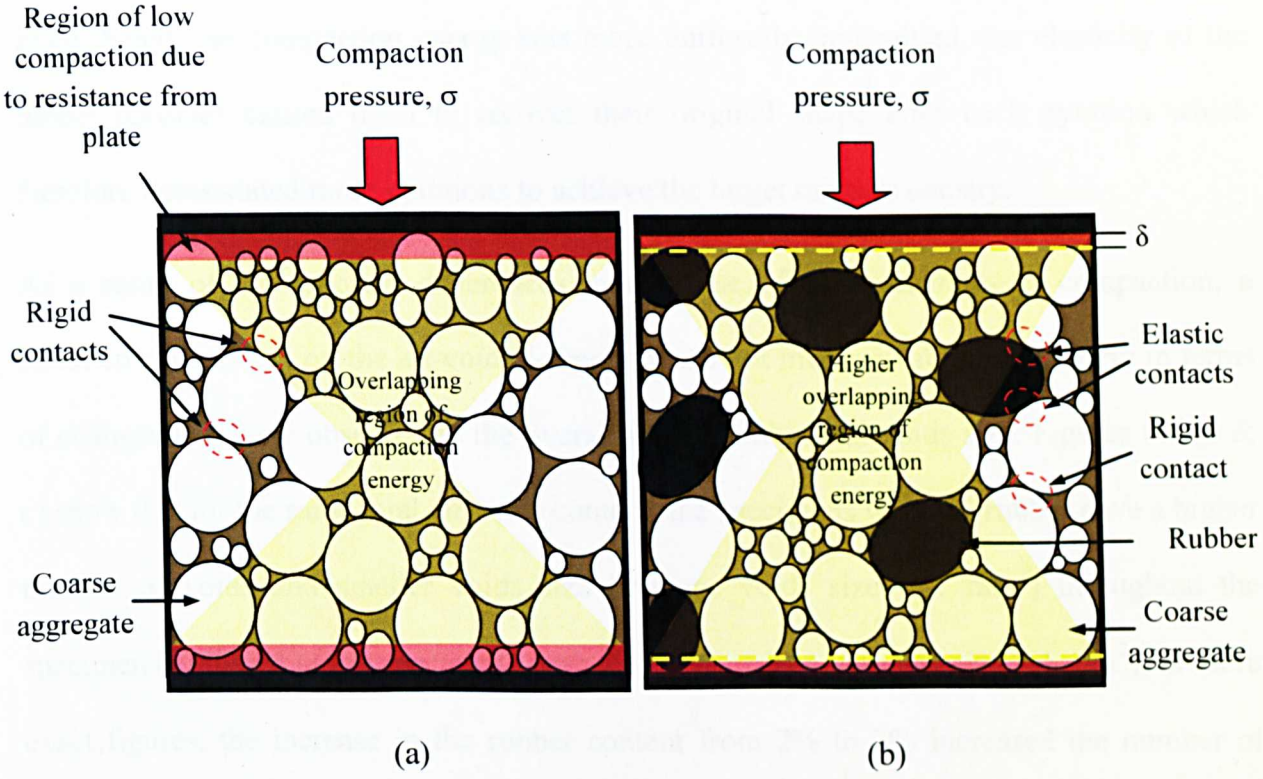

Figure 6.10 Compaction energy distributions within (a) control (b) rubberised mixture (inspired by Thyagarajan et al., 2009)

For the rubberised mixture (refer Figure 6.10b), the rubber particles provide sufficient flexibility to the mixture, causing it to deform by an amount, δ which causes the compaction energy to be transmitted to different levels or areas within the specimen. The rubber particles act as elastic aggregates, whereby they elastically deform during compaction and provide elastic contacts within the mixture. This permits the compaction energy to distribute along the specimen height and facilitates the uniform compaction of the specimen without the compaction effort being concentrated in one area. Such findings offer plausible explanations for the differences in the air voids distributions between specimens and the effect of adding

rubber to the mixture. Despite the aforementioned findings, the author found that a higher number of gyrations were needed to complete the compaction for the rubberised mixture compared to the control mixture in order to counter the elasticity of the rubber particles. Even though the compaction energy was more uniformly transmitted, the elasticity of the rubber particles caused them to recover their original shape after each gyration which therefore necessitated more gyrations to achieve the target mixture density.

As a result of the reported differences in response of the specimens to compaction, a commensurate effect on the air voids formation was not inconceivable, particularly in terms of changes that were observed in the overall voids number and voids size. Figures 6.9 (b & c) show that for the same total air voids content, the specimens with 3% rubber have a higher number of voids and smaller voids size (average voids size < 1 mm^2) throughout the specimen compared to the specimens with 2% rubber (average voids size > 1 mm^2). In more exact figures, the increase in the rubber content from 2% to 3% increased the number of voids by approximately 70%. Comparing the fine and coarse rubber specimens, it is evident that the specimen with fine rubber results in smaller air voids sizes compared to the coarse rubber specimen. However for the control specimen, the average voids size was slightly higher (approximately 1.3 mm^2) than the rubberised mixtures although in reality their voids sizes appeared smaller at certain heights (middle towards the top) and larger at the other heights (middle towards the bottom). To briefly summarise, the results clearly indicate that for the same air voids content, different mixtures would likely produce different air voids formation (associated with the voids content, voids number and voids size) as evidenced earlier. These inconsistencies show that the addition of rubber causes the large air voids to scatter randomly into smaller sizes within the specimen during compaction. This is clearly observed in Figure 6.11, which compares the X-ray CT images of top (T), middle (M) and

bottom (B) sections of all specimens. The bottom and the top levels were compared at 10 mm and 90 mm heights respectively to avoid the effect of surface air voids. The middle section was examined at the height of 50 mm. From the images, it can be seen that in the rubberised mixtures, the air voids are randomly distributed, unlike the control mixture, where more air voids are observed closer to the circumference and thought to be the result of inadequate compaction due to mould confinement.

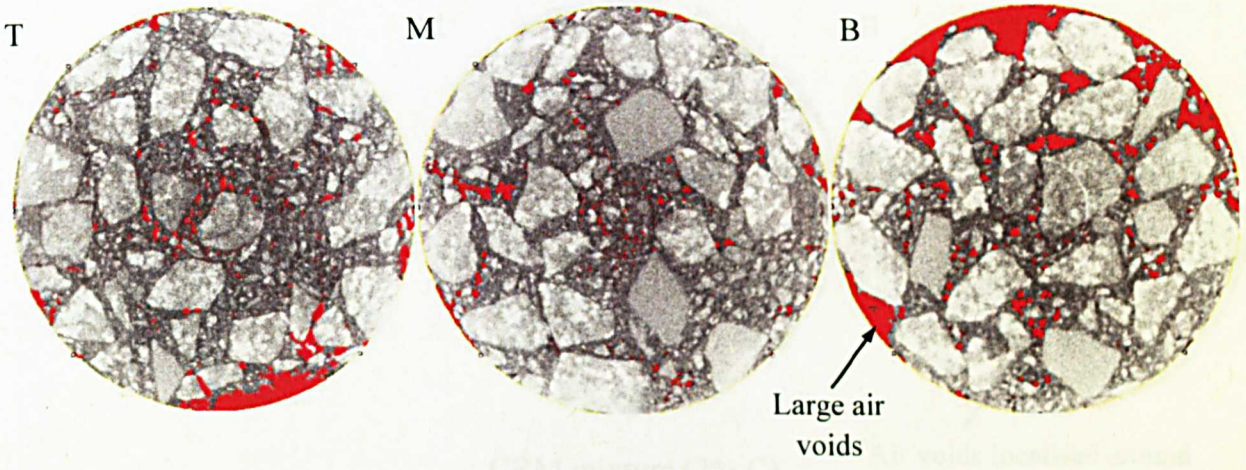

Control mixture (0%)

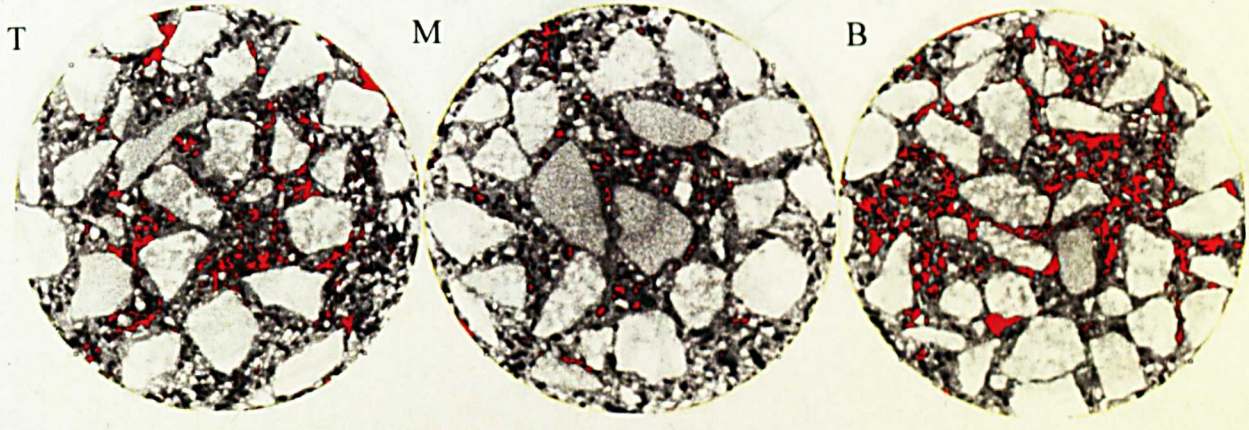

CRM mixture (2% F)

Figure 6.11 continues below

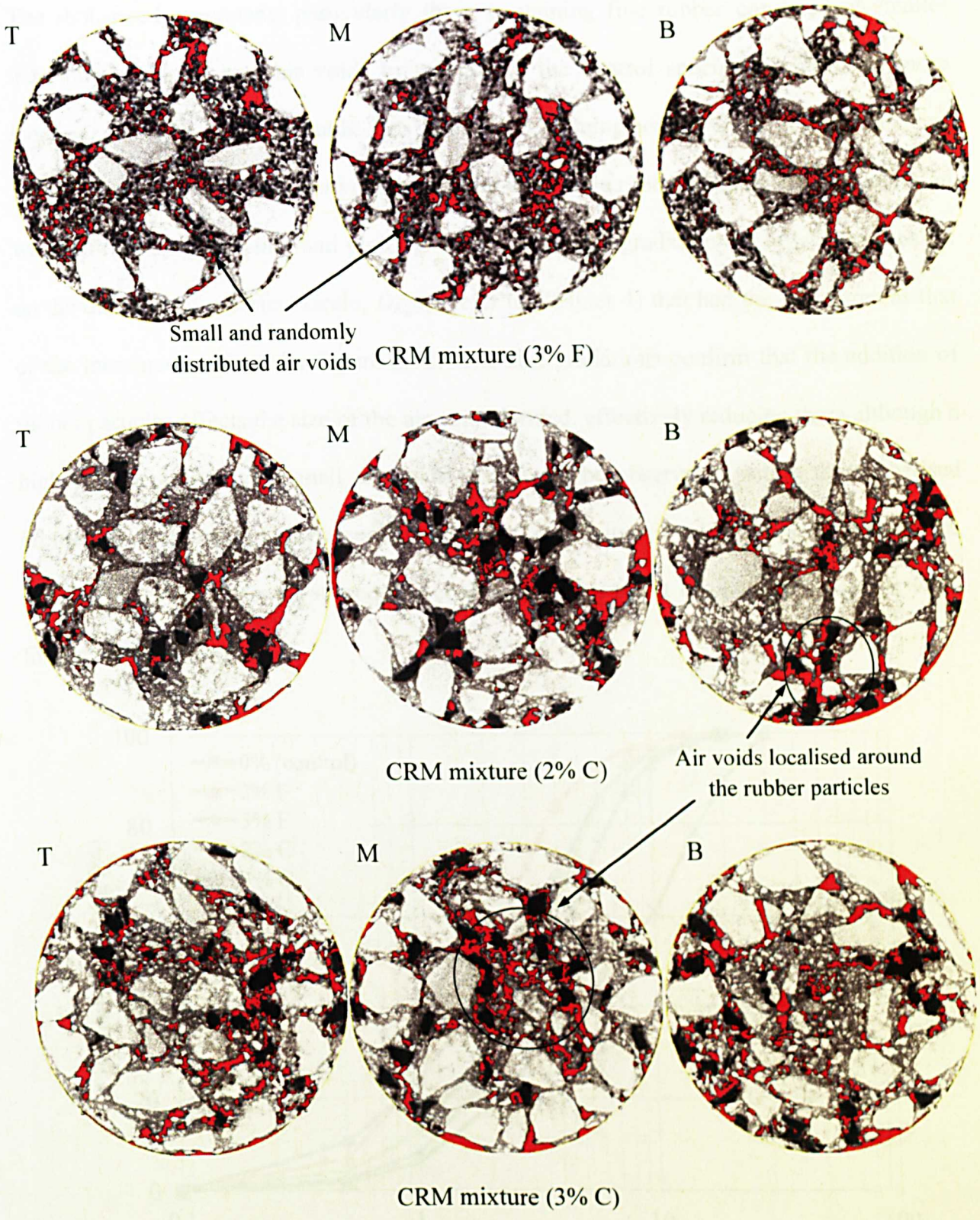

Figure 6.11 X-ray CT images showing the air voids distribution (highlighted in red) in control and CRM specimens at the **T**op (90 mm), **M**iddle (50 mm) and **B**ottom (10 mm)

The rubberised specimens, particularly those containing fine rubber consisted of smaller individual and separated air voids in contrast to the control specimen which had more localised and larger sized air voids. The specimen containing coarse rubber particles also had a wider range of larger sized air voids compared to the fine rubber mixture. This observation was justified by calculating and plotting the air voids size gradation (or distribution) based on the diameter of a perfect circle, D_{EQPC} (refer to Chapter 4) that had the same area as that of the measured voids (refer Figure 6.12). The size gradations confirm that the addition of rubber particles affects the size of the air voids formed, effectively reducing them although a high percentage of those small air voids would still be observable within the rubberised mixtures. Therefore, it can be concluded that, the addition of rubber to asphalt mixtures, affects the effectiveness of subsequent compaction as a result of changes in the air voids formation and distribution.

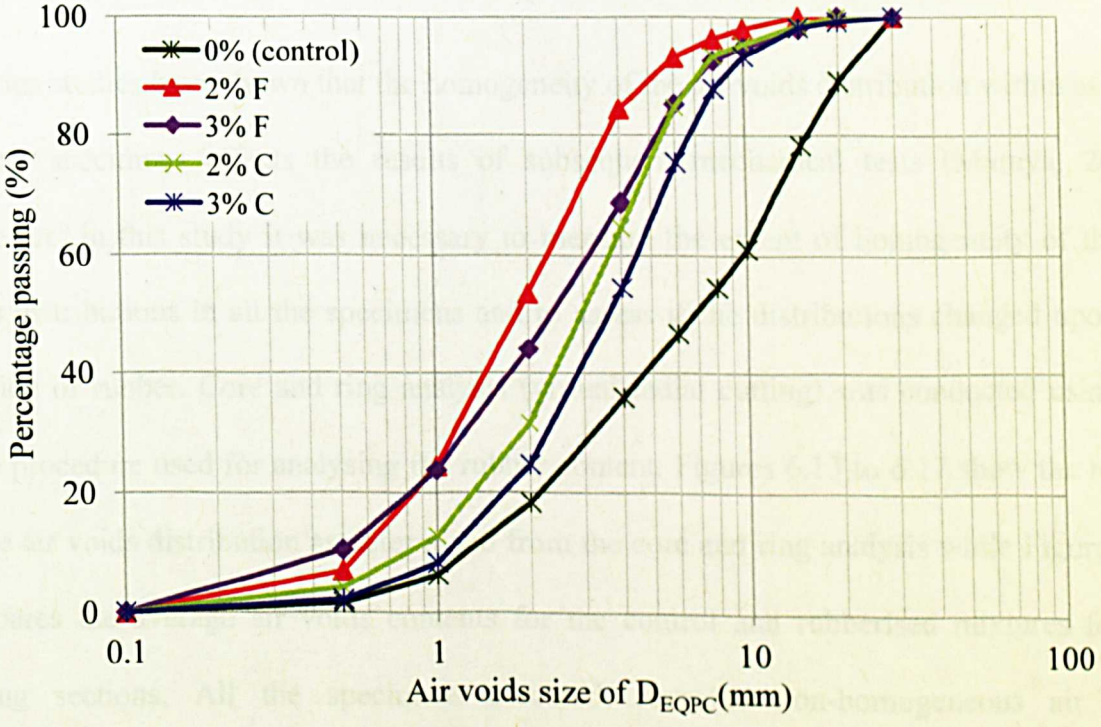

Figure 6.12 Air voids size gradation for different mixtures

This finding is significant because unlike larger voids, small separated voids within the rubberised mixture are more likely to induce smaller strains in the event of the specimen being subjected to loading. The large and localised air voids would likely form weak zones with high stress concentrations and potential to cause instability. Such voids could potentially propagate and connect with each other to form cracks, resulting in severe damage. Interestingly, the X-ray images (Figure 6.11) show that in the specimen containing coarse rubber, the air voids were formed very close to the rubber particles. This observation was significant as it better explained the potential of the surrounding rubber particles to perform as elastic aggregates, to absorb stresses at the crack tip and resist crack propagation caused by mechanical testing. Analysis on the correlation between the air voids and rubber locations was conducted and the results can be found in Section 6.4.

6.3.2 Air Voids Homogeneity

Previous studies have shown that the homogeneity of the air voids distribution within asphalt mixture specimens affects the results of subsequent mechanical tests (Muraya, 2007). Therefore, in this study it was necessary to measure the extent of homogeneity of the air voids distributions in all the specimens and to assess if the distributions changed upon the addition of rubber. Core and ring analysis (virtual radial cutting) was conducted using the same procedure used for analysing the rubber content. Figures 6.13 to 6.17 show the results of the air voids distribution as determined from the core and ring analysis while Figure 6.18 compares the average air voids contents for the control and rubberised mixtures for the cutting sections. All the specimens assessed, revealed non-homogeneous air voids distributions (Figures 6.13 to 6.17). However, the middle core of 25 mm for the control

mixture (as shown in Figure 6.13a) shows the most uniform air voids distribution in the height interval of 10 mm to 95 mm but possesses a very small average void content (large deviation from the total void content). This finding reflects the effectiveness of specimen compaction as acknowledged earlier in Section 6.3.2. A comparison of the control and rubberised mixtures found that more air voids are present at the circumference of the control specimen than the middle section. This phenomenon is believed to occur primarily due to the effect of mould confinement which has resisted the compaction effort in the vicinity of the circumference. This can be observed as shown in Figure 6.19a.

For the rubberised mixtures, the non-uniform air voids distributions and average air voids content determined within the core and ring sections increased as the core diameter was reduced from 100 mm to 25 mm and as the ring size was increased inwardly (from 25 mm to 75 mm). In other words, the aforementioned non-uniformity is adjudged to have been caused by the comparatively large variation in the air voids present within the middle section. This finding can be related to the higher rubber content at the middle section of the specimens, observed earlier in Section 6.2. The extent to which the high rubber content in the middle core section (Figure 6.19b) resists compaction depends on the recovery of the rubber particles. This behaviour has reduced the tendency of the middle section being over-compacted compared to the other sections, as is shown to have occurred in the control specimen. Furthermore it increased the potential of air voids distribution to become more uniform throughout the specimen (particularly for the 100 mm core diameter with 3% rubber content) as shown in Figures 6.15 and 6.17.

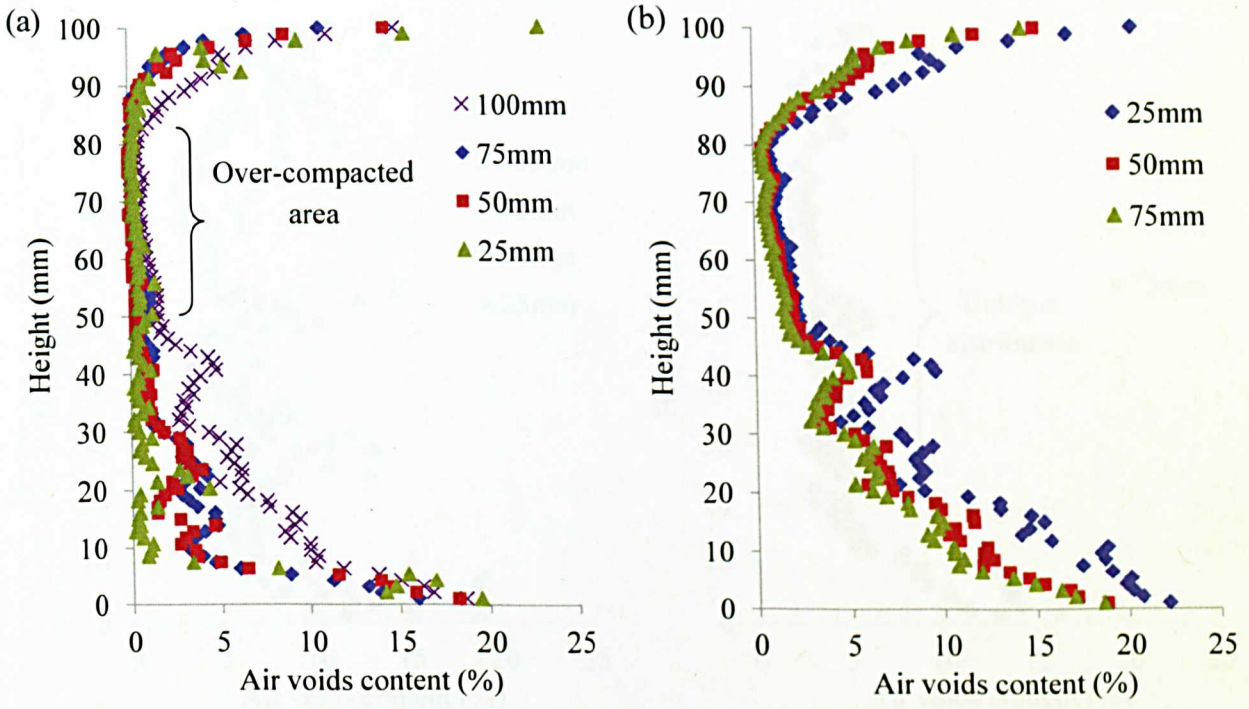

Figure 6.13 Air voids distributions in radial direction for (a) core, C (b) ring, R for control specimen (unmodified)

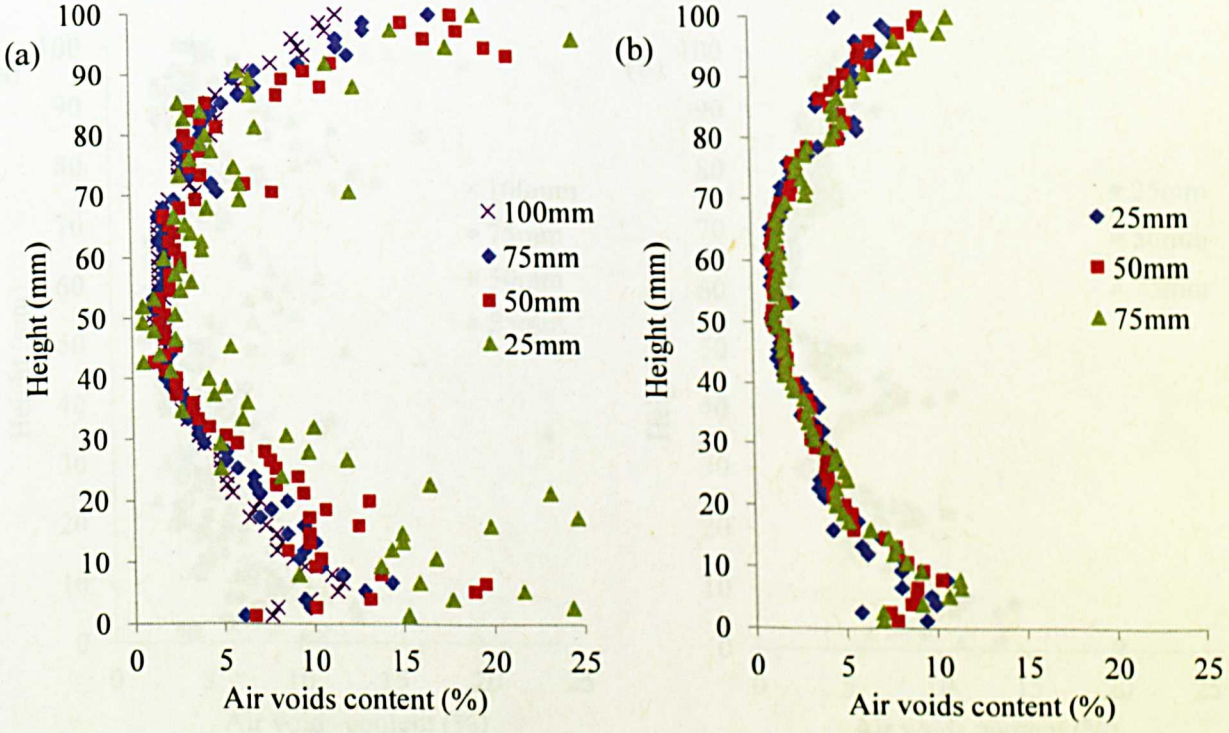

Figure 6.14 Air voids distributions in radial direction for (a) core, C (b) ring, R for specimen with 2% fine rubber (2% F)

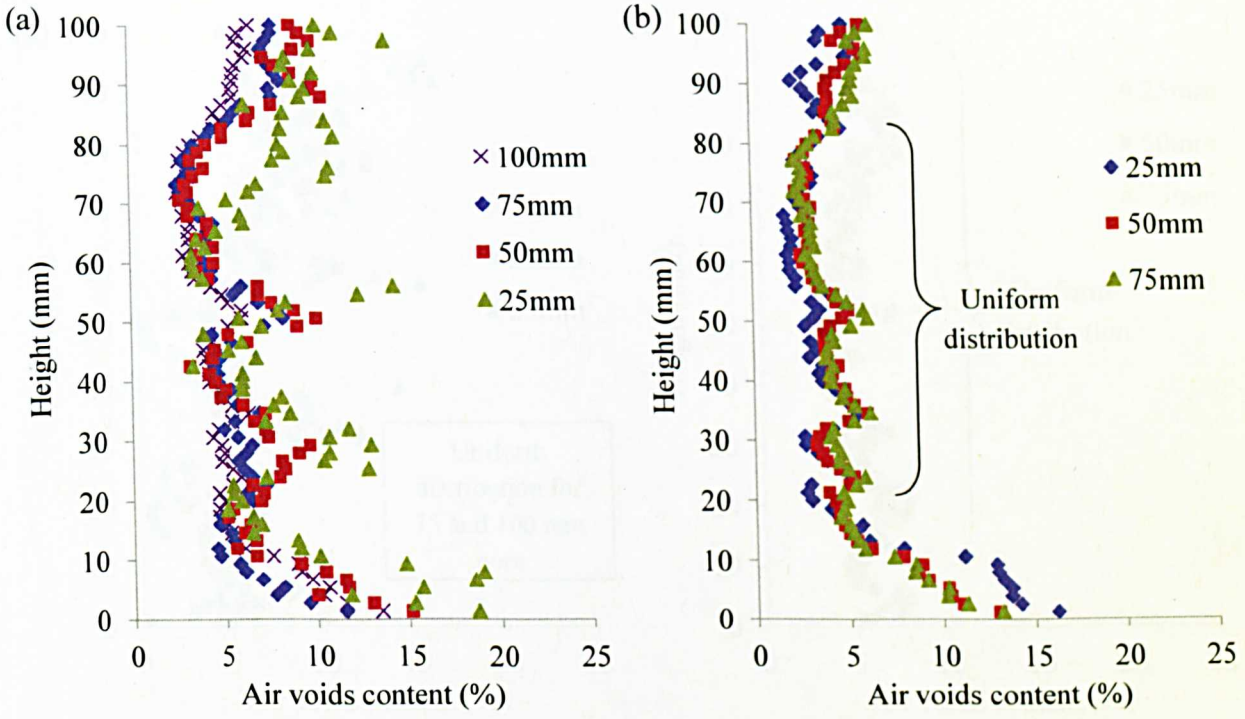

Figure 6.15 Air voids distributions in radial direction for (a) core, C (b) ring, R for specimen with 3% fine rubber (3% F)

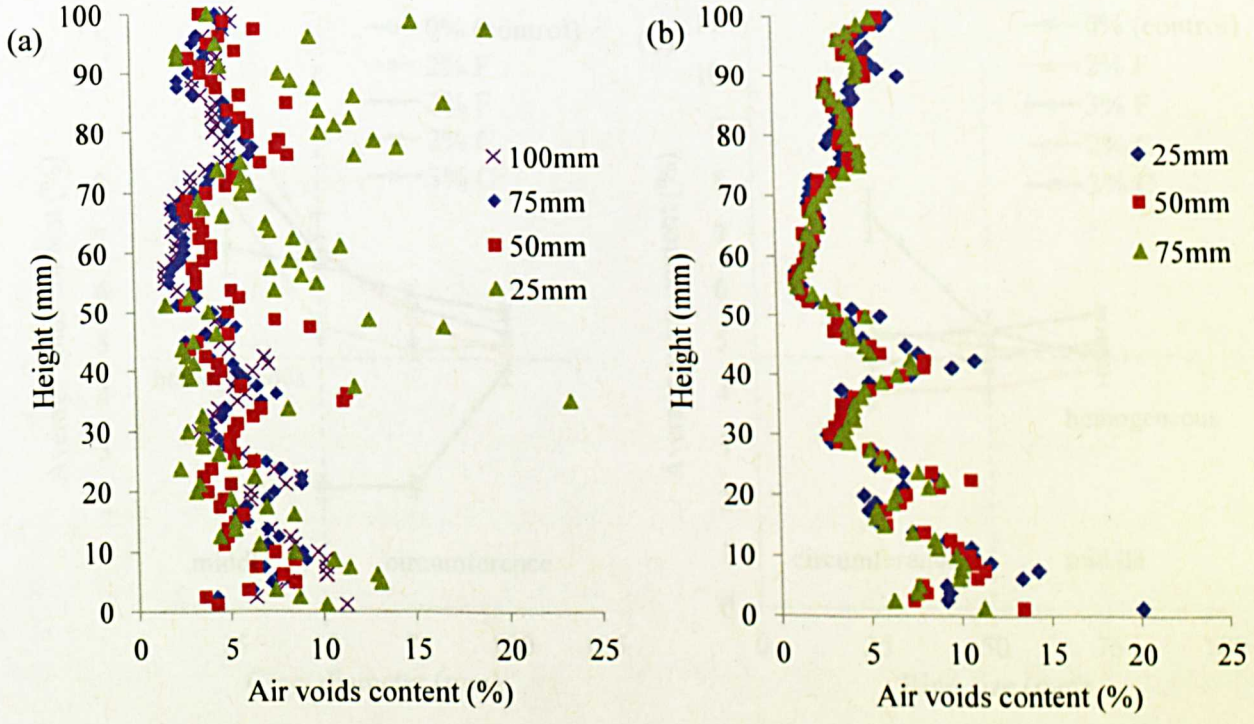

Figure 6.16 Air voids distributions in radial direction for (a) core, C (b) ring, R for specimen with 2% coarse rubber (2% C)

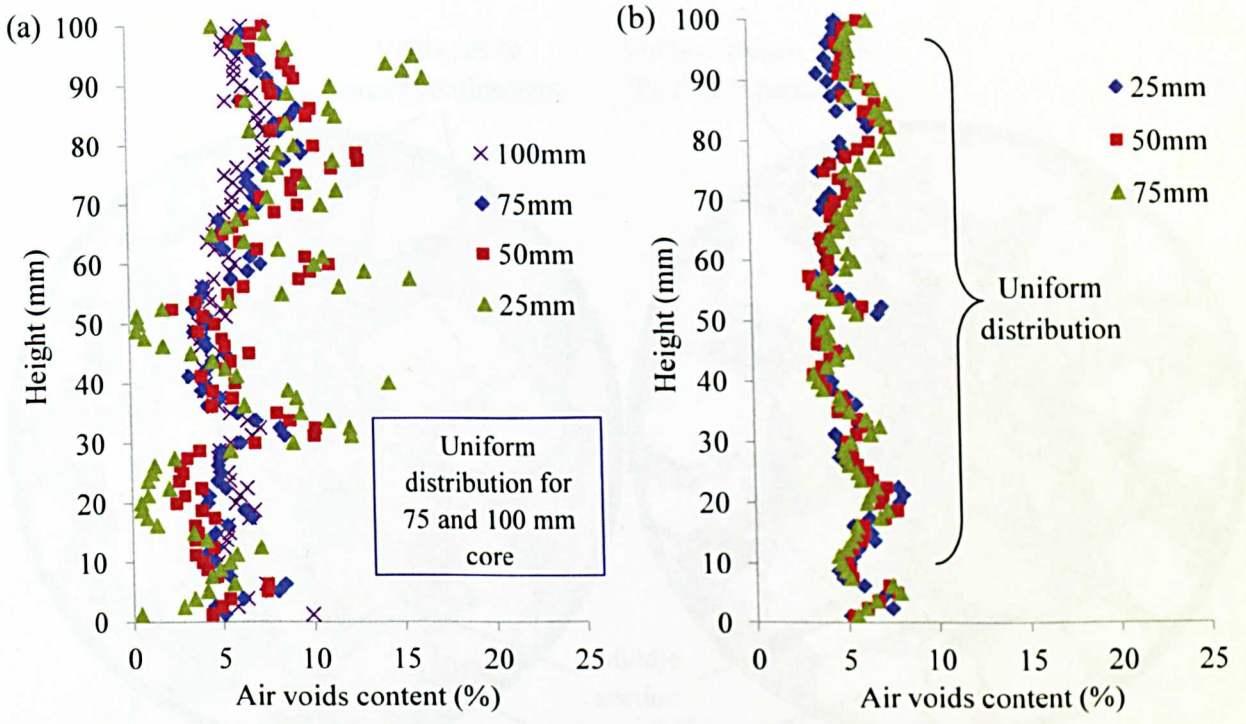

Figure 6.17 Air voids distributions in radial direction for (a) core, C (b) ring, R for specimen with 3% coarse rubber (3% C)

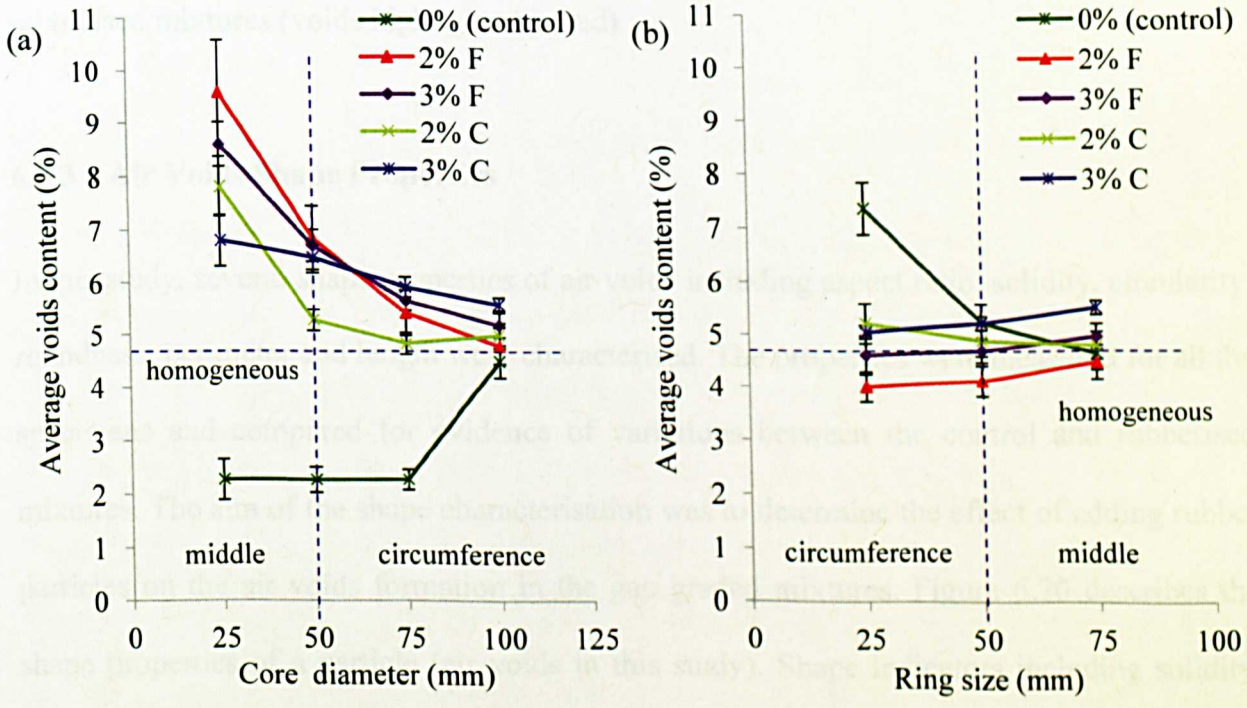

Figure 6.18 Average air voids content (distributions in radial direction) for (a) core, C (b) ring, R for control and rubberised specimens

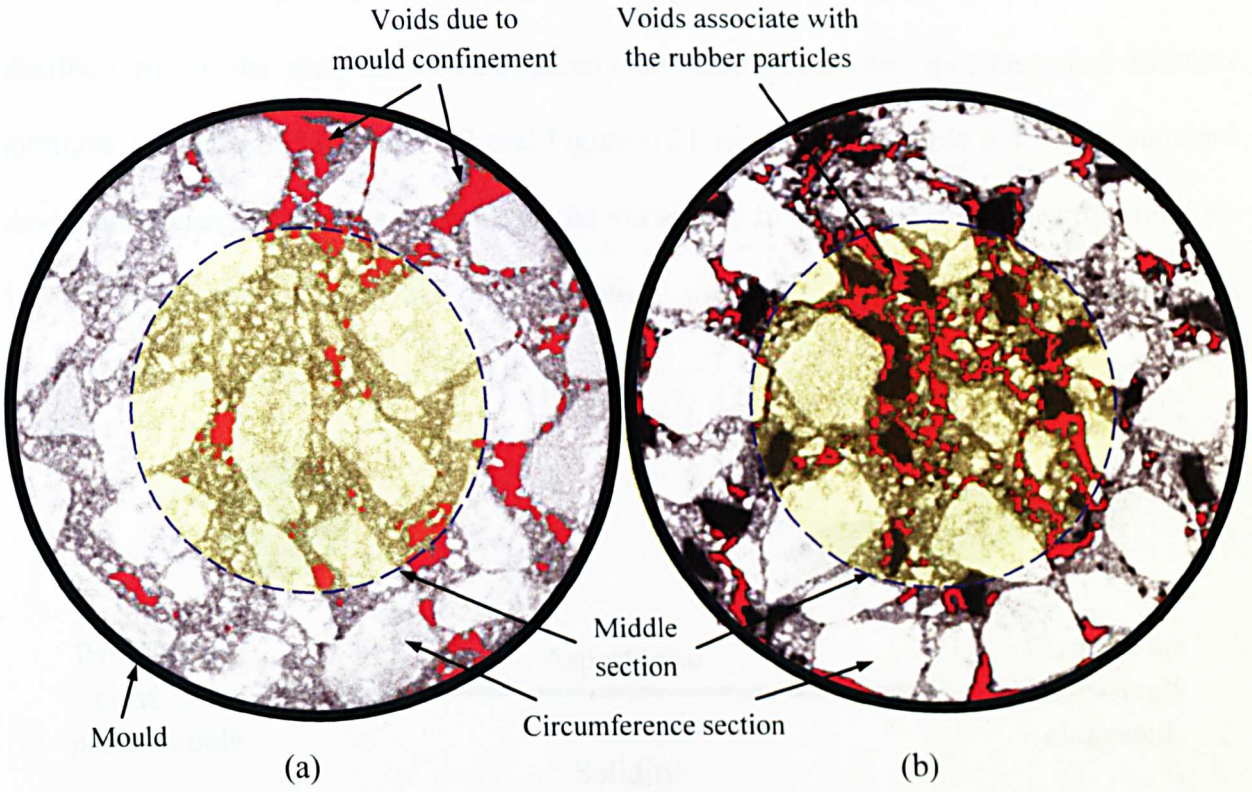

Figure 6.19 Air voids distribution within the core and ring sections for (a) control and (b) rubberised mixtures (voids highlighted in red)

6.3.3 Air Voids Shape Properties

In this study, several shape properties of air voids including aspect ratio, solidity, circularity, roundness, perimeter and length were characterised. The properties were measured for all the specimens and compared for evidence of variations between the control and rubberised mixtures. The aim of the shape characterisation was to determine the effect of adding rubber particles on the air voids formation in the gap graded mixtures. Figure 6.20 describes the shape properties of a particle (air voids in this study). Shape indicators including solidity, circularity and roundness are quoted based on a 0 to 1 scale, where 1 is indicative of a shape that is close to a perfect circle or sphere, while 0 or the inverse value of aspect ratio (i.e. >>

1.0) describe a shape that is increasingly elongated. The average values and detailed distributions of the air voids shape parameters throughout the specimen for different mixtures are presented in Table 6.3 and Figure 6.21 respectively. Table 6.4 shows standard deviation values which are a measure of the variability in the shape properties distributions i.e. the lower the value of standard deviation, the more uniform the shape properties distribution.

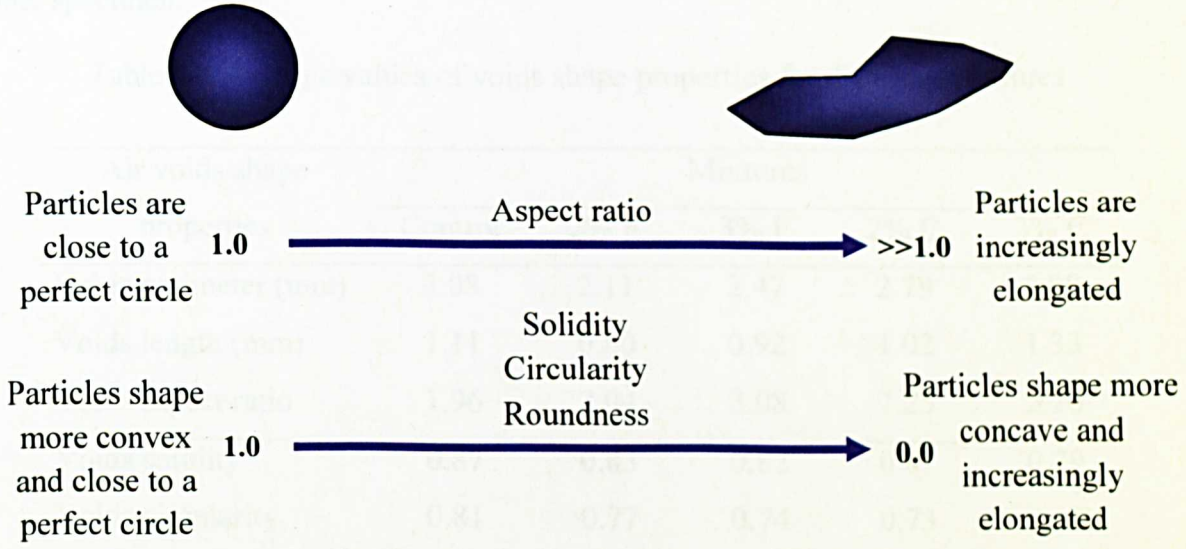

Figure 6.20 Particles shape description

In general, the results showed the shape descriptors including circularity, roundness and solidity to be close to 1, indicating that the air voids were more rounded and more compact in all specimens, particularly in the upper region of the specimen (i.e. between 50 mm to 90 mm heights). It was explained earlier in Section 6.3.1, that this section of the specimens is the most compact portion of the specimen which leads to the conclusion that the more compact the areas the more circular the air voids formation. This is because during compaction the air voids are increasingly filled by the mastic and aggregate particles which decreases the values of perimeter, aspect ratio and length of the air voids within the section. The control mixture appeared to have the most circular air voids with more variation in its

shape properties distribution within the specimen compared to the rubberised mixtures. For the increased rubber content (from 2% to 3%) specimen, the air voids shape became increasingly elongated with high values of voids perimeter, voids length and aspect ratio recorded although with little variation in their distribution. The same observation was made when the fine and coarse rubber specimens were compared, that is, the specimen containing the coarse rubber particles produced more elongated air voids shapes compared to the fine rubber specimen.

Table 6.3 Average values of voids shape properties for different mixtures

Air voids shape properties	Mixtures				
	Control	2% F	3% F	2% C	3% C
Voids perimeter (mm)	3.08	2.11	2.47	2.79	3.98
Voids length (mm)	1.11	0.80	0.92	1.02	1.33
Voids aspect ratio	1.96	2.04	2.08	2.25	2.20
Voids solidity	0.87	0.83	0.82	0.81	0.79
Voids circularity	0.81	0.77	0.74	0.73	0.68
Voids roundness	0.64	0.59	0.57	0.57	0.56

Table 6.4 Standard deviation or variability in the air voids shape properties distribution

Air voids shape properties	Mixtures				
	Control	2% F	3% F	2% C	3% C
Voids perimeter (mm)	1.70	0.56	0.40	0.54	0.57
Voids length (mm)	0.52	0.18	0.11	0.19	0.17
Voids aspect ratio	0.17	0.12	0.05	0.18	0.08
Voids solidity	0.02	0.02	0.01	0.01	0.01
Voids circularity	0.05	0.04	0.02	0.02	0.02
Voids roundness	0.03	0.02	0.01	0.02	0.02

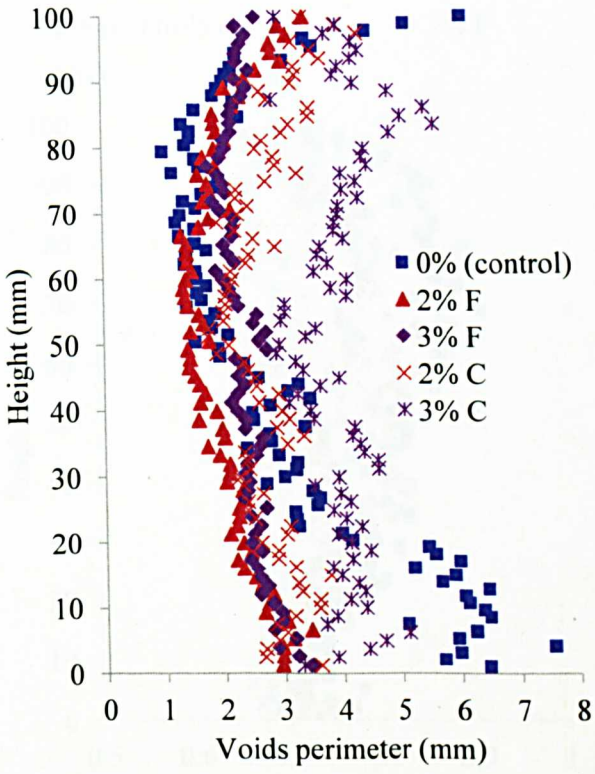

(a)

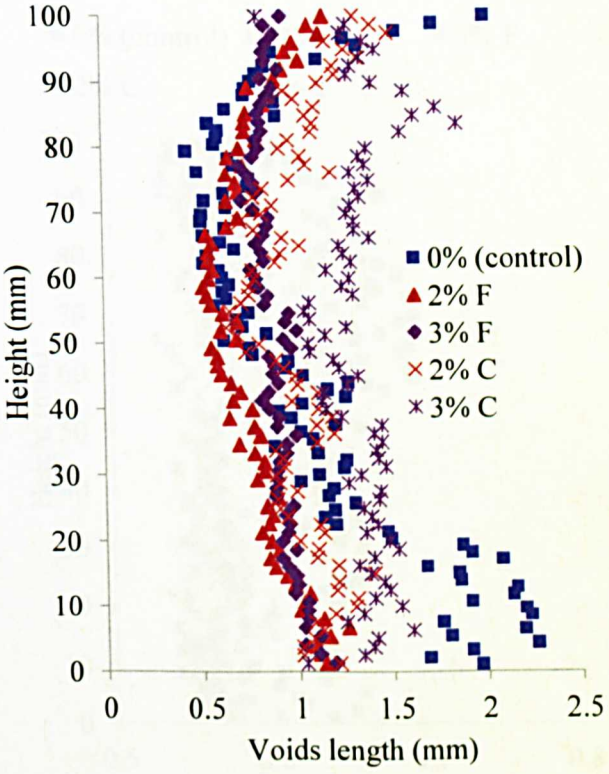

(b)

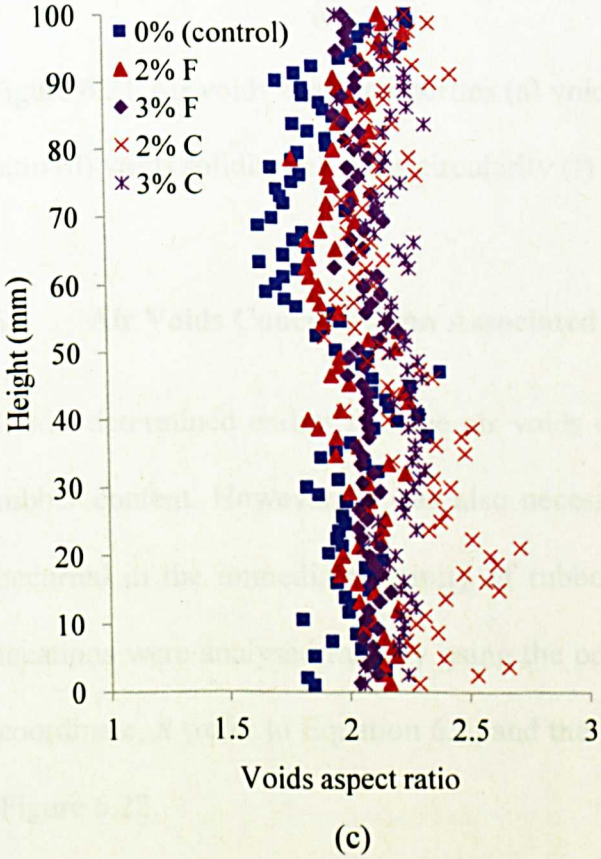

(c)

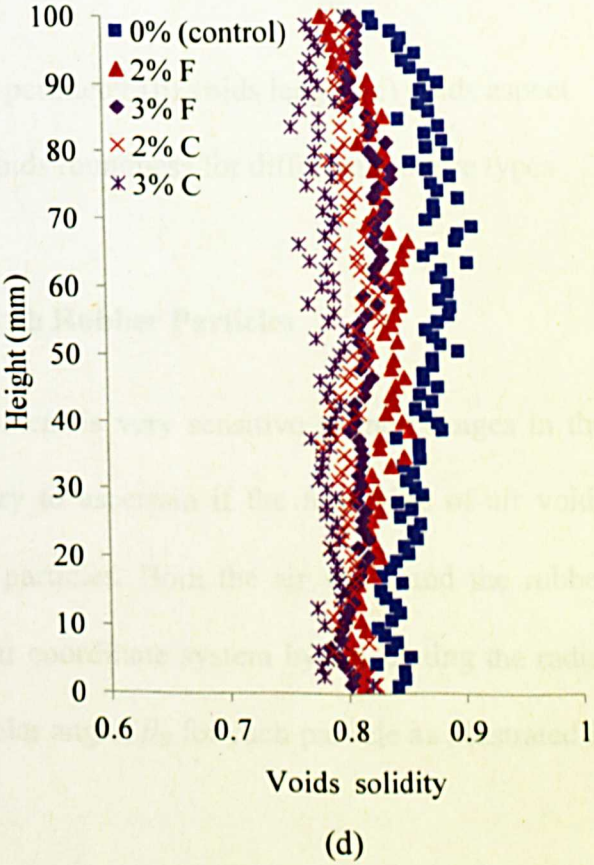

(d)

Figure 6.21 continues below

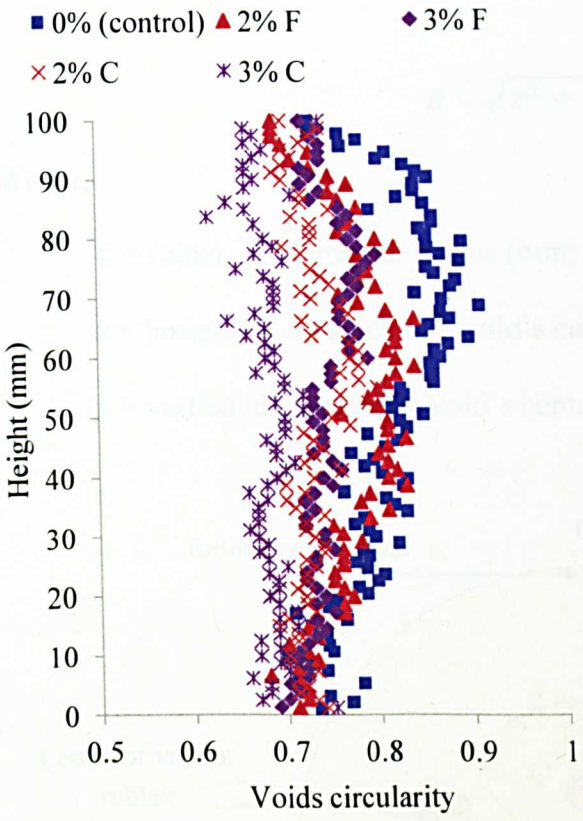

(e)

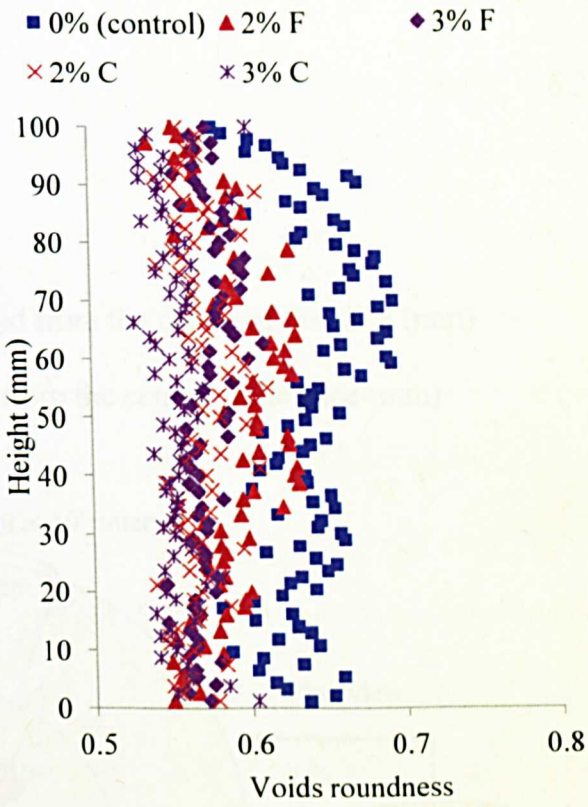

(f)

Figure 6.21 Air voids shape properties (a) voids perimeter (b) voids length (c) voids aspect ratio (d) voids solidity (e) voids circularity (f) voids roundness for different mixture types

6.4 Air Voids Concentration Associated with Rubber Particles

It was determined earlier that the air voids content is very sensitive to the changes in the rubber content. However, it was also necessary to ascertain if the formation of air voids occurred in the immediate vicinity of rubber particles. Both the air voids and the rubber locations were analysed radially using the polar coordinate system by calculating the radial coordinate, R (refer to Equation 6.2) and the polar angle, θ_R for each particle as illustrated in Figure 6.22.

$$R = \sqrt{x^2 + y^2} \qquad 6.2$$

Where,

R = radial coordinate or radius (mm)

x = horizontal distance of a void's centroid from the centre of the slice (mm)

y = vertical distance of a void's centroid from the centre of the slice (mm)

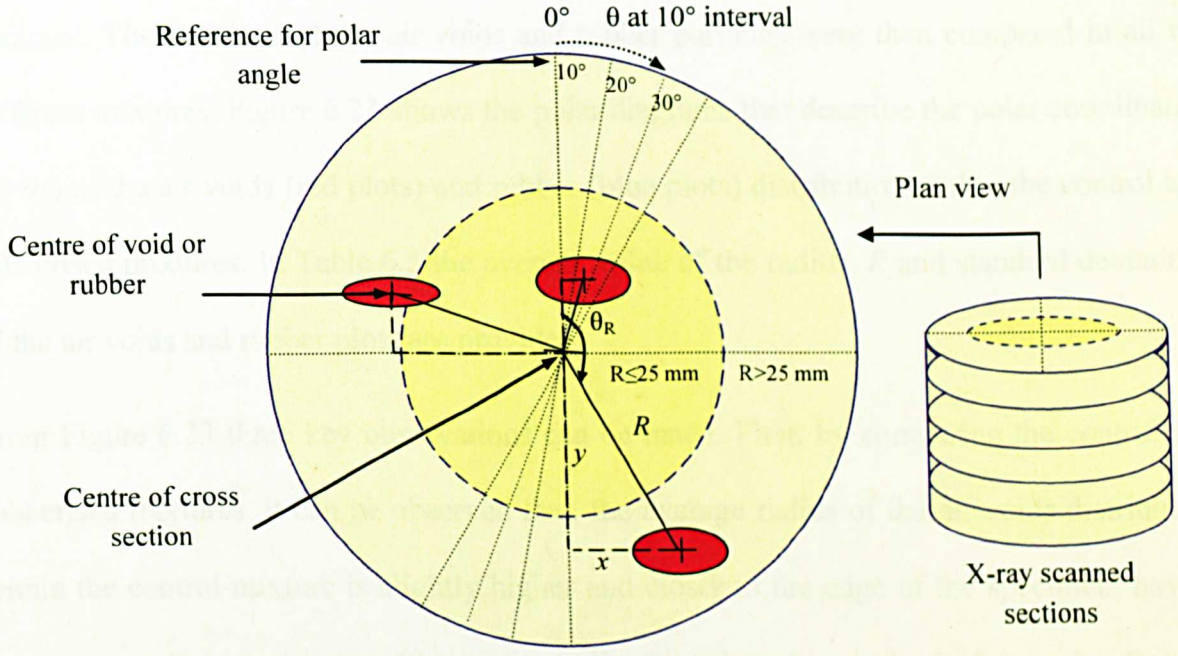

Figure 6.22 Illustration of the radial coordinate and polar angle in a specimen's cross section

This coordinate system adopted is two-dimensional, wherein each particle's centroid on a plane is determined as the distance from the specimen's centre called radius and an angle measured from a fixed reference called polar angle. Particles with lower radius values indicate that they are located nearer to the centre of the specimen, whereas particles with higher radius values are closer to the specimen's circumference. To analyse the voids and rubber locations in this study, the particles were separated into two main groups or sections.

The first group comprised particles within a radius of 25 mm from the centre of the cross section, (inner section), while the second group consisted of particles located closest to the specimen's circumference with radii greater than 25 mm from the centre of the cross section (outer section). The average radius of all particles present was calculated at polar angle intervals of 10°, starting from 0° to 360° in the clockwise direction. Small 10° sections were preferred to avoid any bias when the particle radii were averaged in the area under consideration to ensure that the actual locations of the air voids and rubber particles were obtained. The locations of the air voids and rubber particles were then compared in all the different mixtures. Figure 6.23 shows the polar diagrams that describe the polar coordinates, (R, θ_R) of the air voids (red plots) and rubber (blue plots) distribution within the control and rubberised mixtures. In Table 6.5 the average value of the radius, R and standard deviations of the air voids and rubber plots are provided.

From Figure 6.23 three key observations can be made. First, by comparing the control and rubberised mixtures, it can be observed that, the average radius of the air voids distribution within the control mixture is slightly higher and closer to the edge of the specimen, having an average radius greater than 40 mm. Secondly, the 'blooming pattern' of the polar diagram shows different shapes for the fine and coarse rubber mixtures. The coarse rubber mixtures have a more irregular blooming shape for both the air voids and rubber with more sharp petals in the plots compared to the fine rubber mixtures which have a smoother blooming shape. This was confirmed by the higher values in the standard deviation computed for the specimen with 2% coarse rubber. The sharp petals in the diagram indicate that the rubber particles were likely to localise at that particular point or location. This agrees with previous findings (refer to Section 6.2) wherein the coarse rubber particles were more localised compared to the fine rubber particles which were evenly distributed radially as shown in

Figure 6.2. Different rubber content and sizes added to the specimen produced different blooming shapes for the air voids distributions, indicating that the addition of rubber affects the air voids distribution. Thirdly, the overlap plots in the polar coordinates (refer to Figure 6.23) fairly indicate that the distribution of the air voids and rubber particles within the specimen are almost identical. This is compatible with the observation made earlier in Figure 6.11 where the air voids were found to have developed in the vicinity of the rubber particles. It is also clear that the specimen produced with 3% rubber has more overlap plots than the 2% rubberised mixture. The close values of average radius for air voids and rubber for the specimens containing 3% rubber (both fine and coarse rubber) is likely to indicate that they were close to each other in the mixture.

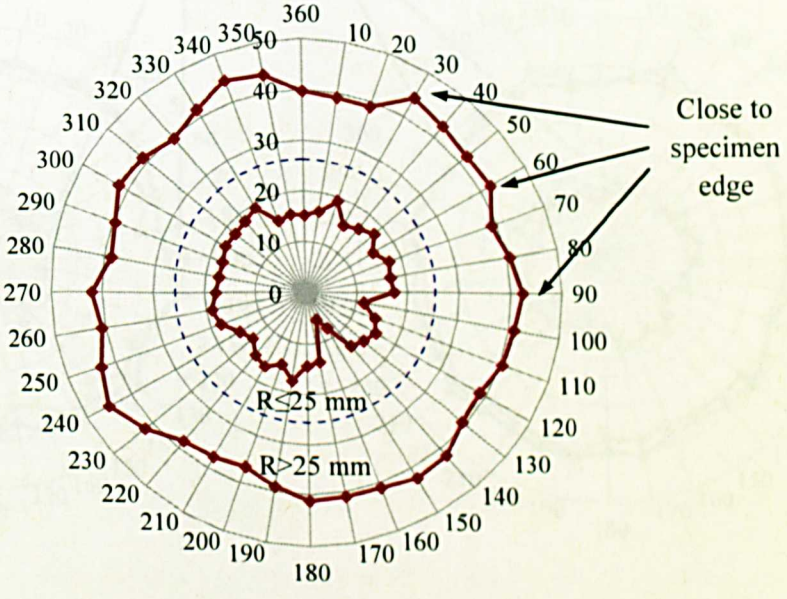

0% rubber (control)

Figure 6.23 continues below

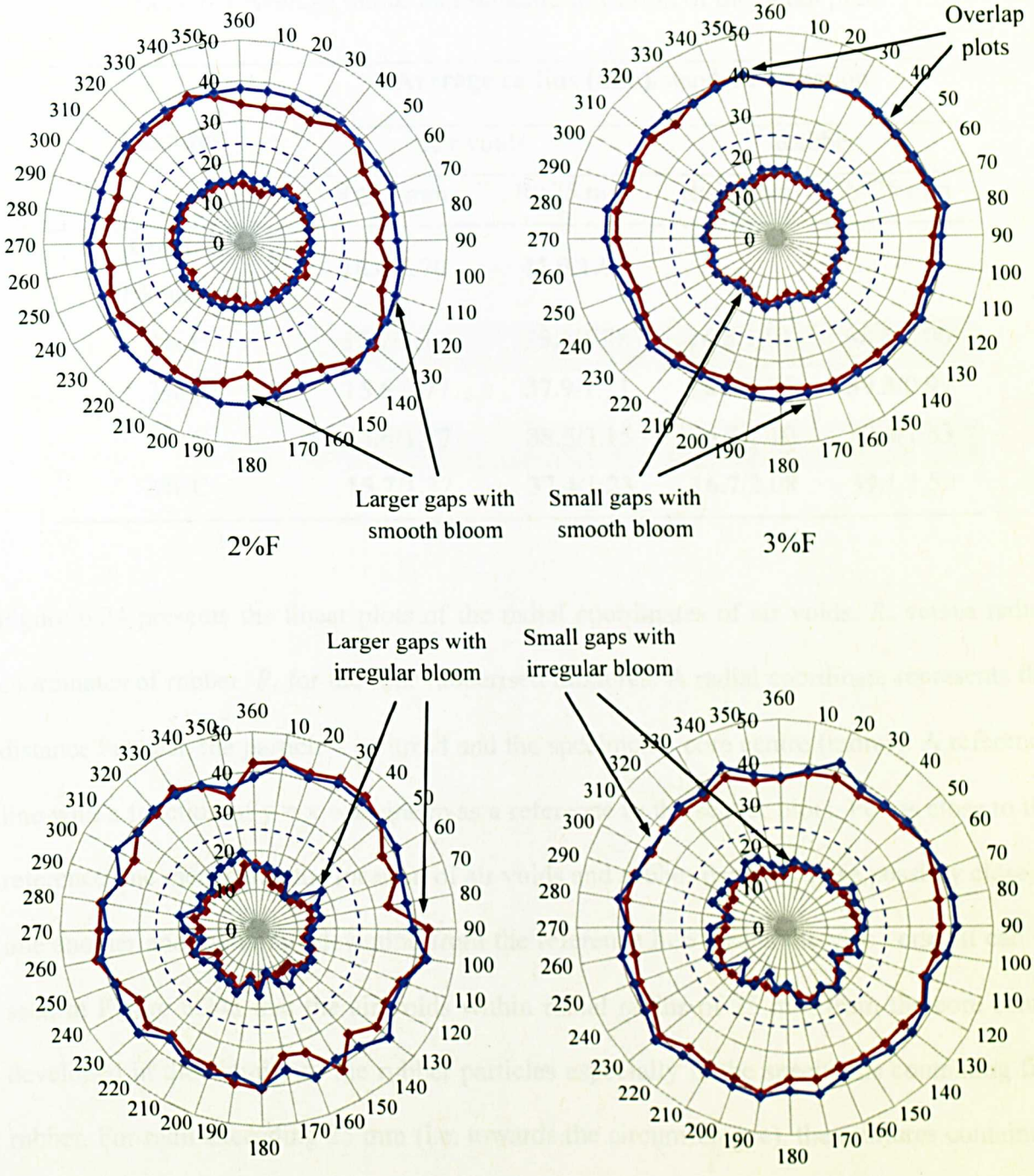

Figure 6.23 Polar diagram showing the average locations of rubber (blue) and air voids (red) close to the specimen's core centre (R≤25 mm) and near the circumference (R>25 mm) for the control and rubberised mixtures

Table 6.5 Average radius and standard deviation of the radial plots

Mixtures	**Average radius (mm)**/standard deviation			
	Air voids		Rubber	
	R≤25 mm	R>25 mm	R≤25 mm	R>25 mm
Control (0% rubber)	**16.0**/2.70	**41.0**/1.93	-	-
2% F	**15.7**/1.17	**35.7**/1.78	**16.5**/1.01	**38.6**/1.00
3% F	**15.6**/0.77	**37.9**/1.11	**16.3**/0.76	**39.3**/0.97
2% C	**13.6**/1.77	**38.5**/3.15	**15.5**/2.10	**39.4**/1.83
3% C	**15.7**/1.37	**37.4**/1.23	**16.7**/2.08	**39.1**/1.59

Figure 6.24 presents the linear plots of the radial coordinates of air voids, R_v versus radial coordinates of rubber, R_r for the four rubberised mixtures. A radial coordinate represents the distance between the particle's centroid and the specimen's core centre (radius). A reference line with a function of y = x was drawn as a reference to the scatter plots. Points close to the reference line means that the location of air voids and rubber particles were possibly close to one another and the points deviating from the reference line means the vice versa. It can be seen in Figure 6.24a that the air voids within radial radius of 25 mm from the core centre developed in the vicinity of the rubber particles especially in the specimens containing fine rubber. For radii exceeding 25 mm (i.e. towards the circumference), the mixtures containing 3% rubber content show an increase in their air voids in the region of the rubber particles (Figure 6.24b). This is likely to describe that both rubber content and rubber particle size contribute to the formation of air voids and to the pattern of the air voids distribution.

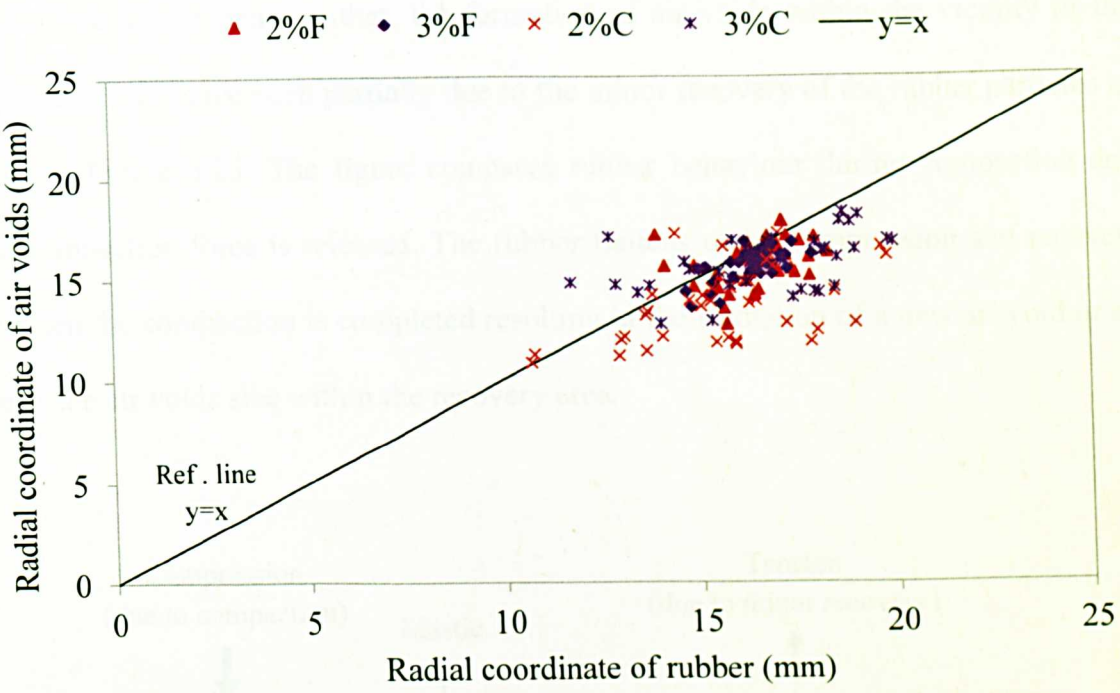

(a)

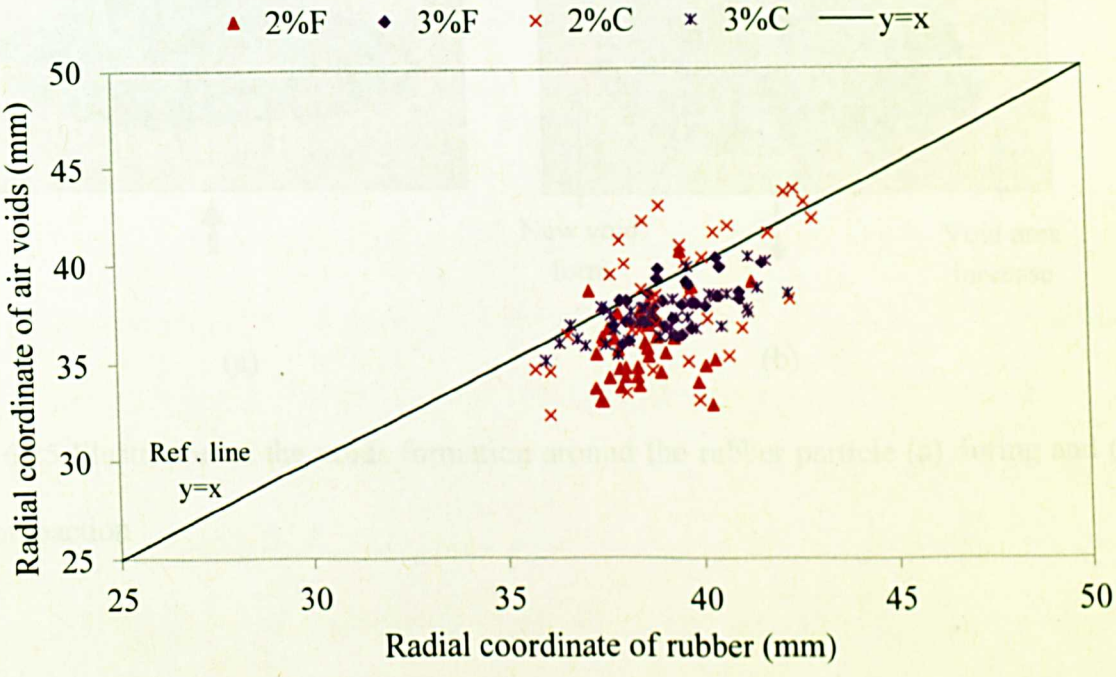

(b)

Figure 6.24 Linear plot of radial coordinate of air voids versus rubber particles that are close to the (a) centre (R≤25 mm) and (b) circumference (R>25 mm) for rubberised mixtures

In addition, the author believes that, the formation of air voids within the vicinity of the rubber particles may have been partially due to the minor recovery of the rubber particles as illustrated in Figure 6.25. The figure compares rubber behaviour during compaction and after the compaction force is released. The rubber flattens under compression and recovers slightly when the compaction is completed resulting in the formation of a new air void or an increase in the air voids size within the recovery area.

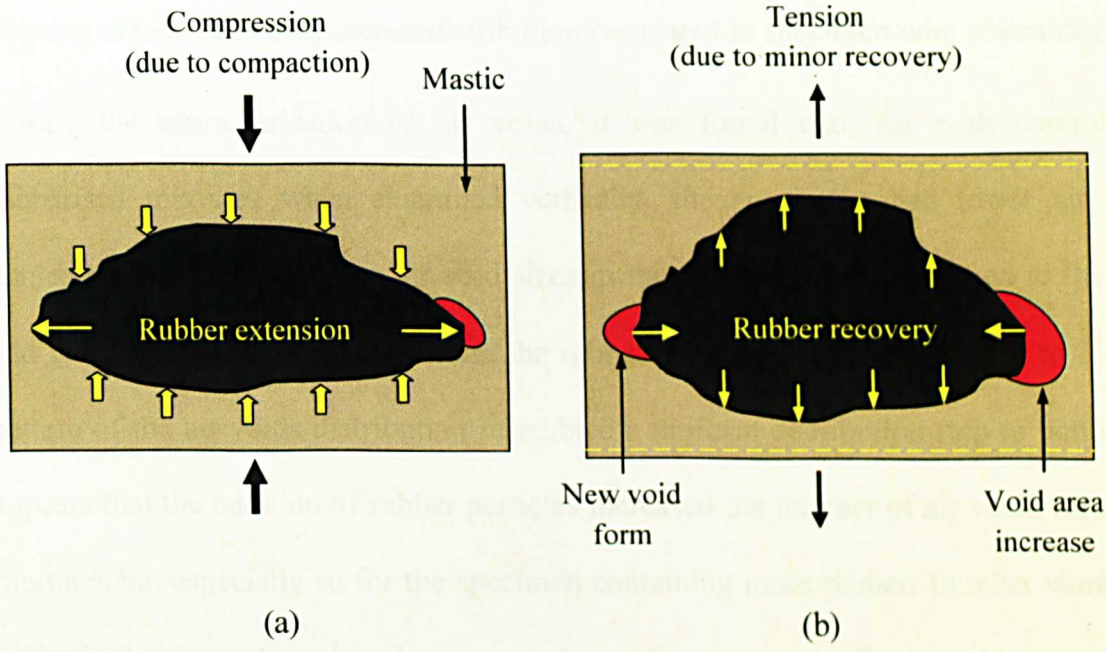

Figure 6.25 Illustration of the voids formation around the rubber particle (a) during and (b) after compaction

6.5 Summary

From the findings, the following conclusions can be drawn:

1. The rubber distribution within the specimen (100 mm core diameter) was found to be vertically well distributed for all rubberised mixtures with only small deviations from the average value of the rubber content. However, for the radial sections the coarse rubber particles formed clusters, while the fine rubber particles were uniformly distributed. Overall, the rubber distribution for the specimen containing 2% rubber was determined as being close to a homogeneous distribution compared to specimen with 3% rubber.

2. During the characterisation of air voids, it was found that, for both control and rubberised mixtures when examined vertically, the specimens had lower air voids contents and smaller average air void sizes in their mid sections compared to their top and bottom sections. However, when the rubber content increased from 2% to 3%, the pattern of the air voids distribution resembled a uniform distribution (top to bottom). It appears that the addition of rubber particles increased the number of air voids for all the mixtures but especially so for the specimen containing more rubber. In other words, the rubberised mixtures produced an even air voids content distribution although the air voids sizes were smaller and more highly scattered than the control specimen which had comparatively more localised air voids at its circumference. The specimens containing coarse rubber possessed a greater air void size range compared to fine rubber mixtures although their respective air voids contents remained volumetrically the same.

3. The analysis of air voids shape properties found that incorporating rubber into asphalt mixtures tends to produce air voids with more elongated shapes while the air voids in the

control mixture were circular. The shape was noted to become increasingly elongated as the rubber particle size increased.

4. Analysis of the proximity of incipient air voids to rubber locations revealed that the air voids were fairly concentrated in the immediate vicinity of rubber particles. Specimens with 3% rubber (fine and coarse) showed a greater correlation between the air voids and rubber locations as observed from the polar coordinate system. This finding supports the initial hypothesis that rubber particles contribute to the formation of the air voids.

5. The addition of rubber to asphalt mixtures using the dry process method does not only serve the function of providing a measure of flexibility to the mixture by the rubber particles acting as elastic aggregates but it also affects the manner of the formation of air voids and their distribution within the compacted specimen.

7.0 MICRO AND MECHANICAL DAMAGE ANALYSIS OF RUBBER MODIFIED ASPHALT MIXTURES

7.1 Introduction

This chapter comprises two main sections that focus on the effect of rubber modification on the properties of gap graded mixtures in damaged condition. Investigations were conducted to assess the response of dry-processed rubberised asphalt mixtures to applied loading. Each section presents results of the damage characterisation for specimens subjected to loading, first in the Uniaxial Monotonic Compression Test followed by cyclical loading in the Indirect Tensile Fatigue Test. Discussions herein mainly relate to the mechanical and microstructural properties of the specimens. The mechanical test data included are laboratory experimental results relating to specimens' deformation or strength characteristics, typically expressed in the form of stresses and strains. For the microstructural damage analysis, several damage parameters were established beforehand to quantify the specimens' air voids and crack properties before and after the specimen undergoes the deformation. To conclude, the damage parameters derived from the micro-structural analysis were correlated with the stiffness results from the laboratory investigation. Both have been discussed further with reference to the different mixture designs and testing variables.

7.2 Uniaxial Monotonic Compression Test

7.2.1 Stress and Strain Analysis

This section explains the deformative behaviour of the specimens when subjected to Uniaxial Monotonic Compression at a constant strain rate. The stress and strain data were analysed with respect to different variables including rubber content and temperature at time of testing. Three mixture types were evaluated in this test namely a control mixture of HRA60/20 (0%crm) and HRA60/20 modified with 2% and 3% fine crumb rubber (2%crm and 3%crm). All the mixtures were kept as consistent as possible (i.e. identical aggregate gradation, bitumen type and air voids content) in order to facilitate meaningful comparisons of the variables. Table 7.1 and Figure 7.1 summarise results indicative of the deformation behaviour of the mixtures that were subjected to compressive loading. The values were averaged from three replicates with the closest properties. The properties of the specimen under compression were evaluated at the maximum stress level. Therefore, each compression test was terminated when stresses reached their peak values. The specimen were tested at 25°C and 40°C till peak stresses were attained as indicated by the stress-strain plots in Figures 7.2 and 7.3 respectively. The following sub-sections discuss the effects of varying rubber content and testing temperature on the mechanical behaviour of the specimens based on the results presented in these figures.

Table 7.1 Summary of Uniaxial Compression Test results at peak (average values)

Test temperature (°C)	Rubber content (%)	Peak/Failure stress (MPa)	Strain at peak (mm/mm)	Secant modulus (at peak) (MPa)
25	0 (control)	2.02	0.035	57.7
	2	2.05	0.068	30.1
	3	2.37	0.063	37.6
40	0 (control)	0.95	0.025	38.0
	2	1.00	0.050	20.0
	3	1.13	0.052	21.7

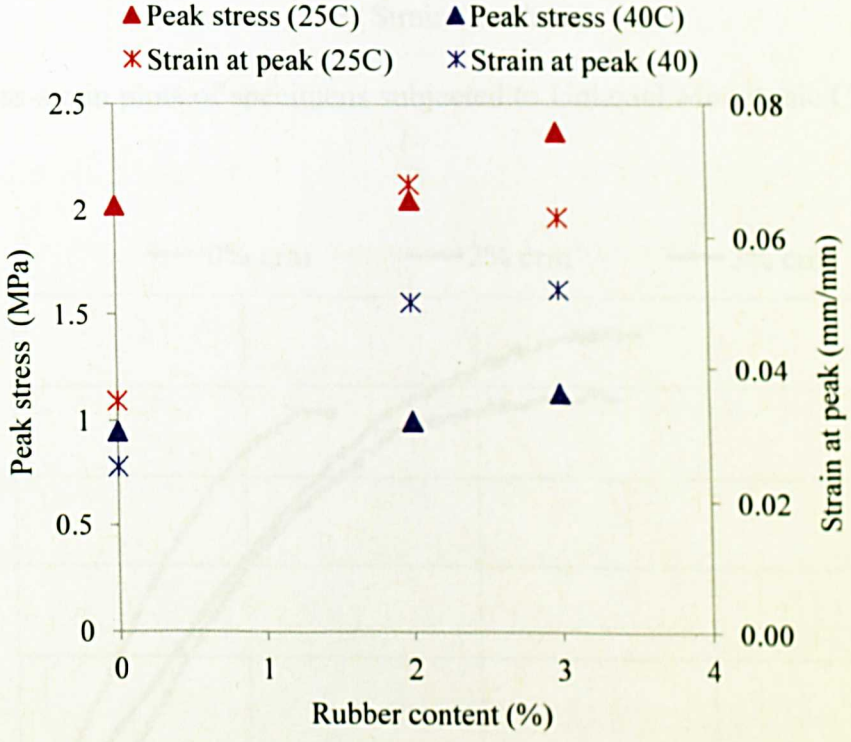

Figure 7.1 Stress and strain at peak tested at 25°C and 40°C for different rubber contents

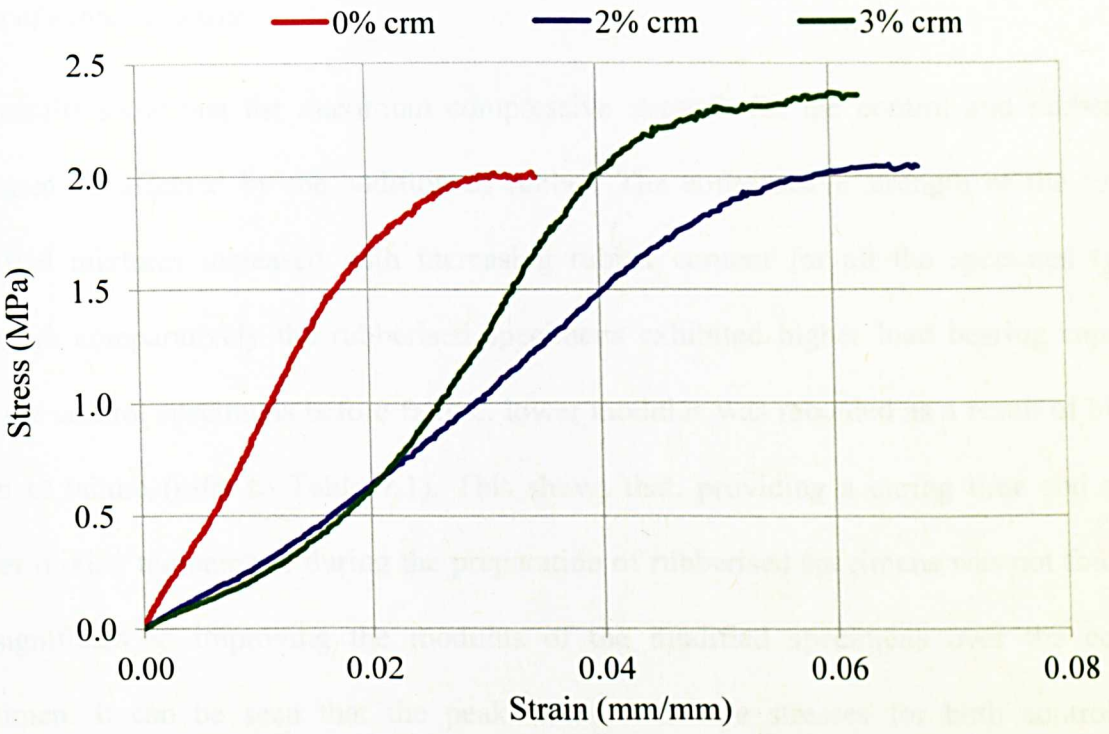

Figure 7.2 Stress-strain plots of specimens subjected to Uniaxial Monotonic Compression at 25°C

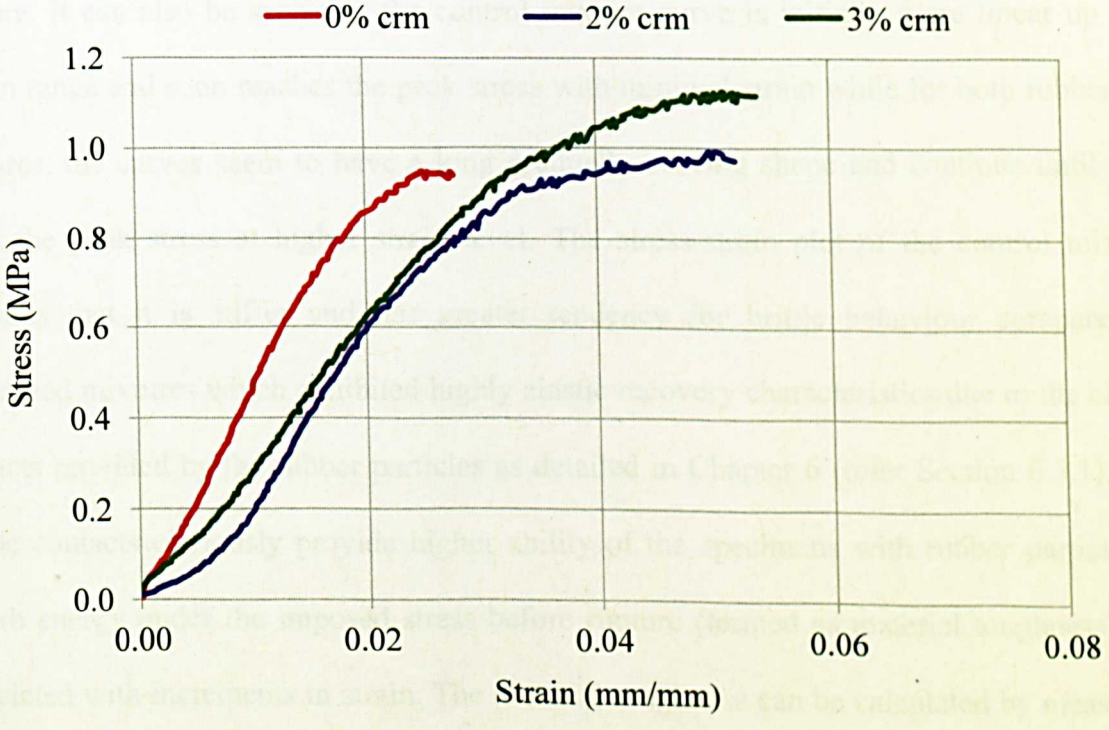

Figure 7.3 Stress-strain plots of specimens subjected to Uniaxial Monotonic Compression at 40°C

Effect of rubber content

The results show that the maximum compressive strength for the control and rubberised specimens is affected by the addition of rubber. The compressive strength of the rubber modified mixtures increased with increasing rubber content for all the specimen types. Although comparatively the rubberised specimens exhibited higher load bearing capacity than the control specimens before failure, lower modulus was recorded as a result of higher strain at failure (refer to Table 7.1). This shows that, providing a curing time and using higher mixing temperature during the preparation of rubberised specimens was not found to be significant to improving the modulus of the modified specimens over the control specimen. It can be seen that the peak stress or failure stresses for both control and rubberised mixtures are comparable although there are differences in their stress-strain plots, in that the linear portion of control mixture plot is steeper than that of the rubberised mixture. It can also be seen that the control mixture curve is initially more linear up to a certain range and soon reaches the peak stress with minimal strain while for both rubberised mixtures, the curves seem to have a long gradually curving shape and continue until they reach the peak stress at higher strain level. The stress-strain plot of the control mixture indicates that it is stiffer and has greater tendency for brittle behaviour compared to rubberised mixtures which exhibited highly elastic recovery characteristics due to the elastic contacts provided by the rubber particles as detailed in Chapter 6 (refer Section 6.3.1). The elastic contacts obviously provide higher ability of the specimens with rubber particles to absorb energy under the imposed stress before rupture (termed as material toughness) and associated with increments in strain. The material toughness can be calculated by measuring the area under the stress-strain curve. Higher material toughness results in greater material

resistance to fracture. Table 7.2 lists energy absorption values for different materials, with rubber having the highest modulus of toughness and energy absorption (Gordon, 1978).

Table 7.2 Energy absorption of various materials (Gordon, 1978)

Material	Maximum strain (%)	Maximum stress (MPa)	Modulus of toughness (MJ/m^3)	Density (kg/m^3)	Maximum energy (J/kg)
Iron	0.03	70	0.01	7800	1.3
Spring steel	0.3	700	1.0	7800	130
Wood	0.3	120	0.5	600	900
Rubber	300	7	10.0	1200	8000

Effect of testing temperatures

The effect of testing temperatures was evaluated at 25°C and 40°C. Increasing the testing temperature appeared to reduce both the compressive strength of the specimens and their toughness. Similar curve patterns were observed at both testing temperatures and increasing the rubber content resulted in a marginal increase in the compressive strength and toughness of the rubberised mixtures over that of the control mixture. The aforementioned behaviour suggests that the rubber particles retained their function as elastic aggregates within the gap graded mixture despite being exposed to a high temperature. The mixture's elasticity is also believed to have been further enhanced through binder modification arising from the rubber-bitumen interaction. Earlier in Chapter 2 it was suggested that the addition of rubber to the mixture could potentially reduce the mixture's temperature susceptibility by enhancing its

elasticity at higher service temperatures. To investigate this possibility further, scanning electron microscopy (SEM) examinations were carried out on mechanically tested specimens to assess the extent of any physical change in the rubberised mixture compared to the control specimen. Figures 7.4 and 7.5 show the deformed specimen after testing with minor dilation having occurred in its middle section and cracks evident on its surface. The specimen was trimmed to form a small cylindrical specimen (of approximate dimension; diameter = 50 mm, height = 15 mm) and its surface was coated with aluminum. Figure 7.6 shows the specimens prepared for SEM scanning. Figure 7.7 shows an SEM backscatter-mode capture of the microstructure of the mastic region of the specimen. At high temperature, the surface of the mastic or binder of the control mixture appears wavy whereas the mastic of fine rubberised mixture seems more compact and smooth with very little distortion. The aforementioned observations are in line with an earlier mentioned point that the addition of rubber particles to asphalt has the potential to reduce its temperature susceptibility, in particular the surrounding mastic by stiffening the bitumen at high temperature. However, the limitation of this aspect of the investigation was that only a small portion of the surface was exposed during scanning. Consequently two specimens of each mixture type were prepared and scanned, and several images were randomly captured at the area that is presumed to be representative of the structure.

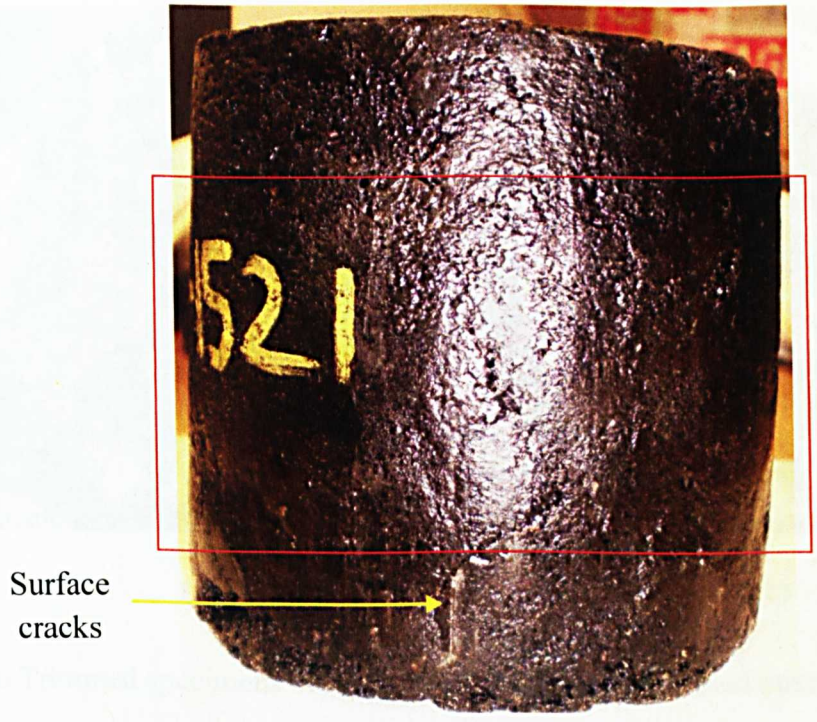

Figure 7.4 Deformed specimen at of the control mixture (test stopped at peak stress)

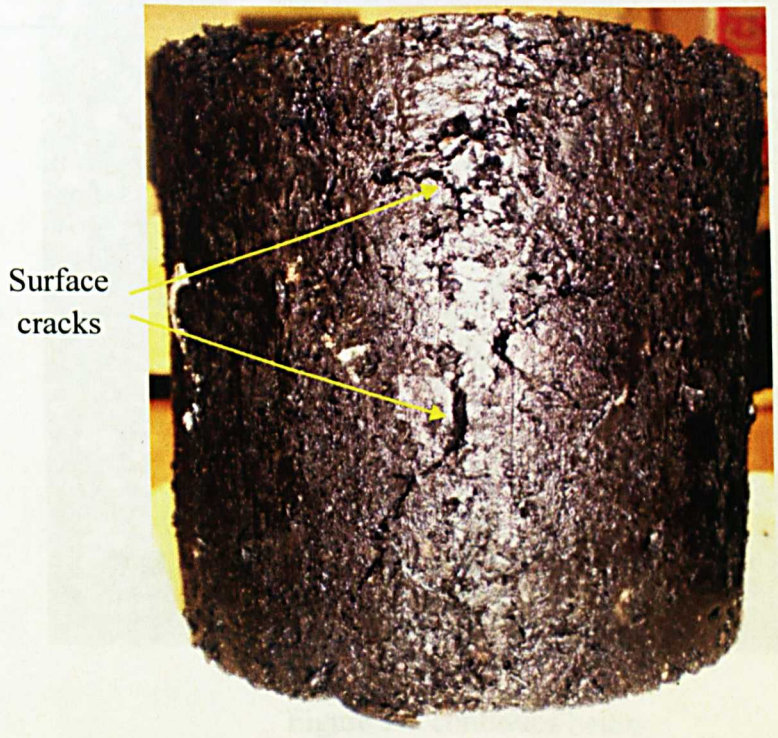

Figure 7.5 Deformed specimen of rubberised mixture (test stopped at peak stress)

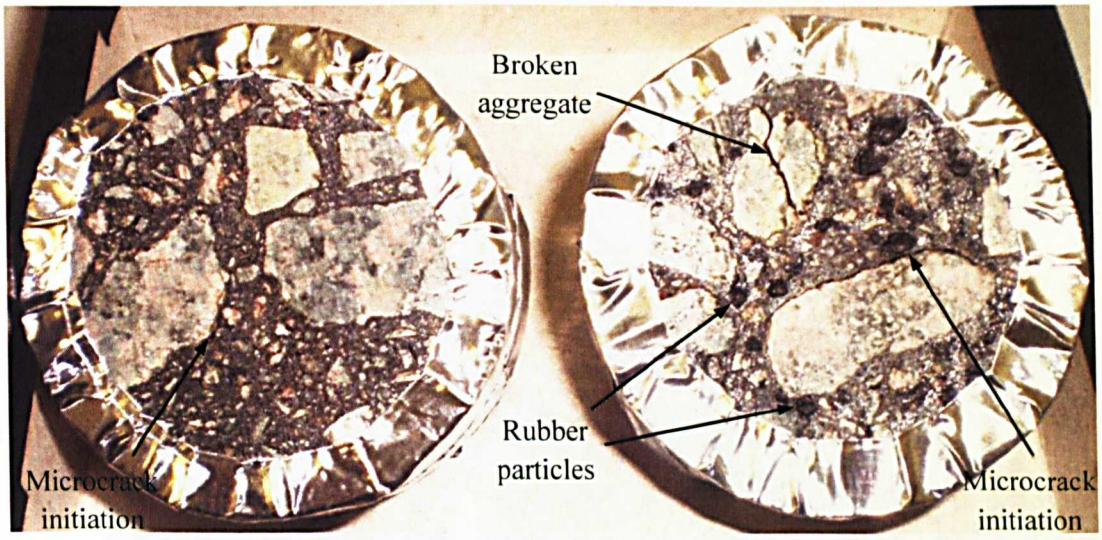

Figure 7.6 Trimmed specimens of the (a) control and (b) rubberised mixture for SEM scanning

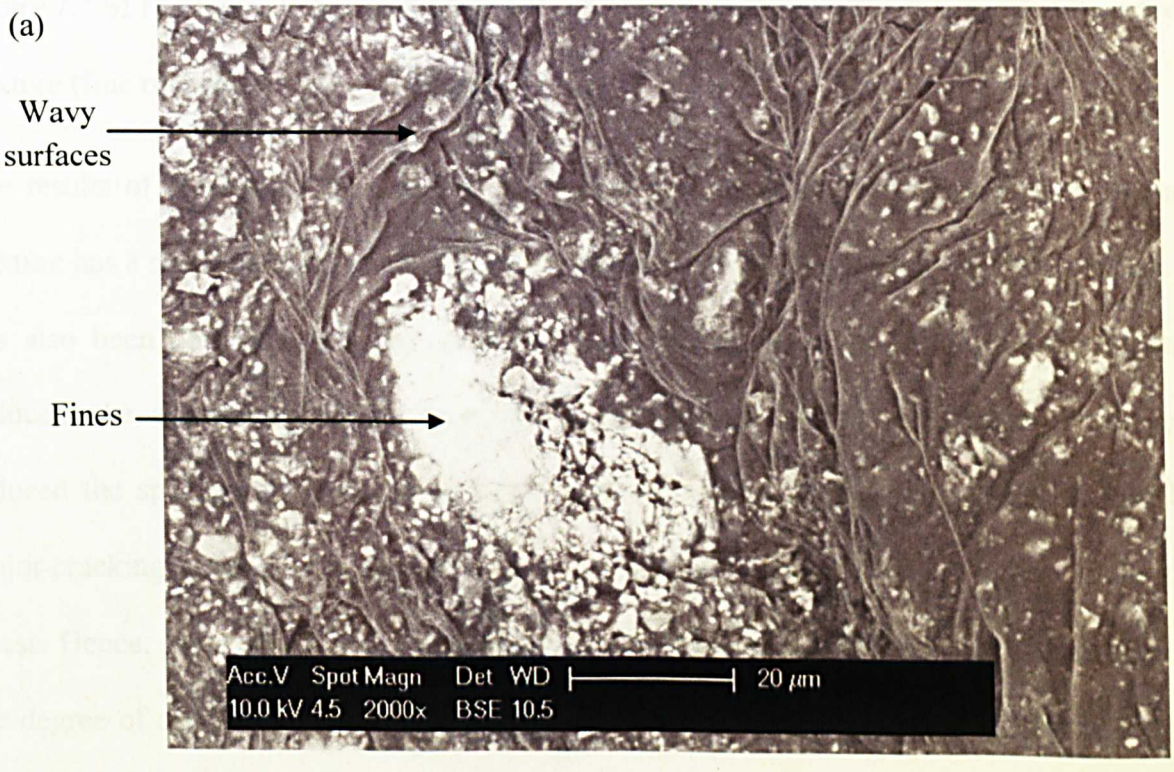

Figure 7.7 continues below

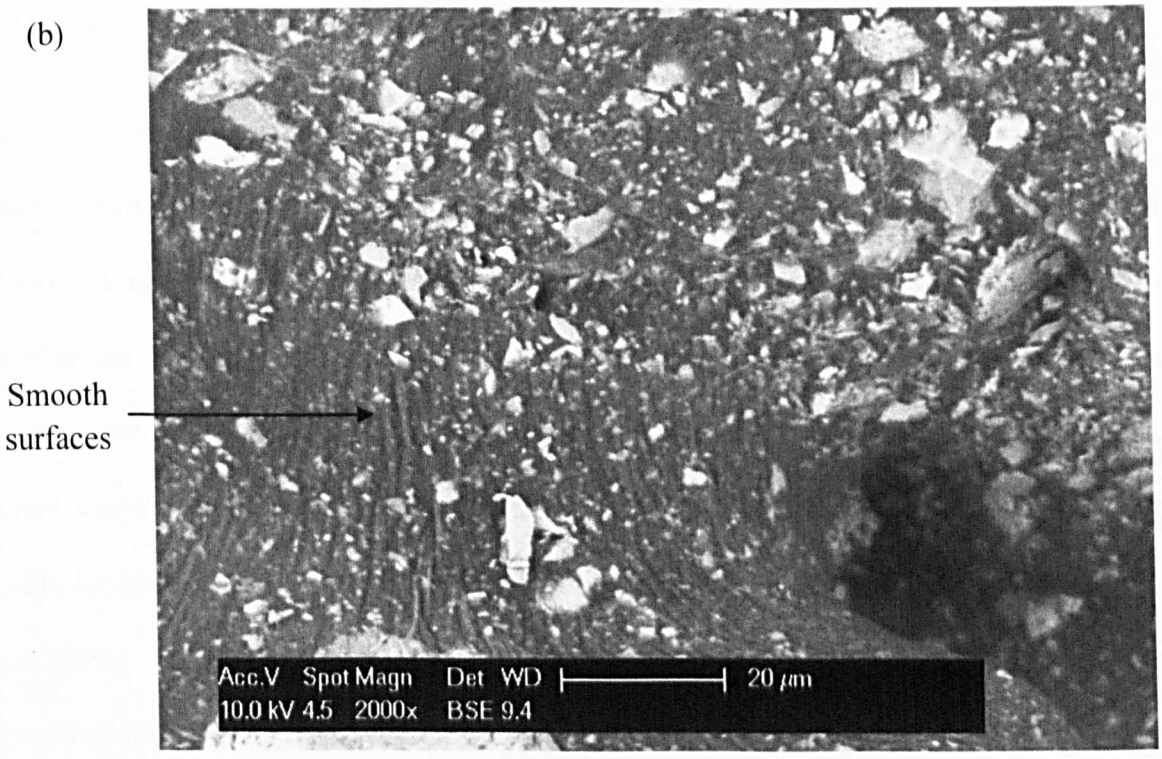

Figure 7.7 SEM images in backscatter-mode of mastic for (a) control mixture (b) rubberised mixture (fine rubber) at high temperature

The results of the simple mechanical tests conducted show that adding rubber to asphalt mixture has a significant effect on the mixture's resistance against permanent deformation. It has also been demonstrated that although the stiffness of the rubberised specimen was reduced, the specimen's ability to resist fracture increased, which in turn would have reduced the specimen's tendency to fail through cracking. However, specimen failure by major cracking when in compression is not usual since the cracks tend to close up under the stress. Hence, the changes in air voids properties distribution can be used to better describe the degree of specimen's damage at failure compared to crack examination. The following section examines the internal structural damage of different mixtures with respect to changes in their voids structure properties after the specimens have been subjected to Uniaxial Monotonic Compression.

7.2.2 Microstructural Damage Analysis

Air voids in asphalt mixtures vary in shape, quantity, size and interconnectivity. In this study, microstructural damage analysis of the deformed specimens was carried out using X-ray CT images by noting the changes in the air void properties within specimens after mechanical tests had been conducted. The measured parameters were categorised as air voids content properties (i.e. voids total area, voids number and average voids size), air voids shape properties (i.e. voids aspect ratio, circularity, roundness and solidity) and air voids location (average radius or the distance between voids' centroid to the centre of a specimen). Table 7.3 shows the average percent changes in the air voids properties for mechanically tested specimens as determined using image analysis for different mixtures and testing temperatures. A positive value recorded for a specific property in the table represents an increase in the magnitude of that property whereas recorded negative values are indicative of decreasing magnitudes of the associated air voids properties.

Statistical analysis of variances (ANOVA) and Student's T-tests were conducted at a 95% level of confidence to determine if the apparent correlations between the two key variables (rubber content and testing temperature) and the changes in the air voids properties were statistically significant. The p values from the ANOVA and Student's T-tests calculated to assess the statistical significance are summarised in Table 7.4. A p value of 0.05 or less indicates that the result associated with that p value under consideration is statistically significant, whereas a p value greater than 0.05 is indicative of a result that is not statistically significant. The values shaded in grey refer to changes in the air voids properties determined to be not statistically significant.

Table 7.3 Summary of the average changes in air voids properties

Air voids properties		Average changes in air void properties (%)					
		25°C			40°C		
		0% crm	2% crm	3% crm	0% crm	2% crm	3% crm
Air voids content properties	Total voids area	19.2	9.6	74.3	93.7	33.1	108.1
	Voids number	-32.3	0.2	9.8	15.5	21.1	28.5
	Ave. voids size	71.2	11.3	59.1	79.3	9.8	62.7
Air voids shape properties	Aspect ratio	10.9	1.8	0.1	12.8	8.3	5.0
	Circularity	-5.0	-1.0	-2.8	-6.7	-1.2	-2.6
	Roundness	-4.9	-1.3	-1.1	-7.3	-3.1	-1.6
	Solidity	-1.6	-0.8	-0.8	-2.9	-0.5	-0.5
Radius (voids location)		-3.3	-2.4	-2.5	2.4	-0.8	1.7

Table 7.4 P-values of ANOVA and Student's T-test for the changes in air voids properties

Air voids properties	P-values				
	Rubber content (0, 2 and 3%) (ANOVA)		Testing temperature (25 and 40°C) (T-test)		
	Test at 25°C	Test at 40°C	For 0% crm	For 2% crm	For 3% crm
Total voids area	0.0001	0.0006	0.0013	0.0025	0.028
Voids number	0.0001	0.2800	0.0001	0.0001	0.0002
Ave. voids size	0.0001	0.0007	0.7100	0.8300	0.7400
Aspect ratio	0.0001	0.0001	0.5300	0.0025	0.0001
Circularity	0.0001	0.0001	0.0840	0.7900	0.6600
Solidity	0.0110	0.0001	0.0052	0.3700	0.065
Roundness	0.0001	0.0001	0.0170	0.0610	0.2600
Radius (voids location)	0.0077	0.3100	0.0780	0.1800	0.3600

It is evident from the p values (tabulated above) that varying the rubber content of specimens had an effect on almost all the air void parameters except the number of voids and average radius value when the specimen was tested at 40°C. On the other hand, varying testing temperature yielded statistically reliable outcomes for only air voids areas and voids number. For the air voids' shape properties, the only statistically significant change for the rubberised mixtures was in the air voids' aspect ratio and in the voids solidity and roundness were determined to be for the control mixture. Through the statistical analysis conducted it is concluded that varying the rubber content of a mixture may contribute to the measured changes in the air voids properties to a greater extent than varying the testing temperature.

The distributions of the air voids properties for different mixtures tested at 25°C and 40°C are shown in Figures 7.8 and 7.9 respectively. The bar graphs compare the changes in the air voids properties for the different mixtures by averaging the air voids properties along the height of the specimens at 5 mm intervals (or 0.05 relative heights). An observation of the individually presented air voids parameter distributions along the specimen's height, led to several noteworthy observations. Significant changes in the properties distribution along the specimen's height were revealed in three main regions referred to as bottom (0-30 mm or 0-0.3 relative height), middle (30-70 mm or 0.3-0.7 relative height) and top (70-100 mm or 0.7-1.0 relative height). Relative height is the ratio of the referred specimen height (at any level) to the total height of the specimen. The total height of the specimen initially before the test was approximately 100 mm, but became less after it was deformed in the compression test. Explanations on the measured parameters of the air voids content properties, air voids shape properties and air voids location are significantly correlated in the following sub-sections with reference to Figures 7.8 and 7.9.

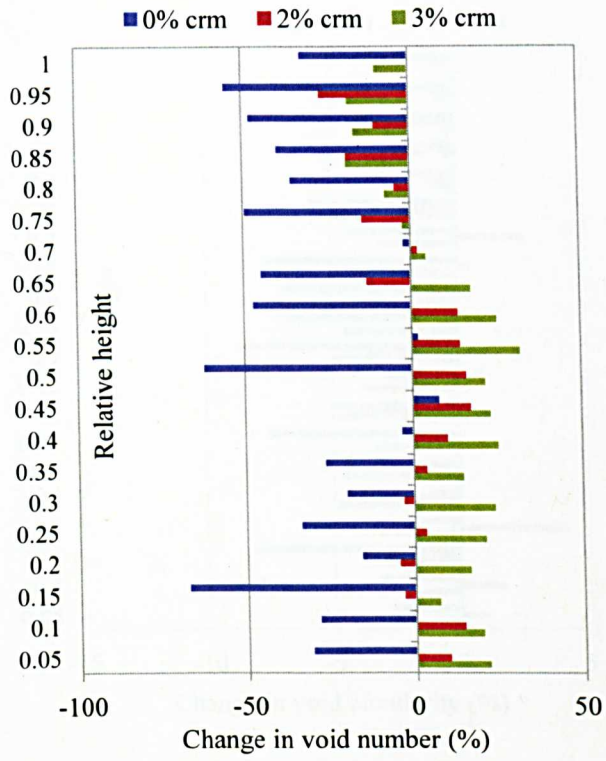

(a)

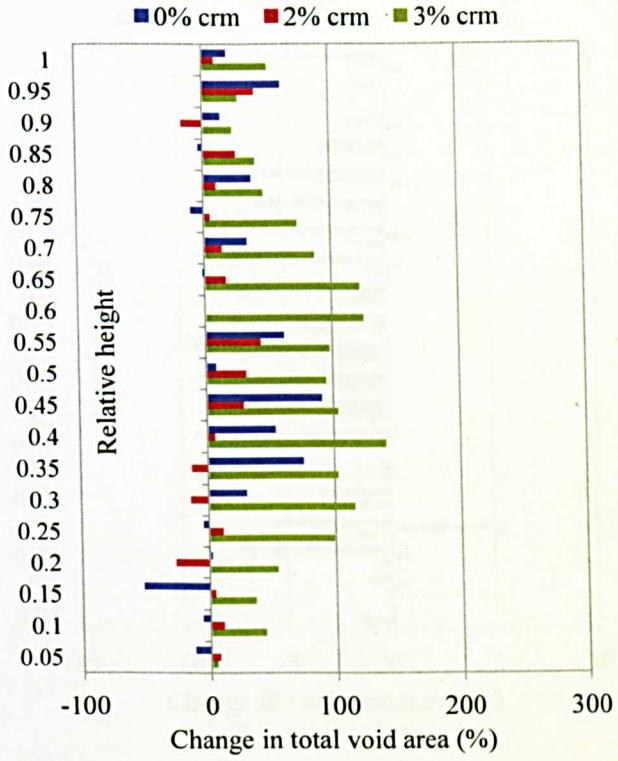

(b)

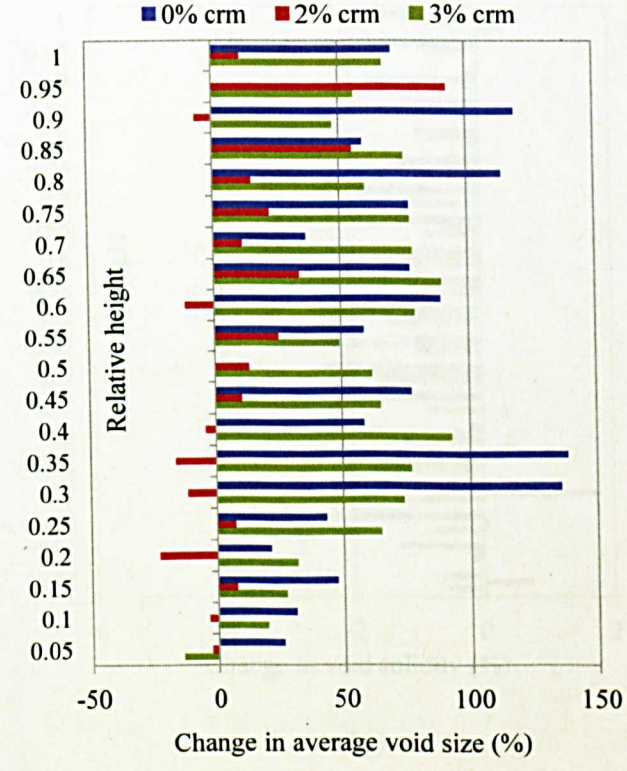

(c)

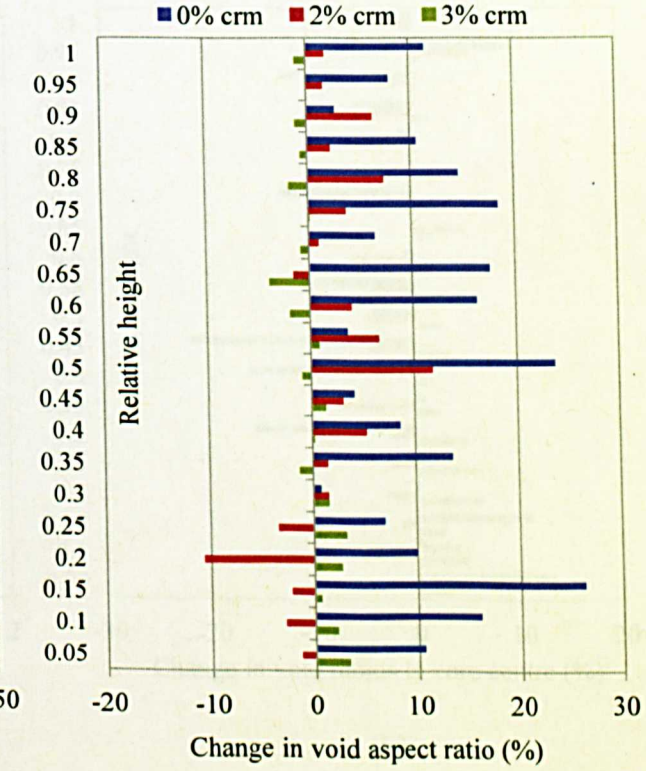

(d)

Figure 7.8 continues below

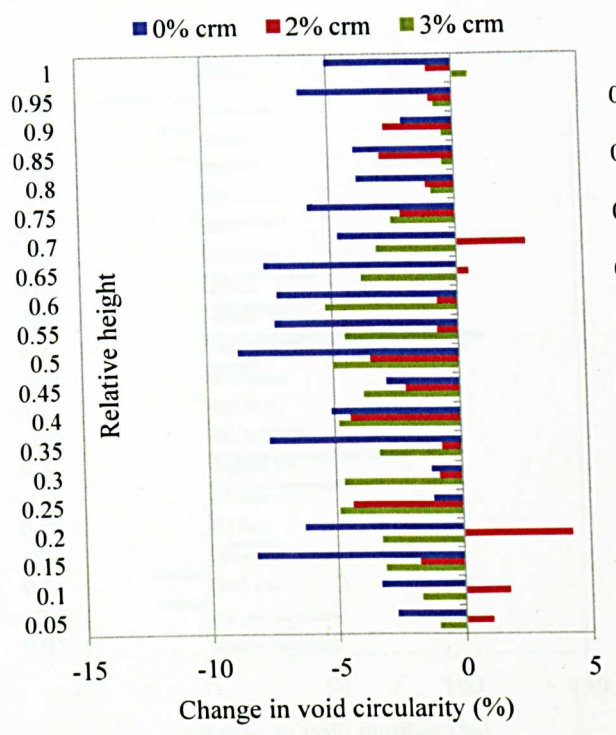

(e)

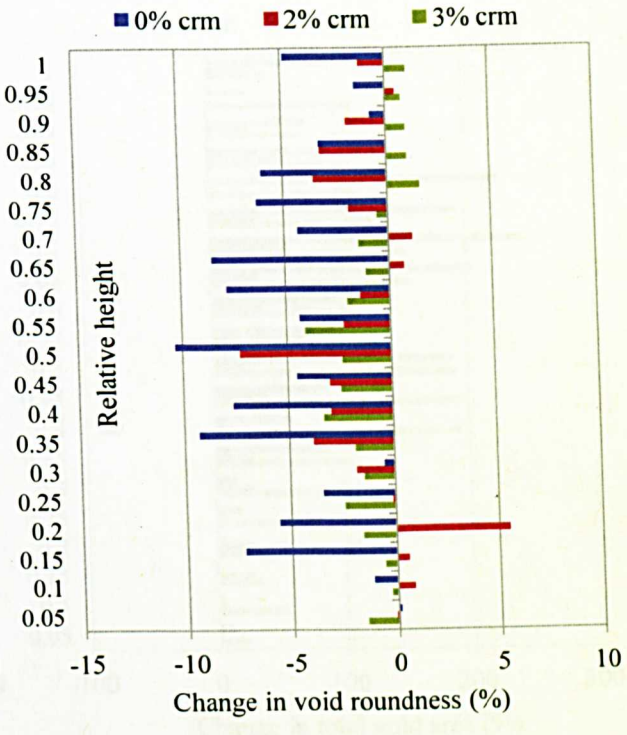

(f)

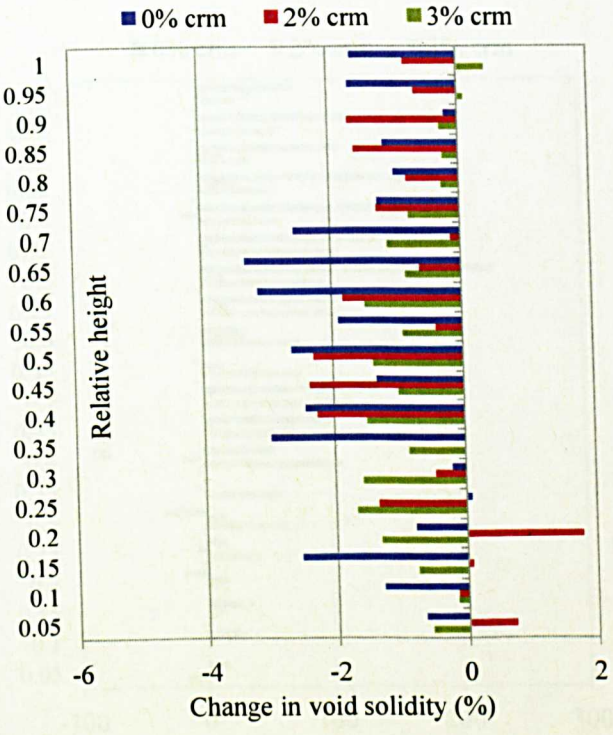

(g)

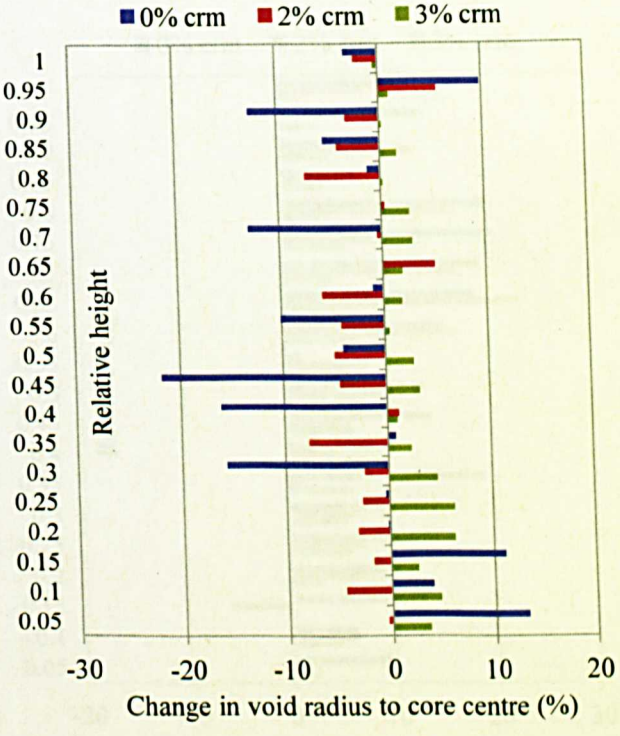

(h)

Figure 7.8 Changes in void properties:(a) total area; (b) number; (c) average size; (d) aspect ratio; (e) circularity; (f) roundness; (g) solidity; (h) radius distribution tested at 25°C

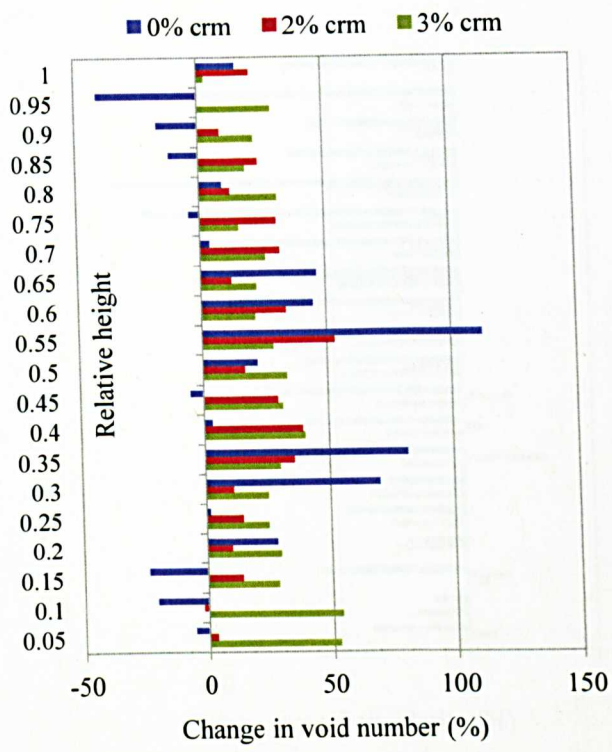

(a)

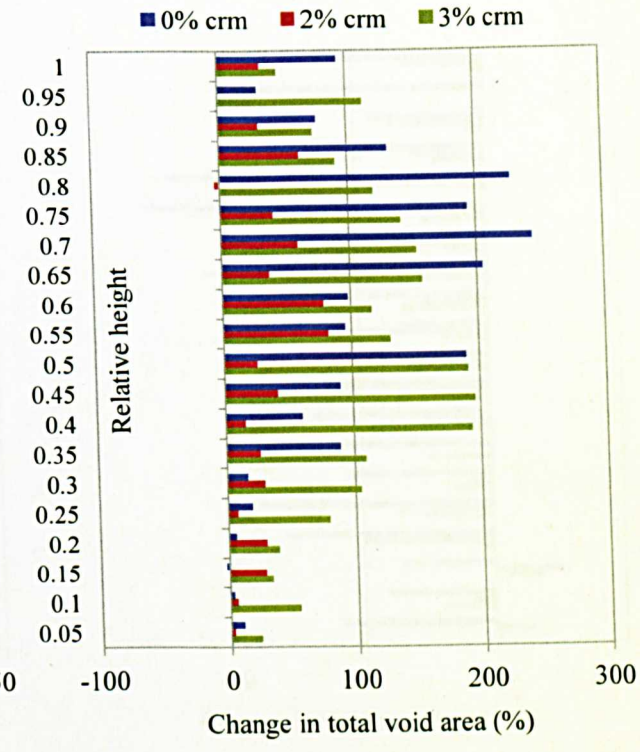

(b)

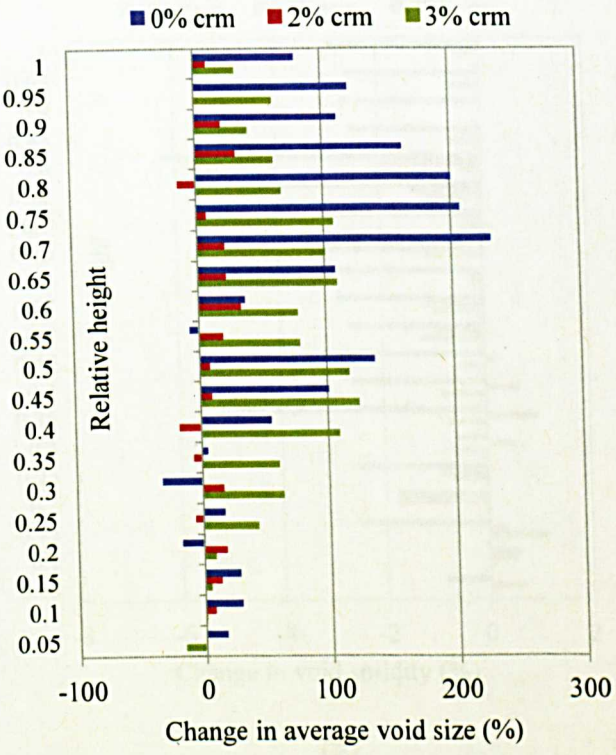

(c)

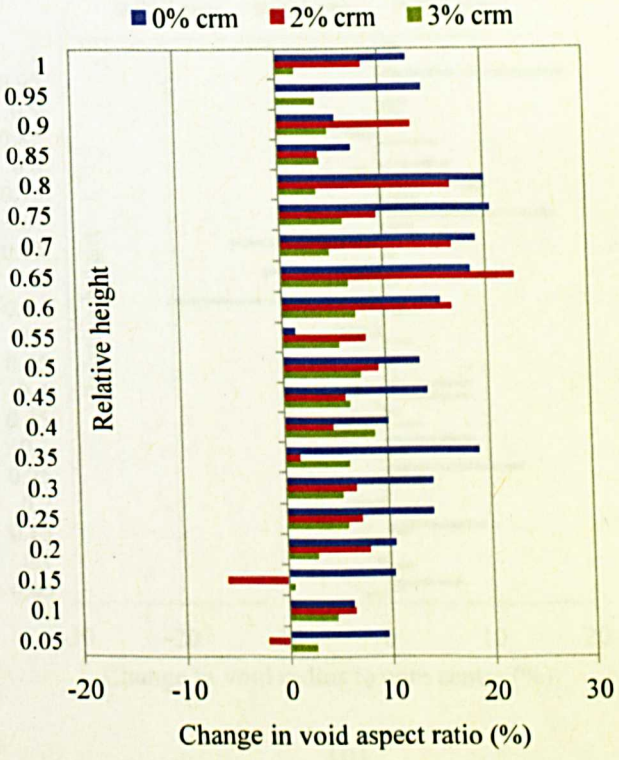

(d)

Figure 7.9 continues below

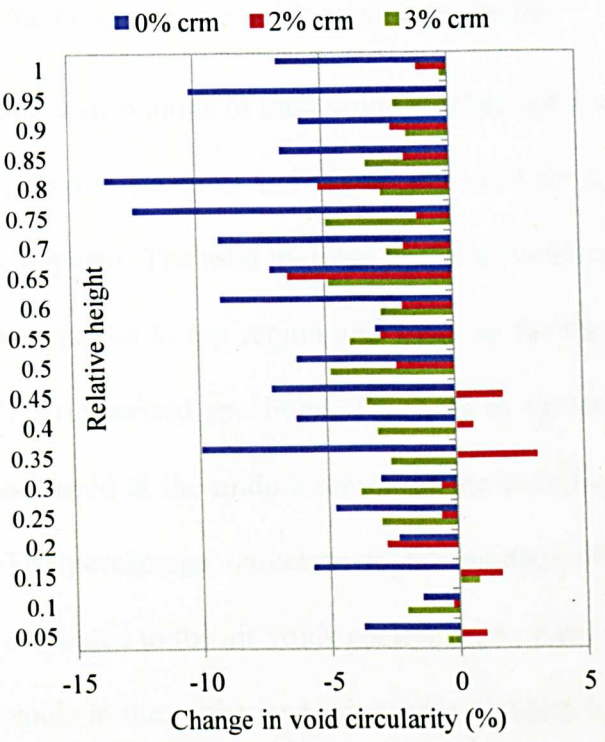

(e)

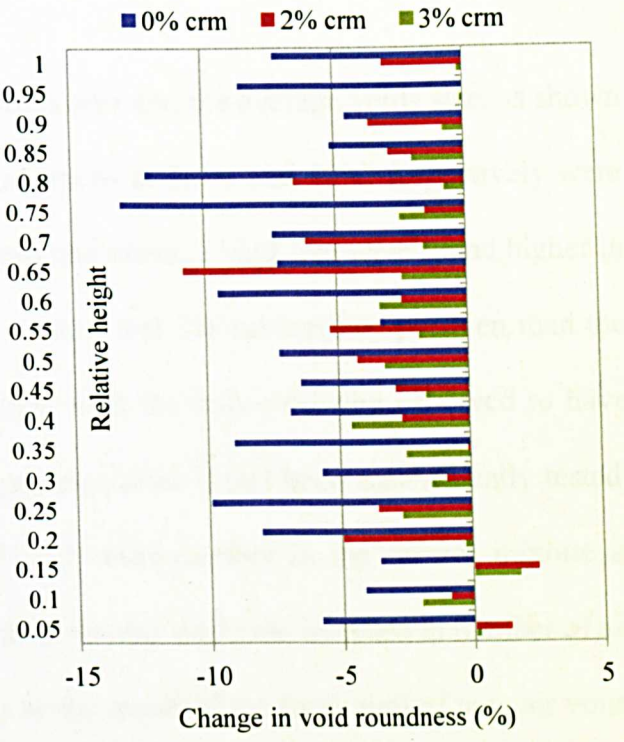

(f)

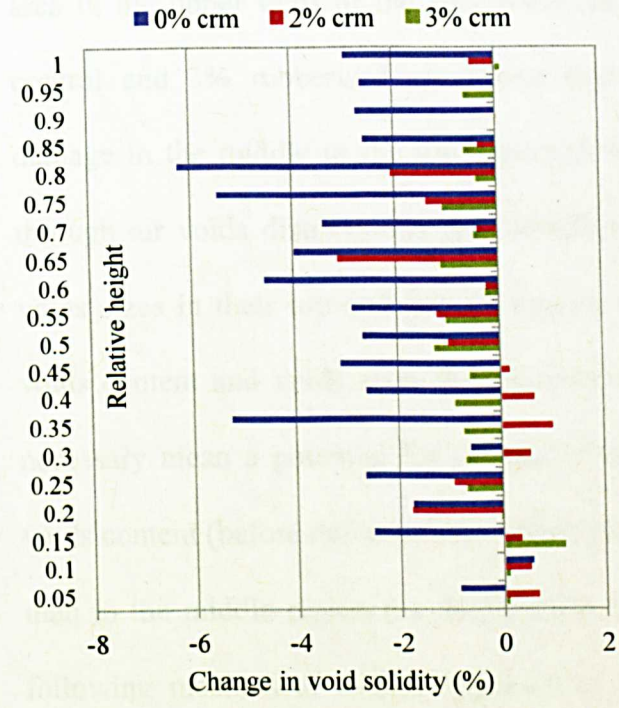

(g)

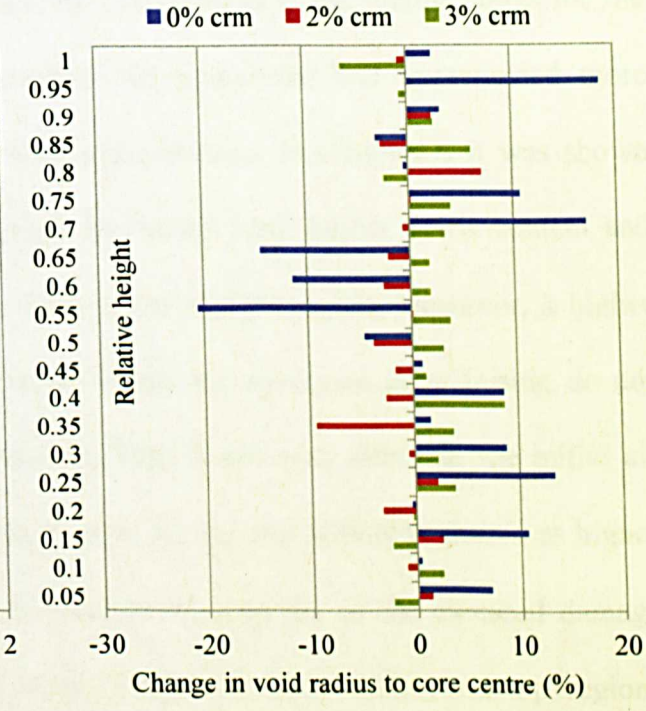

(h)

Figure 7.9 Changes in void properties: (a) total area; (b) number; (c) average size; (d) aspect ratio; (e) circularity; (f) roundness; (g) solidity; (h) radius distribution tested at 40°C

Changes in the air voids content properties

The distributions of total voids number, total voids area and the average voids size, as shown in Figure 7.8 (a-c) and Figure 7.9 (a-c) for specimens at 25°C and 40°C respectively were compared. The total increase in the air voids area and average void size were found higher in the middle to top region and more so for the control and 3% rubberised specimen than the 2% rubberised specimen. This was in agreement with the minor dilation observed to have occurred at the middle region of the tested specimen after it had been mechanically tested. The percentage reduction in the number of total voids number in the control mixture is attributed to the air voids coalescing to form microcracks while the increase in number of air voids in the rubberised mixtures is thought to be the result of the formation of new air voids under the loading. When the specimens were tested at high temperature, their total voids area in the upper third of the specimens increased considerably, exceeding 100% for the control and 3% rubberised specimens indicating the specimens had experienced more damage in the middle to the top region of their cross-section. In Chapter 6 it was shown through air voids distributions that undeformed specimens have higher voids content and voids sizes in their top and bottom regions than in the middle region. However, a higher voids content and voids sizes that initially exist within the specimen prior testing do not necessary mean a potential for damage initiation. This is because, although the initial air voids content (before deformation) in the few slices at the top and bottom regions was higher than in the middle region (as detailed out in Chapter 6), majority of the assessed damage following mechanical testing appeared to have occurred in the middle and top regions (Figures 7.8 and 7.9). Based on this study, the changes in the total voids number and total voids area were identified as two key parameters when describing different damage phenomena that occur within a specimen as a result of deformation. According to Roberts et

al. (1996), Garba (2002) and Song (2004), two main mechanisms occur under permanent deformation namely, densification and shear deformation. By comparing the changes in the voids number and voids area analysed from X-ray images as in Figures 7.8 and 7.9, few observations can possibly be correlated to the damage mechanisms associated with the deformation under compression as summarised in Table 7.5. The association between the damage mechanisms and the air voids properties is then further clarified in the subsequent sub-section with respect to the changes in air voids shape properties.

Table 7.5 Correlation between damage mechanisms and changes in air voids content properties

Damage mechanism	Changes in total voids number	Changes in total voids area	Damage description	Observations from X-ray images analysis
Densification	Decrease	Decrease	- Material's hardening - Air voids closure	- Figure 7.8 (a & b); bottom section (control mixture)
Shear deformation	Decrease	Increase	- Debonding at binder-aggregate interface - Microcracks initiate and coalesce	- Figure 7.8 (a & b); for middle (control) and top sections (all mixtures) - Figure 7.9 (a & b); a few slices at top and bottom for control mixture
	Increase	Increase	- New air voids formed - Microcracks propagation - Dilation caused by the plastic flow - Increase in volume	- Figure 7.8 (a & b); middle section (rubberised mixtures) - Figure 7.9 (a & b); mainly for rubberised mixtures

Changes in the air voids shape properties

Figure 7.8 (d-g) and Figure 7.9 (d-g) show the percentage changes in the air voids shape properties i.e. the aspect ratio, circularity, roundness and solidity. The figures indicate that the air voids became increasingly elongated suggesting that crack growths were initiated within the specimens, under the applied load. With the voids size increase, two adjacent air voids are likely to have coalesced forming an air void with an aspect ratio higher than its pre-coalescing aspect ratios and leading to the initial formation of microcracks (increase in length). When the different mixtures were compared, the formation of cracks in the control mixture was found higher than the rubberised mixtures, evidenced by the increase in aspect ratio and decrease in the circularity, roundness and solidity of the air voids. It was fairly easy to make the aforementioned observations, as the specimens tested at high temperature of 40°C had experienced more damage particularly in the middle region. This again confirms the previous finding on the changes in the air voids content properties, which proposed that a decrease in voids number is indicative of the presence of microcracks and macrocracks in the mechanically tested specimens and such may have contributed to the dilation observed in the middle region of the specimen. The same was observed for 2% rubberised specimen, while the 3% rubberised specimen showed the least likelihood of its air voids shapes becoming cracks. This suggests that, the elongated voids observed in the rubberised specimens in their undeformed state as described earlier in Chapter 6 do not necessarily imply a potential for crack initiation. Overall, even though there was evidence of increasing total air voids area and average voids size of the control and rubberised specimens after deformation, measurements of voids number and shape properties provide a different way of describing air voids properties in terms of air voids formation, growth, connectivity and propagation.

For the control specimen, damage was determined to have occurred as a result of small air voids coalescing to form microcracks, increasing the aspect ratio of the voids and thereby reducing the voids number and circularity value. This finding concurs with two failure types identified by Kim et al. (1997) who asserted that the damage in an asphalt mixture is the result of microcracks that initiate at the interfacial transition zone (ITZ) between bitumen and aggregates (adhesive failure) and within the binder (cohesive failure). Figure 7.10 illustrates the behaviour of a bituminous mixture experiencing cohesive and adhesive failure. Through SEM examination, the aforementioned phenomena were identified in one of the scanned specimens as shown in Figure 7.11.

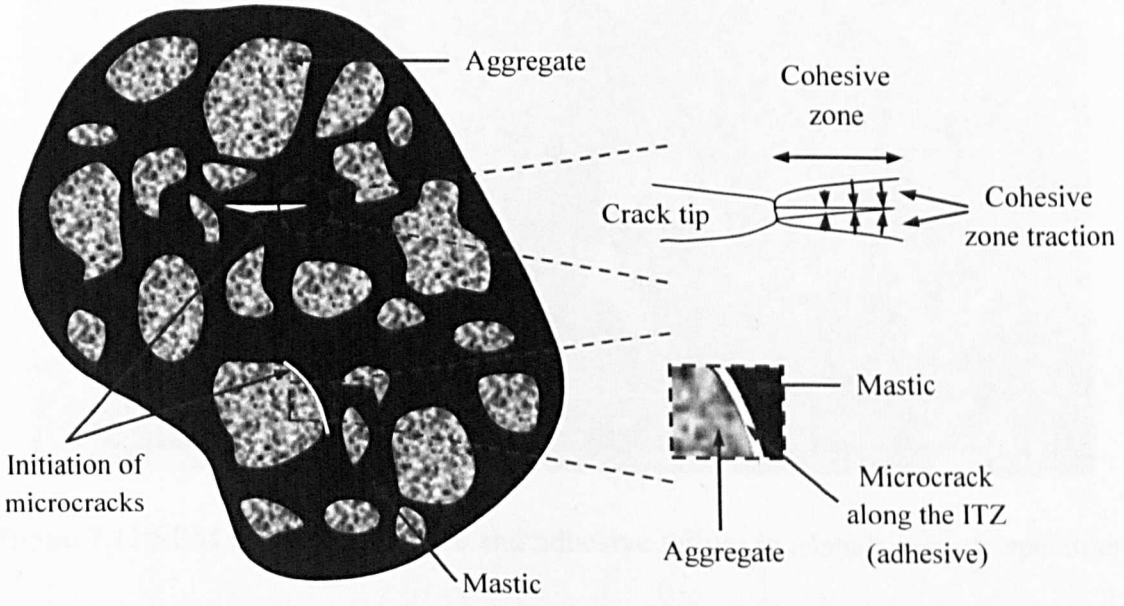

Figure 7.10 Microcracks initiation via cohesive and adhesive failure (inspired from Kim et al., 2007)

In contrast, for the rubberised specimens, the damage resulted in an increase in the number of voids and small decrease in all the shape properties indicates the formation of new air voids after the deformation and less connectivity of the voids to form crack. This is possibly because, the addition of rubber particles into the mixture tends to increase the bitumen's

viscosity through the rubber-bitumen interaction, causing the bitumen to perform as modified binder and has a better resistance against crack formation. Furthermore the ability of the surrounding rubber particles to absorb stresses at the crack tip helps to resist the air voids connectivity and reduce the potential of cracks formation within the rubberised mixtures particularly specimen modified with 3% rubber.

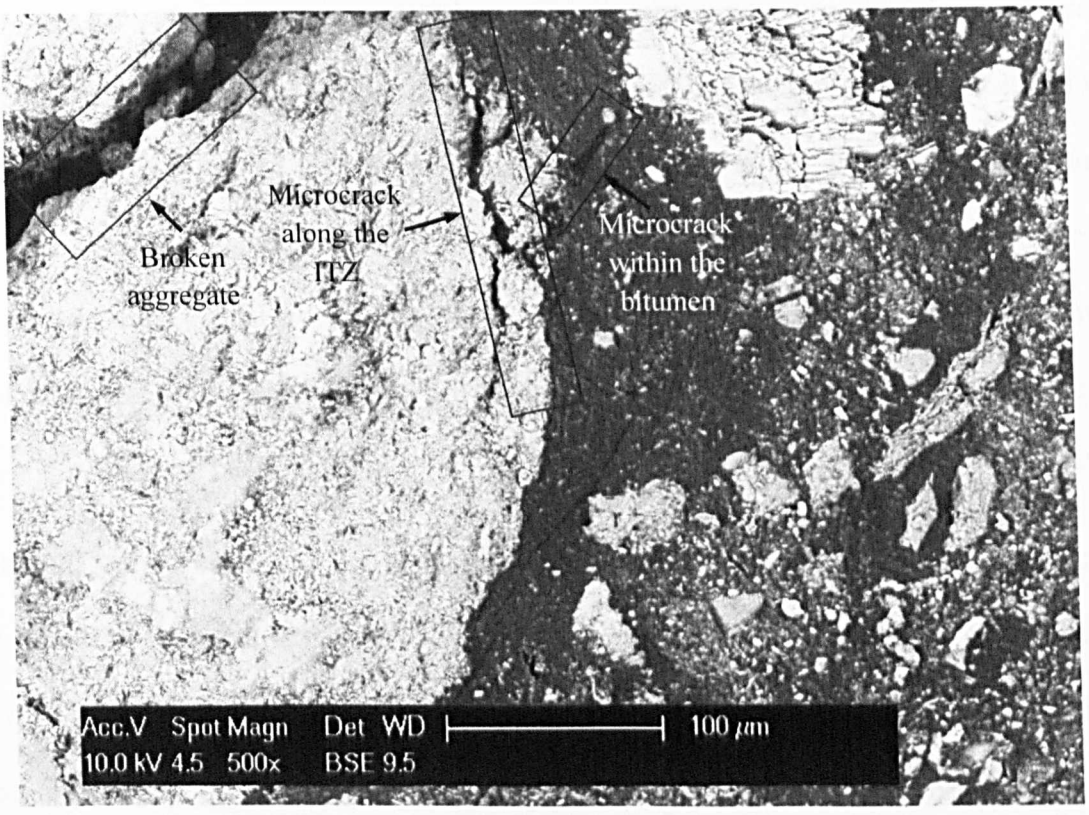

Figure 7.11 SEM image of cohesive and adhesive failure in asphalt mixture specimen

Changes in the air voids location (Radius to core centre)

Distributions of the average radius or distance of the voids from the specimens' core centre for the different mixture types are shown in Figures 7.8h and 7.9h. The measured effect of increasing the testing temperature on the average voids radius was determined as not statistically significant but the addition of rubber particles yielded some interesting results. Values of radii for rubberised specimens on average did not vary much (less than 10%) over

the height of the specimens. Increasing the rubber content of the specimens from 2% to 3%, resulted in the average air voids radius increasing outwardly i.e. towards the circumference. However for the control specimen, the air voids were found having smaller radii indicating that they had contracted, coalesced and propagated inwardly towards the specimen's core centre rather than its circumference. This most likely caused the material in the immediate vicinity of the core centre to develop microcracks and subsequently macrocracks predominantly in the middle region, resulting in a decrease in the radius at that location as compared to the bottom and top regions, thereby causing the minor dilation to the specimen. It was concluded in Chapter 6, that the air voids for the undeformed of the control specimen were predominantly located at the specimen's circumference as a result of mould confinement. Under the loading, the air voids are expected to propagate towards the core centre and reduce the voids radius.

To summarise the findings, major changes in the air voids properties occurred in the control mixture indicating that it was more susceptible to compressive damage than the rubberised mixtures. All the results appeared to conform to the dilation phenomenon that occurred at the middle section of the specimen very well. Furthermore, at 3% rubber content more damage was caused to the specimen than when it contained 2% rubbers albeit less than the damage caused to the control specimen. The results clearly show that the middle region was more susceptible to damage than the top and bottom regions, having experienced higher percent increases in the air voids area and average voids size at that particular location. Figures 7.12 to 7.17 show X-ray images of the damage distribution at three main regions of the specimens with relative heights of 0.1 (bottom), 0.5 (middle) and 0.9 (top) with air voids highlighted in red. The figures compare images of the control and rubberised mixtures before and after mechanically testing both at two test temperatures, 25°C (Figures 7.12 to

7.14) and 40°C (Figures 7.15 to 7.17). It must be noted that the images (before and after deformation) have been compared on the basis of identical height ratios. Due to some movement of the aggregate particles during testing, there are minor differences between sets of compared images. In general it can be observed that the images' characteristics are consistent with the findings described earlier for the measured changes in the air voids properties. For example, severe damage was evident at the middle and top regions of the control specimen with microcracks initiated at the ITZ area following deformation, particularly for the control mixture. This phenomenon is even more prevalent with increasing aggregate sizes due to the manner in which the microcracks tend to bridge between proximal aggregates. In contrast, for the rubberised mixtures, specimen damage (increase in air voids area) is evidenced by the separated air voids that evenly distributed within the specimen's cross section. The cracks formed in the vicinity of the ITZ area were found less than those observed in the control mixture. After being formed, the microcracks and air voids are thought to have propagated to form macrocracks, thereby decreasing the specimen's strength. From the observations, it was determined that damage governed by the changes in air voids structure occurs in a variety of ways as listed below.

i. The size of existing individual air void increasing and propagating to form cracks (refer to Figure 7.17)

ii. Two separated air voids coalescing and propagating to form cracks (refer to Figures 7.14 and 7.15)

iii. New air voids are formed having potential for crack initiation (refer to Figure 7.14)

The aforementioned observations concur with those that previously recorded in Table 7.5. It is also noteworthy that they are not mutually exclusive and can act simultaneously to initiate microcracks and macrocracks under the loading.

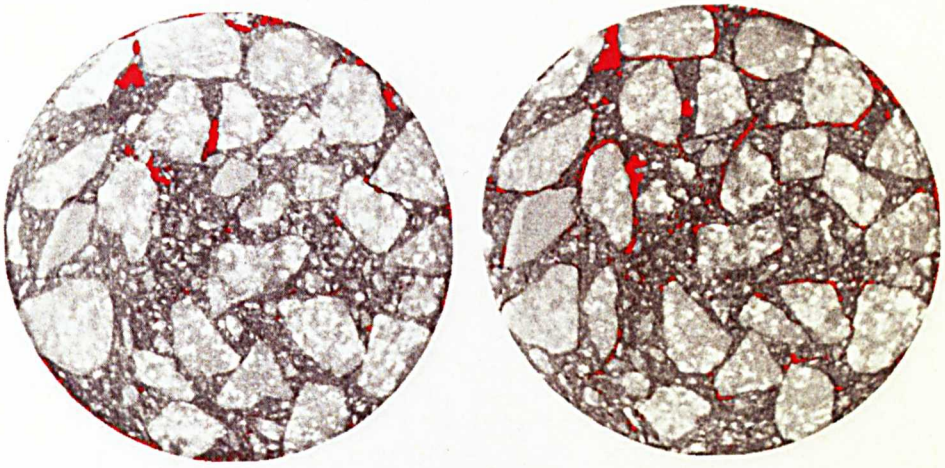

(a) 0.9 relative height (top region)

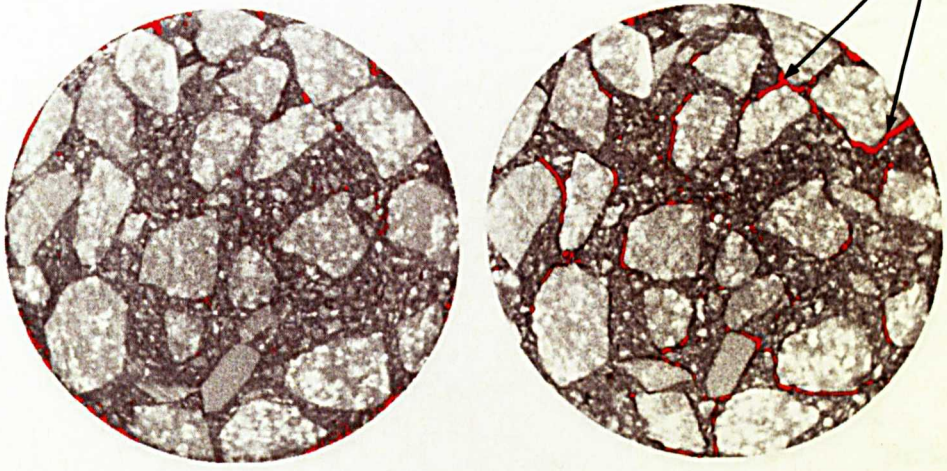

(b) 0.5 relative height (middle region)

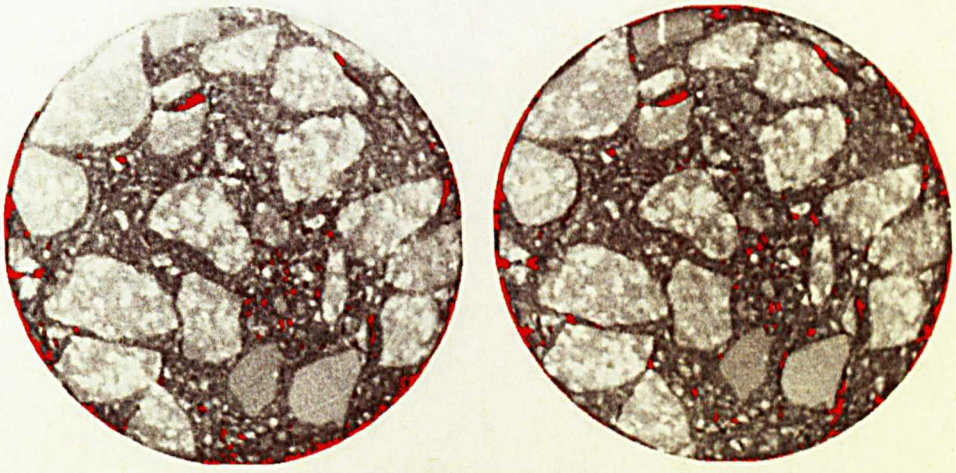

(c) 0.1 relative height (bottom region)

Figure 7.12 Comparison of image slices of unmodified specimen, before (left) and after (right) the deformation at 25°C (Specimen number: 10-1519)

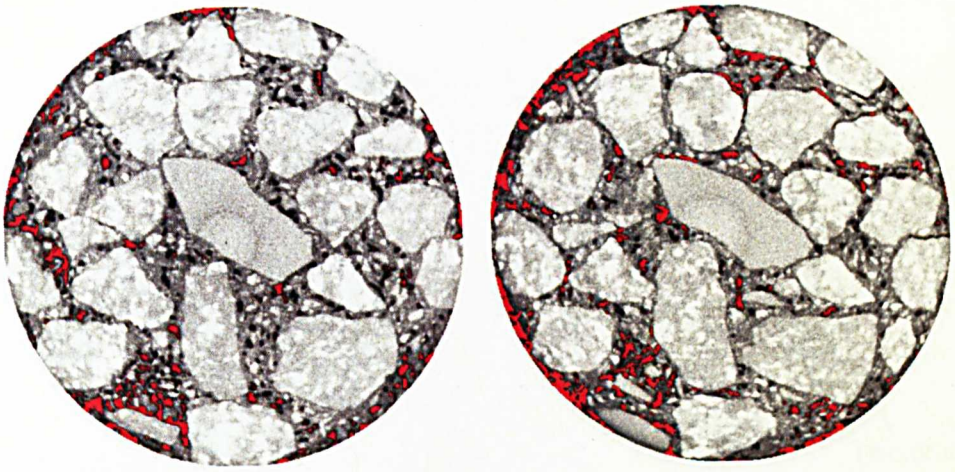

(a) 0.9 relative height (top region)

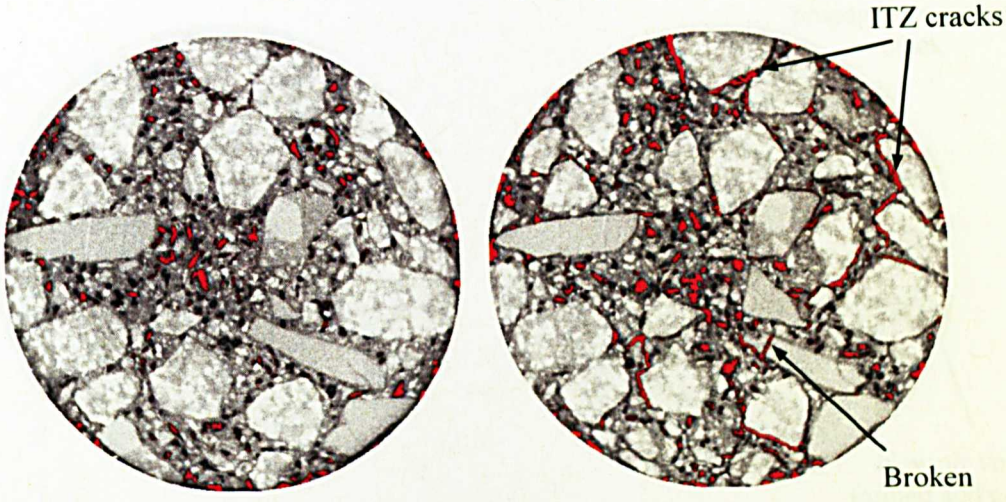

(b) 0.5 relative height (middle region)

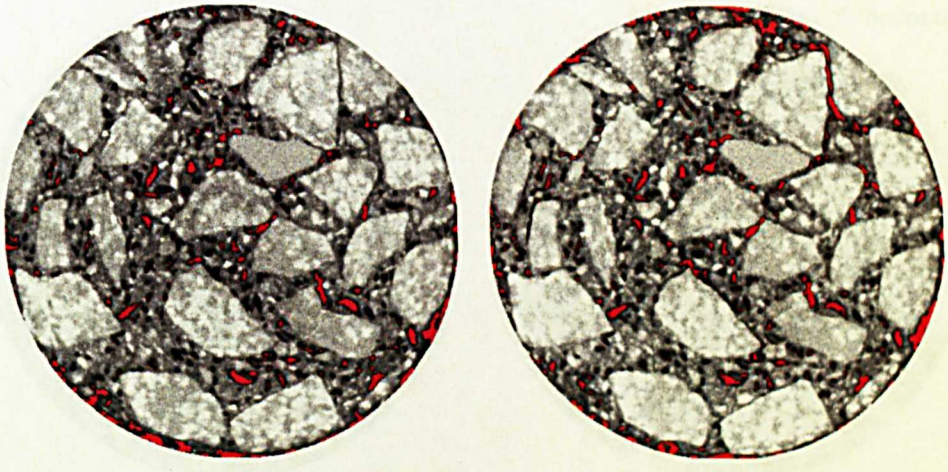

(c) 0.1 relative height (bottom region)

Figure 7.13 Comparison of image slices of modified specimen with 2% rubber, before (left) and after (right) the deformation at 25°C (Specimen number: 10-1530)

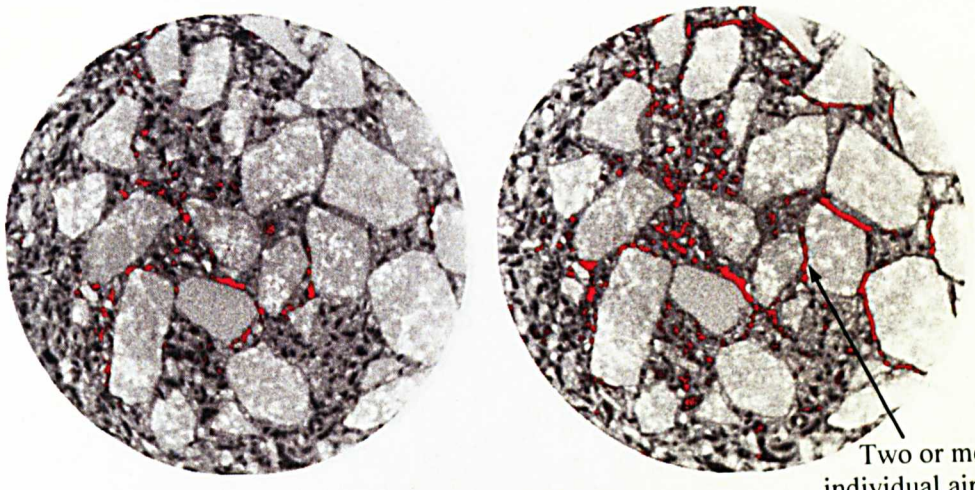

(a) 0.9 relative height (top region)

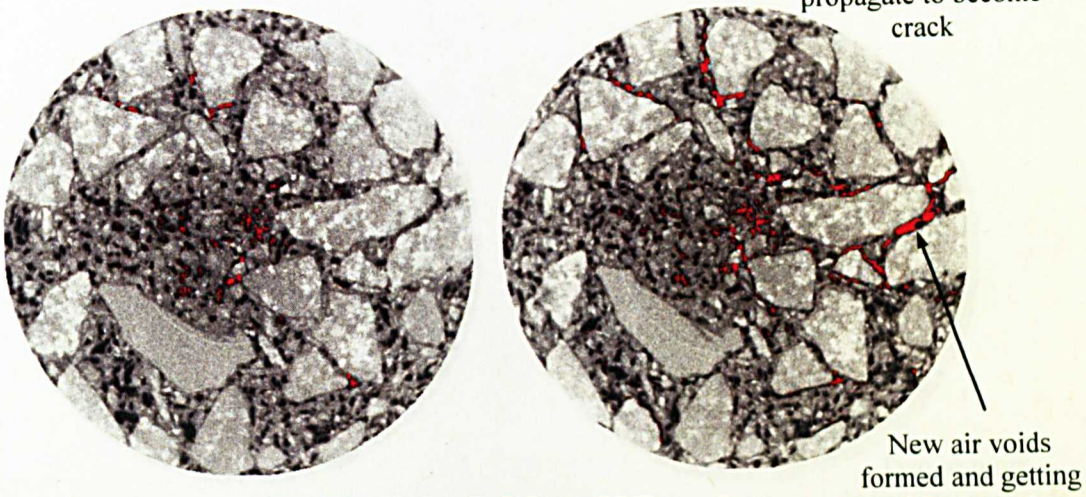

(b) 0.5 relative height (middle region)

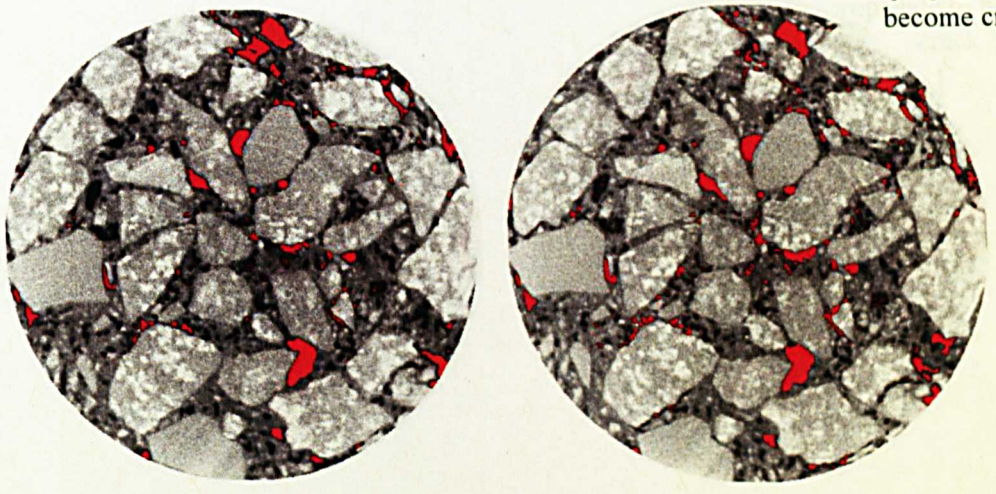

(c) 0.1 relative height (bottom region)

Figure 7.14 Comparison of image slices of modified specimen with 3% rubber, before (left) and after (right) the deformation at 25°C (Specimen number: 10-1985)

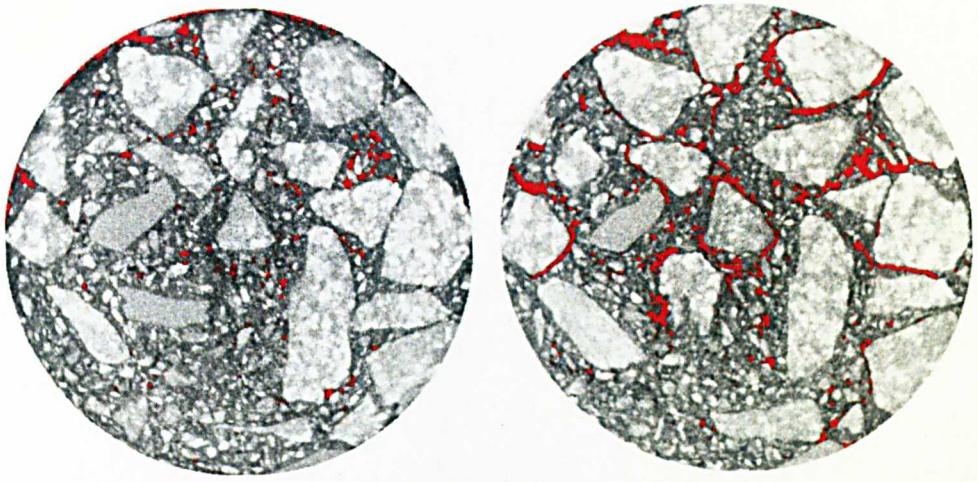

(a) 0.9 relative height (top region)

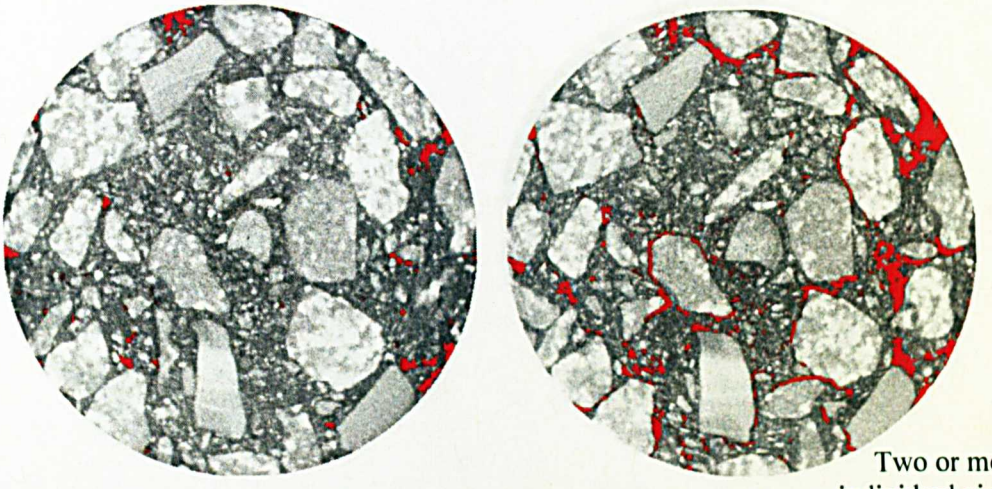

(b) 0.5 relative height (middle region)

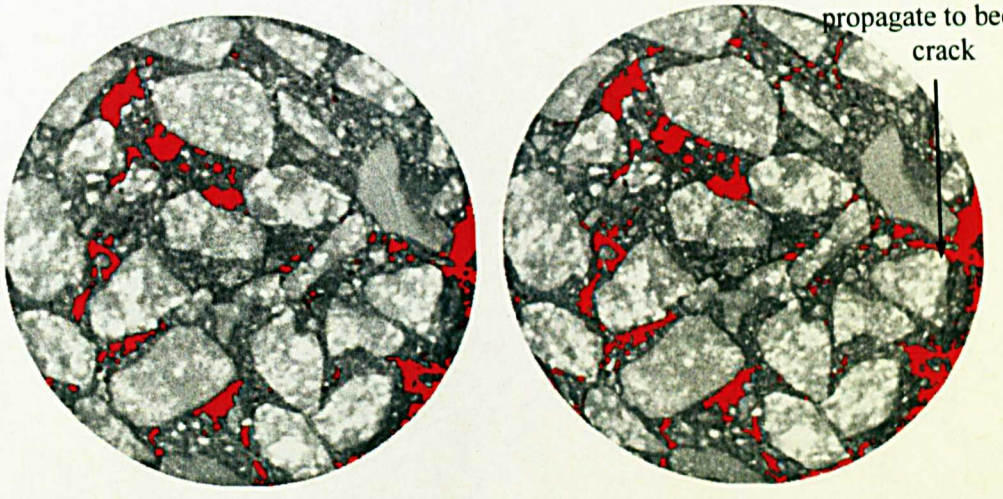

(c) 0.1 relative height (bottom region)

Figure 7.15 Comparison of image slices of unmodified specimen, before (left) and after (right) the deformation at 40°C (Specimen number: 10-1522)

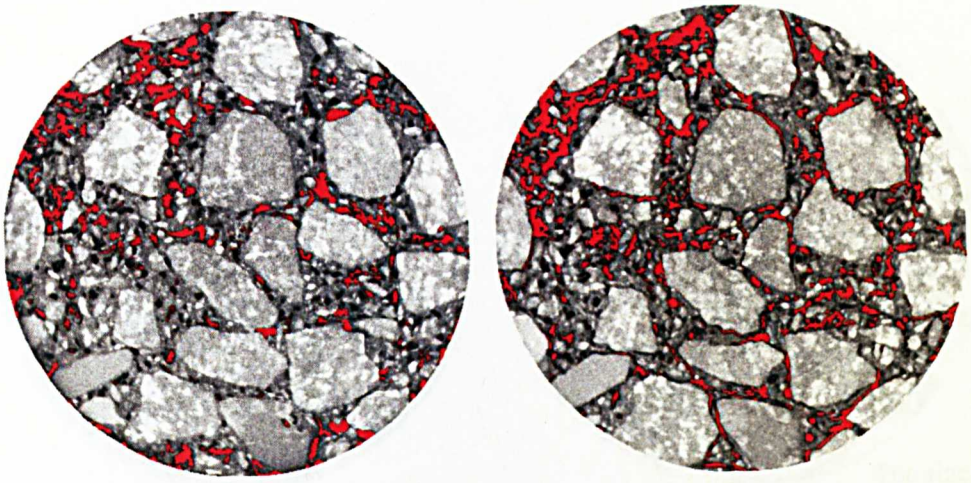

(a) 0.9 relative height (top region)

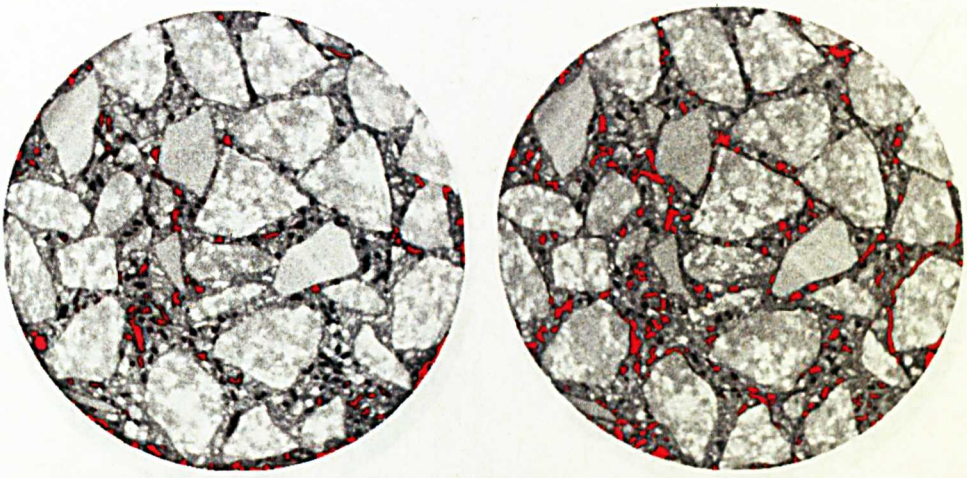

(b) 0.5 relative height (middle region)

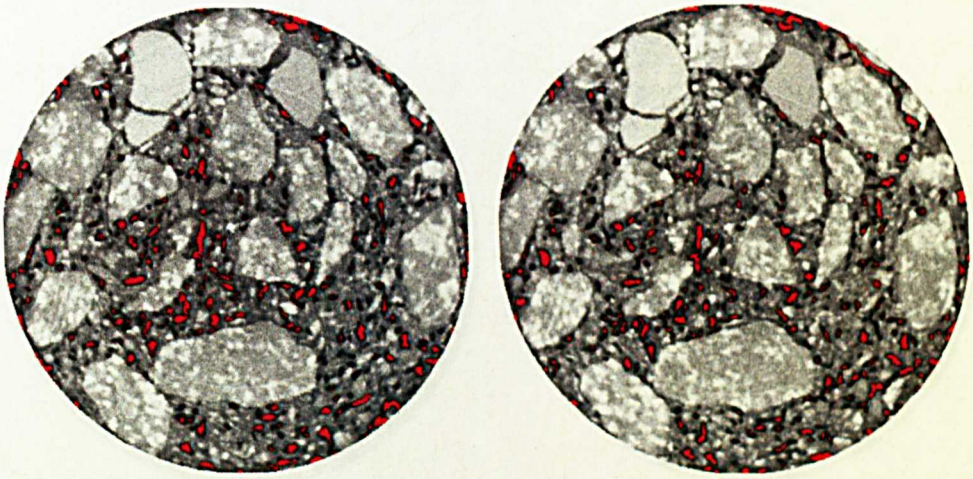

(c) 0.1 relative height (bottom region)

Figure 7.16 Comparison of image slices of modified specimen with 2% rubber, before (left) and after (right) the deformation at 40°C (Specimen number: 10-1527)

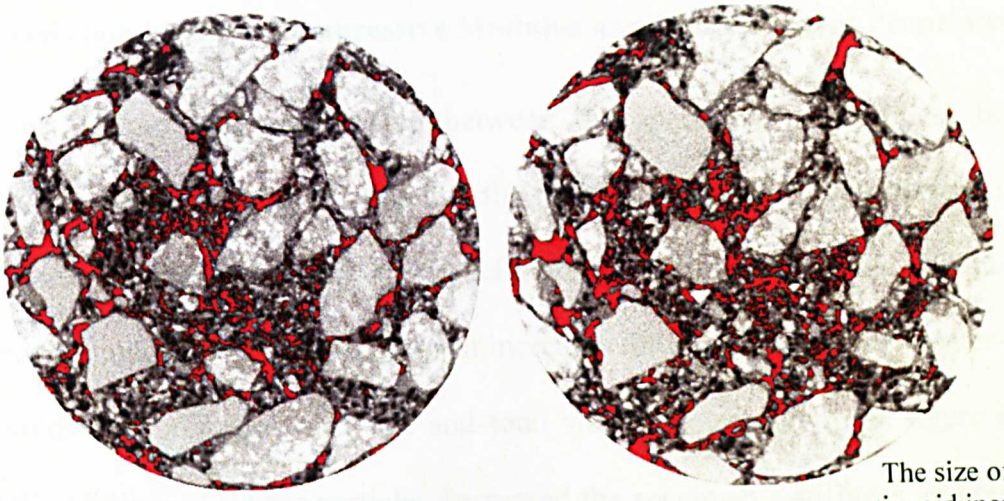

(a) 0.9 relative height (top region)

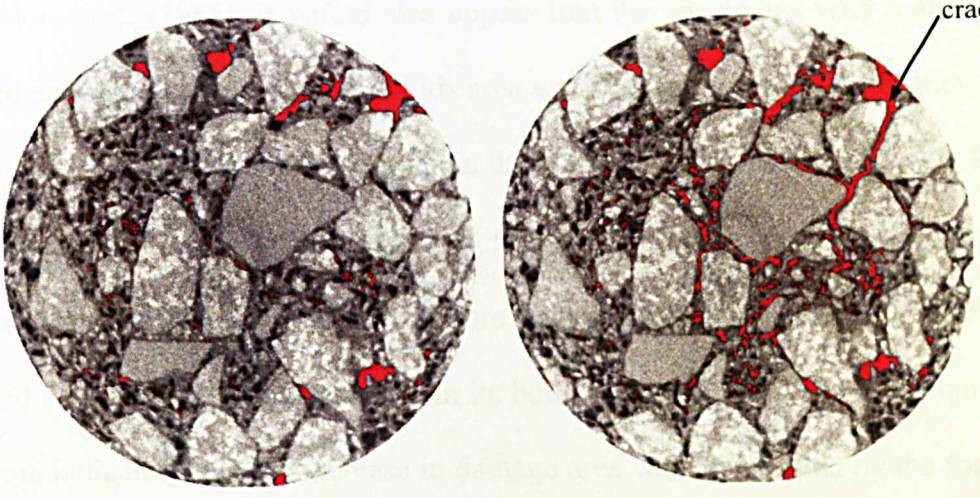

(b) 0.5 relative height (middle region)

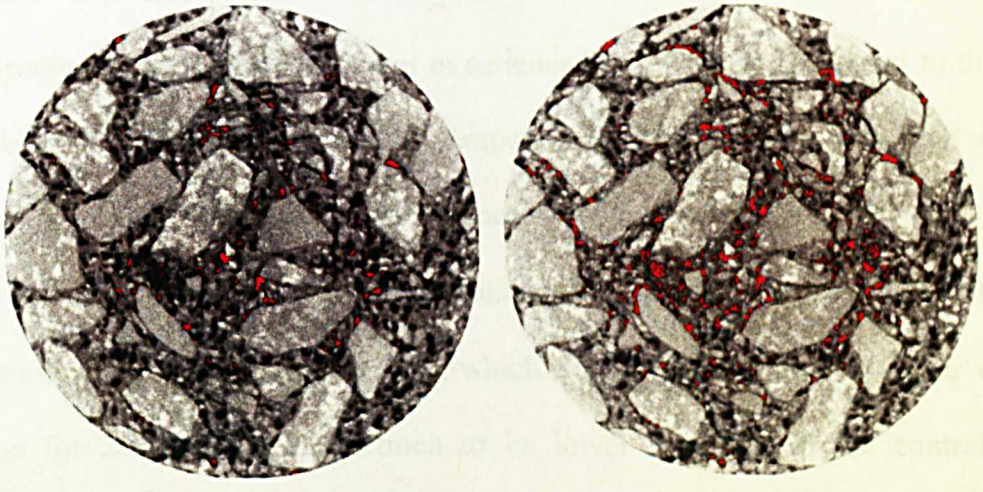

(c) 0.1 relative height (bottom region)

Figure 7.17 Comparison of image slices of modified specimen with 3% rubber, before (left) and after (right) the deformation at 40°C (Specimen number: 10-1984)

7.2.3 Correlation between Compressive Modulus and Voids Content Properties

This section examines the relationship between the specimens' mechanical behaviour determined from the mechanical testing and the microstructure properties determined from the image analysis. Figure 7.18 shows the relationships between the peak modulus of the compression test and their associated percent increases for a few damage parameters namely the total voids area, average voids size and total voids number. From the figure it can be seen that the addition of rubber particles decreased the specimen's stiffness, in concurrence with Takkalou et al. (1985). It would also appear that the specimens with higher modulus experienced an increase in the total air voids area and average voids size after they had been deformed. The decrease in number of voids in the control mixture is evidence that for higher modulus specimen, the voids tend to grow in size and coalesce indicating the damage area were formed and localised within the mixture. In contrast, the specimen with 3% rubber experienced a higher percentage increase in its both total voids area and voids number after deformation, indicating that the increase in damage area was contributed by the formation of new air voids with less potential for the individual air voids to form cracks within the mixture. Specimen containing 2% rubber experienced less damage compared to the control and 3% rubberised specimens for both test temperatures. This result suggests high sensitivity of the mixture to rubber content and is evidenced by the variation in the air voids structure properties for small changes in the rubber content. The results are also consistent with the findings presented earlier in Section 7.2.2, which showed the increase in the air voids area distribution for 2% rubberised specimen to be lower than that of the control and 3% rubberised specimens. In addition, a previous study by Esch (1984) reported that dry process asphalt mixtures demonstrate very low stability and high flow for mixtures sensitive up to 0.5% variation in the rubber content. Therefore, a study of asphalt mixture sensitivity to the

rubber addition is essential to obtain the optimum rubber content that capable of improving the mixture properties.

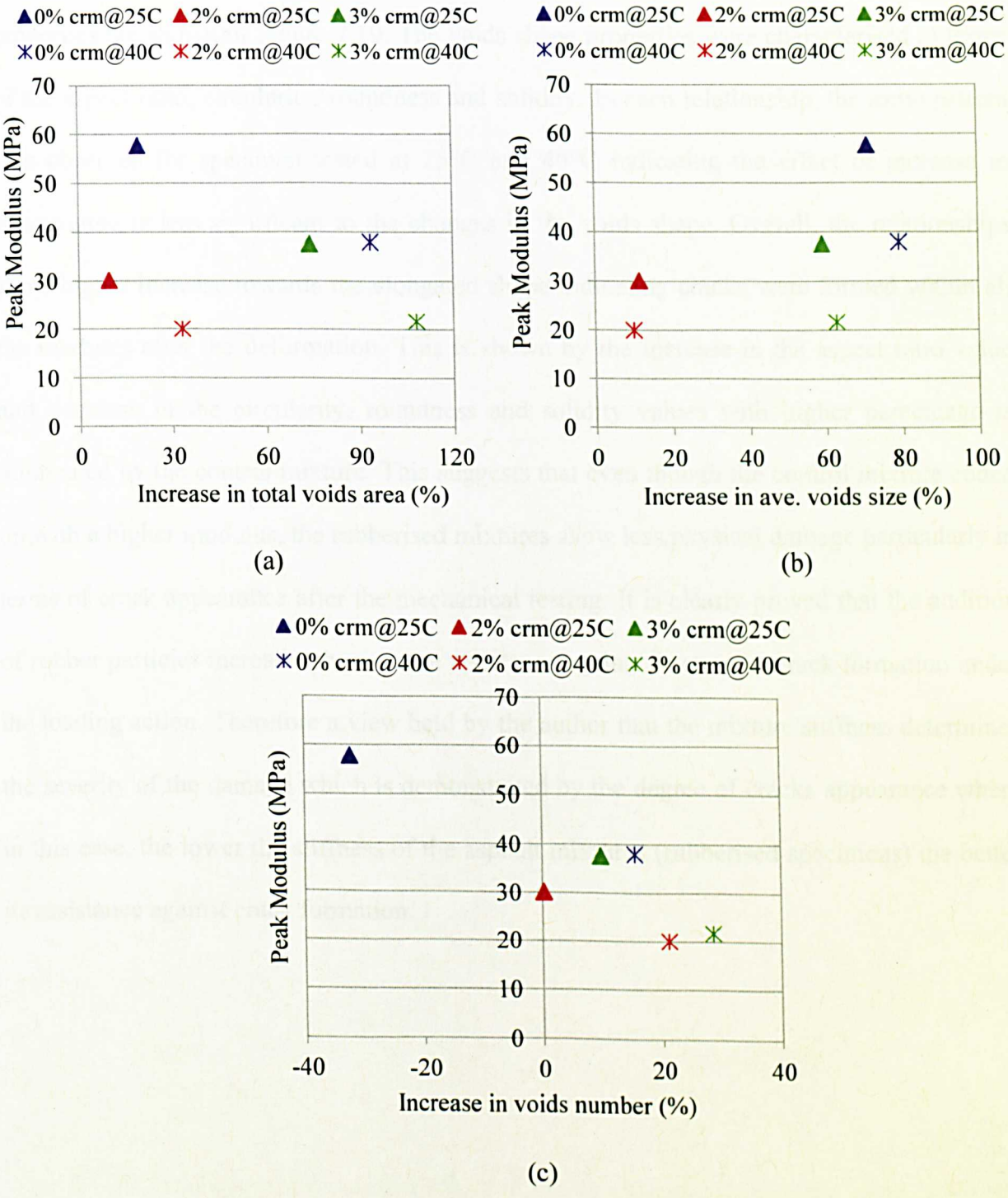

Figure 7.18 Relationships between peak modulus (compressive modulus) and damage parameters from image analysis

7.2.4 Correlation between Compressive Modulus and Voids Shape Properties

The correlations between the compressive modulus and the changes in air voids shape properties are shown in Figure 7.19. The voids shape properties were characterised in terms of the aspect ratio, circularity, roundness and solidity. In each relationship, the same pattern was observed for specimen tested at 25°C and 40°C indicating the effect of increase in temperature is less significant to the changes in the voids shape. Overall, the relationships show higher increase towards the elongated shape indicating cracks were formed within all the mixtures after the deformation. This is shown by the increase in the aspect ratio value and decrease in the circularity, roundness and solidity values with higher percentage is dominated by the control mixture. This suggests that even though the control mixture ended up with a higher modulus, the rubberised mixtures show less physical damage particularly in terms of crack appearance after the mechanical testing. It is clearly proved that the addition of rubber particles increases the mixture resistance against fracture or crack formation under the loading action. Therefore a view held by the author that the mixture stiffness determines the severity of the damage which is demonstrated by the degree of cracks appearance where in this case, the lower the stiffness of the asphalt mixtures (rubberised specimens) the better its resistance against crack formation.

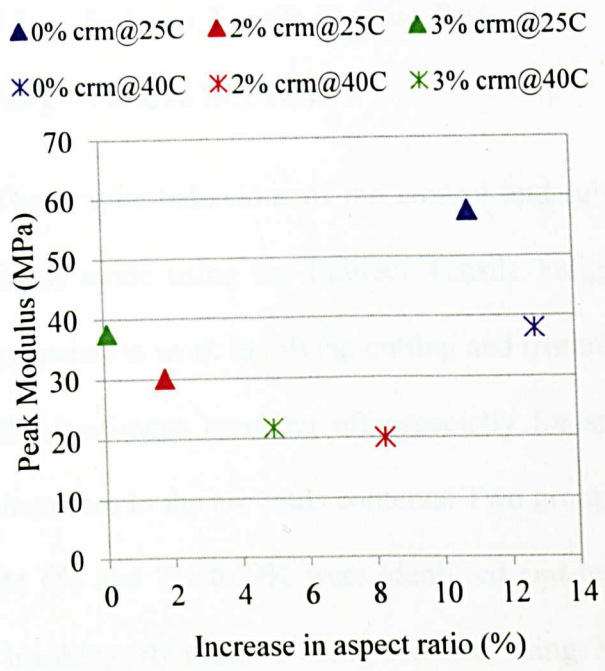

(a)

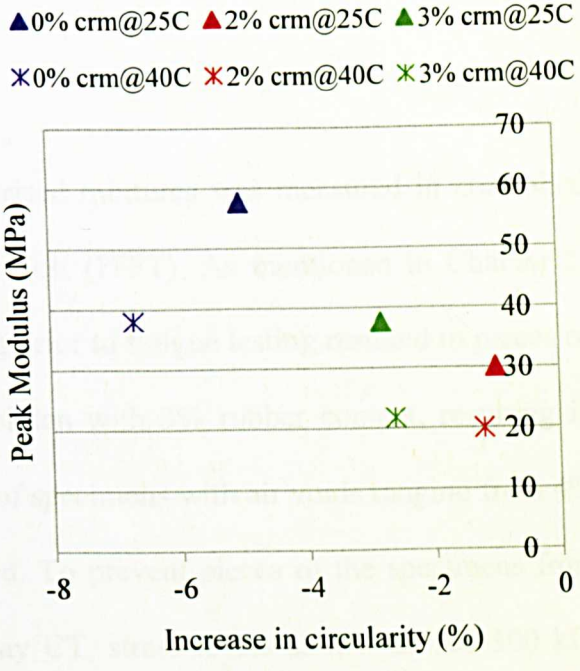

(b)

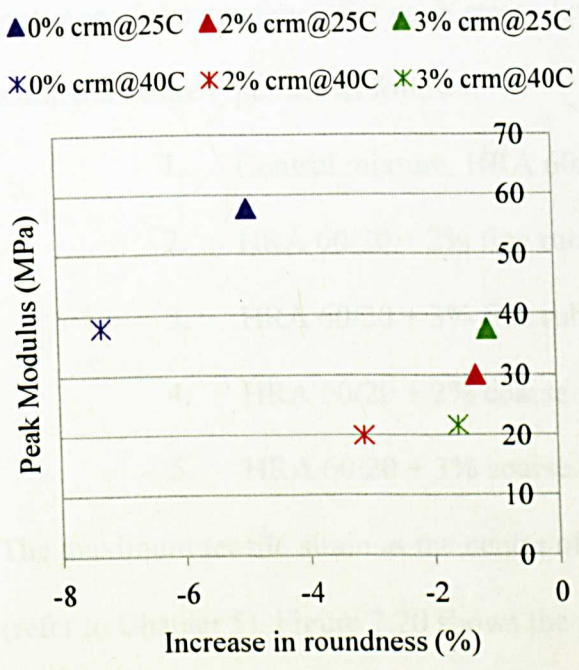

(c)

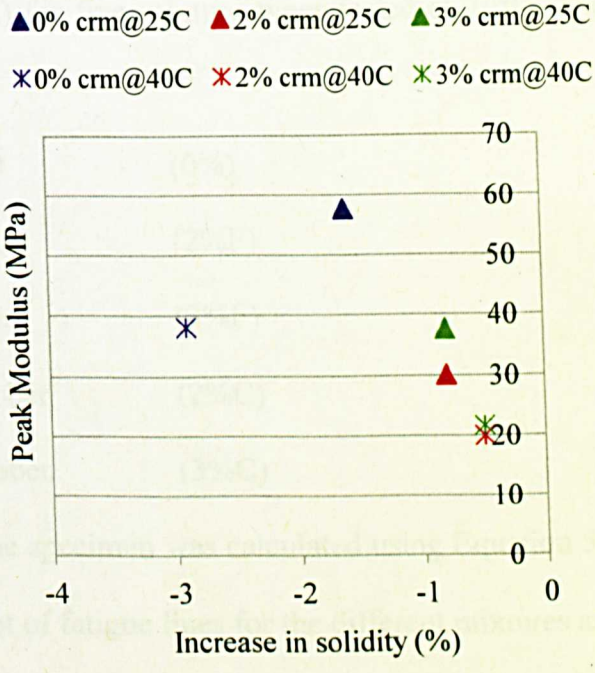

(d)

Figure 7.19 Relationships between peak modulus (compressive modulus) and voids shape properties from image analysis

7.3 Indirect Tensile Fatigue Test

7.3.1 Fatigue Life Data

The fatigue behaviour of the control and rubberised mixtures was measured in controlled stress mode using the Indirect Tensile Fatigue Test (ITFT). As mentioned in Chapter 5, preparation work involving cutting and trimming prior to fatigue testing resulted in pieces of the specimens breaking off especially for specimen with 3% rubber content, resulting in increases in the air voids contents. Two groups of specimens with air voids ranging from 4% to 6% and 7% to 9% were identified and tested. To prevent pieces of the specimens from breaking off prior to being scanned using X-ray CT, stress levels as low as 100-300 kPa were selected for the ITFT test. Table 7.6 summarises the data obtained from a range of specimens (one specimen for each stress level) for five mixture types tested at 20°C. The detailed mixture types are as follows:

1. Control mixture, HRA 60/20 (0%)
2. HRA 60/20 + 2% fine rubber (2%F)
3. HRA 60/20 + 3% fine rubber (3%F)
4. HRA 60/20 + 2% coarse rubber (2%C)
5. HRA 60/20 + 3% coarse rubber (3%C)

The maximum tensile strain at the centre of the specimen was calculated using Equation 5.7 (refer to Chapter 5). Figure 7.20 shows the plot of fatigue lines for the different mixtures and Table 7.7 gives the fatigue life equations, R^2 values and other relevant data from the plot. The equations were used to calculate fatigue lives at the target strain level of 200 με and at the equivalent strains of target fatigue life of 100000 cycles. This is to give a general idea of the mixtures fatigue performance. In addition, Read (1996) recommended that the fatigue

failure in asphalt mixtures usually occurs in the range between 30 με and 200 με. High correlation coefficient of R^2 values (greater than 0.90) for all mixtures show that the data fits the linear regression line very well (as plotted in Figure 7.20).

Table 7.6 Summary data of specimens for ITFT

Mixture type/rubber content (%)	Specimen number	Thickness/ diameter (mm)	Air voids (%)	Stiffness (MPa)	Test stress level (kPa)	Maximum tensile strain	Cycles to failure (N_f)
HRA (60/20)/0	11-1234	40/98	4-6	1500	100	137	9847
	11-393	40/100		1108	150	280	5023
	11-1236	40/100		946	200	433	1419
	11-392	40/100		804	250	637	700
	11-1232	41/100		741	300	830	562
HRA (60/20)/2F	11-1241	41/99	4-6	1200	100	171	16554
	11-1243	40/100		851	150	362	6055
	11-1239	41/100		790	200	519	1068
	11-1245	40/100		685	250	754	750
	11-1238	41/100		620	300	992	421
HRA (60/20)/3F	11-1250	42/101	7-9	505	100	410	3738
	11-1251	40/100		420	150	732	990
	11-1248	41/101		407	200	1025	717
	11-1258	40/100		330	250	1553	400
	11-1249	41/100		316	300	1946	130
HRA (60/20)/2C	11-1261	40/101	4-6	803	100	256	7024
	11-1256	40/100		783	150	393	1057
	11-1248	41/99		749	200	547	659
	11-1259	40/100		670	250	765	300
	11-1260	41/101		500	300	1230	157
HRA (60/20)/3C	11-1267	40/100	7-9	612	100	335	3020
	11-1265	39/100		550	150	559	1002
	11-1269	40/100		534	200	768	313
	11-1262	41/100		490	250	1046	190
	11-1263	40/101		458	300	1343	119

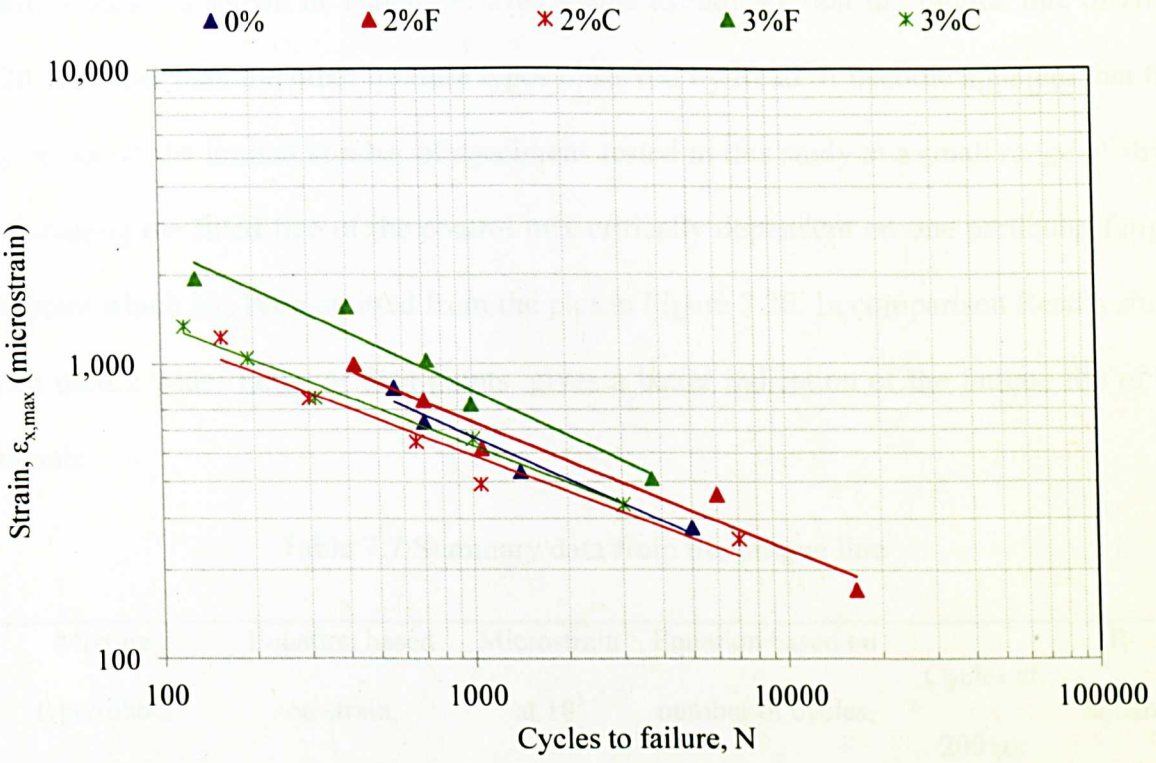

Figure 7.20 Fatigue lines for unmodified and rubberised mixtures tested at 20°C

Factors influencing mixture composition and properties, *c* and *m* as derived from the fatigue lines are summarised in Table 7.8. The values given in the table relate to Equation 7.1 which is a general relationship relating fatigue life to tensile strain.

$$N_f = c \times \left(\frac{1}{\varepsilon_f}\right)^m \qquad 7.1$$

Where,

N_f = number of load applications to initiate a fatigue crack

ε_f = maximum value of tensile strain (microstrain)

c, m = material constant

In order to validate this result, the data was compared to the one obtained by Read (1996) for various mixture types. It can be seen that the slope of the best fitted fatigue line (refer equation for strain) for control mix (HRA60/20) is higher than the various standard materials

tested by Read as shown in Table 7.9. This seems to indicate that the fatigue line of HRA 60/20 is steeper than the other mixture types observed by Read. It become apparent that this may be due to the limited number of specimens tested in this study at a small range of stress level making the fitted line of the control mix critically dependent on one particular fatigue data point which has been omitted from the plot in Figure 7.20. In comparison Read's study, which used a wider range of data points, gives a better indication of the fatigue life of the materials.

Table 7.7 Summary data from the fatigue line

Mixture type/rubber content (%)	Equation based on strain, $\varepsilon_{x,max}$	Microstrain at 10^5 cycles	Equation based on number of cycles, N_f	Cycles at 200 με	R-square (R^2)
HRA (60/20)/0	$\varepsilon = 14731N^{-0.471}$	65.0	$N = 7.08\times10^{8}\varepsilon^{-2.123}$	9225	0.9585
HRA (60/20)/2F	$\varepsilon = 12642N^{-0.432}$	87.5	$N = 3.13\times10^{9}\varepsilon^{-2.315}$	14746	0.9521
HRA (60/20)/3F	$\varepsilon = 23919N^{-0.490}$	84.8	$N = 8.63\times10^{8}\varepsilon^{-2.041}$	17362	0.9519
HRA (60/20)/2C	$\varepsilon = 7887.8N^{-0.402}$	77.1	$N = 4.94\times10^{9}\varepsilon^{-2.488}$	9306	0.9356
HRA (60/20)/3C	$\varepsilon = 9028.3N^{-0.411}$	79.5	$N = 4.21\times10^{9}\varepsilon^{-2.433}$	10614	0.9853

Table 7.8 Material constants for use in Equation 7.1 for the five mixtures tested

Mixture types	c	m
HRA (60/20)/0	7.08×10^{8}	-2.123
HRA (60/20)/2F	3.13×10^{9}	-2.315
HRA (60/20)/3F	8.63×10^{8}	-2.041
HRA (60/20)/2C	4.94×10^{9}	-2.488
HRA (60/20)/3C	4.21×10^{9}	-2.433

Table 7.9 Summary data for all the standard materials tested by Read, 1996

Mixture types (bitumen type)	Equation for strain	Equation for cycle to failure
HRA 30/14 (50 Pen)	$\varepsilon = 4322N^{-0.264}$	$N = 5.93\times10^{13}\varepsilon^{-3.788}$
HRA 40/14 (50 Pen)	$\varepsilon = 1838N^{-0.253}$	$N = 7.99\times10^{12}\varepsilon^{-3.952}$
HRA 50/20 (50 Pen)	$\varepsilon = 3824N^{-0.322}$	$N = 1.34\times10^{11}\varepsilon^{-3.106}$
HRA 30/14 (SBS)	$\varepsilon = 4388N^{-0.241}$	$N = 1.30\times10^{15}\varepsilon^{-4.149}$
HRA 40/14 (SBS)	$\varepsilon = 4301N^{-0.236}$	$N = 2.51\times10^{15}\varepsilon^{-4.238}$
HRA 50/20 (SBS)	$\varepsilon = 5440N^{-0.282}$	$N = 1.86\times10^{13}\varepsilon^{-3.552}$

From Figure 7.20 and Table 7.7, two important observations can be made concerning the rubber modifications investigated. Firstly, fatigue life of the mixture increased as the rubber content of the mixtures was also increased suggesting that the incorporation of rubber increased the flexibility of the mixture. This would likely have been caused by the dual function of the rubber particles in the mixture as was highlighted earlier in the literature (Chapter 2), where the use of fine rubber in asphalt mixture was reported to increase the rubber-bitumen interaction to enhance the binder properties and the coarser rubber particles act as elastic aggregates for better fatigue resistance. This implies that mixtures with greater elastic recovery properties would last longer during fatigue testing due to their ability to recover from deformation after several load cycles i.e. the higher the elasticity of a mixture the better would be its resistance to the fatigue cracking. It is also evident from the data in Table 7.7, that the fatigue life at 200 με for the rubberised mixtures was higher than that of the control mixture which typically had a life at 200 με of 9225 load applications. This is agreed in the case of a thin layered bituminous mixture evaluation, but in contrast for a thick

bituminous layer, the material stiffness is identified to govern the fatigue response, where the higher the material stiffness the greater the fatigue life (Brown, 1978).

Second, it can also be seen from the plots that the mixtures containing fine rubber particles (2%F and 3%F) had a longer fatigue life than the control and coarse rubberised mixtures (2%C and 3%C). This concurs with the literature (Chapter 2) that the spongy surface and higher surface area of fine rubber could increase the rubber-bitumen interaction. The direct contact between the rubber particles and the bitumen resulting in the particles tending to absorb the bitumen lighter fraction (maltenes) thereby increasing the rubber particles sizes via a 'rubber swelling' process. The increase in the rubber size transforms them to physically function as part of the aggregate structure. For coarse rubber, the low surface area and the hardness of the rubber particles, means that they are able to retain their physical shape and rigidity to act as aggregates with insufficient rubber-bitumen interaction. SEM scanning of the rubberised specimens revealed the fine rubber particles to be well embedded within the mastic (Figure 7.21(a&b)). In contrast a large gap was observed around the ITZ area in asphalt mixture containing coarse rubber as shown in Figure 7.21(c&d). This aforementioned is indicative of weak interface bonding or poor adhesion between the rubber and mastic or bitumen. The poor interfacial bonding strength further suggests that the stress transfer mechanism between the rubber particles and the mastic had lessened, and resulted in a higher stress concentration in that particular area. It is when this stress concentration reaches and exceeds specific critical stress intensity or fracture toughness (a material's ability to resist fracture), that cracks begin to grow. These findings confirm that the addition of crumb rubber into asphalt mixtures improves the mixture properties against fatigue failure which is also in agreement with the previous studies by Airey, Collop and Rahman (2004), Takkalou et al., (1985), Esch (1982) and Esch (1984).

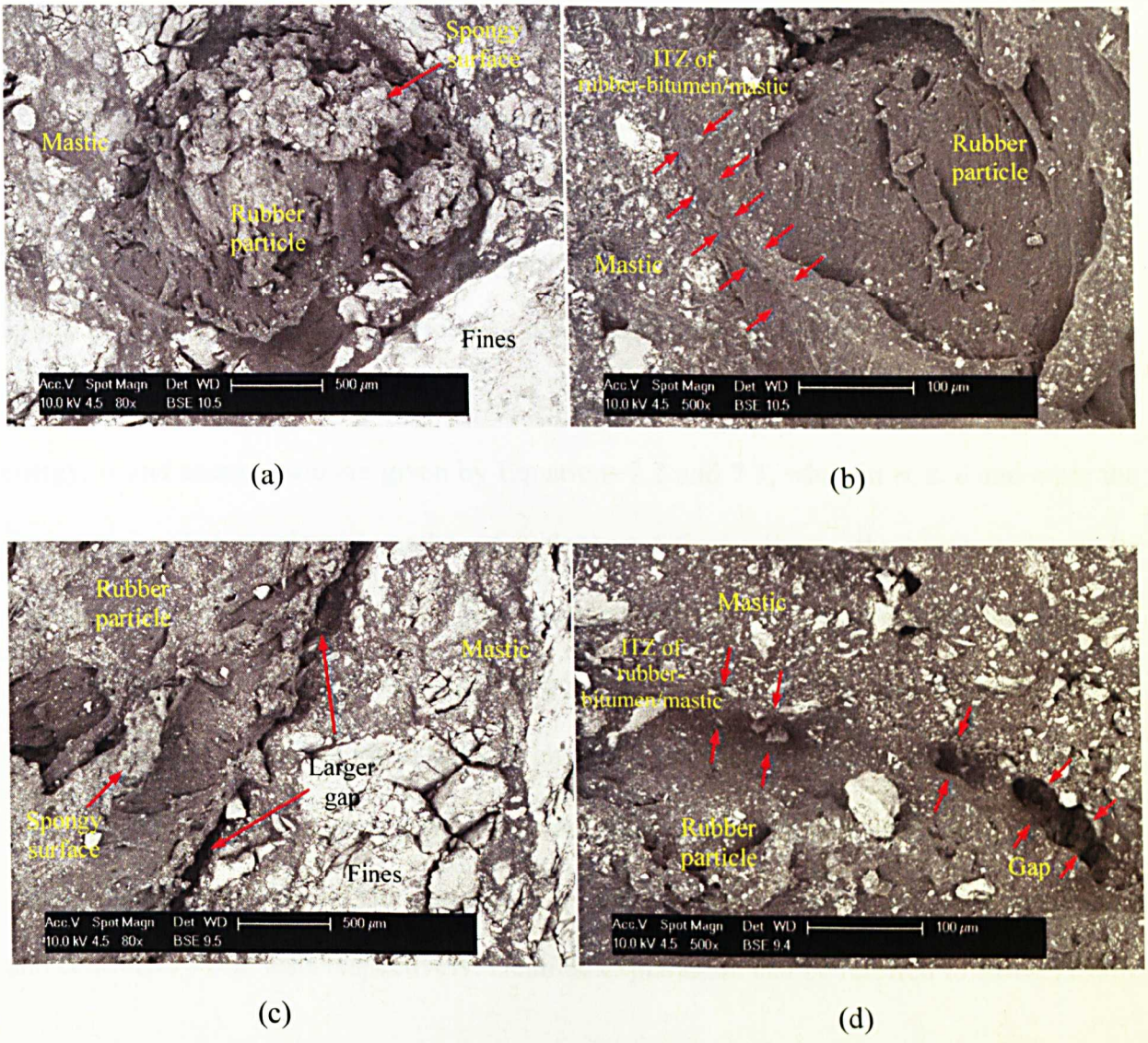

Figure 7.21 SEM scanning of (a-b) fine and (c-d) coarse rubberised mixtures

7.3.2 Crack Initiation and Crack Propagation

One way to explain the nature of damage accumulation leading up to fatigue failure is by utilising the dissipated energy approach. This approach has been used to predict the fatigue behaviour of asphalt mixtures, to establish criteria that clearly define the stages of fatigue failure in terms of microcracks formation, cracks initiation and cracks propagation from the plot of 'Energy ratio' versus number of cycles (refer Figure 7.22). Expressions for dissipated energy, w and energy ratio are given by Equations 7.2 and 7.3, wherein σ, ε, δ and n are the stress, strain, phase angle and number of cycles respectively. Hence, the energy ratio can be written as in Equation 7.4 and σ can be substituted with $E^*\varepsilon$ as shown in Equation 7.5, with E^* as the material's complex modulus. For controlled strain test, ε is constant and $E_o^* \sin\delta_o$ is a constant that can be removed without changing the shape of the curve. Using the same basis for simplifying the energy ratio for controlled stress test, the equivalent ratio or an approximate energy ratio, R can be written as in Equations 7.6 and 7.7 for controlled strain and controlled stress tests respectively. Detailed explanation can be referred to Rowe (1996).

$$w = \pi\,\sigma\,\varepsilon\,\sin\delta \tag{7.2}$$

$$Energy\ ratio = \frac{nw_o}{w_i} \tag{7.3}$$

$$Energy\ ratio = \frac{n(\pi\sigma_o\varepsilon_o \sin\delta_o)}{(\pi\sigma_i\varepsilon_i \sin\delta_i)} \tag{7.4}$$

$$Energy\ ratio = \frac{n(\pi\varepsilon_o^2 E_o^* \sin\delta_o)}{(\pi\varepsilon_i^2 E_i^* \sin\delta_i)} \tag{7.5}$$

$$R_\varepsilon \cong \frac{n}{E_i^*} \tag{7.6}$$

$$R_\sigma \cong nE_i^* \tag{7.7}$$

The approximate energy ratio is plotted against the number of cycles (Figure 7.22) for controlled stress fatigue test of a trapezoidal specimen. For the ITFT, a plot of $(n/\Delta V_d)$

against number of cycles (as in Figure 7.23) produces a similar curve to that shown in Figure 7.22, where n is the number of cycles and ΔV_d is the transient vertical deformation during the ITFT. The fatigue behaviour of an asphalt specimens is clearly shown on both plots, which start with the coalescence of microcracks and progresses to a point of cracks initiation (or macrocrack onset) N_1, followed by a very short crack propagation phase leading up to specimen failure, N_f. The point of crack initiation gives an important indication of the damage accumulated due to the viscous flow of the binder that results in the creation of plastic zone at the end of the fatigue testing (Widyatmoko, Ellis and Read, 2006).

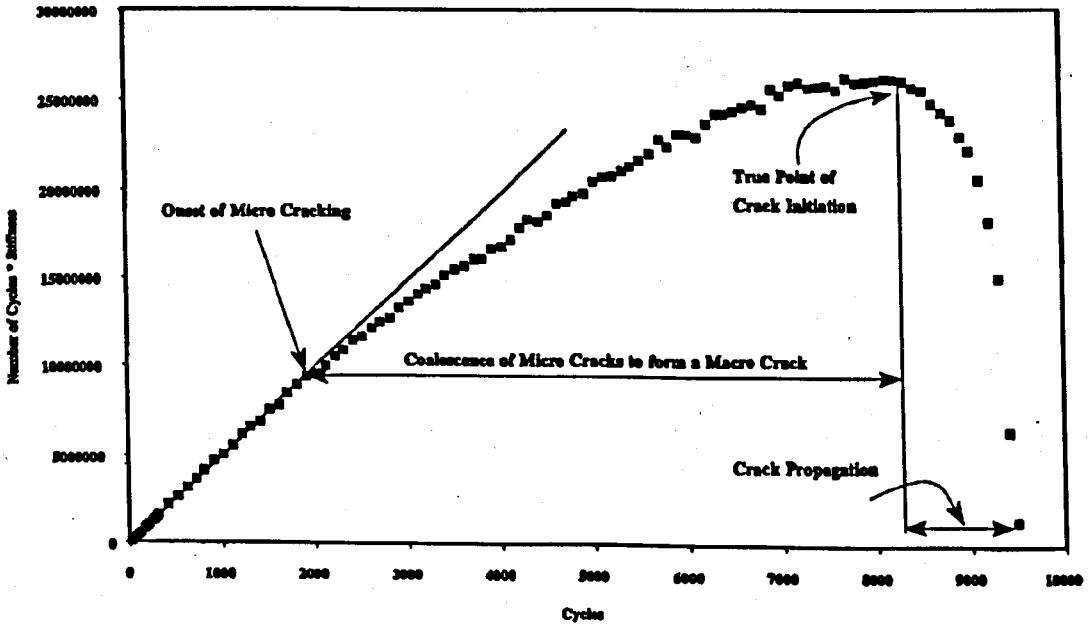

Figure 7.22 Typical plot of approximate energy ratio, R against number of cycles for trapezoidal specimen (Read, 1996)

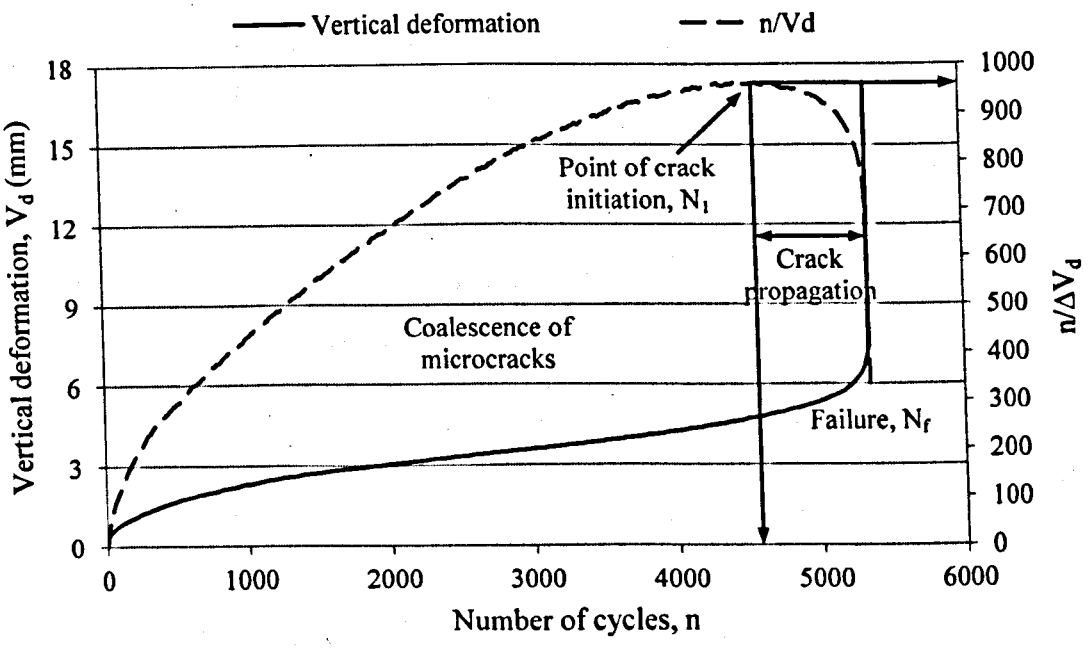

Figure 7.23 Typical plots of vertical deformation and $n/\Delta V_d$ versus number of cycles for an ITFT specimen

Figures 7.24 and 7.25 show plots of vertical deformation, V_d and $n/\Delta V_d$ versus number of cycles for ITFT specimens for the control (0%) and rubberised mixtures (2%F, 2%C, 3%F and 3%C) tested at 100 kPa. For the ITFT, specimen failure is said to occur at a vertical deformation of 9 mm (British Standard, DDABF-2003 ITFT). However the figures show the specimen not to have failed completely at 9 mm. The specimens, especially the rubberised ones appeared capable of supporting more load cycles beyond the 9 mm failure limit.

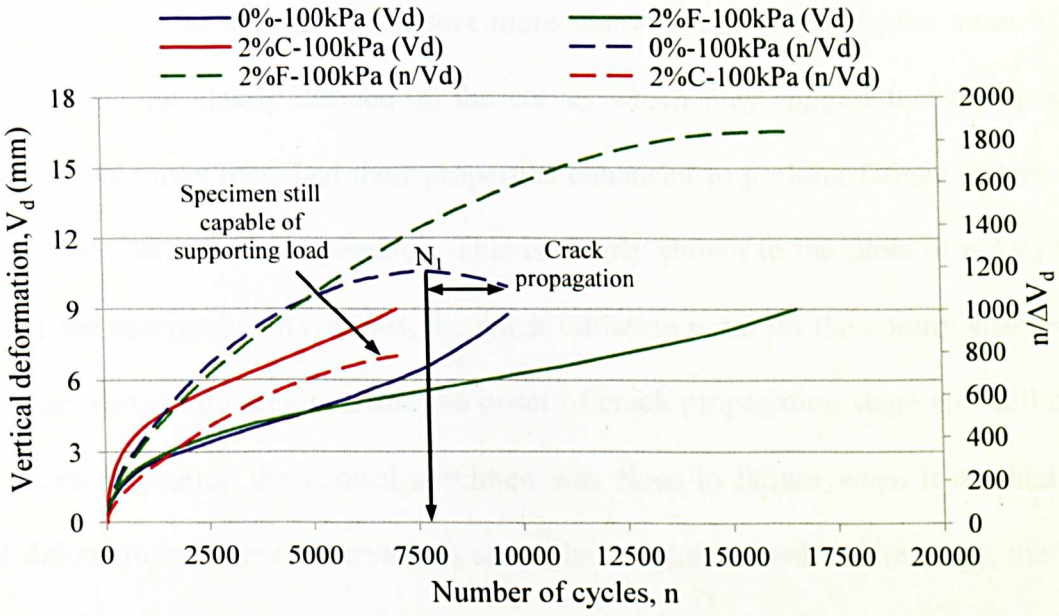

Figure 7.24 Vertical deformation and $n/\Delta V_d$ versus number of cycles for ITFT specimens (0%, 2%F and 2%C) tested at 100 kPa

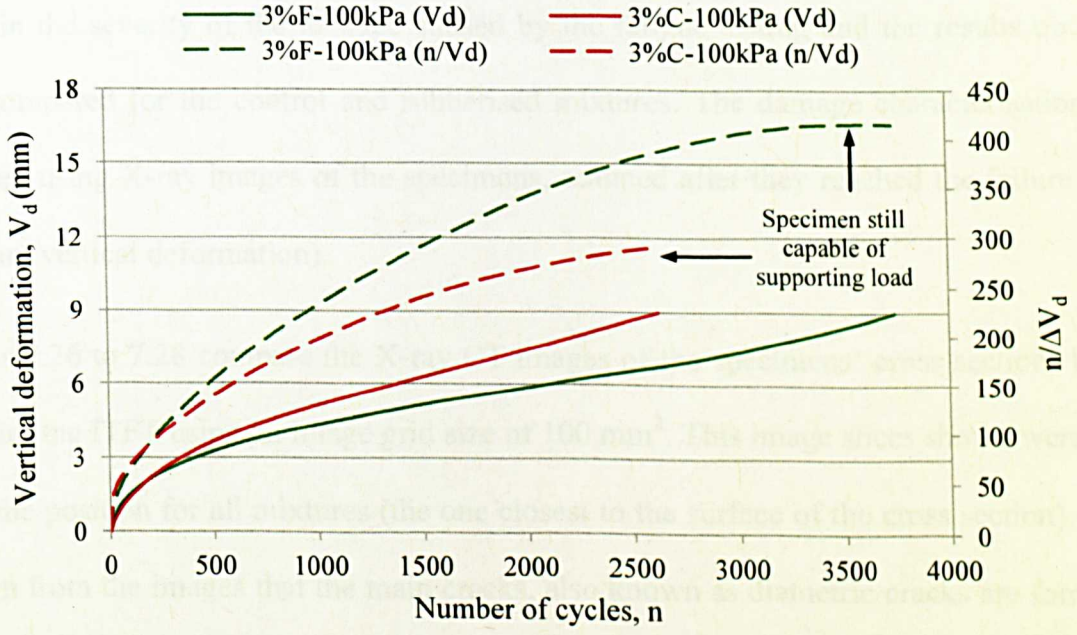

Figure 7.25 Vertical deformation and $n/\Delta V_d$ versus number of cycles for ITFT specimens (3%F and 3%C) tested at 100 kPa

The plots of $n/\Delta V_d$ for the rubberised specimens show that at this limit, the onset of crack propagation was not clearly defined on the curves which may suggest that the specimens containing rubber may have had their properties enhanced to prolong fatigue failure and to resist any associated crack propagation. This is clearly shown in the plots of $n/\Delta V_d$ for the 3% rubberised specimens. In contrast, the crack initiation point for the control specimen, N_1 at maximum vertical deformation and the onset of crack propagation stage are well defined on the curve, indicating the control specimen was close to failure when it reached 9 mm vertical deformation. These observations show that, at the defined failure stage, the fatigue life of the rubberised specimens was underestimated. These observations are consistent with Read et al. (1996), who mentioned the same for polymer modified asphalt mixtures. Following the ITFT, the accumulated damage in the specimens were then further characterised by analysing the properties of the resulting cracks. This was necessary to ascertain the severity of the damage caused by the fatigue testing and the results obtained were compared for the control and rubberised mixtures. The damage characterisation was achieved using X-ray images of the specimens, scanned after they reached the failure stage (at 9 mm vertical deformation).

Figures 7.26 to 7.28 compare the X-ray CT images of the specimens' cross sections before and after the ITFT using an image grid size of 100 mm^2. This image slices shown were from the same position for all mixtures (the one closest to the surface of the cross section). It can be seen from the images that the main cracks, also known as diametric cracks are formed in the middle area of the cross section as highlighted (in red). The remaining portions of the cross-sectional area of the slices show very small increases in air voids area, thought to be possibly caused by specimen disintegration at failure. In this study, cracks were analysed in

the enclosed highlighted region to ensure that only the main cracks initiated due to fatigue failure were taken into consideration. This was done to reduce variations in the measured parameters which would have been affected by the changes in air voids distribution. The areas under consideration were chosen as the 40 mm wide region located at the middle of the specimens' cross sections. The main cracks caused by the loading action were identified to be concentrated within this area (refer to Figure 7.29).

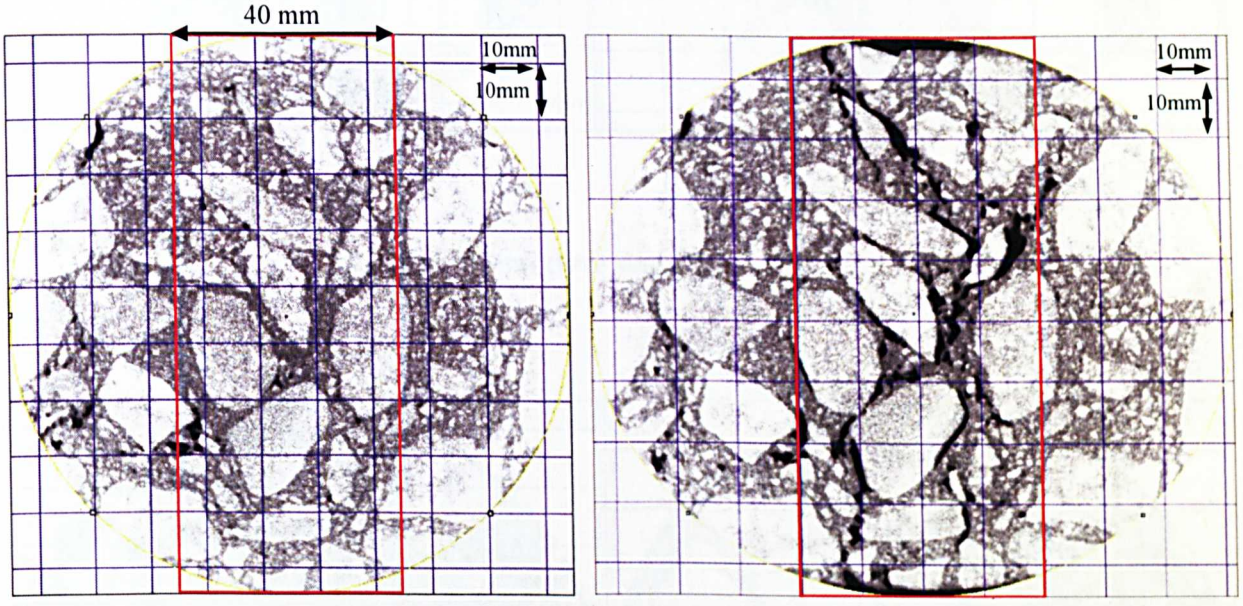

(a) (b)

Figure 7.26 Image of specimen cross section for control asphalt mixture (a) before and (b) after ITFT (tested at 200 kPa)

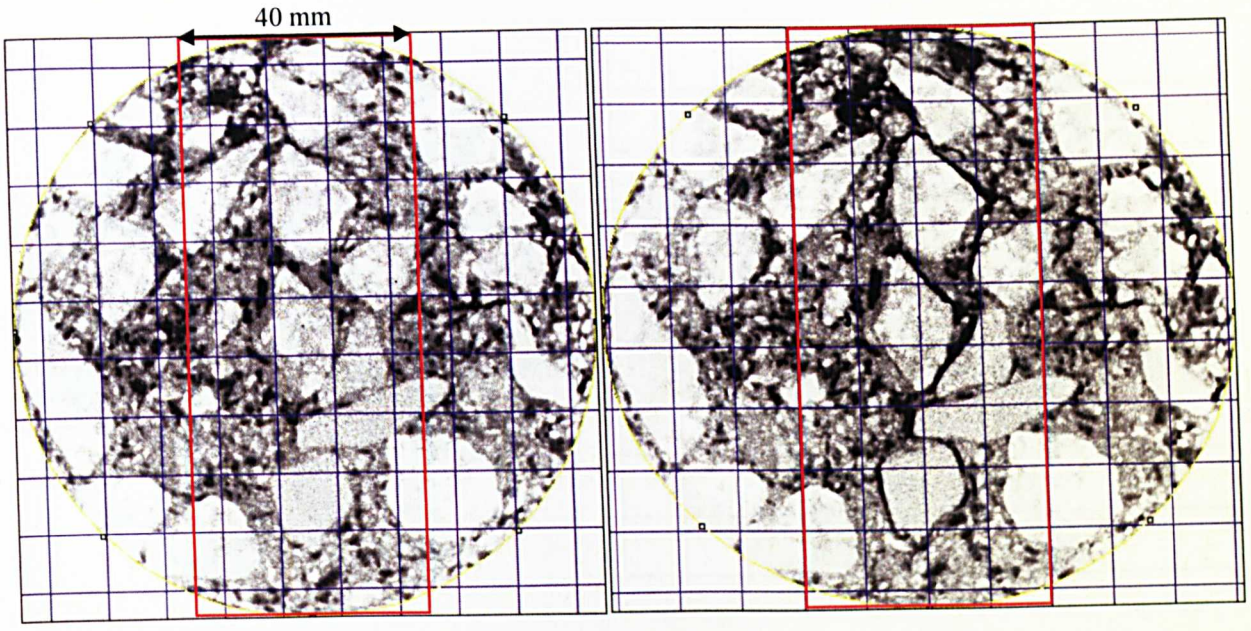

(a) (b)

Rubberised mixture with 2% fine rubber

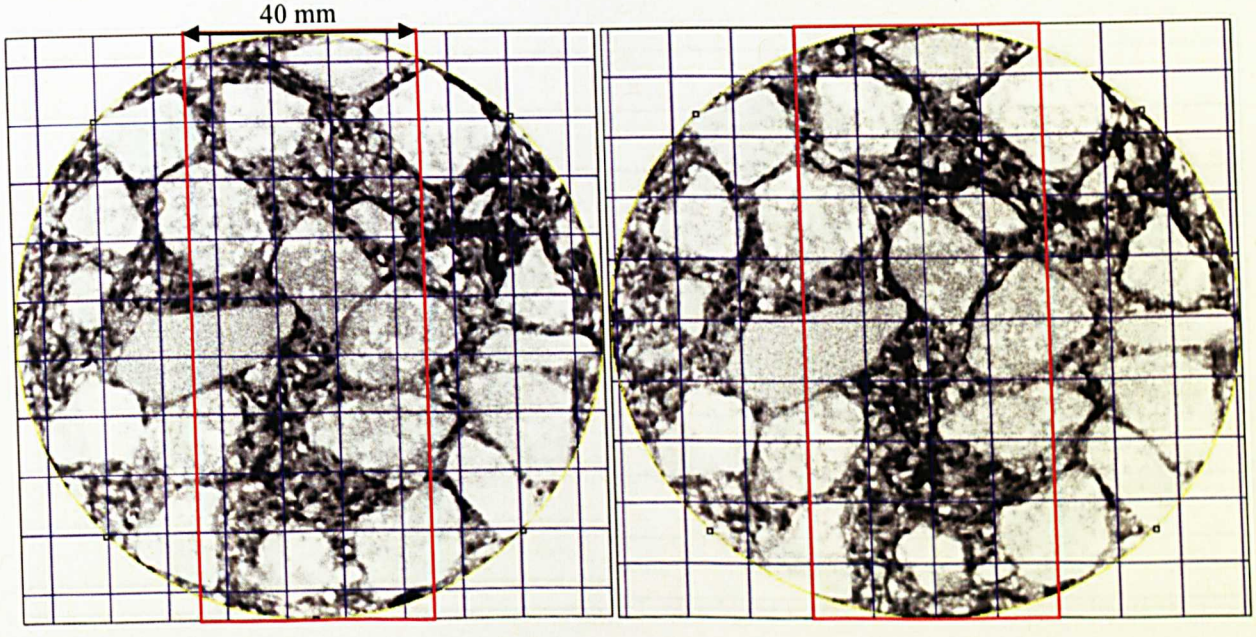

(a) (b)

Rubberised mixture with 3% fine rubber

Figure 7.27 Image of specimen cross section for rubberised mixture (fine rubber) (a) before and (b) after ITFT (tested at 200 kPa)

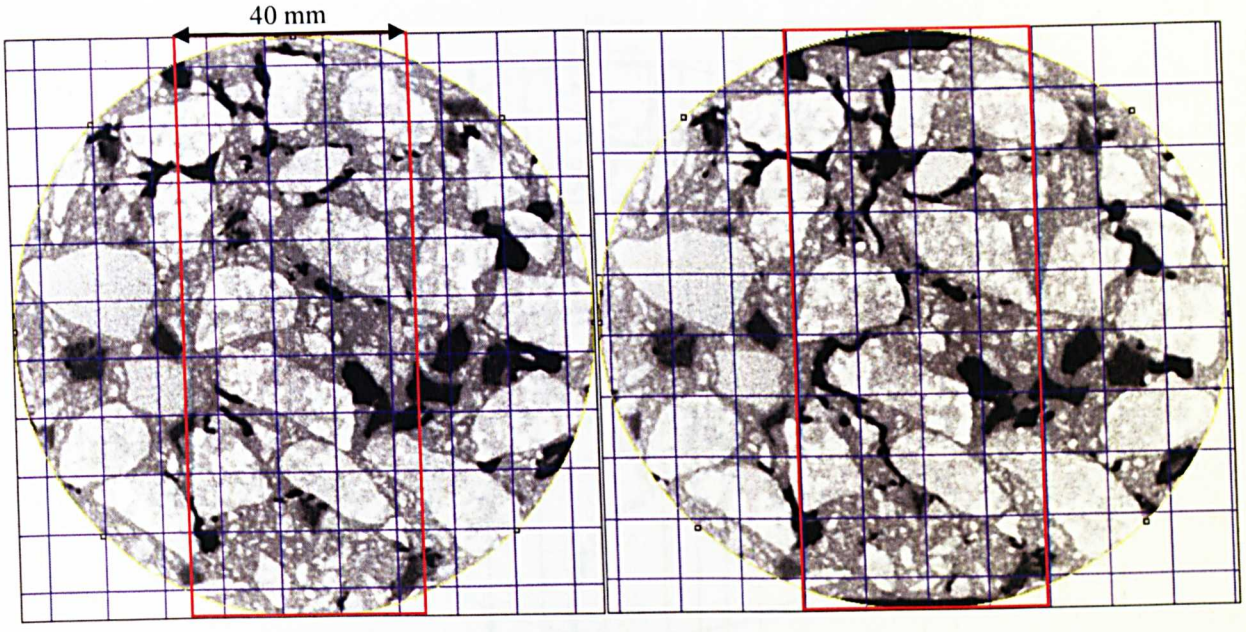

(a) (b)

Rubberised mixture with 2% coarse rubber

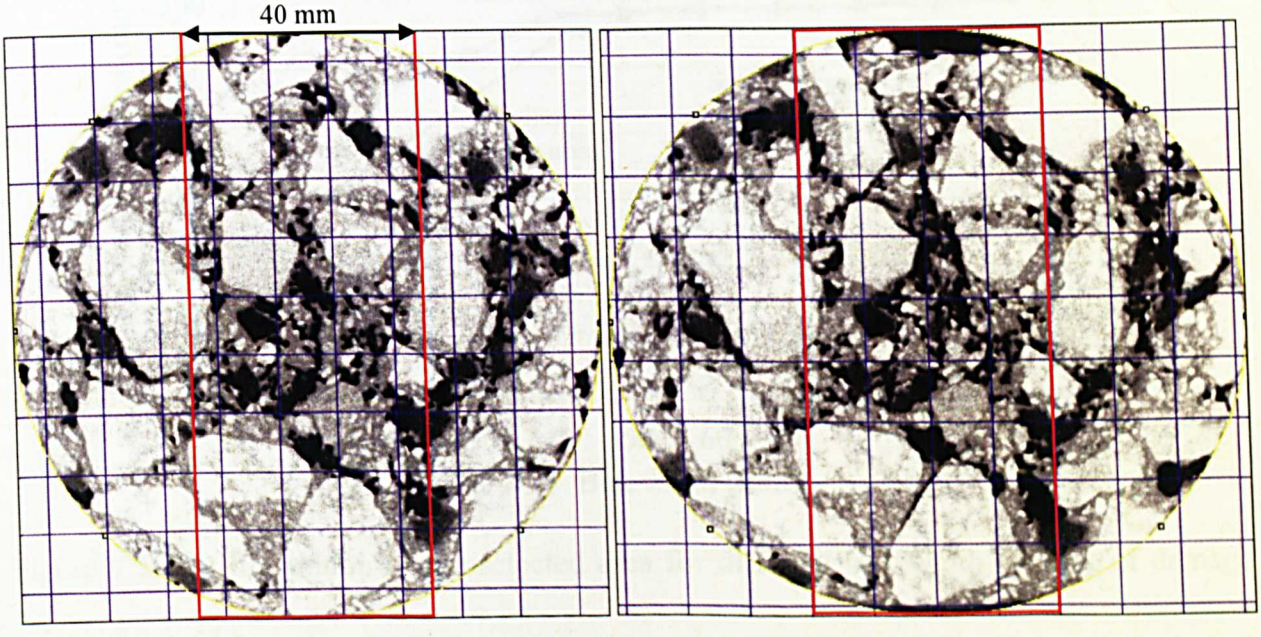

(a) (b)

Rubberised mixture with 3% coarse rubber

Figure 7.28 Image of specimen cross section for rubberised mixture (coarse rubber)

(a) before and (b) after ITFT (tested at 200 kPa)

(a)

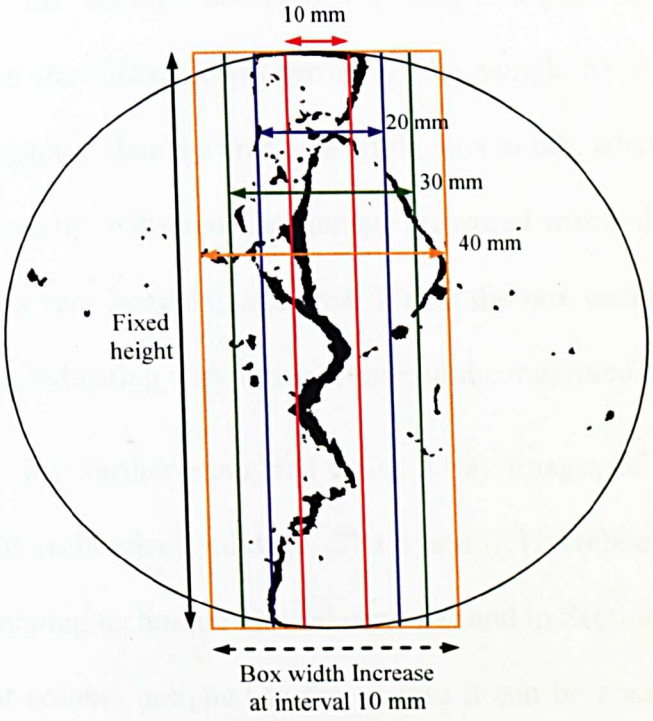

(b)

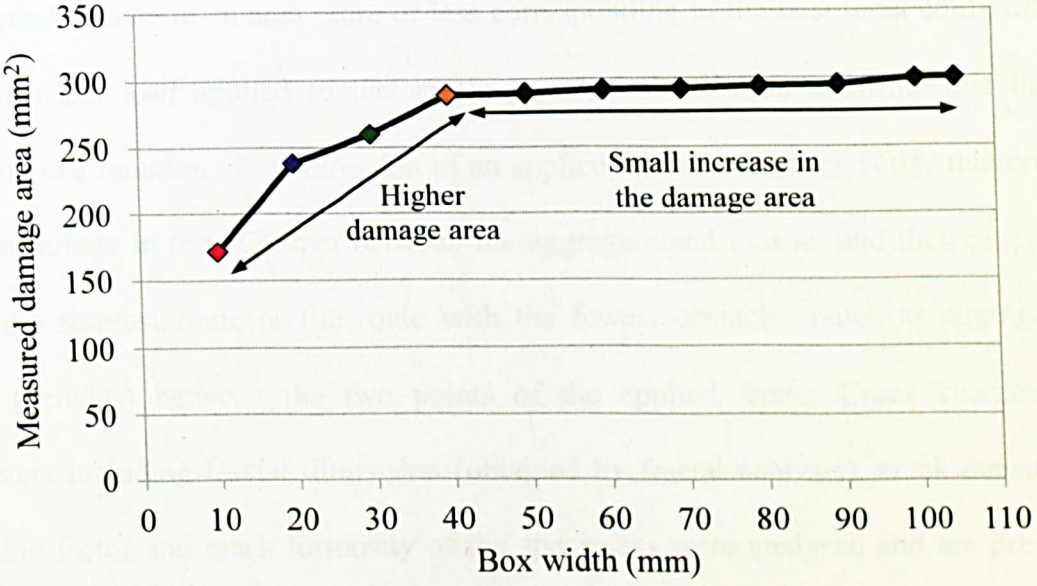

Figure 7.29 (a) Illustration of the selected area for different box width (b) plot of damage area vs box width

Identification of the 40 mm crack envelope was established through an assessment of the damaged specimen at 10 mm intervals from the central 10 mm wide of the specimen, which progressively confirmed damage increasing to a maximum, with a crack envelope 40 mm

wide. Beyond 40 mm, the damage observed was only marginal and would have only introduced variations on the measured properties of the sample as previously mentioned. Figure 7.29b shows the plot of damage area against the box width, where it can be seen that, as the box width increased up to 40 mm, the damage measured within the box area increased significantly indicating a very large damage area. Where the box width exceeds 40 mm, the plot is almost horizontal indicating very little increase in the measured damage area.

The extent of damage was further examined using X-ray images of the damaged area as shown in Figures 7.30 (rubberised mixture, 2%C) and 7.31 (rubberised mixture, 3%C). Details of the X-ray imaging technique utilised can be found in Section 4.3.2.3 of Chapter 4. Based on the different colours assigned to the images it can be observed that the damage area is concentrated in an area more or less corresponding to the positional configuration of the diametrical load applied to the specimen. This observation confirms that the crack formation is a function of the direction of an applied load. The figures verify that cracks are prone to initiate in the ITZ area between the aggregate and mastic, and then propagate by taking the shortest route or the route with the fewest obstacles (such as aggregates and rubber particles) between the two points of the applied stress. Crack characterisation parameters including fractal dimension (obtained by fractal analysis), crack density, crack branching factor and crack tortuosity of the specimens were analysed and are presented in the subsequent sub-sections, where they were compared for the different mixtures. These parameters are excellent for describing the geometric shape of cracks for use in quantitatively assessing the severity of damage in a specimen which could also be correlated to the mixture's mechanical properties.

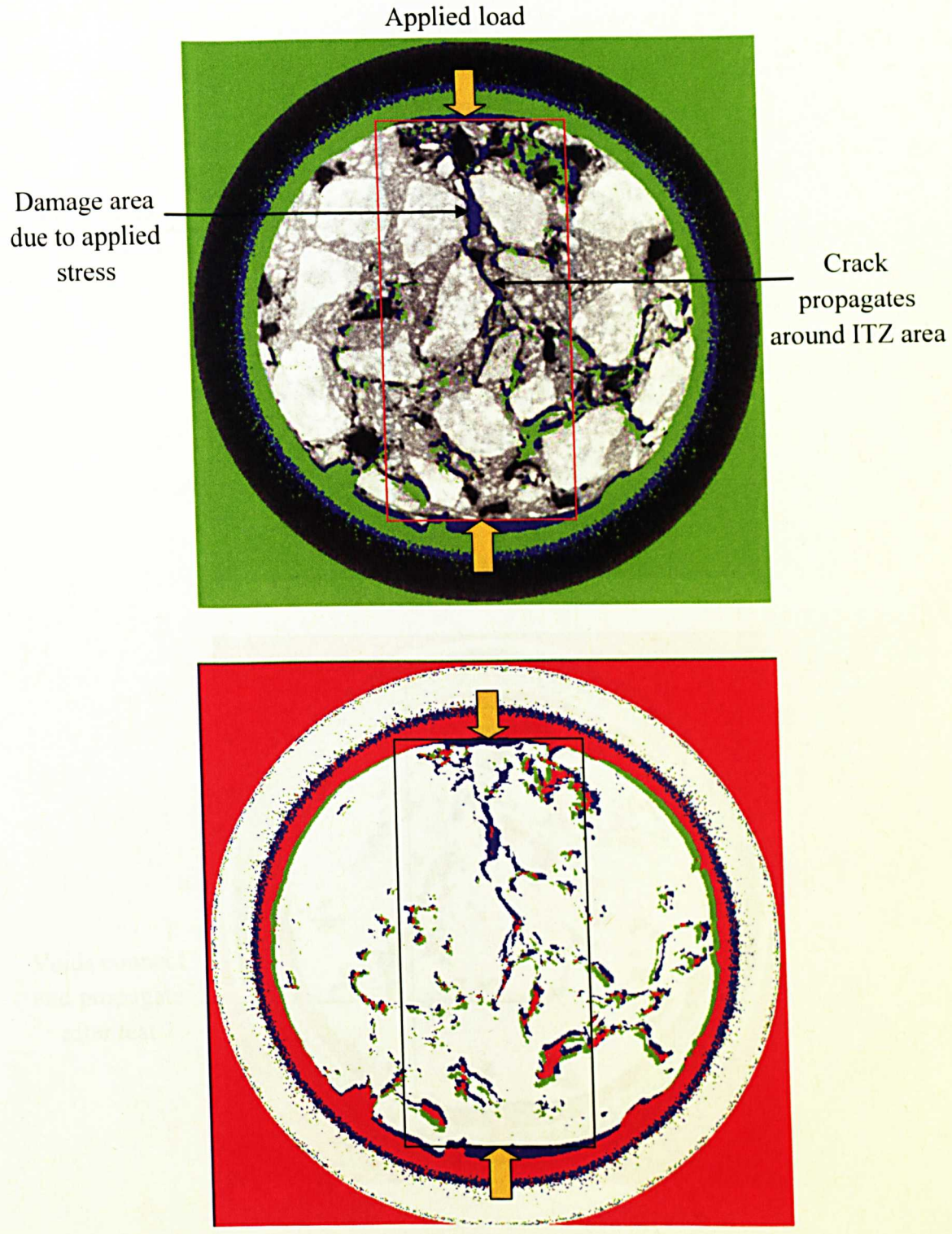

Figure 7.30 Image of the damaged area for rubberised mixture (2%C) tested at 200 kPa

Indicator: Green: voids area before damage, blue: voids area after damage, red: overlap area

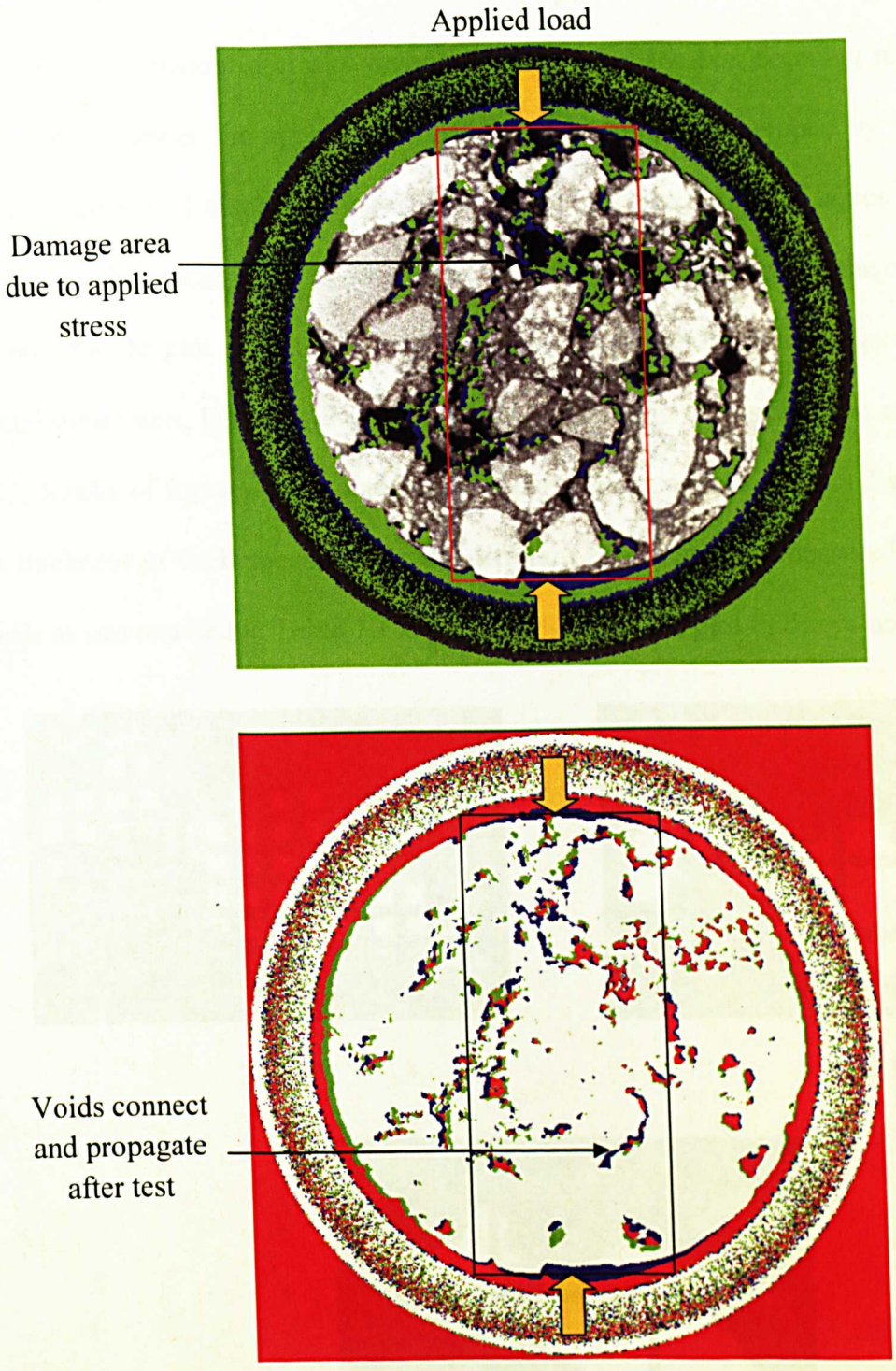

Figure 7.31 Image of the damaged area for rubberised mixture (3%C) tested at 200 kPa

Indicator: Green: voids area before damage, blue: voids area after damage, red: overlap area

Fractal Dimension

The fractal dimension of cracks was determined using the box counting method as detailed in Chapter 4 under the application of FracLac in ImageJ developed by Karperien (1999-2012). Figure 7.32 displays images showing the grids or arrays of boxes of different sizes overlaying the cracks' images. The boxes that contained the pixels of the cracks image were counted for the plot of ln(box count, N) versus ln(box size, ε), which is used to obtain the fractal dimension, D that is the slope of the logarithmic regression line as shown in Figure 7.33. Stacks of images were analysed and the average values of fractal dimension through the thickness of each specimen for the different mixtures were measured at different stress levels as summarised in Table 7.10. Figure 7.34 gives the plot of the values as in the table.

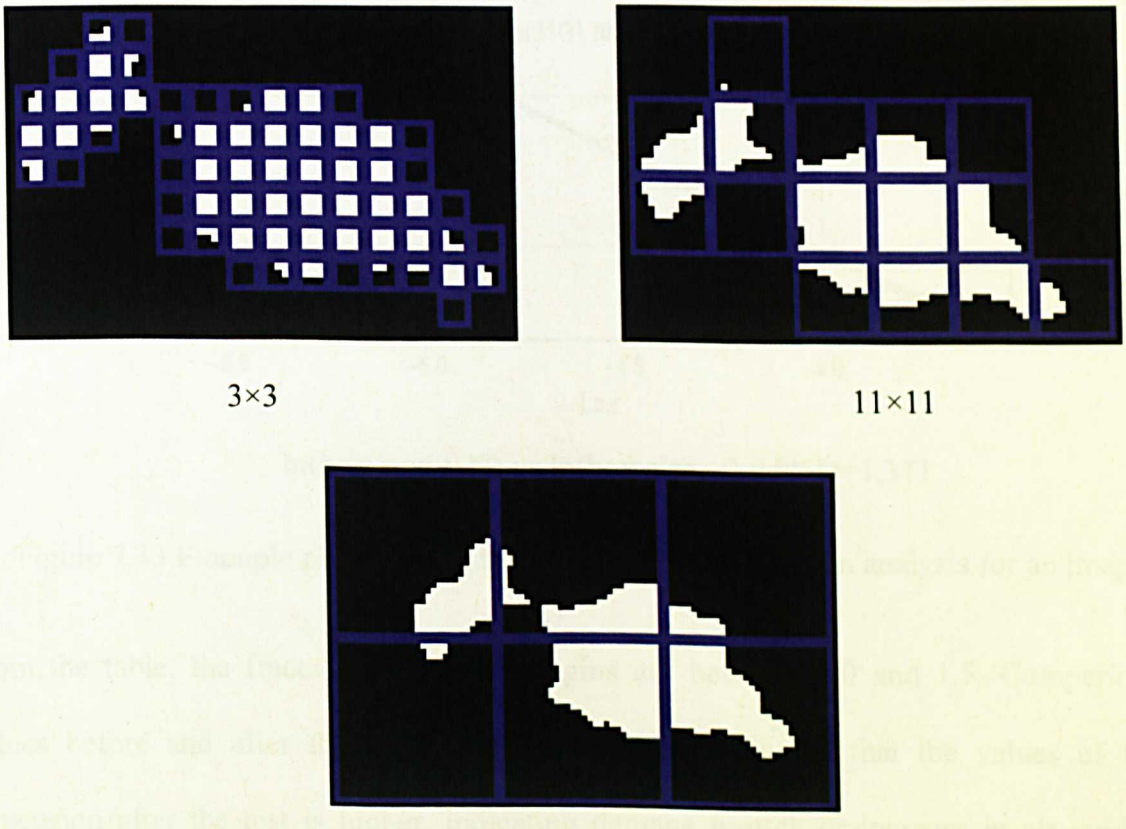

Figure 7.32 Example of a crack image analysed with different grids size (in pixel)

Binary image of cracks

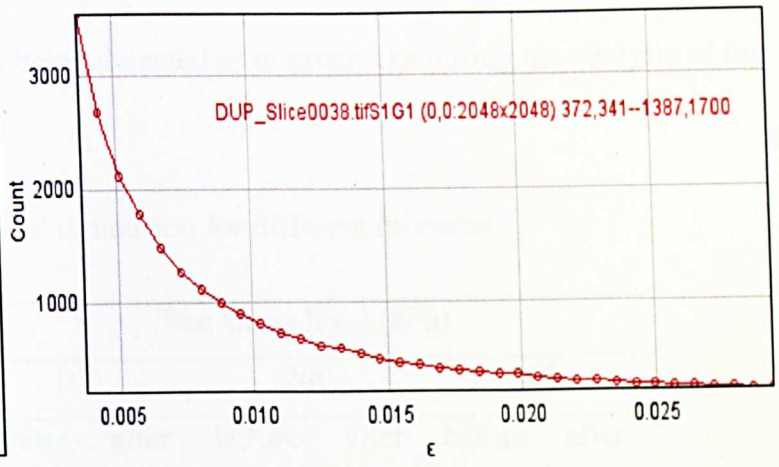

Box count vs box size

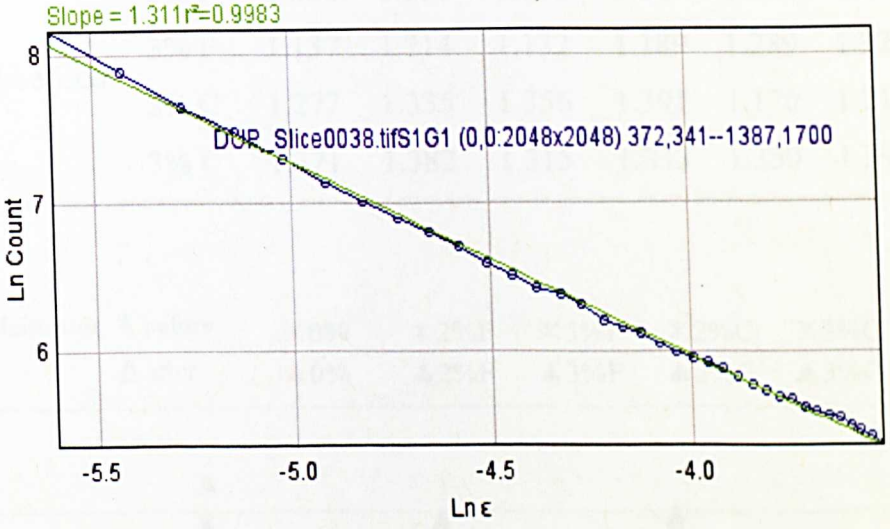

ln(box count, N) vs ln(box size, ε) with D=1.311

Figure 7.33 Example plots obtained from the fractal dimension analysis for an image

From the table, the fractal dimensions margins are between 1.0 and 1.5. Comparing the values before and after the fatigue test, it can be concluded that the values of fractal dimension after the test is higher, indicating damage growth or increase in air voids size (area) and the development of cracks. In this study several replicates of different specimens were tested at different stress levels so it was more useful to compare the increase in the

fractal dimensions before and after the test in order to assess the severity of the resulted cracks as shown in Figure 7.35. This was done to avoid some existing elongated air voids within the specimen (before testing) being detected as microcracks during the analysis of the specimen after it was tested.

Table 7.10 Fractal dimension for different mixtures

Mixture types		Test stress level (kPa)					
		100		200		300	
		before	after	before	after	before	after
Control (0%)		1.390	1.428	1.215	1.310	1.095	1.394
Rubberised	2% F	1.058	1.231	1.076	1.227	1.102	1.264
	3% F	1.137	1.214	1.132	1.189	1.289	1.329
	2% C	1.277	1.335	1.356	1.391	1.170	1.215
	3% C	1.371	1.382	1.315	1.333	1.350	1.393

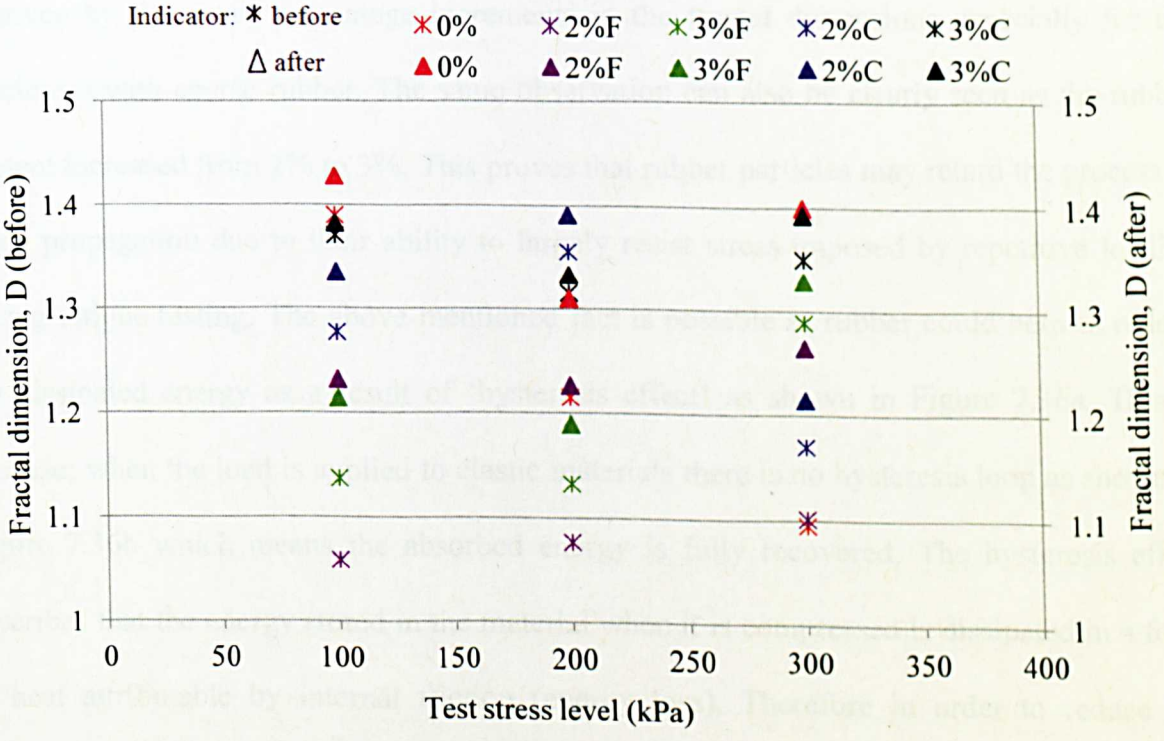

Figure 7.34 Fractal dimension for different mixture types, tested at different stress levels

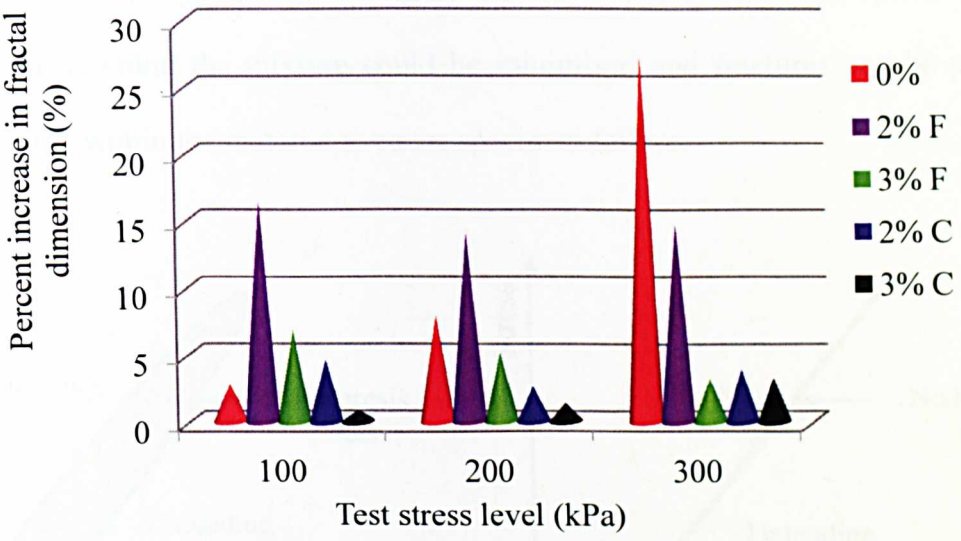

Figure 7.35 Percent increase in fractal dimension values for different mixture types

For the control mixture, it can be seen (in Figure 7.35) that the increase in the values of fractal dimension became higher as the test stress level increased. Both plots (Figures 7.34 and 7.35) show that the addition of rubber particles to the specimens reduced crack growth as given by the small percentage increments in the fractal dimensions especially for the specimens with coarse rubber. The same observation can also be clearly seen as the rubber content increased from 2% to 3%. This proves that rubber particles may retard the process of crack propagation due to their ability to largely resist stress imposed by repetitive loading during fatigue testing. The above mentioned fact is possible as rubber could help to reduce the dissipated energy as a result of 'hysteresis effect' as shown in Figure 7.36a. This is because; when the load is applied to elastic materials there is no hysteresis loop as shown in Figure 7.36b which means the absorbed energy is fully recovered. The hysteresis effect describes that the energy stored in the material when it is compressed is dissipated in a form of heat attributable by internal friction (energy loss). Therefore in order to reduce the material's susceptibility to damage, the dissipated energy by the material during each

loading cycle should be minimised. Through rubberised asphalt mixture, the phenomenon of dissipated energy within the mixture could be minimised and fractures can be prevented from propagating within the material to cause specimen failure.

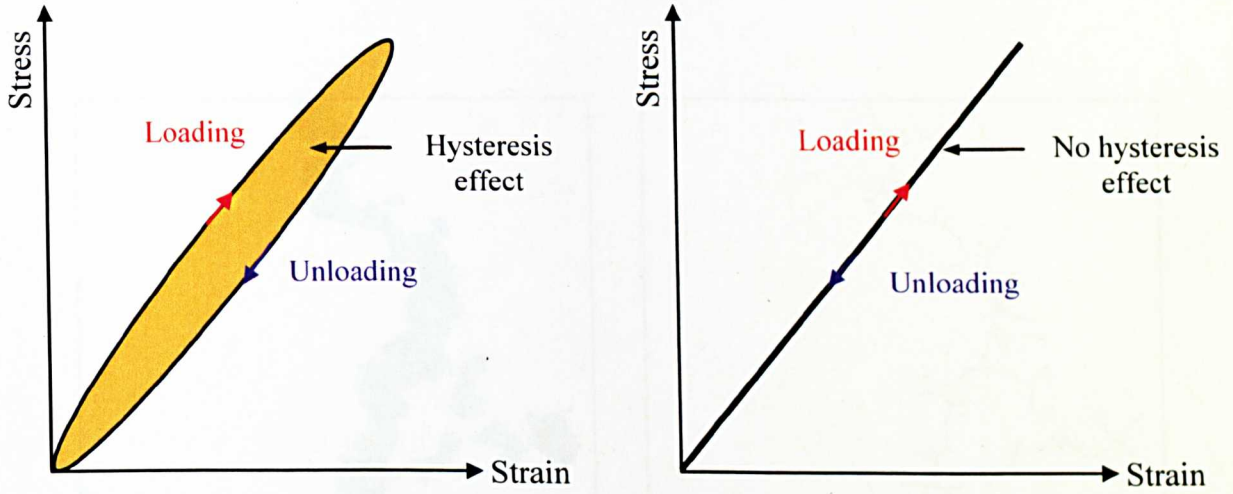

(a) Viscoelastic material (b) Elastic material

Figure 7.36 Illustration of the stress-strain behaviour for viscoelastic and elastic materials

Crack Density, Crack Tortuosity and Crack Branching Factor

Crack density, crack tortuosity and the crack branching factor are other parameters that can be used to describe crack patterns. Resistance to fracture can be correlated with these parameters which have found significant relevance in concrete research in the study of crack propagation behaviour as detailed in Chapter 4. This section will discuss these crack parameters examined from the fracture surfaces of the control and rubberised mixtures after fatigue failure. Besides the use of fractal dimension which takes into account the areas of the cracks, the three headlined crack parameters characterise the crack networks based on the crack length. In this study, the measurement of crack lengths was enabled by the conversion of binary image of crack to crack skeletons as shown in Figure 7.37. Table 7.11 also shows

average values of crack length, area and width for the different mixture types assessed after the fatigue test. The crack density values and percentage increase values (for a range of stress levels) before and after fatigue testing are presented in Table 7.12 and Figure 7.38 respectively.

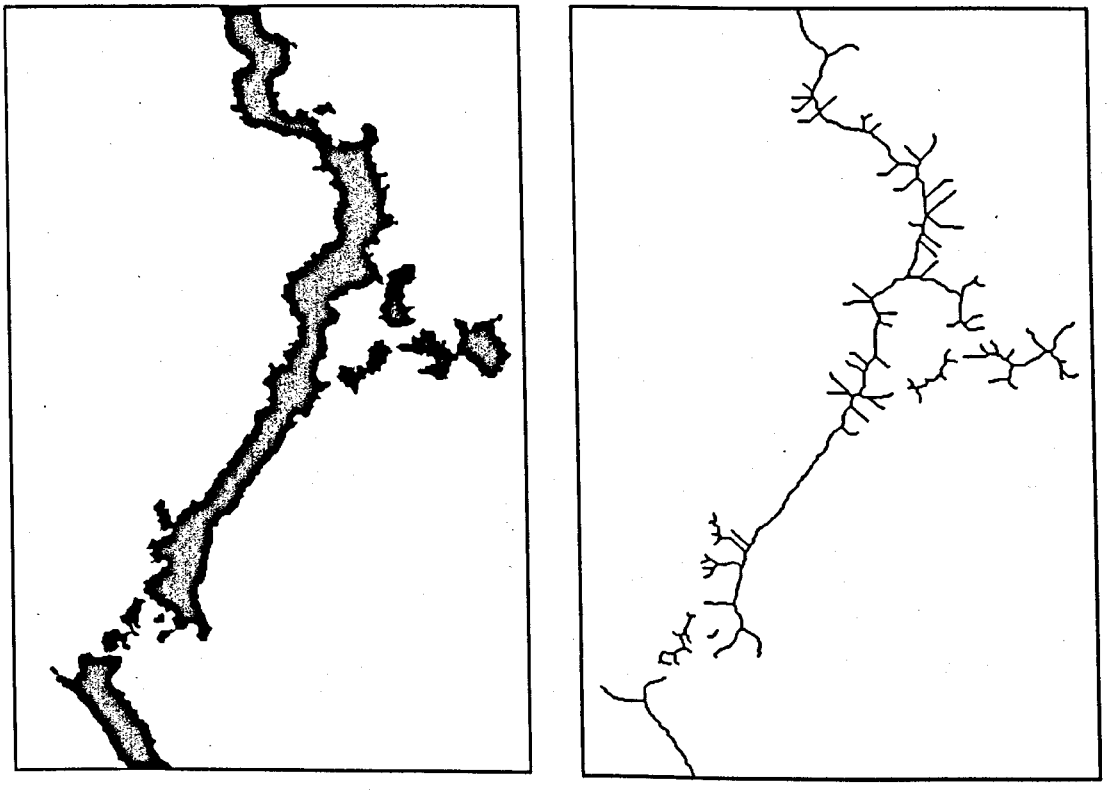

Figure 7.37 Conversion of binary image of cracks into cracks skeleton

Table 7.11 Results of crack characteristics

Mixture types	Test stress level (kPa)	Average length (mm)	Average area (mm^2)	Average width (mm)
0%	100	10.082	0.624	0.062
	200	7.488	0.461	0.062
	300	14.420	0.844	0.060
2%F	100	6.517	0.385	0.059
	200	6.858	0.406	0.059
	300	7.688	0.453	0.059
3%F	100	5.643	0.335	0.059
	200	5.413	0.320	0.059
	300	7.356	0.434	0.059
2%C	100	8.257	0.548	0.066
	200	8.624	0.543	0.063
	300	6.105	0.397	0.065
3%C	100	8.447	0.519	0.061
	200	6.641	0.402	0.061
	300	10.027	0.747	0.074

Table 7.12 Crack density in mm/mm^2 for different mixtures

Mixture types		Test stress level (kPa)					
		100		200		300	
		before	after	before	after	before	after
Control (0%)		0.009	0.063	0.017	0.064	0.014	0.074
Rubberised	2% F	0.014	0.053	0.042	0.096	0.041	0.089
	3% F	0.070	0.105	0.066	0.091	0.129	0.168
	2% C	0.022	0.061	0.026	0.058	0.016	0.034
	3% C	0.089	0.103	0.080	0.085	0.099	0.155

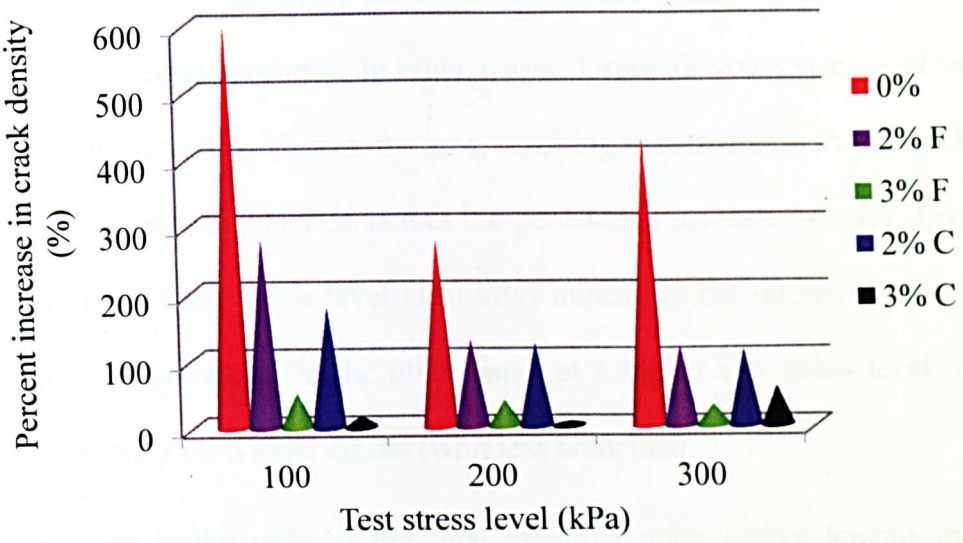

Figure 7.38 Percent increase in crack density values for different mixture types

Crack density is the ratio of crack length to a specified area (mm/mm^2). Consequently an increase in crack density corresponds to more cracks propagating within the area and forming crack networks under the action of loading. From the tables and figure, some interesting results can be seen which describe the crack behaviour for the different mixture types. Overall it is evident that the average length and area of the cracks are higher for the control mixture than the rubberised mixtures implying a higher degree of crack propagation had occurred and highlighting the severity of the damage within the specimen. This observation is in line with the increase in the specimen's crack density value after the fatigue test as shown in Figure 7.38. The mixtures with 3% rubber content show the least increase in crack density and their average crack sizes (length, area and width) were noted to be of a lesser magnitude in the fine rubber specimens than the coarse rubber ones. These results are consistent with the aforementioned results on fractal dimension values which indicated that the addition of rubber particles in the asphalt mixtures had reduced crack growth and improved the mixture's resistance to fatigue failure. It can also be correlated to the finding in

Section 6.3.1 (Chapter 6), that larger air voids sizes were found in the control specimen compared to the rubberised specimen. In other words, larger air voids size could potentially grow into cracks and spreading all over the area, resulting in an increase in the crack density. Another observation from Figure 7.38 is that the percentage increase in crack density value is highest at the lowest test stress level (100 kPa) indicating the initiation of major crack networks within the specimen. On the other hand, at a higher test stress level, the cracks coalesced to form larger individual cracks (with less branches).

The crack tortuosity is the ratio of the total effective main cracks lengths to the total Euclidean lengths of the cracks (mm/mm) and the crack branching factor is the ratio of the total crack branches lengths to the total of effective main cracks lengths, expressed as a percentage. These parameters are instrumental to the determination of fracture topography. Table 7.13 gives the values of crack tortuosity and crack branching factor for the different mixtures tested at different stress level. To aid comparison, the values are also plotted in Figure 7.39. From the results, overall, it is clear that the rubberised specimens produce higher crack tortuosity and crack branching factor values compared to the control mixture indicating improved resistance to crack propagation.

Table 7.13 Crack tortuosity and crack branching factor for different mixtures

Mixture types		Crack tortuosity			Crack branching factor		
		Test stress level (kPa)					
		100	200	300	100	200	300
Control (0%)		1.417	1.392	1.394	21.2	15.8	20.8
Rubberised	2% F	1.386	1.524	1.627	20.2	21.3	22.0
	3% F	1.501	1.475	1.800	23.1	20.4	24.5
	2% C	1.521	1.427	1.428	27.0	18.0	21.4
	3% C	1.495	1.450	1.717	20.1	19.3	26.5

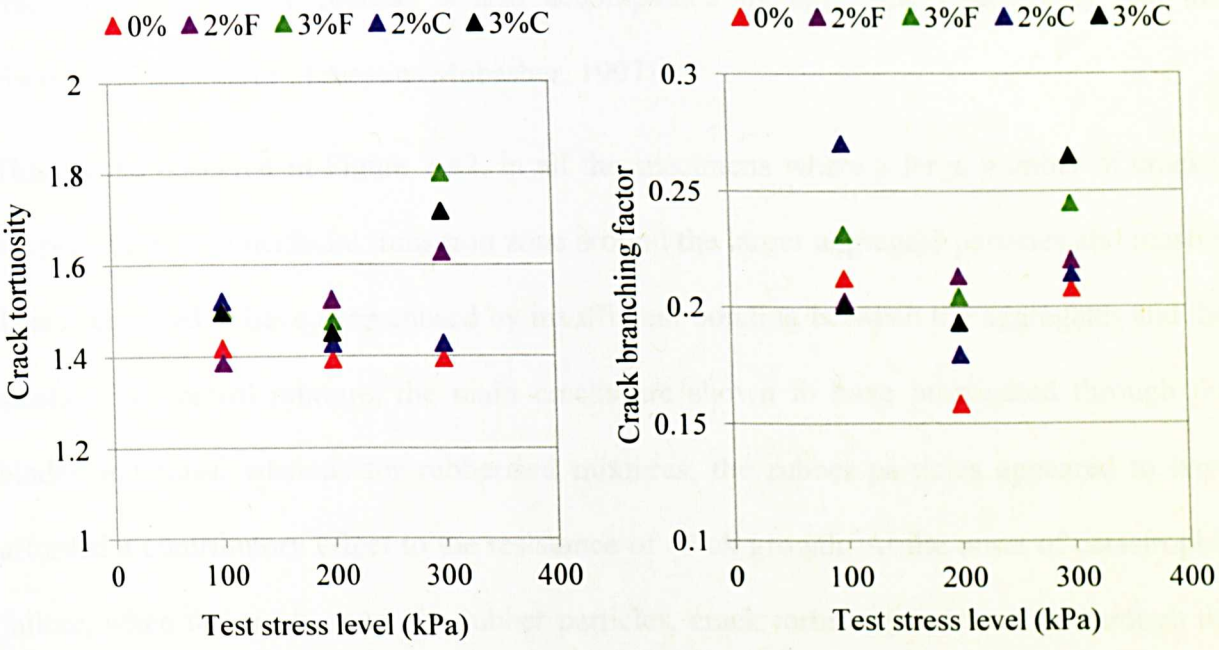

Figure 7.39 Plots of crack tortuosity and crack branching factor for different mixture types

Basically, the greater the value of crack tortuosity of a material, the better the material's capability to resist crack growth. This is the case because the material is able to provide tortuous crack paths to prevent sudden catastrophic crack growth which is known to result in spontaneous fatigue failure because a propagating crack always seeks the path of least resistance (see Figure 7.40). In other words, the catastrophic crack growth is inhibited by 'crack blunting' whereby the plastic deformation prior to crack propagation is increased. By this means, cracks can be arrested and diverted, averting sudden failure of the material. For a crack to propagate in the event of the aforementioned, the cleavage has to find the weakest path and its fracture energy must exceed the cohesive strength of the material at the crack tip zone. Figure 7.41 illustrates the crack growth and plastic region in the vicinity of the crack tip and shows the cohesive traction along the crack surfaces. The plastic region is partitioned into the plastic wake zone behind the crack opening and the active plastic zone ahead of the

crack. In addition, the process is also accompanied by aggregate interlocking and the viscoelastic behaviour of mastic (Mobasher, 1997).

This can be observed in Figure 7.42, in all the specimens where a large number of cracks, are present in the interfacial transition zone around the larger aggregate particles and mastic. This is believed to have been caused by insufficient bonding between the aggregates and the mastic. For control mixture, the main cracks are shown to have propagated through the binder and fines, whereas for rubberised mixtures, the rubber particles appeared to have afforded a contributory effect to the resistance of crack growth. At the onset of catastrophic failure, when the cracks meet the rubber particles, crack tortuosity is increased through the allowance of greater elastic deformation particularly near the crack tip before the cracks selects other weak paths to further propagate under the repetitive load cycles that could improve the material toughness. This is clearly shown in Figure 7.42, especially for the specimen with coarse rubber particles. This is supported by Abell and Lange (1998) who asserted that the crack tortuosity is an important variable affecting the fracture toughness of the material because it has the potential to prevent the localised stress intensity in the vicinity of the crack tip from reaching a critical level where the catastrophic crack propagation occurs.

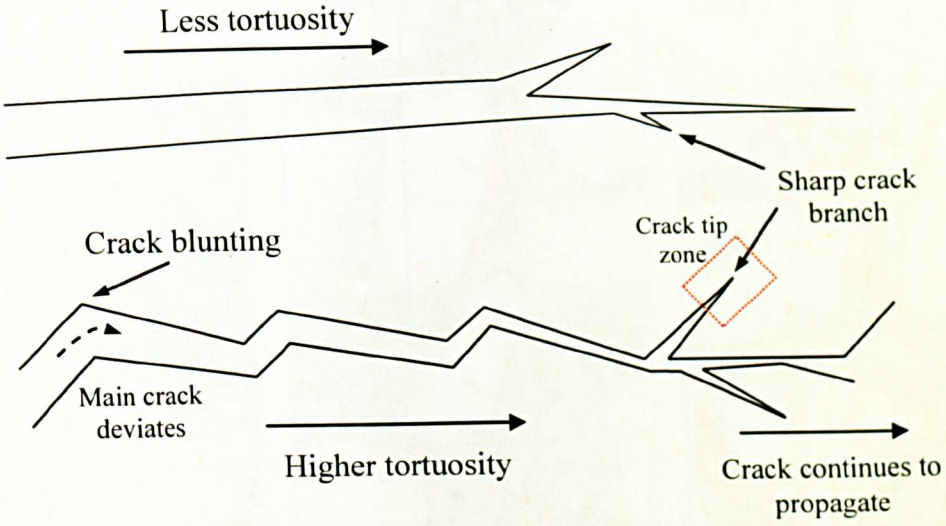

Figure 7.40 Illustration of crack tortuosity in crack growth

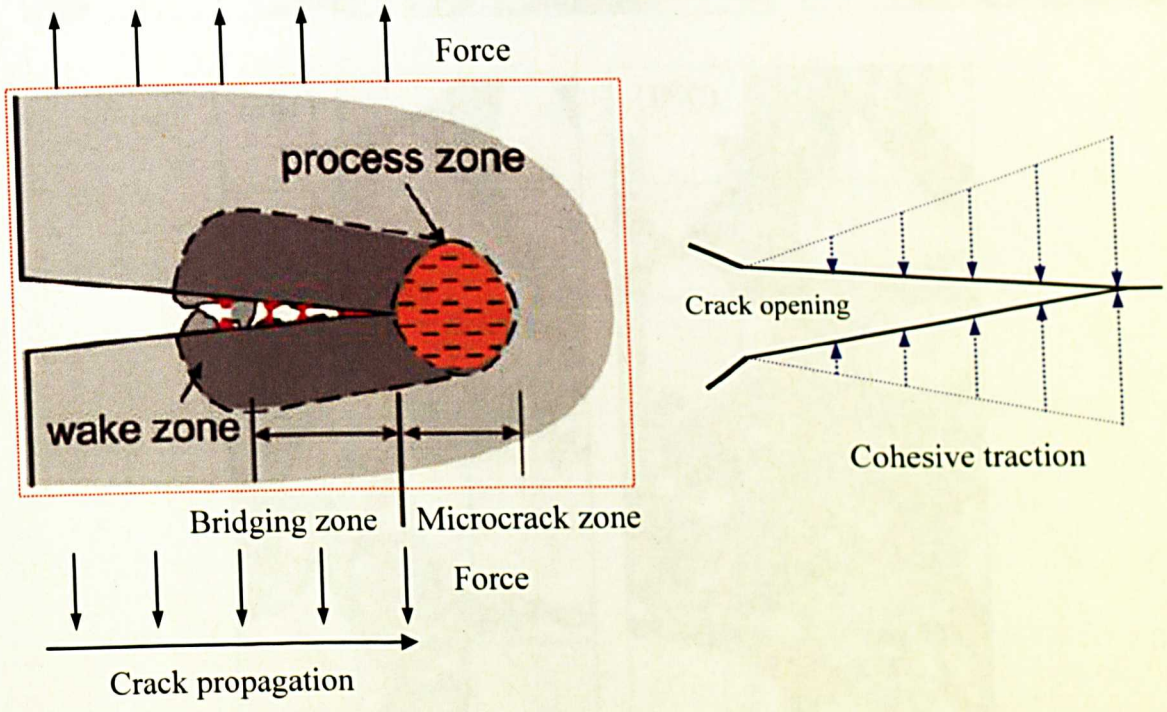

Figure 7.41 (a) Schematic diagrams of the crack tip zone as mark in Figure 7.40 (as in Tschegg, Jamek and Lugmayr, 2011) and (b) cohesive traction along the crack surfaces

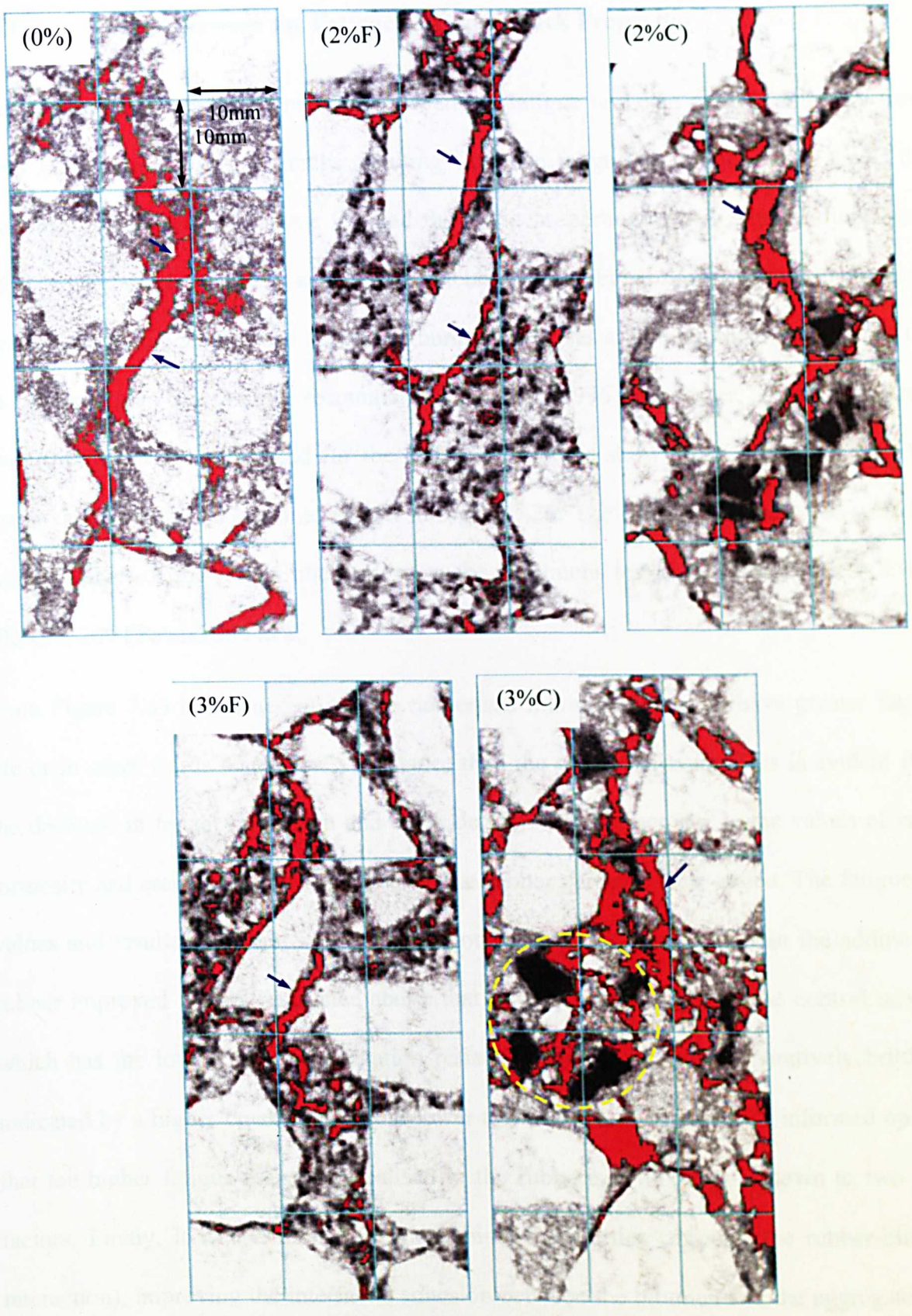

Figure 7.42 Fatigue cracks for different mixture types tested at 100 kPa

7.3.3 Correlation between the Fatigue Life and Crack Properties

This section examines the correlation between the fatigue test data and observations from X-ray CT image analysis of cracks resulting from the fatigue test. Figure 7.43 shows the relationships between the fatigue life and the crack properties namely, fractal dimension, crack density, crack tortuosity and crack branching factor. For this correlation, to facilitate the assessment, fatigue life was defined as number of cycles at 200 με, the upper limit of the 30-200 με fatigue failure range recommended by Read (1996). Moreover, at this microstrain level, the fatigue lives deduced for the different mixtures show good agreement with the results that form the fatigue lines shown in Figure 7.20. The crack properties used were the average values of the results obtained when the specimens tested at different stress levels, 100 kPa, 200 kPa and 300 kPa.

From Figure 7.43 both fine and coarse rubberised mixtures appear to have greater fatigue life or in other words better crack resistance than the control mixture. This is evident from the decrease in fractal dimension and crack density and the increase in the values of crack tortuosity and crack branching factor when the rubber particles were added. The fatigue life values and results from the crack analysis both lead to the conclusion that the addition of rubber improved fatigue resistance above that of the control mixture. The control mixture which has the lowest crack propagation resistance appears to be comparatively brittle as indicated by a higher crack growth and lower tortuosity. It is the author's informed opinion that the higher fatigue resistance realised in the rubberised mixtures is down to two main factors. Firstly, it is due to the enhanced binder properties (through the rubber-bitumen interaction), improving the interfacial adhesion between the bitumen and the aggregates and as well as the cohesiveness of the bitumen itself. In this study, although the degree of binder

modification was not determined, the methods for increasing rubber-bitumen interaction in dry process of preparing rubberised mixtures were implemented during specimen preparation as recommended by previous studies. Second, the rubber particles, acting as elastic aggregates resist the crack propagation by reducing the stress concentration in the vicinity of the crack tip through their inherent ability to absorb energy which consequently increases the fracture toughness of the materials.

Based on the trends of both fatigue data and crack analysis results, the ranking of specimens' resistance to fatigue cracking are summarised in Table 7.14. A comparison of the mixtures reveal that the specimens containing fine rubber particles have a higher fatigue life than the coarse rubberised mixtures, whereas analysis of the crack characteristics showed that specimens with higher rubber content have greater resistance to fatigue cracking.

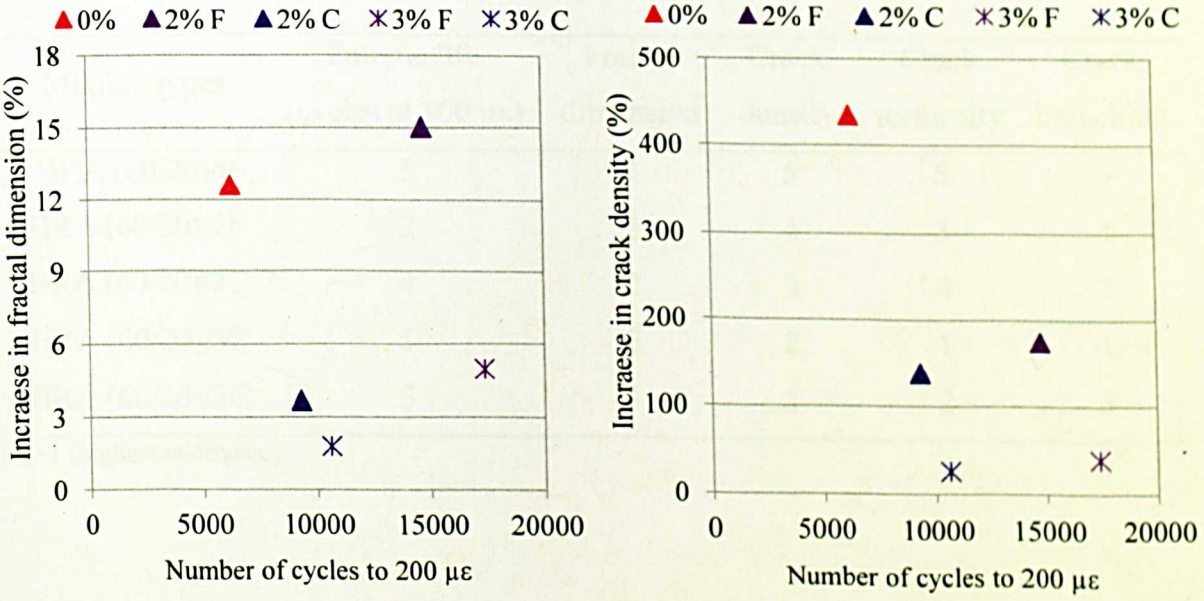

Figure 7.43 continues below

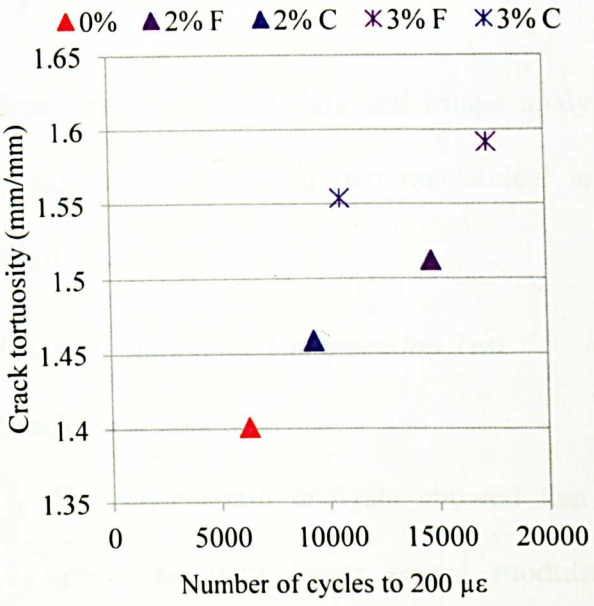

(c)

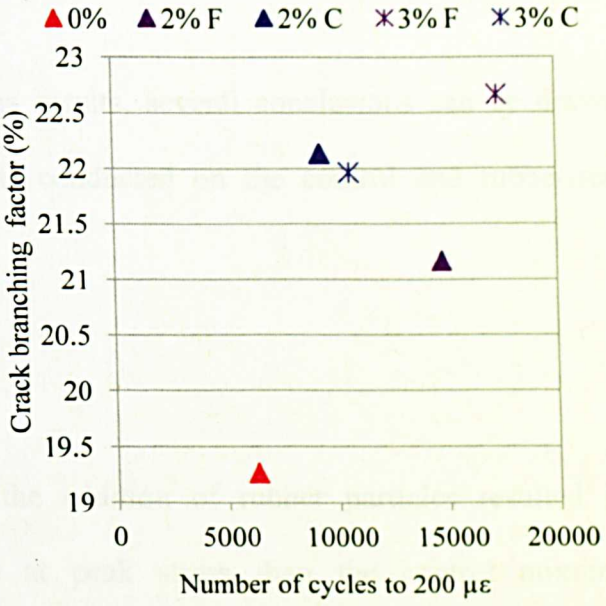

(d)

Figure 7.43 Fracture surface parameters vs number of cycles at 100 με

Table 7.14 Ranking of mixtures according to resistance against fatigue cracking

Mixture types	Fatigue life (cycles at 100 με)	Fractal dimension	Crack density	Crack tortuosity	Crack branching
HRA (60/20)/0	5	4	5	5	5
HRA (60/20)/2F	2	5	4	3	4
HRA (60/20)/2C	4	2	3	4	2
HRA (60/20)/3F	1	3	2	1	1
HRA (60/20)/3C	3	1	1	2	3

Note: 1 (highest resistance)

7.4 Summary

From the mechanical data and image analysis results, several conclusions can be drawn based on the following two mechanical tests conducted on the control and rubberised mixtures.

Uniaxial Monotonic Compression Test

Mechanical data:

i. The stress-strain analysis showed that the addition of rubber particles resulted in specimens with lower secant modulus at peak stress than the control mixture. Furthermore, increasing the rubber content slightly increased the peak modulus albeit remaining lower than the control mixture. The same pattern was observed for the specimens tested at higher temperature.

ii. Rubberised mixtures showed higher material toughness or resistance to fracture under the imposed stress compared to the control mixture as shown by the area under the stress-strain curve (Figures 7.2 and 7.3) describing the behaviour of the specimens.

Image analysis:

iii. Damage analysis conducted by comparing the air voids properties extracted from X-ray images of specimens before and after they were deformed revealed more damage (i.e. increase in voids area and cracks formation) in the middle third of the specimens than at the top and the bottom regions. In this instance the higher air voids content observed in the top and bottom regions prior to the test could not be used as an indication of the damage potential of the specimens. Similarly for the air voids shape properties, elongated air voids were observed at the top and bottom regions before the test but did not necessarily mean they had higher possibility to propagate and become cracks under

the loading action. However this phenomenon was expected to happen during the compression testing. By having low initial air voids content as a result of non-uniform distribution of compaction energy, the process of compression within the specimen under vertical loading with no confining pressure around the circumference has resulted in a significant amount of dilation at the middle region.

iv. For the top and bottom regions, the resulted damage might be contributed by the compaction characteristics as indicated by the higher initial air voids content and elongated shape compared to the middle region.

v. The specimen with 2% rubber was found to have less damage after the compression test. A comparison of the deformed 2% and 3% rubber specimens revealed the latter to have acquired a larger increase in voids area, voids number and voids size but had reduced the potential of crack formation within the specimen as shown by the changes in voids shape properties, indicating that rubber particles have potential to reduce crack growth.

Indirect Tensile Fatigue Test

Mechanical data:

i. The rubberised mixtures were found to a higher fatigue resistance than the control mixture, with the specimens containing higher rubber content demonstrating even greater fatigue life.

ii. The specimens containing fine rubber exhibited longer fatigue life affirming the dual functions of the rubber particles to improve the binder properties and act as elastic aggregates. Furthermore, by having the highest modulus of toughness, the rubber particles demonstrated the tendency to absorb stresses at the crack tip and resist crack propagation under the repetitive loading.

iii. The dissipated energy concept is very useful in describing the fatigue behaviour or the crack stages under repetitive loading particularly the formation of microcracks and macrocracks.

Image analysis:

iv. The characterisation of crack properties showed that more severe cracks were present in the control mixture than the rubberised mixtures which agrees with the observation that the lower a material's stiffness, the better its resistance to crack propagation.

v. The main cracks of the specimens containing rubber propagated more divergently than those of the control mixture which were straighter, confirming the higher crack resistance of the rubberised mixtures. The crack was observed to be concentrated at the central region of the specimen cross section and randomly propagated in the direction of the applied load. Majority of the cracks were initiated along the interfacial transition zone between the aggregate and the mastic or bitumen.

vi. Fractal dimension, crack density, crack tortuosity and the crack branching factor are very good indicators for characterising the fracture topography for a better explanation of the severity of the cracks growth.

vii. Correlations between the crack properties characterised as per the fracture surfaces and the fatigue life data from laboratory investigation show good agreement regarding improved resistance of rubberised mixtures to fatigue failure.

8.0 CONCLUSIONS AND RECOMMENDATIONS

8.1 Introduction

Inconsistent results stemming from decades of previous studies assessing the mechanical properties of dry mixed rubberised asphalt mixtures' necessitated a study focusing on developing an alternative approach for the evaluation of the rubberised asphalt mixture properties. This was achieved in this study by relating the quantified internal structure of rubberised asphalt mixtures to their mechanical behaviour. This is possible because asphalt mixtures are complex heterogeneous materials and their individual materials properties have a signficant contribution to the mixtures behaviour. Therefore if the properties of rubberised asphalt mixtures can be microstructurally characterised and related to the mixtures mechanical behaviour under specified conditions, it follows on that by altering the modification parameters (e.g. different rubber contents and gradings added to the mixture), evaluations to the mixture can be made comprehensively for further improvements. To this end, different techniques or perspectives of rubberised asphalt mixtures characterisation were explored in this study. The mixtures were investigated at a micro-level using X-ray CT scanning combined with image analysis techniques to obtain a thorough understanding of their internal structure and correlation to mechanical failure. The changes observed as a result of introducing varying amounts and gradings of rubber into asphalt mixtures were compared to a control mixture. Consequently, several conclusions were drawn and recommendations made for future investigations.

8.2 Conclusions

Conclusions are drawn here in accordance with the objectives specified prior to the investigation in the following three key areas:

i. Imaging and Thresholding Techniques for Identifying the Internal Structure of Rubberised Asphalt Mixtures

Investigation: Image acquisition, image processing and image analysis methods were utilised in the aforementioned study area. These involved X-ray CT scanning and the application of various algorithms and imaging tools from imaging software packages. Parameters and procedures adopted for the image processing and image analysis were established as the investigation evolved.

Conclusions:

- ✓ Through this investigation, X-ray CT has been confirmed to be a powerful non-destructive method for capturing the images of the internal structure of rubberised asphalt mixtures. This is necessary because any cutting and trimming works conducted on this particular mixture to assess their microstructure properties will result in losing their structural integrity.
- ✓ The image processing techniques adopted consisted of three main operations namely, image enhancement, image thresholding and morphological operations. Image thresholding of the rubberised asphalt mixtures proved most challenging because it required segmentation of the different material phases identified in the X-ray images, specifically the air voids, rubber particles, mastic and aggregates. The variations in the image grey levels, particles contacts and particles arrangement within the captured

X-ray images made it difficult to separate them for analysis. Thus, it was concluded that material selection is a very important factor that determines the clarity of the complex structures within the X-ray images. In other words, the higher the difference in materials' densities, the better the contrast between images of the materials would appear. Also, the larger the size of the particles used, the easier it would be to recognise objects of interest and separate them from other mixture constituents.

✓ The study has shown that stereology is a viable technique for the 3D interpretation based on 2D planar sections of asphalt materials. The 2D analysis utilised in this study simplified the process of image analysis and aided the development of quantitative relations between the materials microstructure and properties. However 3D analysis could have arguably provided more reliable results due to its emphasis on the internal structure of the materials.

✓ For the microstructure quantification, a few parameters relating to the amount, size, shape and distribution of the property of interest were considered suitable for describing, measuring and interpreting the microstructural features within X-ray images. Thus changes in those parameters before and after mechanical testing became reliable indicators of the degree of damage that had occurred within a specimen. Additionally, fractal dimension and crack properties were also interesting parameters to characterise the fracture surfaces caused by the damage.

✓ The principle of superposition which applied the mathematical logical operations was adopted for extracting the damaged area within X-ray images. In doing this, it was possible to identify the areas of damage concentration in specimens, typified by

increases in the air voids content and differentiate them from existing air voids in the graphical representations examined.

✓ This study demonstrated that no single or universal imaging technique can solve all the scenarios of image processing and image analysis. However, its flexibility and unlimited number of possible image transformations and tools make it possible to find the best solution for any specific imaging problem. The techniques developed in this study are simply an attempt to produce guidelines for use in the analysis of the images of rubberised asphalt mixtures.

ii. Effect of Rubber Addition on the Internal Structure Distribution of Asphalt Mixtures

Investigation: The internal structure of the control and rubberised asphalt mixtures (with different mixture variables) were X-rayed, analysed and described with reference to their air voids properties and rubber particles distributions in their undamaged state.

Conclusions:

✓ Analysis of the rubberised asphalt mixtures revealed that the rubber distribution was affected by both the gradation and the content of the rubber particles added to the mixtures. The rubber particles were found to be well distributed along the specimen's height. In radial direction, the fine rubber particles appeared well distributed while the coarse rubber particles tended to be localised in the specimens' cross sections. Furthermore, as the rubber content of the mixtures increased, the rubber particles showed a greater tendency to form patches within the specimen.

- ✓ Characterisation of the air voids showed that increasing rubber content affects air voids formation. A higher number of air voids with close to homogeneous distribution were observed in the rubberised mixtures with the air voids being scattered within the cross section as compared to the air voids in the control mix which were more concentrated near the specimen's circumference. The specimen having finer rubber particles produced smaller air voids size in comparison to the specimen that had coarse rubber particles and the control mix. Also, the shape of the air voids formed was noticed to become more elongated as rubber content of the mixture was increased.
- ✓ Analysis of the air voids formation associated with the location of rubber particles revealed that more air voids were more likely to form and localise within the area of rubber particles which gives a view that the rubber particles could influence the air voids formation. Their elastic behaviour under the compaction effort resulting in the rubber particles deforming and recovering repeatedly which could cause the formation of air voids within their surrounding area.

iii. Micro and Mechanical Damage Characterisation of the Rubberised Asphalt Mixtures

Investigation: A laboratory study was conducted to evaluate the mechanical behaviour of control and rubberised asphalt mixtures using Uniaxial Monotonic Compression Test and Indirect Tensile Fatigue Test. Microstructural damage of the mixtures were analysed by comparing their X-ray CT images before and after the mechanical tests. Both mechanical and microstructural properties were then correlated to reveal any relationship between them. Magnified images of the damage areas were also captured using the Scanning Electron Microscope (SEM) for closer assessment and justification.

Conclusions:

- ✓ Introducing rubber particles into the asphalt mixtures resulted in a general decrease in the modulus of the rubberised mixtures at peak stress in comparison to the control mix which yielded a higher strain value. Surprisingly however, the severity of microstructural damage in the rubberised mixtures, expressed in terms of changes in air voids content and shape properties were noted to be less than the control mix. This highlighted the capacity of rubberised mixtures to sustain load under compression which despite being reduced, produced less physical damage in terms of the microcrack formation or crack growth.

- ✓ Good correlations were observed between the crack properties and the fatigue test data of the rubberised mixtures in that both agreed that the rubber addition into the mixture increases the fatigue life of the mixture indicating a greater resistance against the fatigue cracks compared to the control mix. Higher rubber content and finer rubber size were identified as the keys to enhance the fatigue resistance of the asphalt mixtures. In other words, rubber modification may reduce the stiffness but extend the fatigue life of the mixture.

- ✓ The fracture pattern of the control mix was noted to be different from those of the rubberised mixtures. Majority of the cracks observed initiated and propagated considerably within the interfacial transition zone (ITZ), between mastic or binder and aggregate particles, possibly affecting the asphalt mixture's strength and fracture behaviour. The author believes that the aforementioned properties can be enhanced by improving the adhesive bonding strength of the ITZ area.

- ✓ In both tests, the rubber particles showed their capacity to store energy or absorb stress to keep the material less susceptible to damage and increase their load carrying capacity. The rubber particles can also be described as crack-arrestors at the crack tip which control the crack growth or keep them small to prevent catastrophic failure.
- ✓ From the image analysis, it was shown that air voids and crack properties are significant indicators in characterising the damage in asphalt mixtures from a microstructural point of view.
- ✓ Overall, there were good agreements between the mechanical and microstructural properties in assessing the effect of adding crumb rubber in asphalt mixture. The implication of this is that it links the microstructure and the macroscopic response of rubberised asphalt mixtures to provide an improved understanding of the modified mixtures in addition to facilitating a more accurate interpretation of experimental results for the improvement of rubberised asphalt mixtures.

8.3 Recommendations for Further Investigation

This work has laid the foundation for development of methodologies for the characterisation of the microstructure properties of rubber modified asphalt mixtures. The following recommendations may be of interest in future research endeavours:

- ✓ This study was conducted using a gap graded of hot rolled asphalt mixture, modified with different rubber content and sizes. It is therefore recommended to apply the same methodology to a different mixture types e.g. a dense graded asphalt mixture because it is regularly used in pavement construction and has been shown to perform well in most applications. Furthermore, the prospect of combining a range of aggregate sizes in itself offers a different challenge to image analysis study.

- ✓ In this study, the addition of rubber has been shown to improve properties of asphalt mixture in terms of its flexibility and recovery characteristics. This is thought to be the result of improved bitumen cohesive properties or the rubber particles functioning as elastic aggregates. However the extent of modification or the relative contributions offered by either effect were not thoroughly investigated. Consequently, there is a need for further studies to assess the aforementioned benefits. In addition, a wider range of rubber sizes and rubber contents added to the asphalt mixtures may be used.

- ✓ The development of a detailed image program that undertakes both image processing and image analysis procedures is recommended and will prove very useful and less tedious than the process undertaken in this study. Because of the time it would take to develop and validate such a program, expertise knowledge of computer programming will be very helpful.

- ✓ Investigation into how specimen damage evolves during the mechanical test is recommended, i.e. conducted in such a way that allows the mechanical test to be stopped and the tested specimens are X-rayed repeatedly at predetermined stresses. This would help to better define the development of microstructural damage towards the failure. However, in this study, it was also seen that the elasticity of the rubber particles in the rubberised mixtures led to the tested specimen experiencing a considerable amount of strain recovery due to the improved flexibility of the mixtures. The extent of such recovery and its significance is therefore recommended for a more thorough understanding of the modification process and its implications before conducting the aforementioned damage investigation for rubberised asphalt mixture.

- ✓ To obtain more reliable test data, it is also recommended that several other factors such as the effect of temperature, moisture and aging be incorporated into future mechanical tests. This is important in order to obtain data that simulates field conditions and for parametric analysis.

Recommendation for Field Application

The outcomes of this study contribute considerably to the furtherance of knowledge and understanding of the microstructure of the dry mixed rubberised asphalt mixtures in their undamaged and damaged states. Correlations between microstructure properties and mechanical test results proved that the addition of crumb rubber in hot rolled asphalt mixture (HRA 60/20) has a significant effect on its mechanical behaviour. Specifically, it leads to a reduction in modulus of the pavement but produces less fracture surfaces and also increases the pavement's fatigue life and crack resistance. As a result of this, the use of crumb rubber modifier in HRA 60/20 should be given more consideration for further investigation in the future. If crumb rubber is added to HRA 60/20 specified for binder course layer, it could potentially reduce the effects of the layers typically low stiffness modulus while increasing the fatigue resistance of the pavement when it is subjected to traffic loading.

REFERENCES

Abell, A. B., & Lange, D. A. (1998). Fracture mechanics modeling using images of fracture surfaces. *International Journal of Solids and Structures, 35*(31-32), 4025-4034.

Airey G.D., Collop A.C., & Rahman, M. M. (2004). Mechanical properties of crumb rubber modified asphalt mixtures. *3rd Eurasphalt & Eurobitume Congress*, Vienna.

Airey, G. D., Rahman, M. M., & Collop, A. C. (2003). Absorption of bitumen into crumb rubber using the basket drainage method. *International Journal of Pavement Engineering, 4*(2), 105-119.

Akcaoglu, R., Tokyay, M., & Celik, T. (2005). Assessing the ITZ microcracking via scanning electron microscope and its effect on the failure behavior of concrete. *Cement Concrete Research, 35*(2), 358-363.

Akhavan, A., Shafaatian, S. M. H., & Rajabipour, F. (2012). Quantifying the effects of crack width, tortuosity and roughness on water permeability of cracked mortars. *Cement and Concrete Research, 42*(2), 313-320.

Amirkhanian, S. N. (2001). *Utilization of crumb rubber in asphaltic concrete mixtures-south carolina's experience*. Report Draft, South Carolina Department of Transportation, U.S. Department of Transportation: The Federal Highway Administration.

Arasan, S., Yener, E., Hattatoglu, F., Akbulut, S., & Hinislioglu, S. (2010). The relationship between the fractal dimension and mechanical properties of asphalt concrete. *International Journal of Civil and Structural Engineering, 1*(2), 165-170.

Berube, D., & Jebrak, M. (1999). High precision boundary fractal analysis for shape characterization. *Computers & Geosciences, 25*, 1059-1071.

Braz, D., Lopes, R. T., & Motta, L. M. G. (1999). Analysis of the percentage voids of test and field specimens using computerised tomography. *Nuclear Instruments and Methods in Physics Research, A422*: 942-948.

British Standards Institution. (1997). Test for geometrical properties of aggregates - Part 1: Determination of particle sizes distribution - *Sieving method.* BS EN 933-1 (1997), BSI, London.

British Standards Institution. (2000). Tests for mechanical and physical properties of aggregates. Determination of particle density and water absorption, BS EN 1097-6:2000, BSI, London.

British Standards Institution. (2000). Methods of test for petroleum and its products: Bitumen and bituminous binders - *Determination of softening point - Ring and ball method.* BS EN 1427:2000, BSI, London.

British Standards Institution. (2000). Methods of test for petroleum and its products: Bitumen and bituminous binders - *Determination of needle penetration.* BS EN 1426:2000, BSI, London.

British Standards Institution. (2001). Coated Macadam (Asphalt Concrete) for Roads and Other Paved Areas - Part 4: *Specification for constituent materials and for mixtures.* BS 4987-1:2001, BSI, London.

British Standards Institution. (2002). Bituminous mixture: Test method for hot mix asphalt - Part 5*: Determination of the maximum density.* BS EN 12697-5:2002, BSI, London.

British Standards Institution. (2003). Methods of test for petroleum and its products: Bitumen and bituminous binders - *Determination of viscosity of bitumen using a rotating spindle apparatus.* BS EN 13302:2003, BSI, London.

British Standards Institution. (2003). *Method for the determination of the fatigue characteristics of bituminous mixtures using indirect tensile fatigue.* DDABF-2003 ITFT, BSI, London.

British Standards Institution. (2003). *Method for the indirect tensile stiffness modulus of bituminous mixtures.* DD 213: 1993 ITSM, BSI, London.

British Standards Institution. (2005). Hot rolled asphalt for roads and other paved - Part 1: *Specification for constituent materials and asphalt mixtures.* BS 594-1:2005, BSI, London.

British Standards Institution. (2006). Bituminous mixtures: Material specification - Part 4: *Hot rolled asphalt.* BS EN 13108-4:2006, BSI, London.

British Standards Institution. (2007). Methods of test for petroleum and its products: Bitumen and bituminous binders: Measurement of density and specific gravity - *Capillary-stoppered pyknometer method.* BS EN 15326:2007, BSI, London.

British Standards Institution. (2007). Bituminous mixtures: Test methods for hot mix asphalt - Part 35: *Laboratory mixing.* BS EN12697-35:2004, BSI, London.

British Standards Institution. (2007). Bituminous mixtures: Test methods for hot mix asphalt - Part 31: *Specimen preparation by gyratory compactor.* BS EN 12697-31:2007, BSI, London.

Brown, S. F. (1978). *Material characteristics for analytical pavement design: In developments in highway pavement engineering* (1st ed.). London: Applied Science, 41-92.

Cao, W.D. (2007). Study on properties of recycled tire rubber modified asphalt mixture using dry process. *Construction and Building Materials, 21,* 1011-1015.

Chehovits, J. G., Hicks, Gary R., & Lundy, J. (1993). A mix design procedures. *Proceedings of the CRM Workshop,* Arlington, Texas.

Epps, J.A. (1994). *Uses of recycled rubber tires in highways.* NCHRP Synthesis of Highway Practice 198, Transportation Research Board, Washington, D.C.

Erdem, S. (2011). *Impact load-induced microstructural damage of concrete made with unconventional aggregates.* PhD. Thesis, University of Nottingham, Nottingham.

Esch, D. C. (1982). *Construction and benefits of rubber modified asphalt pavements.* Transportation Research Record 860, Transportation Research Board, Washington, D.C.

Esch, D. C. (1984). *Asphalt pavements modified with coarse rubber particle - Design, construction and ice control observations. Alaska* (Report No. FHWA-AK-RD-85-07). U.S. Department of Transportation: The Federal Highway Administration.

Gallego, J.; M.A. Del Val & R. Tomás. (2000). A spanish experience with asphalt pavements modified with tire rubber. *Proceedings of the Asphalt Rubber 2000 Conference*. Portugal, pp. 673-687.

Garba, R. (2002). *Permanent deformation properties of asphalt concrete mixtures.* PhD. Thesis, Norwegian University of Science and Technology, Trondheim, Norway.

Garboczi, E. J. (2002). Three-dimensional mathematical analysis of particle shape using x-ray tomography and spherical harmonics: Application to aggregates used in concrete. *Cement and Concrete Research, 32*, 1621-1638

Gawel, I., Stepkowski, R., & Czechowski, F. (2006). Molecular interactions between rubber and asphalt. *Industrial & Engineering Chemistry Research, 45*(9), 3044-3049.

Geng, M., Dou, Y., & Li, X. (2011). Study of micro-structure of asphalt mixture based on fractal theory. *Mechanic Automation and Control Engineering (MACE), 2nd International Conference*, pp. 2582-2584.

Glinicki, M. A., & Litorowicz, A. (2006). Crack system evaluation in concrete elements at mesoscale. *Bulletin of the Polish Academy of Sciences, Technical Sciences, 54*(4), 371-379.

Gonzalez, R. C., & Woods, R. E. (1992). *Digital image processing.* Boston: Addison-Wesley Publishing Company, Inc.

Gonzalez, R. C., & Woods, R. E. (2008). *Digital image processing* (3rd ed.). United States: Prentice Hall.

Gordon, J. E. (1978). *Structures*. New York: Plenum Publ. Co.

Gowda, G. V., Hall, D. K., & Elliot, R. (1996). *Arkansas' experience with rubber modified mixes using marshall and SHRP level I mix design methods.* Transportation Research Record 1530, Transportation Research Board, Washington, D.C.

Kachanov, L. M. (1986). *Introduction to continuum damage mechanics*. Dordrecht: Martinus Nijhoff Publishers.

Kachanov, L. M. (1958). *On creep rupture time*. Izv. Acad. Nauk SSSR, Otd. Techn. Nauk, 8, 26-31.

Karperien, A. (1999-2012). *FracLac for ImageJ,* version 2.5. http://rsb.info.nih.gov/ij/plugins/fraclac/FLHelp/Introduction.htm.

Harvey, A. S., & Curtis, T. M. (1990). *Evaluation of PlusRide™ - A rubber modified plant mixed bituminous surface mixture*. Final Report, Physical Research Unit, Office of Materials and Research, Minnesota Department of Transportation.

Hassan, N. A., Airey, G. D., Khan, R., & Collop, A. C. (2012). Nondestructive characterisation of the effect of asphalt mixture compaction on aggregate orientation and segregation using x-ray computed tomography. *International Journal of Pavement Research and Technology, 5*(2), 84-92.

Heitzman, M.A. (1992). *State of the practice for the design and construction of asphalt paving materials with crumb rubber additive* (Report No. FHWA-SA-92-022). U.S. Department of Transportation: The Federal Highway Administration.

Hunter, A. E., Airey, G. D., & Collop, A. C. (2004). *Aggregate orientation and segregation in laboratory compacted asphalt specimens*. Transportation Research Record 1891, Transportation Research Board, Washington, D.C., 8-15.

Kandhal, P. S., & Hanson, D. I. (1993). A CRM technology. *Proceedings of the CRM Workshop*, Arlington, Texas.

Khan, R. (2009). *Quantification of microstructural damage in asphalt*. PhD. Thesis, University of Nottingham, Nottingham.

Ketcham, R. A., & Carlson, W. D. (2001). Acquisition, optimization and interpretation of x-ray computed tomographic imagery: Applications to the geosciences. *Computers and Geosciences, 27*, 381-400.

Kim, S., Loh, S. W., Zhai, H., & Bahia, H. (2001). *Advanced characterization of crumb rubber-modified asphalts, using protocols developed for complex binder*. Transportation Research Record 1767, Transportation Research Board, Washington, D C, 15-24.

Kim, Y. R., Allen, D. H., & Little, D.N. (2007). A computational constitutive model for predicting nonlinear viscoelastic damage and fracture failure of asphalt concrete mixtures. *International Journal of Geomechanics, 7*(2), 102-110.

Kim, Y. R., Lee, H. J., Kim, Y., & Little, D. N. (1997). Mechanistic evaluation of fatigue damage growth and healing of asphalt concrete: Laboratory and field experiments. *Proceedings 8th International Conference on Asphalt Pavements, International Society for Asphalt Pavements*, University of Washington, Seattle, Washington, pp. 1089-1107.

Kutay, M. E., Arambula, E., Gibson, N., & Youtcheff, J. (2010). Three-dimensional image processing methods to identify and characterise aggregates in compacted asphalt mixtures. *International Journal of Pavement Engineering, 11*(6), 511-528.

Landis, E., & Keane, D. (1999). X-ray micro-tomography for fracture studies in cement-based materials. *International Society of Optical Engineering, 3772*, 105-113.

Lee, S. J., Akisetty, C. K., & Amirkhanian, S. N. (2007). The effect of crumb rubber modifier on the performance properties of rubberized binders in HMA pavements. *Construction and Building Materials, 22*, 1368-1376.

Lee, S. J., Amirkhanian, S. N., & Shatanawi, K. (2006). Effect of reaction time on physical and chemical properties of rubber-modified binders. *International Rubber Conference*. Compendium of Papers CDRom, Lyon, France.

Lemaitre, J., & Desmorat, R. (2005). *Engineering damage mechanics*. New York: Springer.

Maire, E., Babout, L., Buffiere, J. Y., & Fougeres, R. (2001). Recent results on 3D characterization of microstructure and damage of metal matrix composites and a metallic foam using x-ray tomography. *Journal of Materials Science and Engineering, A319-321*, 216-219.

Masad, E., Jandhyala, V. K., Dasgupta, N., Somadevan, N., & Shashidhar, N. (2002). Characterization of air void distribution in asphalt mixes using x-ray computed tomography. *Journal of Materials in Civil Engineering, 14*(2), 122- 129.

Masad, E., Little, D. N., Tashman, L., Saadeh, S. Al-Rousan, T., & Sukhwani, R. (2003). *Evaluation of aggregate characteristics affecting HMA concrete performance* (Report

No. ICAR 203-1). Texas A&M University System College Station, Texas: Texas Transportation Institute.

Masad, E., Muhunthan, B., Shashidhar, N., & Harman, T. (1999a). *Effect of compaction procedure on the aggregate structure in asphalt concrete.* Transportation Research Record 1681, Transportation Research Board, Washington, D.C., 179-185.

Masad, E., Muhunthan, B., Shashidhar, N., & Harman, T. (1999b). Internal structure characterization of asphalt concrete using image analysis. *Journal of Computing in Civil Engineering (Special Issue on Image Processing), 13*(2), 88-95.

Masad, E. (2004). X-ray computed tomography of aggregates and asphalt mixes. *Materials Evaluation Journal*, 775- 783.

Mathias Leite, L. F., Almeida da Silva, , Edel, G., Goretti da Motta, L., & Herrmann do Nascimento, L. A. (2003). Asphalt rubber in Brazil: Pavement performance and laboratory study. *Proceedings of the Asphalt Rubber 2003 Conference*, Brasilia, Brazil.

Michette, A. G., & Buckley, C. J. (1993). *X-ray science and technology.* London: Institute of Physics Publishing.

Mihashi, H., Ahmed, S. F. U., Mizukami, T., & Nishiwaki, T. (2006). Quantification of crack formation using image analysis and its relationship with permeability. *Restoration of Buildings and Monuments, 12*(4), 335–348

Mobasher, B., Mamlouk, M. S., & Lin, H. M. (1997). Evaluation of crack propagation properties of asphalt mixtures. *Journal of Transportation Engineering, 123*(5), 405-413.

Muraya, M. (2007). Homogeneous test specimens from gyratory compaction. *International Journal of Pavement Engineering, 8*(3), 225-235.

Olivares F., Schultz B., Fernández, M., & Moro, B. (2009). Rubber-modified hot mix asphalt pavement by dry process. *International Journal of Pavement Engineering, 10*(4), 277-288.

Oliver, J. W. H. (1981). *Modification of paving asphalts by digestion with scrap rubber.* Transportation Research Record 821, Transportation Research Board, Washington, D.C.

Paterson, T. (2007). *An investigation into the damage evolution of idealized bituminous composites using x-ray computed tomography.* Master's Thesis, University of Nottingham, Nottingham.

Pinheiro, J. H. M., & Soares, J. B. (2003). The effect of crumb rubber gradation and binder-rubber interaction time on the asphalt-rubber mixture (dry process). *Proceedings of the Asphalt-Rubber Conference 2003,* Brasilia, Brazil, pp. 707-718.

Putman, B. J., & Amirkhanian, S. N. (2006). Crumb rubber modification of binders: Interaction and particle effects. *Asphalt-Rubber 2006 Conference,* Palm Springs, California, USA.

Qingli, D., & Martin, H. S. (2004). Parametric model study of microstructure effects on damage behavior of asphalt samples. *International Journal of Pavement Engineering, 5*(1), 19-30.

Rahman, M. M. (2004). *Fundamental characterisation of dry process crumb rubber modified asphalt mixtures.* PhD. Thesis, University of Nottingham, Nottingham.

Razavi, R. M. (2006). *Characterisation of microstructure and internal displacement field of sand using x-ray computed tomography.* PhD. Thesis, Washington State University.

Read, J., & Whiteoak, D. (2003). *Shell bitumen handbook* (5th ed.). London: Thomas Telford.

Read, J. M. (1996). *Fatigue cracking of bituminous paving mixtures.* PhD. Thesis, University of Nottingham, Nottingham.

Reschner, K. (2006). *Scrap tire recycling: A summary of prevalent disposal and recycling methods.* <http://www.entire- engineering.de/Scrap_Tire_Recycling.pdf>.

Roberts, F. L., Kandhal, S., Brown, E. R., Lee, D. Y., & Kennedy, T. W. (1996). *Hot mix asphalt materials, mixture design, and construction* (2nd ed.). NAPA Research and Education Foundation 585.

Rowe, G. M. (1996). *Application of dissipated energy concept to fatigue cracking in asphalt pavements.* PhD. Thesis, University of Nottingham, Nottingham.

Rubber Manufacturers Association, Washington D. C. USA. *Scrap Tires Markets.* http://www.rma.org/scrap_tires/scrap_tire_markets/scrap_tire_characteristics/

Rubber Manufacturers Association. (2004). *U.S. Scrap Tire Markets* (2003 Edition). Washington, D.C.

Saadeh, S., Masad, E., Garboczi, E., & Harman, T. (2003). Aggregate shape analysis using x-ray Computed Tomography. *Proceedings of the 11th Symposium of the International Center for Aggregate Research*, Austin.

Schuler, T. S., Pavlovich, R. D., Epps, J.A., & Adams C. K. (1986). *Investigation of materials and structural properties of asphalt-rubber paving mixtures.* Volume I-(Report No. FHWA-RD-86/027). U.S. Department of Transportation: The Federal Highway Administration.

Shi, B., Murakami, Y., Wu, Z., Chen, J., & Inyang, H. (1999). Monitoring of internal failure evolution in soils using computerisation x-ray tomography. *Journal of Engineering Geology, 54*(3-4), 321-328.

Smith, T. G., Lange, G. D., & Marks, W. B. (1996). Fractal methods and results in cellular morphology-dimensions, lacunarity and multifractals. *Journal of Neuroscience Methods, 69*, 123-136.

Song, J. M, Lui, T. S., Chang, Y. L., & Chen, L. H. (2005). Compositional effects on the microstructure and vibration fracture properties of Sn-Zn-Bi Alloys. *Journal of Alloys and Compounds, 403*, 191-196.

Song, I. (2004). *Damage analysis in asphalt concrete mixtures based on parameter relationships.* Ph.D. Thesis. Texas A & M University, US.

Sonka, M., Hlavac, V., & Boyle, R. (1998). *Image processing, analysis and machine vision* (2nd ed.) United States: International Thomson Publishing Company.

Sprawls, (1993). *Characteristics and structure of matter: Physical principles of medical imaging* (2nd ed.). Madison, WI: Medical Physics Publishing. http://www.sprawls.org/ppmi2/.

Stephen, L. R. (1993). *Fundamental principles of polymeric materials* (2nd ed.). Canada: Wiley-Interscience Publication, John Wiley & Sons, Inc.

Stroup-Gardiner, M., Chadbourn, B. C., & Newcomb, D. E. (1996). *Babbitt, Minnesota: Case study of pretreated crumb rubber modified asphalt concrete.* Transportation Research Record 1530, Transportation Research Board, Washington, D.C., 34-42.

Stroup-Gardiner, M., Newcomb, D.E., & Tanquist, B. (1993). *Asphalt-rubber interactions.* Transportation Research Record 1417, Transportation Research Board, Washington, D.C., 99-108.

Sun, H., & Ding, J. (2011). The comparison of fractal dimensions of cracks on reinforced concrete beam. *Advanced Materials Research, 291-294*, 1126-1130.

Takkalou, H. B., Hicks, R. G., & Esch, D. C. (1985). *An effect of mix ingredient on the behavior of rubber-Modified Mixes* (Report No. FHWA-AK-RD-86-05A). U.S. Department of Transportation: The Federal Highway Administration.

Takallou, H. B., Hicks, R. G., & Esch, D. C. (1986). *Effect of mix ingredients on the behavior of rubber-modified mixtures.* Transportation Research Record 1096, Transportation Research Board, Washington, D.C.

Takallou, H. B., & Hicks, R. G. (1988). *Development of improved mix and construction guidelines for rubber-modified asphalt pavements.* Transportation Research Record 1171, Transportation Research Board, Washington, D.C., 113-120.

Takallou, H.B. (1988). *Development of improved mix and construction guidelines for rubber modified asphalt mixtures.* Transportation Research Record 1171, Transportation Research Board, Washington, D.C.

Tashman, L., Masad, E., Little, D., & Lytton, R. (2004). Damage evolution in triaxial compression tests of HMA at high temperatures. *Association of Asphalt Paving Technologists, 73*, 53-87.

Tashman, L., Masad, E., Peterson, B., & Saleh, H. (2001). Internal structure analysis of asphalt mixes to improve the simulation of superpave gyratory compaction to field conditions. *Journal of the Association of Asphalt Paving Technologists, 70*, 605-645.

Tashman, L., Wang, L. B., & Thyagarajan, S. (2007). Microstructure characterisation for modelling HMA behaviour using imaging technology. *International Journal of Road Materials and Pavement Design, 8*(2), 207-238.

Tashman, L. (2003). *Microstructural continuum model for asphalt concrete*. Ph.D. Thesis, Texas A & M University, US.

Thyagarajan, S., Tashman, L., Masad, E., Bayomy, F. (2009). The heterogencity and mechanical response of hot mix asphalt laboratory specimens. *International Journal of Pavement Engineering, 11*(2), 107-121.

Tsai, D. M. (1995). *A fast thresholding selection procedure for multimodal and unimodal histograms*. Pattern Recognation Letters, 16, 653-666.

Tschegg, E. K., Jamek, M., & Lugmayr, R. (2011). Fatigue crack growth in asphalt and asphalt-interfaces. *Engineering Fracture Mechanics, 78*, 1044-1054.

Underwood, E. E. (1970). *Quantitative stereology*. Massachusetts: Addison-Wesley Publishing Co.

Vincent, D., Chantel, D. L. R., & Olivier, B. (2010). Influence of the compaction process on the air void homogeneity of asphalt mixtures samples. *Construction and Building Materials, 24*(6), 885-897.

Voyiadjis. G. Z., & Kattan, I. (2006). *Advances in damage mechanics: Metals in metal matrix composites and introduction to fabric tensors* (2nd ed.). London: Elsevier.

Wang, L. B., Paul, H. S., Harman, T., & D'Angelo, J. (2004). Characterization of aggregates and asphalt concrete using x-ray tomography. *Association of Asphalt Paving Technologists, 73*, 467-500.

Wang, L. B., Frost, J. D., & Shasidhar, N. (2001). *Microstructure study of westrack mixture from x-ray tomography images*. Transportation Research Record 1767, Transportation Research Board, Washington, D.C., 85-94.

Wang, L. B., Frost J. D., Voyiadjis, G. Z., & Harman, T. (2003). Quantification of damage parameters using x-ray tomography images. *Mechanics of Materials, 35*, 777-790.

Widyatmoko, I., Elliott, R.C., Grenfell, J., Airey, G.D., Collop, A.C., & Waite, S. (2009). Characteristics of rubberised bitumen blends. *Proceedings of the Asphalt Rubber 2009*, Nanjing, China.

Widyatmoko, I., Ellis, C., & Read, J.M. (1999). Energy dissipation and the deformation resistance of bituminous mixtures. *Materials and Structures, 32*, 218-223.

Wojnar, L. (1999). *Image analysis: Applications in materials engineering.* Boca Raton, FL: CRC Press.

Xiao, F., Putman, B. J., & Amirkhanian, S. N. (2006). Laboratory investigation of dimensional changes of crumb rubber reacting with asphalt binder. *Asphalt-Rubber 2006 Conference,* Palm Springs, California, USA.

Yue, Z. Q., Bekking, W., & Morin, I. (1995). *Application of digital image processing to quantitative study of asphalt concrete microstructure.* Transportation Research Record 1492, Transportation Research Board, Washington, D C, 53-60.

Yue, Z. Q., & Morin, I. (1996). Digital image processing for aggregate orientation in asphalt concrete mixtures. *Canadian Journal of Civil Engineering, 23*, 480-489.

Zelelew, H. M., & Papagiannakis, A. T. (2011). A volumetrics-based thresholding algorithm for processing asphalt concrete x-ray CT images. *International Journal of Pavement Engineering, 12*(6), 543-551.

Zhiming, S. (2009). *Characterisation of asphalt concrete mixtures: Microdamages and healing.* Germany: VDM Verlag Dr. Müller Aktiengesellschaft & Co. KG, Saarbrüken.